MOLECULAR GAS AND STAR FORMATION IN NEARBY STARBURST GALAXY MERGERS

MOLECULAR GAS AND STAR FORMATION IN NEARBY STARBURST GALAXY MERGERS

By

HAO HE, M.SC.

A Thesis
Submitted to the School of Graduate Studies
in the Partial Fulfilment of the Requirements
for the Degree
Ph.D. of Science

McMaster University

McMaster University

Doctor of Philosophy (2023)

Hamilton, Ontario (Physics and Astronomy)

TITLE: Molecular Gas and Star Formation in Nearby Starburst Galaxy Mergers

AUTHOR: Hao He, M.Sc. (McMaster University)

SUPERVISOR: Dr. Christine D. Wilson

NUMBER OF PAGES: xxii, 254

Abstract

In this thesis, I aim to understand the interplay between giant molecular clouds (GMCs) and star formation in nearby starburst galaxy mergers. I start with a case study on the unique star formation products, young massive clusters (YMCs), in a typical starburst galaxy merger, the Antennae. Based on the Atacama Large Millimeter/submillimeter Array (ALMA) radio continuum data, I identify 6 potential YMCs in the Antennae overlap region. I further perform virial analyses on these YMCs combining the radio continuum data and archival CO 2-1 data and confirm these radio sources are bound structures that are likely to be future star clusters. I also cross match our detected YMCs with optical clusters identified using Hubble Space Telescope (HST) data and find a good correspondence in the number of produced total ionizing photon, but a significant position offsets between these two types of objects, which suggests these radio detected YMCs are going through an emerging stage out of GMCs. I further compare the YMC stellar mass and gas mass with GMC-scale properties and find more than 50% of GMC star formation happens in these YMCs, with more massive GMCs tending to produce more massive YMCs. Overall, my study provides a rare sample of embedded YMCs and points out the close connection between GMC properties and YMC formation.

I then approach the open question of the interplay between GMCs and star formation from the molecular gas side by quantifying GMC dynamical states and correlating these GMC quantities with star formation rate (SFR). In this study I perform a comparison between the observed galaxy mergers from the ALMA telescope and the simulated mergers from the idealized Feedback In Realistic Environment (FIRE) simulation. I find that GMCs in the simulated mergers before the merging event are similar to the observed GMCs in normal spiral galaxies, which suggests the success in the simulation to reproduce realistic GMCs. After the merging, GMCs become

denser, more turbulent and less gravitationally bound. I measure the virial parameter of the simulated GMCs and find that the virial parameter variation is similar to the star formation rate (SFR) variation, which suggests that starburst events are responsible for dispersing GMCs and making them less gravitationally bound. I also correlate GMC virial parameter with gas depletion time, which indicates how fast the star formation activity is using up all the available gas, and find no correlation between these two quantities. Our results suggest that star formation activities are more complicated than what we thought and large-scale environmental factors might be responsible for regulating star formation activities in starburst mergers.

I then constrain GMC physical properties from the observational side by applying RADEX modeling to multiple CO and ^{13}CO observational data. Specifically, I aim to constrain the CO-to-H$_2$ conversion factor (α_{CO}) that is crucial for measuring GMC surface density and virial parameter. I find that α_{CO} values in the Antennae are $\sim$ 4 times smaller than that of the Milky Way, and hence GMCs in the Antennae are less gravitationally bound than normal spiral galaxies, which is consistent with the prediction of my previous simulation project. I further correlate α_{CO} with multiple physical quantities and observables and find strong correlations between α_{CO} and CO J=1-0 intensity, optical depth, ^{13}CO/^{12}CO ratio, velocity dispersion and virial parameter. Compared with literature studies, I confirm that the low α_{CO} in starburst systems is caused by low optical depth due to GMCs out of virial equilibrium. My study also provides potential calibration tools to measure α_{CO} spatial variation within individual galaxies.

These projects provide a starting point for us to understand the molecular gas and star formation in the most extreme starburst environments. It is crucial to expand analyses of individual galaxies in these projects to a broader, more statistically significant sample to understand the universal physics that regulates star formation activities in these systems.

Acknowledgments

I would like to thank my supervisor Dr. Christine Wilson for accompanying me all along through this journey. Since our first meeting seven years ago, you have always been a wonderful teacher to me in science, a good friend to me in life and a role model to me in my career. I will miss our weekly meeting where we had open and honest science argument, miss our time together at conference where you introduced me to all these astronomy big names and miss the casual chat we have at numerous social events where you told me all the fun anecdotes.

I would also like to thank the members of my committee, Dr. Laura Parker and Dr. James Wadsley, for all the genuine help you provided in my research. You inspired me to think from a different perspective, challenged me so that I can improve my work to perfection and encouraged me by celebrating every step of my achievement.

I would also like to thank my ALMA internship supervisor, Dr. William Dent, for the remote but wholehearted support to my project during the Covid time. I miss all the fun meetings we had in discussing ALMA instrumentation and observation scheduling. I am looking forward to meeting you in person in the future.

Thank you to all the people in P&A department, new and long departed, who made it my second home. Thank you, Nathan, Rob and Jeremy, for your help in sidewalk astronomy activities. Your unconditional support and enthusiasm in outreach inspired me to become a better organizer. Thanks to my friend and frequent squash partners, Blake, Lili, Ryan and Billy, for the interesting and intense match where we fully relieve ourselves from the stress of work. Thank you, Dr. Jiayi Sun, for all the fun conversations we have on every aspect of academia life. Your knowledge and insights expanded my view to the entire field. Thank you, Lisa and Hyunjin, for all the mulberry picking together in the summer, which is full of fun and joy. Thank you, Afshin, for coffee you invited me and joyful discussions we had about us and

the world. Thank you, Celine, for being a patient teacher and friend to teach me German and German cultures, which will be extremely helpful when I move there for my postdoc.

Thank you to my roommates, Peng Dong, Kezhuan Gu and Guang Wang, for all the walks we took, all the dinners we had and all the jokes we made. Living in another country is always a challenge but your company made my life easier and more fun.

Finally thank you to my parents Chunmei Lyu and Jiyue He for the wholehearted support throughout my entire life. You are like the beacon to me when I sail through this journey. Even though sometimes I feel depressed or dejected, I will never lose the sense of direction in my life because of you.

Contents

List of Figures

List of Tables

List of Abbreviations

AGN Active Galactic Nucleus.

ALMA Atacama Large Millimeter/Submillimeter Array.

CFE the cluster formation efficiency.

CMD Color Magnitude Diagram.

CMF Cluster Mass Function.

CMZ Central Molecular Zone.

CNM Cold Neutral Medium.

CO carbon monoxide.

EMPIRE EMIR Multi-line Probe of the ISM Regulating Galaxy Evolution.

FIR far-infrared.

FUV far ultra-violet.

GCs Globular Clusters.

GMCs giant molecular clouds.

HST Hubble Space Telescope.

IFU integral field unit.

IR infrared.

ISM interstellar medium.

JWST James Webb Space Telescope.

LMC Large Magellanic Cloud.

LTE local thermal equilibrium.

LVG large velocity gradient.

ngVLA The Next Generation Very Large Array.

PAH Polycyclic Aromatic Hydrocarbons.

PDF probability density function.

PHANGS-ALMA Physics at High Angular resolution in Nearby GalaxieS with ALMA.

PWV precipitable water vapour.

SDSS Sloan Digital Sky Survey.

SED spectral energy distribution.

SF star forming.

SFR star formation rate.

SKA Square Kilometre Array.

SMC Small Magellanic Cloud.

SMGs submillimeter galaxies.

SNe supernovae.

UV ultra-violet.

VLA Very Large Array.

WIM Warm Ionized Medium.

WNM Warm Neutral Medium.

YMCs Young Massive Clusters.

Co-authorship

Chapters 2, 3 and 4 and Appendix A of this thesis contain original scientific research written by myself, Hao He. Chapter 2 has been published as a peer-reviewed journal article in the Astrophysical Journal (ApJ). The citation for this work is: He, H.; Wilson, C. D.; Brunetti, N.; Finn, M.; Bemis, A.; Johnson, K. 2022, "Embedded Young Massive Star Clusters in the Antennae Merger", ApJ, 928, 57. This work was co-authored with my supervisor Dr. Christine D. Wilson. The remaining authors, Dr. Nathan Brunetti, Dr. Molly Finn, Dr. Ashley Bemis and Dr. Kelsey Johhnson, aided in preparing the observing proposal and provided helpful comments and suggestions on the article draft. Chapter 3 has been published as a peer-reviewed journal article ApJ. The citation for this work is: He, H.; Bottrell, C.; Wilson, C.D.; Moreno, J.; Burkhart, B.; Hayward C.C.; Hernquist, L.; Twum, A. 2023, "Molecular Gas and Star Formation in Nearby Starburst Mergers", ApJ, 950, 56. This work was co-authored with my supervisor Dr. Christine D. Wilson. The second author, Dr. Connor Bottrell, converted the original simulation data into mock observational data and provided helpful comments and suggestions on the article draft. The forth author, Dr. Jorge Moreno, led the simulation project that provided data analysed in this work and provided helpful comments in the article draft. The remaining coauthors, Dr. Blakesley Burkhart, Dr. Christopher C. Hayward, Dr. Lars Hernquist and Angela Twum, provided helpful comments and suggestions on the article draft. Chapter 4 is in preparation and will be submitted to a peer-reviewed journal. The author list is : He H., Wilson C.D. This work was co-authored with my supervisor, Dr. Christine D. Wilson. Appendix A has been published as a peer-reviewed journal article in the Publications of the Astronomical Society of the Pacific (PASP). The citation of this work is: He, H.; Dent, W.R.F; Wilson, C. D. 2022, "Tracking ALMA System Temperature with Water Vapor Data at High Frequency", PASP, 134, 125001. This work was co-authored with my ALMA insternship supervisor, Dr. William R.F. Dent, and my supervisor Dr. Christine D. Wilson.

I hereby grant an irrevocable, non-exclusive license to McMaster University and Library and Archives Canada to reproduce the material as part of this thesis.

Chapter 1

Introduction

1.1 Galaxy Evolution and Star Formation

In our universe, there are countless galaxies, each an assembly of billions of stars. Based on observations, we classify these galaxies into multiple types (e.g. elliptical, spiral and merging galaxies) based on their shapes. Recent studies (Springel & Hernquist 2005; Mac Low 2013) show that galaxies can transform from one type to another, and this transformation process (a.k.a. galaxy evolution) is closely tied to the evolution of our universe. Therefore, to understand how our universe became the way it is, it is crucial to understand the physics that drives this galaxy evolution.

The most well-known galaxy classification scheme is the "Hubble Tuning Fork" (Fig. 1.1). On the left of the Hubble tuning fork are elliptical galaxies, arranged in order of higher ellipticity from left to right. In the right part of the diagram are spiral galaxies that are sub-categorized into barred and unbarred galaxies based on the existence of the central bar feature. From the left to right, the central bulge feature becomes less dominant while the spiral arm feature becomes more prominant. Compared to elliptical galaxies, spiral galaxies appear bluer, which suggests a higher fraction of young stars and hence higher star formation rate (SFR) at present (Fig. 1.2). Early theories (e.g. Toomre 1977) suggest that ellipticals can be formed through the merging of spiral galaxies. In observations, we have also found various signatures from past merging events in those giant ellipticals. For example, more than half of the giant ellipticals in the center of galaxy clusters are found to have multiple nuclei that

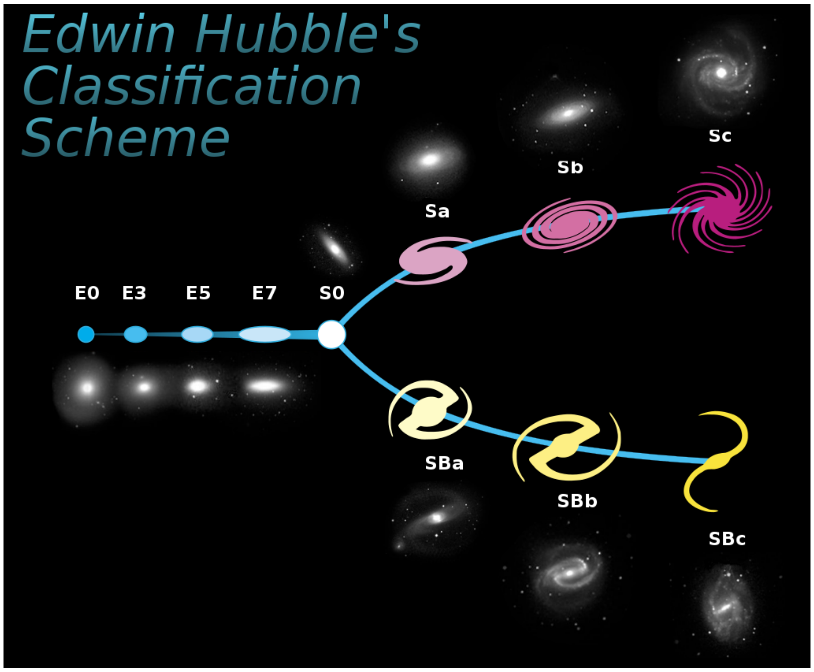

Figure 1.1: Hubble tuning fork diagram (credit: NASA & ESA).

have velocities different from the overall velocity of the galaxy (Carroll & Ostlie 2017). Furthermore, the merging scenario can help to explain the morphological-density relation (Oemler 1974), which shows that giant ellipticals tend to appear in the central dense region of galaxy clusters while the spirals are generally found in the less dense periphery. This evolution path also requires certain physical mechanisms to suppress or stop star forming (SF) activities in the resultant elliptical galaxies, known as galaxy quenching. It has been found that galaxy quenching involves both large-scale galactic environmental contributions (e.g. ram pressure stripping, strangulation) and small-scale secular evolution contribution (e.g. morphological quenching). Therefore, it is important to study detailed structures of each type of galaxy and build connections between different structural properties.

1.1.1 Milky Way and Nearby Spiral galaxies

Spiral galaxies are one of the most common type of galaxies in our local universe. Our home galaxy, the Milky Way, is a spiral galaxy with a strong bar (a.k.a barred galaxy Gerhard 2002). Since we live inside the Milky Way, we are able to study different structures and components of the Milky Way in extreme detail, which provides us insights on physical properties of other nearby spiral galaxies. The Milky Way is composed of stellar disk, molecular disk, H I disk, stellar halo and dark matter halo (Carroll & Ostlie 2017). The Milky Way has stellar mass of 10^{11} $\mathrm{M}_\odot$. Most of the Milky Way mass is in the form of dark matter, which is the dominant component of the dark halo. The dark matter halo has size of $\sim$ 200 kpc. The stellar halo is mainly composed of globular clusters, which are believed to be formed right after the birth of the universe. The Milky Way also has thick (scale height $H \sim 1$ kpc) and thin stellar disk ($H \sim 0.35$ kpc), with radius of $\sim$ 25 kpc. The stellar population in the thin disk is younger than those in the thick disk, which suggests that the star formation activities recently happened in the thin disk (Carroll & Ostlie 2017). In the Milky Way disk, there is also various gas component. Specifically, there is an H I disk that extends to the similar radius of the stellar disk ($\sim$ 25 kpc Carroll & Ostlie 2017). Besides the H I disk, there are various molecular H_2 clouds spread across the Milky Way inner disk. It is believed that star formation activities are still happening in these molecular clouds (Lada et al. 1993). Specifically, the Milky Way center has a large molecular gas reservoir, known as the Central Molecular Zone (CMZ). However, it is found that the CMZ has relatively low SFR (Lu et al. 2019). This makes the CMZ an interesting target to study how different environmental factors contribute to the SF activity.

However, the Milky Way is not quite representative of typical spiral galaxies. Based on the total stellar mass and SFR of the Milky Way, it falls into the category of green valley galaxies (Bland-Hawthorn & Gerhard 2016). In contrast, most spiral galaxies occupy the upper half of the contour in the Fig. 1.2 parameter space, which suggests that typical spiral galaxies have more active SF activities than our Milky Way. It is widely believed that green-valley galaxies represent a transition stage from blue spirals to red giant ellipticals.

Spiral galaxies can be further sub-categorized based on the existence and prominence of the central bulge, bar and spiral arms. These structures are commonly found in nearby spiral galaxies. Specifically, two thirds of nearby spiral galaxies are found to have bars (e.g. de Vaucouleurs 1963; Eskridge et al. 2000; Menéndez-Delmestre et al. 2007; Masters et al. 2011). In addition, many of these spiral galaxies, specifically early-type spirals, have inner ring features at the center (Comerón et al. 2014; Buta et al. 2015). These structural features have significant impact on the spatial arrangement of the cold ISM, which is the fuel for SF activities, and hence the spatial variation

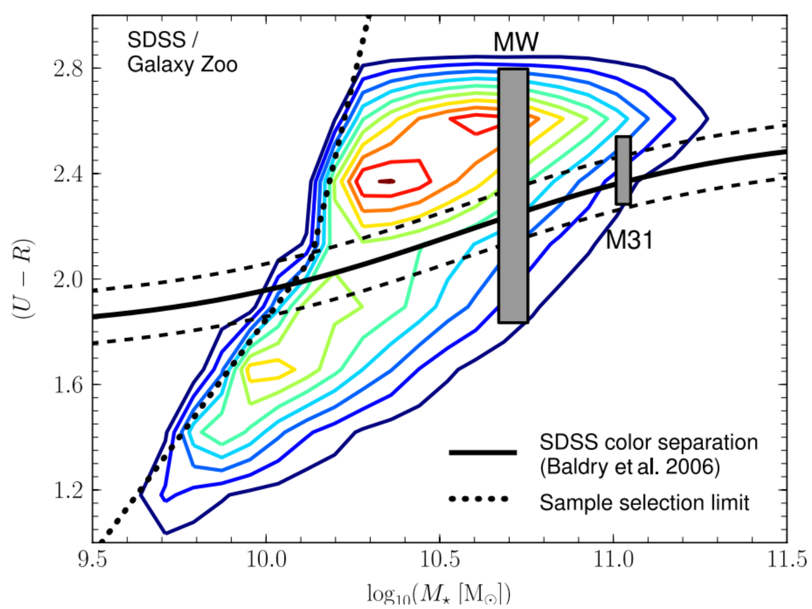

Figure 1.2: (U-R) color versus stellar mass ($M_\star$) contour for SDSS galaxies (Mutch et al. 2011). The contours are linearly spaced. The dotted line indicates the detection limit for the sample. The solid line indicates the best-fit division line for the bimodal distribution. The bounding dashed lines enclose the green-valley region. The gray rectangles indicate the location and uncertainty of the Milky Way and M 31 in this parameter space.

of SFR. For example, it has been found that galactic bars act to funnel the gas from the outer disk into the central region, and hence enhance the central SFR (e.g. Chown et al. 2019). Furthermore, most of cold ISM and SFR lies in structures, such as spiral arms and inner rings. The spatial alignment between these stellar structures and the ISM and SFR distributions suggests that the galactic gravitational potential plays an important role in governing gas and star formation distribution (e.g. Schinnerer et al. 2013; Sormani et al. 2020). In contrast, the central bulge can induce morphological quenching by maintaining the disk stability (e.g. Martig et al. 2009). Due to the complexity of spiral galaxy structures and the large dynamic range of spatial scales involved in SF activity, it is challenging but yet crucial to build quantitative models on how large-scale structures influence SF activities. So far, only a few works (e.g. Meidt et al. 2018) have made this attempt.

1.1.2 Merging Galaxies

Galaxy Mergers in Cosmological Context

In our universe, merging galaxies play an important role in galaxy evolution. Specifically, galaxy merging is responsible for producing a large portion of elliptical galaxies (Toomre 1977). One imminent consequence of merging activities is that it could produce starburst galaxies, specifically for major mergers where two galaxies have similar masses. In theory, when two galaxies collide with each other, the angular momentum of the gas disk decreases, which induces gas inflow towards the center and triggers starburst activities in the center (e.g. Mihos & Hernquist 1996). Observational comparison between galaxy mergers and normal star forming galaxies in our local universe confirms this scenario (e.g. Violino et al. 2018; Pan et al. 2019; Thorp et al. 2022). Furthermore, high-redshift observations find that the cosmic star formation history is tightly related to the overall galaxy merging history. The measured average SFR volume density peaks at z $\sim$ 2 (Madau et al. 1998), which also corresponds to the era when the fraction of mergers of peaks (10%, Ryan et al. 2008). However, recent observations of galaxies around the epoch of the star formation peak (e.g. Rodighiero et al. 2011; Stott et al. 2013; Lofthouse et al. 2017) indicate that the major merger frequency is too low to make a major contribution to SFR enhancement at that time. Alternative explanations are that the SFR enhancement is either due to more frequent minor merger events (e.g. Kaviraj 2014a,b) or simply higher gas fractions in secular galaxies (e.g. Dekel et al. 2009; Tacconi et al. 2010; Geach et al. 2011; Béthermin et al. 2015; Martin et al. 2017). Bournaud et al. (2015) also suggests in their simulations that star formation in major merger and high-redshift galaxy disks might have different modes. To disentangle these factors, we need to perform both statistical studies of large galaxy merger samples and case-by-case studies on resolved star formation properties in individual mergers.

Observed Local Starburst Mergers

In the 1980s , the IRAS satellite identified a new class of galaxies with extremely high infrared (IR) luminosity (Sanders & Mirabel 1996), known as ultra/ luminous infrared galaxies, or (U)LIRGs ($L_{\rm IR} > 10^{11}$ L$_\odot$ for LIRG and $L_{\rm IR} > 10^{12}$ L$_\odot$ for ULIRG). In these environments, most UV or optical radiation from young stars has been absorbed by the dust (Howell et al. 2010) and re-radiated at infrared wavelengths, results in the extremely high IR luminosity. Multi-wavelength comparisons, specifically the comparison with optical (Sanders et al. 1988) and H I data (Iono et al. 2005), showed that those objects are mostly merging pairs with extended tidal features. Based on the morphology, these mergers have been categorized into different stages along the merging event sequence (Fig. 1.3). It is found that mergers in the final coalescing stage tend to have the highest infrared luminosity and hence constitute most of the ULIRGs (e.g. Larson et al. 2016; Stierwalt et al. 2013). For interactive pairs before the final coalesce, those studies also show that major mergers, which consists of two gas rich spirals with similar masses, generally have higher IR luminosity and hence higher SFR than minor mergers and secular galaxies. These results are generally consistent with simulation predictions (e.g. Cox et al. 2008).

However, a significant fraction of IR radiation in U/LIRGs can come from an Active Galactic Nucleus (AGN), which brings degeneracy in determining SFR in those systems. It has been found that $\sim$ 18% of LIRGs and $\sim$ 60% of ULIRGs show AGN signatures (Petric et al. 2011; U et al. 2012). Furthermore, $\sim$ 10% of overall U/LIRGs are found to have AGN contributing more than 50% of the total IR luminosity. Various methods have been generally applied to determine AGN IR contribution, such as spectral energy distribution (SED) fitting and measurement of Polycyclic Aromatic Hydrocarbons (PAH) equivalent width (e.g. Díaz-Santos et al. 2017). However, it still remains challenging to accurately quantify the AGN IR contribution due to the low-spatial resolution of IR data. The recent launch of the James Webb Space Telescope

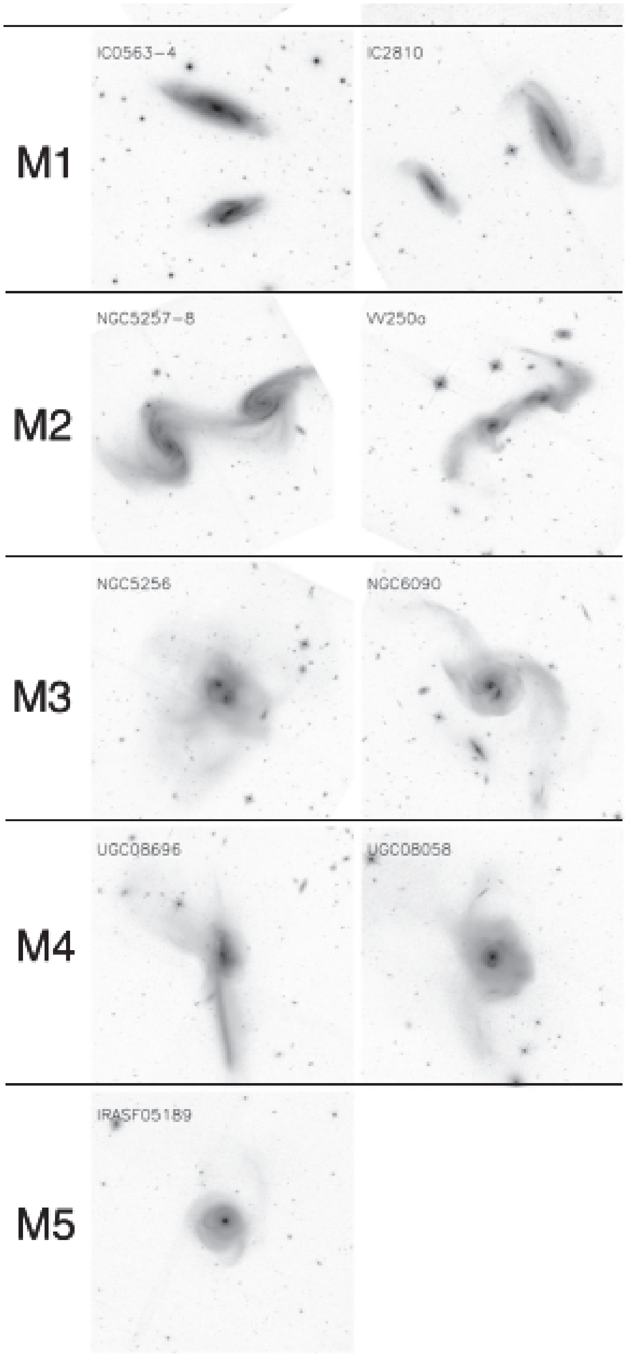

Figure 1.3: Example of different merging stages from the GOALS sample (Larson et al. 2016). The images shown are from Hubble Space Telescope (HST) I band images. From M1 to M5 represents the time sequence of merging events from early interaction to final coalesce.

(JWST) will greatly help us to disentangle the IR contribution from AGN activities in the very centers of merging galaxies (Rich et al. 2023).

Alternatively, various studies have tried to detect SFR in U/LIRGs using radio continuum. In theory, the free-free portion of the radio continuum comes from H II gas ionized by young stars, and hence can be used to calculate SFR (see Murphy et al. 2011, for detailed discussion). The radio continuum has much better resolution than the IR observations and suffers less dust extinction than optical or UV observations. Condon et al. (1991) performed the first subkiloparsec-scale radio continuum study of a sample of 40 local U/LIRGs at 8.4 GHz using the Karl G. Jansky Very Large Array (VLA). They found that most of their dust-obscured nuclei are powered by starbursts, with many as compact as 100 pc in size. Higher frequency and resolution observations (Barcos-Muñoz et al. 2017; Song et al. 2022) find that those compact radio regions can be as small as 30 pc. These compact regions can have SFR surface density reaching 1000 $M_\odot yr^{-1}$ pc^{-2}, a factor of 100 times higher than star forming regions with similar size in normal spiral galaxies (Song et al. 2022). Thompson et al. (2005) argue that these star-forming regions have reached the Eddington limit and their maximal capability to form stars in pressure balance. Therefore, we would expect different star forming modes and feedback mechanisms in those extreme starburst regions.

Based on the scenario that the starburst events in U/LIRGs are triggered by the molecular gas concentration due to tidal interactions, we would expect these systems show different molecular gas properties than normal spiral galaxies. For now, most U/LIRGs have CO observations from the SMA (Wilson et al. 2008) and Nobeyama (Yamashita et al. 2017). These high resolution observations of ^{12}CO have confirmed that for most mergers, the gas is concentrated near the center (e.g. Wilson et al. 2008). Moreover, the gas mass in the central region of mergers is significantly higher than isolated spiral galaxies (Yamashita et al. 2017). Several U/LIRGs (e.g. NGC 2623 and NGC 5258 Evans et al. 2008; He et al. 2020) have also been found to show off-center gas concentrations, which could be due to a compressive tidal field (Renaud et al. 2014).

Simulation of Galaxy Mergers

Early galaxy merger simulations (e.g. Hernquist 1989; Barnes & Hernquist 1991, 1996; Mihos & Hernquist 1996) showed that merging can reduce the angular momentum

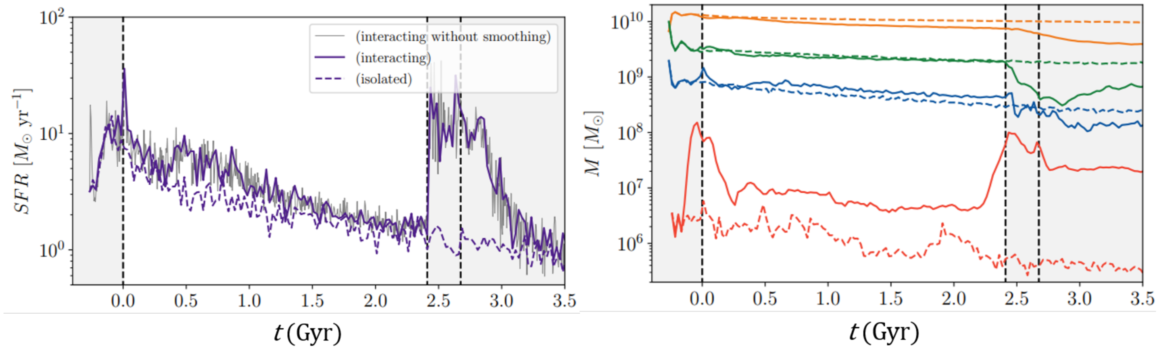

Figure 1.4: The SFR (left) and gas (right) evolution for a major merger as a function of time in simulations (Moreno et al. 2019). The three vertical dashed lines represent the time for the first, second passage and final coalesce. The solid lines represent the merger simulation while the dashed lines represent the control isolated galaxy simulation. In the right panel, the red, orange, green and blue represent hot ionized, warm neutral/ionized medium, cold neutral medium and molecular gas, respectively.

of the gas in the outer disk and bring gas inflow towards the center, hence causing a starburst event in the center. They showed that these starburst events generally happen following the close encounter between the two galaxies and the most intense one happens during the final coalesce stage (see Fig. 1.4). This intense starburst event will also deplete the majority of the molecular gas and eventually quench the star formation (e.g. Cox et al. 2008; Moreno et al. 2019), which is consistent with observations (e.g. Ellison et al. 2022) that shows post-mergers are more likely to have a shutdown of SFR following a previous starburst event. In addition, simulations (e.g. Renaud et al. 2014) show that gas concentration and starburst activities can also happen in the off-center region where a compressive turbulence field is dominant through tidal interactions.

Follow-up simulations (e.g. Cox et al. 2008) showed that the galaxy evolution path during the merging events is greatly affected by the pre-selected orbits and orientations, as well as the initial galaxy properties, such as stellar mass, gas fraction and bulge fraction. Specifically, these simulations show that major mergers with mass ratio close to 1 can enhance the SFR to the maximum extent. Due to complications from these factors, it remains challenging to compare merger simulations with observations. One approach is to sample simulation parameter space and find the optimal parameter sets that match a specific observed merger. One of the most popular observed targets to match is NGC 4038/9 (the Antennae), a starburst major merger that is going through the second peri-centric passage as suggested by simulations (Karl et al. 2010; Privon et al. 2013; Renaud et al. 2015). Privon et al. (2013) further performed simulation matches to 4 representative mergers (Arp 240, NGC 4038/9, Mice, NGC 2623) at different merging stages. These simulations are generally expensive and suffer from large parameter degeneracy using different star formation and stellar feedback models (see discussion in Karl et al. 2013).

Another approach is to run cosmological simulations and compare statistical properties of the observed and simulated mergers. Large-scale cosmological simulations, such as Illustris (Vogelsberger et al. 2014), Horizon-AGN (Dubois et al. 2014), EAGLE (Schaye et al. 2015), MassiveBlack-II (Khandai et al. 2015), SIMBA (Davé et al. 2019), IllustrisTNG (Pillepich et al. 2018) and FLAMINGO (Schaye et al. 2023) have produced vast number of galaxies spanning spatial scales across at least 100 Mpc, which enables statistical comparisons between complete samples of mergers and normal galaxies as well as observations and simulations. Under these simulation frameworks, a series of studies (e.g. Patton et al. 2013; Martin et al. 2017; Rodríguez Montero et al. 2019; Patton et al. 2020) find a major trend that smaller separation between two merging galaxies corresponds to higher SFR enhancement, which is consistent with observational measurements with Sloan Digital Sky Survey (SDSS) data (e.g. Scudder et al. 2015; Knapen et al. 2015).

Another challenge from the simulation side is the difficulty to model the multiphase ISM, specifically the cold-dense phase gas (molecular gas) that is directly related to the star formation. Recent simulations have made progress in incorporating realistic chemical networks and resolving small-scale ISM physics. However, most of these works are focused on normal spiral galaxies (e.g. Jeffreson et al. 2020; Benincasa et al. 2020) and only few studies have been performed on mergers. Narayanan & Krumholz (2014) show in their merger simulation that the SFR enhancement is well correlated with an increase in molecular gas properties, such as volume density, temperature and velocity dispersion. Moreno et al. (2019) perform idealized merger simulation under the FIRE-2 framework (Hopkins et al. 2018) and find that SFR enhancement is mostly correlated with an increasing amount of ultra-dense gas ($n > 1000$ cm^{-3}). Li et al. (2022) perform an Antennae-like major merger simulation under the SMUGGLE framework (Marinacci et al. 2019) and find that merging events can enhance SFR as well as the fraction of stars formed in star clusters, known as Cluster Mass

Function (CMF). Besides the idealized simulations mentioned above, several high-resolution cosmological zoom-in merger simulations have been performed to study details of mergers within a more realistic cosmological context. Rey et al. (2022) has performed a Milky-Way mass galaxy simulation under the VINTERGATAN framework (Agertz et al. 2021) and find that merging events can trigger SFR enhancement by increasing the amount of ultra-dense gas generated from tidal compression. However, they argue that this mechanism is not active at high redshift ($z > 4.8$) due to the lack of galactic disk structure.

1.2 Phases of the Interstellar Medium

The ISM is gas and dust that fill the space between stars. The ISM is an important component of the Milky Way and accounts for $\sim 15\%$ of total Milky Way mass. Based on the temperature, density and ionizing fraction, ISM gas can be categorized into different phases, as shown in Table 1.1. The thermal pressure for each ISM component is roughly the same (on the order of $\sim 10^3 - 10^4$ K cm^{-3}), which suggests that all these ISM components exist in a stable form. The existence of a multi-phase ISM requires certain cooling and heating mechanisms to drive the energy flow through the entire system. Generally speaking, the gas cools down through gravity-led infall and radiation from certain ISM species. This process will eventually lead to the collapse of molecular clouds and formation of new stars, which will provides various stellar feedback (e.g. photon ionization, radiation heating and supernovae) that heats up and disperses the surrounding ISM. These processes involve complex physics at various scales and are crucial for us to understand the galactic ecosystem.

In this section, I will briefly talk about H II regions and the Cold Neutral Medium (CNM) that are tightly related to the star formation activities at small scales (~ 100 pc). Molecular gas and related topics are discussed in a separate section.

1.2.1 H II regions

H II regions are created when UV radiation from stars ionizes and heats the surrounding gas. These UV photons, which are mostly created by massive O and B stars, carry energy greater than the hydrogen ionization potential (13.6 eV, equivalent to ~ 90 nm) and can therefore separate ions and electrons. The ions and electrons can recom-

Table 1.1: Summary of different ISM components in the Milky Way

ISM	M (10^9 $M_\odot$)	T_k (K)	n (cm^{-3})	how observed
corona gas	–	5×10^5	3×10^{-3}	• UV and X-ray • radio synchrotron radiation
warm ionized gas	1.0	8×10^3	0.3	• Optical lines • pulsar dispersion
warm neutral gas	4.0	8×10^3	0.5	• H I 21 cm line • optical and UV absorption lines
H II regions	0.05	10^4	$1 - 10^5$	• optical lines • radio free-free radiation
cold neutral	3.0	80	50	• H I 21 cm line • Optical and UV absorption lines
molecular	2.0	10	> 300	• Molecular lines (CO , C I, etc.) • dust FIR radiation

Adapted from Stahler & Palla (2004), Draine (2011) and Tielens (2005).

bine and emit series of recombination lines. In the mean time, free electrons can also scatter off from ions and hence generate free-free continuum emission. If these H II regions are in steady states, we would expect that they reach ionization equilibrium, where the ionization rate equals the recombination rate. Based on this balance, the size of H II regions can be determined. Strömgren (1939) first derive the size of H II regions in the case where a spherical volume of interstellar gas of uniform density is ionized by a central source, known as Stömgren radius, as

$$R = 1.2 \left(\frac{10^3 \text{ cm}^{-3}}{n} \right)^{2/3} \left(\frac{Q\left(H^0\right)}{5 \times 10^{49} \text{ photons s}^{-1}} \right)^{1/3} \text{ pc}, \tag{1.1}$$

where $Q\left(H^0\right)$ is total number of ionizing photons. Size/radius of H II regions is a key parameter to determine their pressure equilibrium state (Barnes et al. 2021, 2022). Their measurements show that typical H II regions in nearby galaxies generally have radii of 5 – 40 pc.

For a stable H II region, another important constraint is the energy balance, which is the balance between heating and cooling. The major heating mechanism for H II regions is photo-ionization (Tielens 2005). The cooling, on the other hand, depends on the metallicity of H II regions. For pure hydrogen nebulae without heavy elements, the major cooling channels are electron free-free emission and hydrogen recombination line emission. In this case, the H II electron temperature (T_e) derived from the energy balance is close to the central star effective temperature ($\sim 10^5$ K). This is expected to happen for H II regions ionized by the first generation of stars in the universe. For H II regions with heavy elements, which is generally the case in our local universe, the cooling process is much more effective through collisionally excited lines of these heavy elements (e.g., carbon, oxygen, and nitrogen) and hence the derived electron temperature is much lower ($\sim 10^4$ K), which is consistent with observations in the Milky Way (Tielens 2005). In fact, electron temperature variation for H II regions in the Milky Way is dominated by the metallicity variation and hence can be used as the metallicity probe (Osterbrock & Ferland 2006). In observations, T_e can be directly measured using radio (e.g. Balser et al. 2015; Wenger et al. 2019; Pineda et al. 2019) or optical auroral lines (e.g., O IIIλ4363, N IIλ5755, S IIIλ6312, O IIλ7320, 7330, summarized in Kreckel et al. 2022). These measurements are generally done by optical integral field unit (IFU) instruments, such as MUSE.

Since H II regions are directly created by ionizing photons from young massive stars, we can use emission from H II regions to measure the SFR. Based on stellar population synthesis models (e.g. Starburst99, Leitherer et al. 1999), the SFR can be calculated from the total number of ionizing photon number ($Q\left(H^0\right)$) using equation (Murphy et al. 2011)

$$\left(\frac{\mathrm{SFR}}{M_{\odot}\mathrm{yr}^{-1}}\right) = 7.29 \times 10^{-54} \left[\frac{Q\left(H^0\right)}{\mathrm{s}^{-1}}\right] \tag{1.2}$$

Note that this equation assumes a solar metallicity and a continuous constant SFR over a timescale of 100 Myr. Specifically, the SFR measurements depend on the star formation history of the system. If the observed system (e.g. young star clusters) has a much younger age than the timescale for the first supernovae to go off, we would expect the total ionizing photon number to trace the total stellar mass of the system. Under the assumption of single stellar population generated from an instantaneous starburst event, the stellar mass can be calculated as (Leroy et al. 2018)

$$M_{\star}\left(M_{\odot}\right) = 2.5 \times 10^{-47} \left[\frac{Q\left(H^0\right)}{\mathrm{s}^{-1}}\right] \tag{1.3}$$

To measure $Q\left(H^0\right)$ and hence SFR, we can either use hydrogen recombination lines or the radio free-free continuum emission. For hydrogen recombination lines, the most widely used one is the Hα line, the first line of the Balmer series. However, Hα suffers from dust extinctions that absorbs the optical photons and re-radiates the photons at IR wavelength for star forming galaxies with rich gas content. One method to account for the dust extinction in measured SFR is to combine the Hα and IR data, such as 24 μm data (Calzetti et al. 2007). Alternative methods include combining Hα with other hydrogen recombination lines, such as Hβ (using the Balmer decrement technique Calzetti et al. 1996), Paα (Calzetti et al. 2007) and Paβ (Cleri et al. 2021; Giménez-Arteaga et al. 2022). Another concern in using Hα to trace the SFR is the contribution from the Warm Ionized Medium (WIM). In the Milky Way, most recombination line emission (e.g. Hα) comes from these compact H II regions although most of the ionized gas resides in the WIM (Tielens 2005). However, for nearby galaxies, specifically starburst galaxies, WIM can contribute more than 60% of the Hα emission (e.g. the Antennae, Weilbacher et al. 2018). The energy sources of the WIM are still not clear. Spectral features, such as emission line ratios and ionizing spectrum, suggest that the WIM has additional ionizing sources besides the leaky photons from compact H II regions (see detailed discussion in Haffner et al. 2009). Therefore, it might add complication to use hydrogen recombination lines to trace SFR.

Radio free-free continuum emission is another SFR tracer that is related to H II regions. Compared to optical hydrogen recombination lines, radio continuum suffers almost no dust extinction. In radio observations, it is crucial to separate free-free continuum from the synchrotron radiation and dust grey-body emission to extract this component. A widely-applied approach is to fit an SED model to data at multiple frequencies assuming a power law function with a fixed spectral index for each component (Fig. 1.5). The free-free emission is optically thin generally above 5 GHz with spectral index of -0.1 (Allen & Kronberg 1998). The dust emission from surrounding cold gas is also mostly optically thin and generally follows a gray-body spectrum with spectral index of (2+β), where β is the dust opacity spectral index with values between 1 and 2 (Gordon et al. 2014). Synchrotron radiation generally comes from the supernovae remnants, with a spectral index of $\sim$ -0.8 (Murphy et al. 2011). Observations of H II regions show that synchrotron radiation is generally insignificant since most stars in H II regions are just formed and have not reached the supernovae stage (Ginsburg et al. 2016; Costa et al. 2021). Most radio continuum work on H II regions in starburst galaxies has been done using the VLA telescope. Condon et al. (1991) first performed the radio continuum study on 40 U/LIRGs with

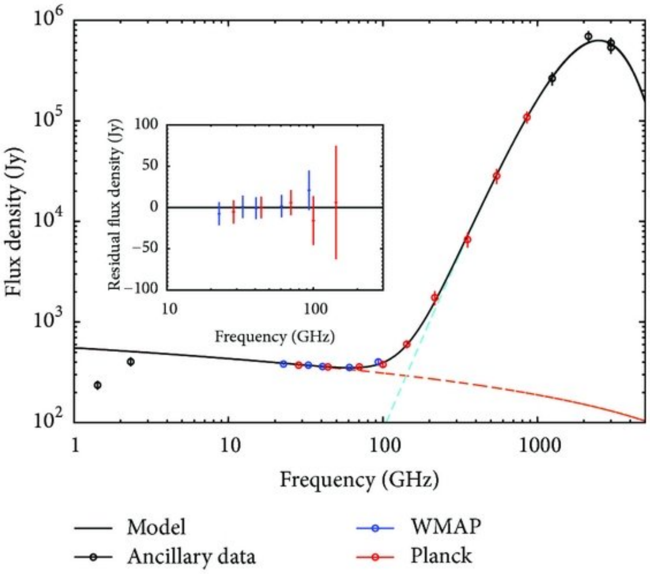

Figure 1.5: Spectral energy distribution for the Orion Nebulae (Dickinson 2013). The black solid line is the best-fit total SED while the red and blue dashed lines indicate best-fit free-free and dust continuum SED. The blue, red and black points are data from WMAP, Planck and the literature. We can see the free-free component is dominant at lower frequencies while the dust continuum is dominant at higher frequencies.

VLA observations at 84 GHz and found a relatively constant ratio between radio continuum and far-IR radiation in starburst galaxies, which suggests that radio free-free continuum can be used as a SFR tracer. With the upgraded bandwidth of the VLA, higher frequency observations are applied to these U/LIRGs (e.g. Barcos-Muñoz et al. 2017; Song et al. 2022), which allows higher resolution to resolve individual compact H II regions as well as less synchrotron radiation contamination. Moreover, recent works (e.g. Matthews et al. 2021) start to apply radio continuum observations from the VLA Sky Survey to probe the cosmic star formation history and find a relatively good agreement between radio SFR history and IR SFR history. The primary limitation to apply radio continuum as an SFR tracer in both the local and high-redshift universe is the low sensitivity of current instruments, which can only detect a small number of the strongest sources. In the near future, the construction and commissioning of Square Kilometre Array (SKA) and The Next Generation Very Large Array (ngVLA) will greatly increase the sensitivity and resolution of radio observations at the frequency range of 1 – 100 GHz.

1.2.2 Cold Neutral Medium

The CNM is one of two stable neutral ISM components that are mainly comprised of neutral hydrogen (H I). Compared to the other neutral gas component, the Warm Neutral Medium (WNM), the CNM has much colder temperature ($\sim$ 50 – 100 K) and higher density ($\sim$ 50 cm^{-3}). While the two components have comparable total mass, the CNM is more compactly distributed in small regions with size of $\sim$ 100 pc (Tielens 2005). In contrast, the WNM is more diffuse and fills most of the space in the Milky Way plane (volume filling factor of $\sim$ 60% Tielens 2005). There are also $\sim$ 20% of neutral gas in the intermediate unstable states (Heiles & Troland 2003) between these two phases (Murray et al. 2018a).

To keep the CNM in a steady state requires a balance between H_2 photodissociation and formation. H_2 molecules are mainly dissociated through far ultra-violet (FUV) absorption in the Lyman and Werner transitions in the wavelength range of 912 – 1100 Å. The excited H_2 molecule becomes photo-dissociated (10% of probability) or cascades down to its original state and emitting a series of IR photons (Black & Dalgarno 1976; Black & van Dishoeck 1987). The FUV radiation can be less effective deeper into the cloud due to dust extinction. H_2 self-shielding is also effective in preserving hydrogen molecules when the H_2 column density is greater than 10^{14} cm^{-2}

(Tielens 2005), which is important for H_2 formation in the early universe. The formation of the H_2 molecule is through quantum tunneling on the surface of dust grains (Tielens 2005) or combination between hydrogen and H^- (Glover 2003). Another important balance for a stable CNM phase is the energy balance between heating and cooling. In the CNM temperature regime, the cooling of the CNM is mainly through heavy metal lines, primarily the C II line at 158 μm (Tielens 2005). The heating process is mainly dominated by photo-electric heating through PAH molecules (Tielens 2005). In this process, far-UV photons carry enough energy to release electrons from the surface of the PAH grain. These free electrons can then heat up the dust and gas through collisional processes.

This neutral gas can only be observed directly using the 21-cm (1.4 GHz) hyperfine line in the microwave regime of the electromagnetic spectrum, produced by the spin flip of a hydrogen atom's electron. The 21-cm line is generally optically thin, but can be optically thick for clouds with H I column density greater than 10^{20} cm^{-2} (Tielens 2005). However, with H I observations alone, it is hard to separate optically thick CNM from optically thin WNM component. In our Milky Way, the CNM can be unambiguously detected through H I absorption towards bright background sources (e.g. Murray et al. 2018b; Jameson et al. 2019). However, this technique can only be applied to a small number of lines of sight. For extra-galactic H I studies, the H I observations further suffer from poor resolution, which blend in WNM components in our detection. A new technique to differentiate these two components is to take high velocity resolution H I spectra at each individual line of sight with resolution greater than 100 pc. If H I is optically thick, then the spectrum will have a "top-hat" shape instead of the general Gaussian line profile. Due to the high-resolution requirement, these studies are only done for the nearest galaxies (e.g. M31, M33) using VLA observations (e.g. Braun et al. 2009; Koch et al. 2021). In the future, the deployment of the SKA will enable us to apply this new technique to a more complete sample of nearby galaxies.

Another topic of interest is the ratio between H_2 and H I, which is an indicator of how fast molecular gas reservoir is replenished. Studies of the correlation between cold gas (H I + H_2) and SFR surface density (e.g. Bigiel et al. 2008; Leroy et al. 2008) show that the H I surface density saturates at a maximal value of 10 $M_\odot$ pc^{-2}, which suggests that molecular gas is dominant in the higher surface density regime. Observations of nearby galaxies (Wong & Blitz 2002; Blitz & Rosolowsky 2006) also show a tight correlation between the H_2-to-H I ratio and the external pressure with a power-law slope of ~ 1, which is consistent with the theoretical expectation (e.g. Elmegreen 1993) and simulation predictions (e.g. Robertson & Kravtsov 2008). However, all of these studies can only probe H I at kpc scales and hence are unable to show if H I directly converts to H_2 at large scales or it first self-collapses into GMC-like structures and then goes through the conversion to H_2. High resolution SKA H I data can help us to disentangle this degeneracy.

1.3 Molecular Gas

1.3.1 Observation of Molecular Gas

Molecular gas is the fuel for star formation activity and therefore is crucial to the evolution of galaxies. It is known that 70 % of regular matter by mass in the universe is hydrogen. Therefore, we would expect the majority of the molecular gas is H_2. However, because H_2 requires high temperatures to be excited, we cannot derive the H_2 mass directly from its emission lines. Similarly, helium is also stable and hard to excite. Therefore, we generally rely on rotational transitions of other molecules that are much less abundant as molecular gas tracers. We refer to readers to Fig. 10.9 in Tielens (2005) for a summary of most common molecular gas tracers.

After helium, the most abundant elements in the ISM are carbon and oxygen. In cold environments, they will form carbon monoxide (CO). CO is more easily excited compared with H_2, with an excitation temperature of 5.53 K. The critical density of H_2 for ^{12}CO J=1-0 emission is about 2200 cm^{-3} (Bolatto et al. 2013). The critical density for a molecular line $j \rightarrow k$ is traditionally defined as the density for which the net radiation decay rate from the higher transition j to the lower transition k equals the collisional excitation rate from lower k to higher j in the optically thin case. The critical density is generally considered as the density above which we start to see linear increase in molecular emission as gas density increases. For optically thick lines, such as ^{12}CO J=1-0, the critical density will be reduced due to photon trapping as $n_{\mathrm{eff}} = n_{\mathrm{crit}}/\tau$ (Shirley 2015), where τ is the optical depth. For ^{12}CO J=1-0 the typical optical depth value is about 2–10. Therefore, the effective critical density of ^{12}CO J=1-0 is close to the typical cold molecular gas density. Recently, ^{12}CO J=2-1 has started to become more favoured as a molecular gas tracer due to observational capabilities to achieve better resolution and sensitivity within a given amount of observing time. Therefore, quantifying the ^{12}CO J=2-1/1-0 ratio is critical for this alternative choice. It is generally found that this ratio ranges from 0.5 – 1.0 with median value of 0.7 for nearby galaxies (e.g. Leroy et al. 2021). However, for starburst U/LIRGs, the ^{12}CO J=2-1/1-0 ratio saturates towards 1.0 (e.g. Montoya Arroyave et al. 2023), which suggests both transitions are thermally excited. This result is consistent with theoretical calculations based on typical starburst gas properties (Salak et al. 2019) and simulation predictions (Bournaud et al. 2015). For high-redshift observations ($z > 2$), ^{12}CO J=4-3 or higher J transitions are used to trace the molecular gas as low J CO lines are redshifted out of observing frequency window (e.g. Dessauges-Zavadsky et al. 2019; Cassata et al. 2020). It is also critical to constrain ratios between these lines relative to ^{12}CO J=1-0 to accurately quantify molecular gas mass in these high-redshift galaxies, which has only been done by few studies. Michiyama et al. (2021) show that the ^{12}CO J=4-3/1-0 ratio for U/LIRGs has a median value of ~ 0.3 but spans a wide range between 0.1 – 0.8. Studies of high-z submillimeter galaxies (SMGs) show a ^{12}CO J=4-3/1-0 ratio of ~ 0.8, which suggests CO transitions in these galaxies are highly excited either due to higher gas temperature or volume density (Tielens 2005).

CO isotoplogues, such as ^{13}CO and C^{18}O, can also be used as molecular gas tracers. Compared to ^{12}CO, they are significantly less abundant. The typical ^{13}CO/^{12}CO line ratio is ~ 0.1 (e.g. Jiménez-Donaire et al. 2017; Cormier et al. 2018) for Milky Way and nearby spiral galaxies and ~ 0.03 for starburst U/LIRGs (Sliwa et al. 2017a; Brown & Wilson 2019). In comparison with ^{13}CO, C^{18}O is generally 7 to 10 times weaker in normal spiral galaxies (Langer & Penzias 1990; Jiménez-Donaire et al. 2017). However, for starburst U/LIRGs, C^{18}O can have comparable brightness as ^{13}CO (Greve et al. 2009; Matsushita et al. 2009; Brown & Wilson 2019). Since these CO isotopologues are less abundant, they are generally optically thin and therefore would be expected to better trace the amount of molecular gas. Specifically, for resolved gas structures at sub-GMC scales ($\lesssim$ 10 pc) where the systems are not necessarily in virial equilibrium, ^{12}CO is no longer a reliable tracer for calculating molecular gas mass (see detailed discussion in Section 1.3.4). In this case, CO isotopologue lines are a natural choice. Currently most observational work is focused on ^{13}CO lines since they are generally brighter than C^{18}O lines. In our Milky Way, the gas column density derived from ^{13}CO lines for subregions of individual giant molecular clouds (GMCs) is generally in agreement with other methods, such as dust extinction mapping (e.g. Pineda et al. 2010) and C I lines (e.g. Shimajiri et al. 2013). For nearby galaxies, due to the limited sensitivity and resolution of current instruments, most studies are focused on kpc-scale ^{13}CO variation relative to ^{12}CO lines. Cormier et al. (2018) performed a ^{13}CO and ^{12}CO comparison for nearby galaxies in the EMIR Multi-line Probe of the ISM Regulating Galaxy Evolution (EMPIRE) survey and they find the ^{13}CO-to-H$_2$ conversion factor has similar scatter to the ^{12}CO-to-H$_2$ conversion factor by comparing these two lines with dust emission. Note that the conversion from ^{13}CO line intensity to H$_2$ column density generally assumes that ^{13}CO lines are in local thermal equilibrium (LTE) condition (excitation temperature equal to gas kinetic temperature) and share the same excitation temperature and beam filling factor as ^{12}CO lines. However, since ^{13}CO lines are generally optically thin, they do not experience photon trapping and therefore have critical density $\sim$ 10 times higher than the corresponding ^{12}CO lines (Leroy et al. 2017). Therefore, ^{13}CO lines are probably subthermally excited in diffuse gas regions. In this case, it generally requires radiative transfer modeling of multiple ^{13}CO lines to constrain column density.

Besides CO and its isotopologues, the atomic carbon (C I) is an alternative molecular gas tracer due to its simple 3-level fine structure lines. Since both C I $^3P_1 -^3 P_0$ (rest frequency: 492.16 GHz) and C I $^3P_2 -^3 P_1$ (rest frequency: 809.344 GHz) lines are optically thin, the C I column density can be easily determined using excitation temperature derived from relative ratio between those two lines. Observations of nearby galaxies (Jiao et al. 2019; Dunne et al. 2022) show that C I luminosity is proportional to ^{12}CO J=1-0 luminosity across a wide range of galaxy populations, which favors C I as an alternative molecular gas tracer.

There are also molecular lines proposed as tracers of denser gas components. In extra-galactic studies, HCN and HCO$^+$ are the two most widely used dense gas tracers (e.g. Gao & Solomon 2004), with gas critical density generally above 10^5 cm^{-3} (Jiménez-Donaire et al. 2017). However, there is an argument between Galactic and extra-galactic observers on whether HCN and HCO$^+$ trace the dense clumps inside GMC. Observations for the Orion clouds (Pety et al. 2017) show that a large fraction of HCN is observed in diffuse gas regions similar to ^{12}CO while most N$_2$H$^+$ is observed in dense cores, which suggests N$_2$H$^+$ is a more reliable dense gas tracer. However, extra-galactic kpc-scale observations (Jiménez-Donaire et al. 2023) show that the ratio between HCN and N$_2$H$^+$ is relatively constant.

ALMA telescope

Most of these molecular rotational transitions lie in the wavelength range of 0.3 – 3 mm, and hence require observations from submillimetre telescopes. Currently, the world's largest and most powerful submillimetre telescope is the Atacama Large Millimeter/Submillimeter Array (ALMA), located on the Atacama Desert of northern Chile with elevation of 5000 m. It consists of fifty four 12 m dishes and twelve 7 m dishes. It has nine receivers that covers the spectral range of $\sim$ 40 – 950 GHz (Band 1 and Band 3 – 10). ALMA has total collecting area of 6560 m^2, 30 times larger than the collecting area of SMA and 3 times larger than that of NOEMA. In addition, the high elevation of the site significantly reduces the amount water vapor, measured by precipitable water vapour (PWV), which is the biggest factor in attenuating the celestial submillimetre signal (Condon & Ransom 2016), especially at high frequencies ($>$ 300 GHz). The average PWV for ALMA is $\sim$ 3 times lower than the PWV at NOEMA and $\sim$ 5 times lower than that at the VLA site (Bulter 1998, MMA memo Cortés et al. 2020, `https://www.iram.es/IRAMES/weather/tauMeter.html`). Altogether, ALMA achieves the highest sensitivity among all the submillimetre telescopes. Furthermore, as the largest submillimetre interferometry telescope, ALMA can achieve resolutions of 0.05 arcsec at 100 GHz (Band 1) and 0.005 arcsec at 800 GHz (Band 10). Currently, ALMA is going through a receiver upgrade. With the new wideband receiver, ALMA will double its bandwidth to 16 GHz and increase its correlated bandwidth by a factor of 4 to 68 (depending on the observing frequency bands), which will significantly increase the sensitivity and enable capture of multiple molecular lines in single observing tuning. The upgrade is expected to finish by 2030.

Data used in this thesis are mainly from Band 3, which covers radio continuum at $\sim$ 100 GHz, ^{12}CO J=1-0 and ^{13}CO J=1-0, Band 6, which covers radio continuum at $\sim$ 220 GHz and ^{12}CO J=2-1, ^{13}CO J=2-1 lines and Band 7, which covers the radio continuum at $\sim$ 350 GHz and ^{12}CO J=3-2 line. The ALMA calibration work in the appendix covers high frequency observations from Band 7 – 10, with PWV of $\sim$ 0.5 mm during observations.

1.3.2 Giant Molecular Clouds

GMCs in the Milky Way

CO observations show that molecular gas in our Milky Way exists in the form of GMCs (Tielens 2005). These GMCs are the major sites of star formation in our Milky Way (Lada et al. 1993). Therefore, it is crucial to characterize GMC properties in order to understand the interplay between gas and star formation. Based on early observations, Larson (1981) summarize three basic laws for GMCs in the Milky Way, which are:

1. GMCs have a relatively constant surface density
2. GMCs have a size-linewidth relation of $\sigma_v \propto R^{0.5}$ (R is GMC radius and σ_v is GMC velocity dispersion)
3. GMCs are mostly in virial equilibrium.

These are called Larson's laws. However, early observations were limited to GMCs in our solar neighborhood. These three laws are not independent. Any one of the laws can be derived if the other two laws hold. Later large Milky-Way surveys gradually built up a complete sample GMC catalog across the entire Galactic plane (references in Heyer & Dame 2015). One of the major observational challenges is to accurately identify individual cloud structures, which suffers from technical difficulties, such as velocity crowding, cloud blending and resolving ambiguous kinematic distances. With improving spatial and velocity resolution of our instruments as well as more accurate methods to measure the distance (e.g. masers, Honma et al. 2012, Reid et al. 2014), it is possible to synthesize the 3-dimensional information in CO data cubes to resolve individual clouds. At the same time, new techniques to decompose cloud structures from observational data cubes have been developed (e.g. Dendrogram Rosolowsky et al. 2008) to systematically solve the cloud identification challenges, specifically for regions with crowded clouds. These new techniques have been applied to recent observational studies (e.g. Rice et al. 2016; Rico-Villas et al. 2020; Miville-Deschênes et al. 2017; Colombo et al. 2019; Lada & Dame 2020) and result in a complete sample with more than 1000 GMCs. This new complete GMC sample allows for a statistically robust test of the three Larson's laws. These studies have clearly shown that GMC properties are not uniform in the Milky Way and are tied to the large-scale environment. Specifically, GMC surface density can decrease by a factor of 100 from the Galactic Center to the outer disk. The size-linewidth relation (Larson's second law) still seems to hold for GMCs in Galactic disk (e.g. Rice et al. 2016). However, GMCs in the Galactic center are found to have $\sigma_v \sim 5$ times higher than the value for GMCs in Galactic disk with a similar radius. Furthermore, GMCs in the outer Galactic disk generally show a smaller σ_v compared to those in the inner Galactic disk. Therefore, Larson's first and second law seems to result from limited cloud sample size. In contrast, most studies find that Larson's third law still holds for GMCs in a wide range of environments (Heyer & Dame 2015). The virial equilibrium indicates a balance between kinetic and gravitational potential energy, which indicates that GMCs are probably in a steady process to collapse and form stars instead of being dispersed in a short time. Assuming GMCs have a simple spherical structure, the virial parameter, $\alpha_{\rm vir}$, can be calculated as (Sun et al. 2018)

$$\begin{aligned}\alpha_{\rm vir} &= \frac{9\ln 2}{2\pi G}\frac{\sigma_v^2}{\Sigma_{\rm mol} R} \\ &= 5.77\left(\frac{\sigma_v}{\rm km\ s^{-1}}\right)^2\left(\frac{\Sigma_{\rm mol}}{\rm M_\odot}\right)^{-1}\left(\frac{R}{\rm 40pc}\right)^{-1},\end{aligned} \tag{1.4}$$

where $\Sigma_{\rm mol}$ is the GMC surface density, σ_v is the GMC velocity dispersion and R is the GMC radius. If $\alpha_{\rm vir}$ is lower than 1, it suggests GMCs are unstable and will collapse to form stars. On the other hand, high $\alpha_{\rm vir}$ means GMCs are out of gravitational bound state and cannot collapse purely by self-gravity. GMCs in the Milky Way are generally found to have $\alpha_{\rm vir}$ of $1 - 10$ (Heyer & Dame 2015). There are also systematic variations in $\alpha_{\rm vir}$ among GMCs in different Galactic regions. For example, GMCs in the CMZ generally have higher $\alpha_{\rm vir}$ by a factor of ~ 2 those in the disk (Oka et al. 2001), which might explain why these GMCs are less efficient in forming stars (Lu et al. 2019). On the other hand, GMCs in the outermost radii of the Milky Way also exhibit much higher $\alpha_{\rm vir}$ (Heyer et al. 2001). One possible explanation for such high $\alpha_{\rm vir}$ is that these GMCs are sustained by external pressures.

According to the turbulence star formation model (e.g. Krumholz & McKee 2005; Hennebelle & Chabrier 2011; Padoan & Nordlund 2011), the efficiency for a GMC to form stars is directly linked to the GMC dynamical state, especially the Mach number (ratio between σ_v and sound speed) and $\alpha_{\rm vir}$. However, recent observations (Lee et al. 2016) show that the observed scatter in the efficiency per free-fall time ($\epsilon_{\rm ff}$) is significantly larger than the predicted scatter from these models. Recent simulations applying modified turbulence models with a power-law tail in the gas density distribution (e.g. Burkhart 2018; Grudic et al. 2019) suggest that the spread of clouds at different evolutionary stages, which involves cloud collapsing and stellar feedback, can contribute to the observed scatter. For example, $\epsilon_{\rm ff}$ can be artificially enhanced during the gas dispersal stage because of the extremely short gas depletion time due to no gas left.

GMCs in nearby galaxies and PHANGS-ALMA survey

To expand our understanding of GMCs in different galactic environments, we need to observe GMCs in different types of nearby galaxies. The extra-galactic study of GMCs started to take off from the early 2000s with the progress in instrumentation and observing techniques. Compared to Milky Way observations, extra-galactic observations can look at GMCs from a face-on perspective, which eliminates the distance ambiguity and reduces the blending of clouds along the same line of sight. Early extra-galactic observations (references in Fukui & Kawamura 2010) were focused on very nearby systems, such as the Small Magellanic Cloud (SMC), the Large Magellanic Cloud (LMC), M 31 and M 33, etc. In general, they found that GMCs in these nearby systems were still generally in virial equilibrium with the ^{12}CO J=1-0 luminosity proportional to the GMC virial mass. The size-linewidth relation also holds for very nearby galaxies but with a very limited dynamic range of size and a relatively large scatter in σ_v. One of the biggest uncertainties in measuring GMC mass and its related quantities, such as $\Sigma_{\rm mol}$ and $\alpha_{\rm vir}$, is the varying CO-to-H_2 conversion factor, $\alpha_{\rm CO}$. Specifically, the SMC has extremely low metallicity compared to our Milky Way and hence is expected to have much higher $\alpha_{\rm CO}$, which makes GMCs in SMC super-virialized ($\alpha_{\rm vir} \sim 0.1$) compared to other galaxies (Bolatto et al. 2003; Leroy et al. 2011). We also note that most of these early works were done for low-mass galaxies primarily due to the inability of our instruments to probe galaxies further away.

To build a more comprehensive understanding of the connection between GMC properties and galactic environments, the logical next step is to conduct a CO imaging survey for a large, representative sample of galaxies with homogeneous data quality. Since 2013, ALMA's operation has enabled such a GMC survey. The recently completed Physics at High Angular resolution in Nearby GalaxieS with ALMA (PHANGS-ALMA) survey marks a great progress in our understanding of GMCs at a wide range of galactic environments. PHANGS-ALMA is designed to map the ^{12}CO J=2-1 emission from 90 nearby star-forming galaxies with resolution of $\sim 30 - 150$ pc. The required sensitivity for each galaxy is set to detect individual GMCs with mass greater than 10^5 $\mathrm{M}_\odot$. The selected galaxies satisfy the criterion to have a relatively low inclination angle ($i < 75°$) and be relatively massive ($\log_{10} M_\star\,[M_\odot] \gtrsim 9.75$) and actively star forming ($\mathrm{SFR}/M_\star > 10^{-11}$ yr^{-1}). Among the 90 galaxies, the majority (74 of 90) are spiral galaxies, with an additional 16 early-type galaxies. For the spiral galaxies, $\sim$ 50% show strong bar features and 30% show central ring features (Stuber et al. 2023). The diverse morphological types in the PHANGS sample allows the study of GMCs in different local star-forming environments.

Overall, PHANGS-ALMA has made successful detections of over 100,000 GMCs (Sun et al. 2020a), which also poses challenges on the data analyses. Traditional methods to decompose individual cloud structures from 3D CO data cubes (e.g. CPROPS, Rosolowsky & Leroy 2006) are computationally expensive and sensitive to specific input parameters. A pixel-based approach has been widely applied for the initial analyses of GMC properties using PHANGS data (Leroy et al. 2016; Sun et al. 2018, 2020a). This approach assumes each image beam with signal detection is an individual GMC if the image beam size is comparable to the GMC actual size. The image beam is nyquist-sampled so each pixel is also representative of an individual GMC. Compared to the traditional cloud decomposition methods, this approach requires minimal assumptions and can be easily applied to many datasets in a uniform way. However, this approach is also more affected by superposition of multiple clouds along the same line of sight. Sun et al. (2022) make a comparison between this new approach and the traditional approach and find they generally give consistent results. However, the pixel-based approach gives higher velocity dispersion for GMCs in the center, where clouds are much more crowded.

One of the major PHANGS-ALMA science goals is to build up the complete demographics of GMCs and measure how GMC populations depend on host galaxy and location in a galaxy. Sun et al. (2018) perform a pilot study on 15 nearby galaxies and find that GMCs generally still show a relatively narrow range of α_{vir} ($\sim 1 - 10$) across a wide range of Σ_{mol} of over three orders of magnitude. In contrast, these GMCs have a turbulent pressure range of over four order of magnitudes, which suggests that different galaxies drive their molecular gas with hugely different pressures at cloud scales. With a larger sample, Sun et al. (2020a) further explore systematic variations

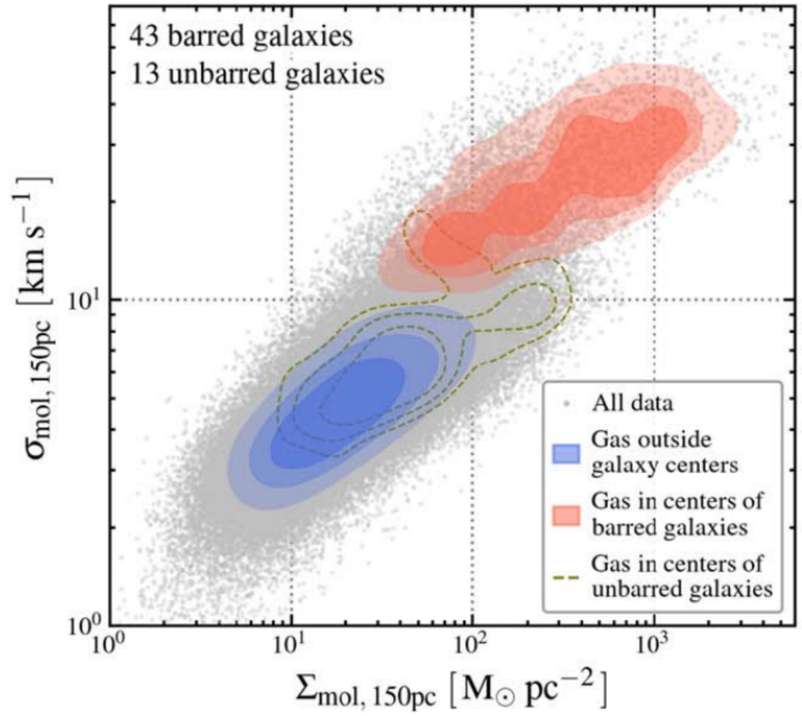

Figure 1.6: Velocity dispersion versus surface density for GMCs in the PHANGS survey (Sun et al. 2020a). The gray data points are all GMCs in PHANGS galaxies. The salmon shaded and brown dashed contours represent GMCs in the center of barred and unbarred spiral galaxies, respectively. The blue shaded contours represent GMCs out of the center of all spiral galaxies.

of GMC properties across different environments. They find a clear radial dependence of GMC Σ_{mol}, σ_v and α_{vir}, with higher values in the center (Fig. 1.6). Specifically, the higher α_{vir} in the center is consistent with Milky Way observations and seems to suggest GMCs in the center are more weakly bound, which could be due to higher external pressure set by higher stellar mass contribution to the gravitational potential energy (Meidt et al. 2018; Gensior et al. 2020). However, they also note that the measured α_{vir} trend is sensitive to the adopted α_{CO} prescription. Combining multi-wavelength data, Sun et al. (2022) perform a thorough analyses on the correlation between GMC properties and global galaxy properties and resolved kpc-scale local environmental properties for all PHANGS galaxies. They find that GMC properties have a much stronger connection to the local environments than to global galaxy properties, which implies universal physical laws to regulate GMC formation and evolution across different galaxy types.

GMCs in Starburst Galaxy Mergers

GMCs in starburst galaxy mergers are less well studied compared to GMCs in nearby isolated galaxies, which is mainly due to the small number of mergers within the distance range for GMC-resolution observations (e.g. Wei et al. 2012; Ueda et al. 2012; Whitmore et al. 2014; Elmegreen et al. 2017; Brunetti et al. 2020; Brunetti 2022; Sánchez-García et al. 2022; Bellocchi et al. 2022). So far, studies of GMC demographics and dynamical states have only been performed on a few starburst merger systems (e.g. NGC 3256 and the Antennae, Brunetti 2022). These studies show that GMCs in starburst mergers generally have much higher gas surface densities and velocity dispersions than those in normal spiral galaxies. Furthermore, GMCs in NGC 3256 seem to have $\alpha_{\rm vir} \sim 5$ times higher than those in normal spiral galaxies (Brunetti et al. 2020), which suggests that merging interactions can drive GMCs to be more turbulent and less gravitationally bound. GMCs in the merger center generally have higher $\alpha_{\rm vir}$ than those in the disk. However, due to the limited galaxy sample size, it is difficult to draw statistically robust conclusions on how GMC properties evolve across various merging stages

On the simulation side, only a handful of studies (e.g. Teyssier et al. 2010; Renaud et al. 2014; Fensch et al. 2017) are capable of probing the cold gas at $\sim$ pc scale starting from cosmological scales. Using a comprehensive library of idealized galaxy merger simulations based on the FIRE-2 physics model, Moreno et al. (2019) show that SFR enhancement is accompanied by an increase in the cold dense gas reservoir. However, similar to observations, most simulation GMC studies are focused on normal spiral galaxies (e.g. Benincasa et al. 2020; Jeffreson et al. 2022) and only a few (Li et al. 2022) are focused on galaxy mergers.

1.3.3 Modelling Molecular Gas Properties

From ^{12}CO observations, we can directly infer GMC CO luminosity, velocity dispersion and size. However, it is still challenging to infer actual physical properties, such as kinetic temperature ($T_{\rm kin}$), volume density ($n_{\rm H_2}$) and surface density ($\Sigma_{\rm mol}$) of individual GMCs. The gas physical properties can affect our $\alpha_{\rm CO}$ choice to convert CO luminosity to actual GMC mass and surface density (Narayanan et al. 2011). Furthermore, differences in gas physical properties in normal star forming galaxies and starburst mergers might explain the difference in gas depletion time ($t_{\rm dep}$) that determines how fast molecular gas is depleted with ongoing SFR between these two systems. Specifically, simulations (e.g. Teyssier et al. 2010) show that gas in starburst mergers is more efficient to form stars (has shorter t_{dep}) due to an increasing fraction of gas in the higher density regime that satisfy the criterion to form stars. Therefore, it is crucial to constrain the physical properties of the molecular gas to tackle these open questions.

If only one or two molecular lines are detected, the gas physical properties can be derived under some theoretical assumptions. One example is the LTE assumption, which assumes the excitation temperature of specific lines is equal to the gas kinetic temperature. This assumption generally holds for warm, dense gas where the collisional excitation is sufficient (Salak et al. 2019). A specific case is that one can use a combination of ^{12}CO lines (generally optically thick) and ^{13}CO lines (generally optically thin) to derive gas kinetic temperature and column density (Nishimura et al. 2015). If multiple optically thin lines are observed, a widely adopted approach is to use a "rotation diagram" (e.g. Goldsmith & Langer 1999) to determine the column density and excitation temperature by a fit to the line intensities as a function of upper level energy. Under LTE conditions, the obtained excitation temperature is roughly equal to the kinetic temperature. However, the LTE assumption does not always apply, specifically for optically thin lines that can be subthermally excited in the density regime below the line critical density (Jiménez-Donaire et al. 2017).

A more advanced approach is to allow the excitation temperature to vary for individual lines, and solve for the excitation temperature and optical depth of each line under the assumption of statistical equilibrium. Currently, the mostly commonly used non-LTE radiative transfer code is RADEX (Van Der Tak et al. 2007). In RADEX, for a given temperature, volume density and the column density of the molecular species that generates the line, RADEX will return the excitation temperature, optical depth and brightness temperature of that line. The RADEX calculation starts with the LTE assumption and then calculates the escape probability based on assumed geometrical structures of the homogeneous medium (RADEX allows for three geometrical structures, "uniform sphere", "expanding sphere" and "plane parallel sheet"). The escape probability directly constrains the radiation field, which then determines the level population, excitation temperature and optical depth. The new optical depth provides a new estimate of the escape probability and another iteration starts until the converged solution is found. In a real application, we have brightness temperature measurements of multiple molecular lines and we can in return infer the most likely temperature, volume density and the column density that can generate our measured brightness temperature values.

Most RADEX work for nearby galaxies uses CO and its isotoplogue lines since they are generally the brightest molecular lines we can observe. Before the appearance of RADEX, the most well-known modeling is the large velocity gradient (LVG) modeling. Early studies using LVG modeling on Milky Way clouds (e.g. Wilson et al. 1999), nearby galaxies (Wilson et al. 1997) and starburst mergers (Downes & Solomon 1998) generally suffered from the limited number of CO lines due to the sensitivity limitation of the instruments to observe high frequency, high J CO lines. Including CO isotoplogues, such as ^{13}CO lines, also introduces another free parameter of [CO]/[^{13}CO] abundance ratio. The launch of the Herschel Space Observatory gives us access to high J CO lines up to J=13-12. Studies combining all these CO transitions (Rangwala et al. 2011; Viti et al. 2014; Papadopoulos et al. 2014; Harrington et al. 2021) show that it requires an additional phase of molecular gas that is warmer/-denser than the cold gas that is mainly responsible for low J CO emissions. However, it is still under debate whether this second medium is warmer or denser. In addition, extra-galactic studies (e.g. Kamenetzky et al. 2017; Finn et al. 2022) show that, due to the limited resolution to resolve individual GMCs, we need to introduce another free parameter called the "beam filling factor" to take into the beam dilution effect that reduces our measured brightness temperature.

With the advent of ALMA, it is now possible to constrain spatially resolved gas properties in individual galaxies. Sliwa et al. (2017b) compiled a list of starburst mergers with RADEX modeling constraints on kinetic temperature and volume density, as shown in Fig. 1.7. Generally they find that advanced mergers, such as Arp 220, NGC 2623 and VV 114 have a warmer and less dense molecular gas component than the early/intermediate mergers, such as Arp 299, NGC 1614 and NGC 4038/9. This difference can be tied to the merger evolutionary sequence. At the early stage when the merging process just started, the molecular gas is funnelled into the central region and drives the average gas volume density up. At the later stage of the merging events, the starburst events and/or AGN activities will heat up and disperse the gas, making it warmer and more diffuse. However, it is important to note that RADEX modeling generally has a degeneracy between higher temperature or higher density since both factors will increase the excitation temperature (see detailed discussion in

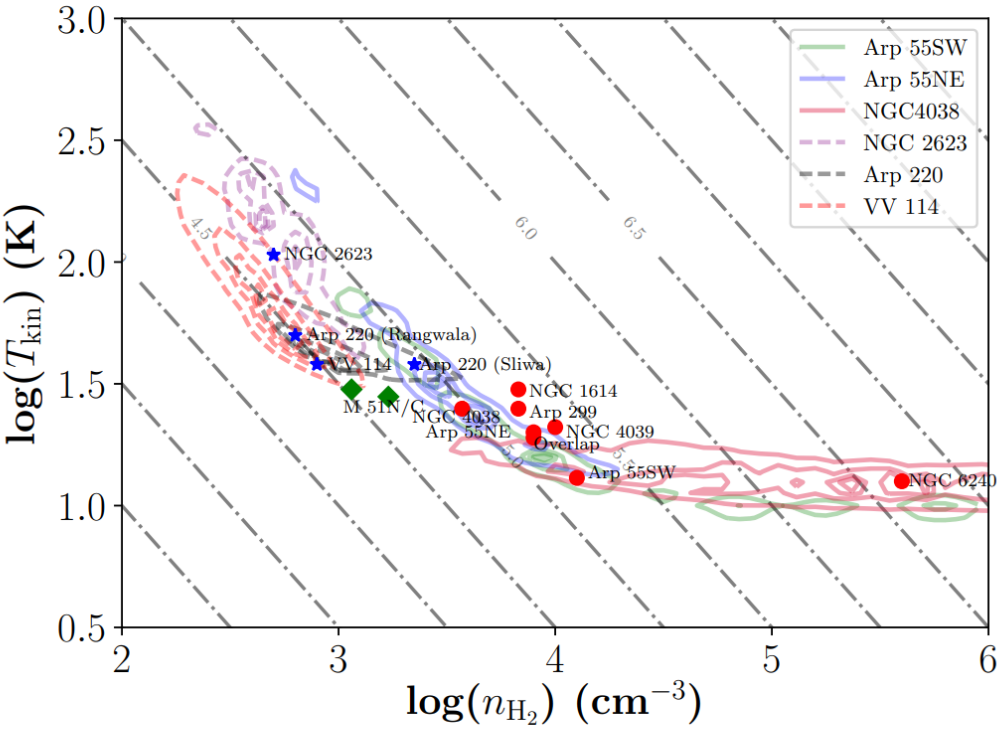

Figure 1.7: RADEX constrained temperature versus volume density for U/LIRGs (Sliwa et al. 2017b). Individual points represent the most probable solution while the colored contours represent 55, 80, 90, 95% most probable solution distribution. Dashed color contours denote advanced mergers with solid contours denote early, intermediate stage mergers. Diagonal dot-dashed lines indicate constant pressure ($\log P$).

Gong et al. 2020). Instead, the thermal pressure, which is the product of temperature and density, is better constrained (Kamenetzky et al. 2017).

1.3.4 Determining the CO-to-H$_2$ Conversion Factor

As ^{12}CO J=1-0 is widely used to measure the molecular gas mass, it is crucial to constrain the CO-to-H$_2$ conversion factor, $\alpha_{\rm CO}$

$$\alpha_{\rm CO} = \frac{M_{\rm mol}}{L_{\rm CO(1-0)}} = \frac{\Sigma_{\rm mol}}{I_{\rm CO(1-0)}} \left[\frac{\rm M_{\odot}}{\rm K\ km\ s^{-1} pc^2}\right] \tag{1.5}$$

From a theoretical point of view, $\alpha_{\rm CO}$ can be dependent on both small-scale GMC properties, such as temperature, volume and surface density (Gong et al. 2020, and references therein), and kpc-scale environmental properties, such as metallicity, galactic disk surface density and velocity dispersion (e.g. Wolfire et al. 2010; Narayanan et al. 2012; Kazandjian et al. 2015; Renaud et al. 2019; Gong et al. 2020; Hu et al. 2022). Therefore, it has been a challenge to come up with a unified $\alpha_{\rm CO}$ prescription. Furthermore, the assumptions that go into observational measurements of $\alpha_{\rm CO}$ are also affected by these environmental factors. Therefore, determination of $\alpha_{\rm CO}$ is still an open question. Here we introduce some of most common methods to determine $\alpha_{\rm CO}$.

Virial Method

In our Milky Way, GMCs are observed to have ^{12}CO J=1-0 luminosity proportional to the virial mass (e.g. Solomon et al. 1987), which is an indication that GMCs are in virial equilibrium. Extra-galactic studies of nearby galaxies confirm that GMCs are generally in virial equilibrium (references in Bolatto et al. 2013). Therefore, we can measure the GMC virial mass and use it to calibrate $\alpha_{\rm CO}$. The fiducial value of the Milky Way $\alpha_{\rm CO}$ measured with this method is 4.3 $\mathrm{M_\odot}$ (K km s^{-1} pc^2)$^{-1}$, with a scatter of 30%. Including GMCs in nearby galaxies gives us similar $\alpha_{\rm CO}$ value but with a scatter of 0.4 dex (factor of 2.5).

The caveat of this method is its basic assumption that GMCs are in virial equilibrium. Specifically, GMCs in starburst galaxy mergers might not be gravitationally bound (Brunetti et al. 2020; Brunetti & Wilson 2022). Even for GMCs in normal spiral galaxies, a factor of $\sim 2-3$ scatter in $\alpha_{\rm CO}$ determined through the virial method might reflect actual variation in GMC boundedness states. Furthermore, it has been found that the resolution of the observation also affects $\alpha_{\rm CO}$ values determined through the virial method. Specifically, observations of LMC and SMC (e.g. Fukui et al. 2008; Hughes et al. 2010; Mizuno et al. 2001; Bolatto et al. 2003) show that higher resolution observations yield smaller $\alpha_{\rm CO}$ values. This scale dependence could be due to the fact that lower-resolution observations might associate physically distinct clouds that are not bound together, hence over-predicting the $\alpha_{\rm CO}$. However, it is not clear at which optimal scale we can find most bound structures. The virial method also gives lower $\alpha_{\rm CO}$ values than dust based methods for low-metallicity dwarf galaxies (e.g. Bolatto et al. 2003; Leroy et al. 2011). One argument is that the virial method measures $\alpha_{\rm CO}$ of CO bright regions while the dust-based method also include the diffuse gas component that is less CO bright along the same line of sight.

Dust-based estimate of α_{CO}

Since CO lines are generally optically thick, CO tracing molecular gas relies on the assumption that GMCs are in virial equilibrium. Therefore, a more direct approach to determine molecular gas mass and surface density is to measure the intensity of optically thin tracers. One option is to use dust emission as dust is expected and observed to be well mixed with gas. The measured dust optical depth can then be converted to the gas column density assuming a constant dust emissivity per nucleon, which is the product of the gas-to-dust mass ratio and dust optical properties. Milky Way studies (e.g. Planck Collaboration XIX. et al. 2011) show that the dust optical depth has a tight proportional correlation with the total hydrogen column density (N(H I) + $2N$ (H_2), H_2 is traced by CO emission). They also find a certain H_2 component that is not well traced by CO emission, known as CO dark clouds (Grenier, Casandjian & Terrier 2005; Wolfire, Hollenbach & McKee 2010). Further analyses with γ-ray emission (e.g. Grenier, Casandjian & Terrier 2005) find that these CO-dark components can take up 40% – 400% of the CO-bright mass in small local molecular clouds.

In extra-galactic observations, *Spitzer* and *Herschel* allows for the dust approach to be applied for nearby galaxies. To date, Sandstrom et al. (2013) performed the most comprehensive analysis using the dust approach to constrain α_{CO} across the disk of 22 nearby galaxies. To constrain α_{CO} for individual kpc-size regions, they develop a self-consistent way to simultaneously constrain α_{CO} and gas-to-dust ratio. They measure a median α_{CO} of ~ 2.5 $\mathrm{M}_{\odot}$ (K km s^{-1} $\mathrm{pc}^2)^{-1}$ for these nearby galaxies. Furthermore, they find a significant anti-correlation between α_{CO} and metallicity that is consistent with theoretical expectations. Less metallicity will result in lower abundance of CO and dust to shield the far-UV radiation and lead to higher fraction of CO-dark molecular gas with higher α_{CO}. So far, the α_{CO} dependence on metallicity is relatively well calibrated (e.g. Schruba et al. 2012; Accurso et al. 2017) and has been applied to several recent works (e.g. Sun et al. 2020a,b; Pessa et al. 2021; Sun et al. 2023). Wilson et al. (2008) apply the dust-based approach to U/LIRGs in comparison with ^{12}CO J=3-2 data and find a similar gas-to-dust ratio of $\sim$ 100 to normal spiral galaxies. Generally, the gas-to-dust ratio for all nearby galaxies is $\sim$ 50 – 150 (Dunne et al. 2022).

Multi-line Radiative Transfer Modeling

Observations of multiple CO lines or a combination of CO and other molecular lines can allow us to constrain the gas physical conditions that generate CO emission. Specifically, including optically thin lines can help with constraints on CO optical depth and hence the column density. Due to the requirement of multiple lines, this technique is observationally expensive and hence generally applied to galaxy central regions with bright CO emission. Studies of individual galaxies (e.g. Israel et al. 2006; Watanabe et al. 2011; Meier & Turner 2004) show that α_{CO} in the center of nearby galaxies is generally 2 – 10 times lower than the fiducial Milky Way value of 4.3 $\mathrm{M}_{\odot}$ $(\mathrm{K\ km\ s^{-1}\ pc^{2}})^{-1}$. In contrast, α_{CO} in galaxy disk (Schinnerer et al. 2010, e.g.) are similar to the Milky Way value. The central depression of α_{CO} could be due to the larger stellar potential that exerts additional pressure to bind GMCs that are out of virial equilibrium, which generally have lower α_{CO} (Bolatto et al. 2013).

The multi-line modeling approach has also been widely applied to constrain α_{CO} in U/LIRGs. Downes & Solomon (1998) applied this approach to several U/LIRGs and found that α_{CO} in these U/LIRGs was generally 4 times smaller than the fiducial Milky Way value. They also found adopting a Milky Way α_{CO} would yield unreasonable gas mass that exceeds the dynamical mass. Their α_{CO} value is also consistent with the modeling on individual starburst galaxies (e.g. Papadopoulos & Seaquist 1999; Zhu et al. 2003; Sliwa et al. 2012) with lower IR luminosity. Early theoretical works (Downes et al. 1993) suggest that in a more general case, CO luminosity should be proportional to the geometric mean of the gas mass and virial mass. For GMCs in starburst mergers with higher α_{vir}, CO is over-luminous due to the higher virial mass, which results in a lower α_{CO}. Simulations (e.g. Narayanan et al. 2011) also suggest that the lower α_{CO} in U/LIRGs is either due to the higher gas temperature or higher velocity dispersion (hence higher α_{vir}) for GMCs in starburst mergers. Studies on a large sample of U/LIRGs (Papadopoulos et al. 2012) suggest the kinematic factor is dominant in bringing down the α_{CO} values. However, most of the multi-line modeling is limited by the resolution of CO observations and hence not able to directly constrain the GMC physical properties.

The major limitation of the multi-line modeling is that it is unable to constrain the $[\mathrm{CO}]/[\mathrm{H_2}]$ abundance ratio. The commonly adopted fiducial value is between 8×10^{-5} and 3×10^{-4} (e.g. Watson et al. 1985; Lacy et al. 1994). This $[\mathrm{CO}]/[\mathrm{H_2}]$ abundance ratio can shift the absolute α_{CO} value by a factor of 5. It is argued that, for warm star-forming clouds, which are generally found in starburst systems, 3×10^{-4} is a more appropriate value (Lacy et al. 1994). Another limitation is that, similar to the virial method, multi-line modeling is biased towards CO bright regions, which generally have lower $\alpha_{\rm CO}$.

1.4 Kennicutt-Schmidt Relation and Related Star Formation Theories

Observations of nearby galaxies show a tight power-law relation between global SFR and total amount of cold gas (CNM and molecular gas), generally known as the "Kennicutt-Schmidt" relation. Kennicutt (1998) first quantitatively measured this global correlation and obtained a power-law slope of 1.4 ± 0.05. An updated analysis (Kennicutt & De Los Reyes 2021) on an expanded sample of nearby galaxies finds a slightly steeper slope of 1.5 ± 0.05. With improved resolution and sensitivity of instruments, follow-up studies (e.g. Kennicutt et al. 2007; Bigiel et al. 2008; Leroy et al. 2008) are able to map out cold gas and SFR distribution within individual galaxies. In this case, this relation is better characterized by the surface density of cold gas and SFR, which removes the artificial correlation that can happen to random two variables due to scale dependence (“the bigger, the brighter”). These resolved studies find that the SFR surface density ($\Sigma_{\rm SFR}$) has a stronger correlation with molecular gas surface density ($\Sigma_{\rm mol}$) than with the total surface density of the cold gas. In fact, H I surface density alone shows little correlation with $\Sigma_{\rm SFR}$ and saturates at ~ 10 M$_\odot$ pc^{-2} (Blitz & Rosolowsky 2006). The power-law slope of the $\Sigma_{\rm SFR}$ versus $\Sigma_{\rm mol}$ relation is ~ 1, which suggests a relatively constant depletion time ($t_{\rm dep} = \Sigma_{\rm mol}/\Sigma_{\rm SFR}$) of 10^9 yr for nearby spiral galaxies. However, studies of U/LIRGs (e.g. Daddi et al. 2010; Genzel et al. 2010; Wilson et al. 2019, also see left panel in Fig. 1.8) show a steeper power-law slope of ~ 1.4 in the high $\Sigma_{\rm SFR}$ regime. In general, U/LIRGs have have $t_{\rm dep}$ of $\lesssim 10^8$ yr. This difference in $t_{\rm dep}$ between U/LIRGs and normal spiral galaxies implies real physical difference in the star formation process.

Various theories have been proposed to explain the double power-law behavior in the Kennicutt-Schmidt relation. Gao & Solomon (2004) first propose that $\Sigma_{\rm SFR}$ is instead tighly correlated with dense gas surface density traced by HCN, instead of bulk molecular gas that is traced by CO emission (also see right panel of Fig. 1.8).

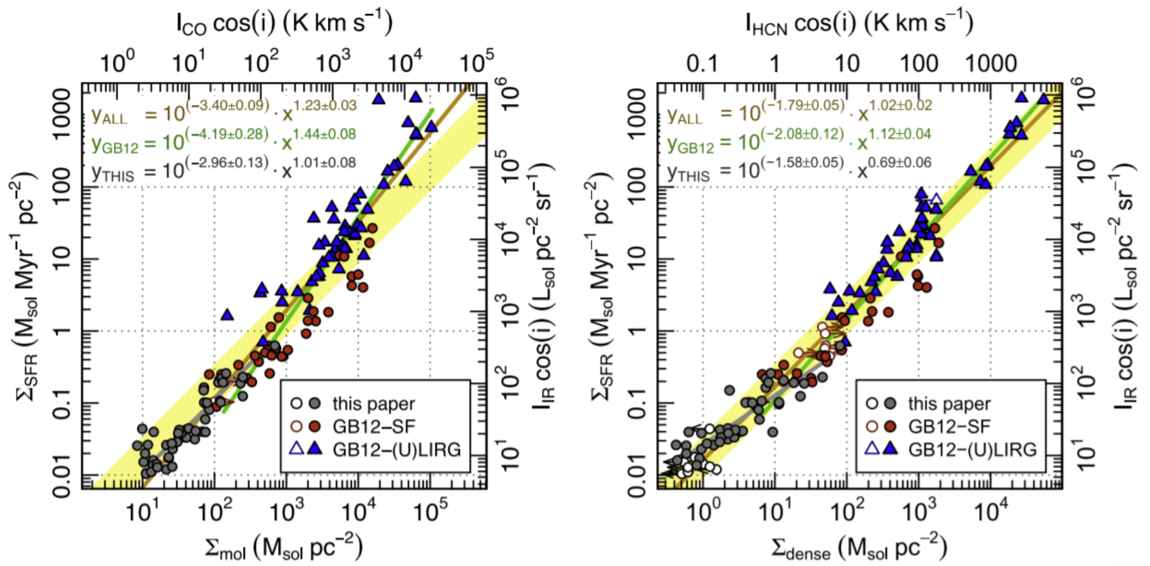

Figure 1.8: The comparison of the Kennicutt-Schmidt law for (Left) Σ_{mol} traced by CO and (Right) Σ_{dense} traced by HCN on kpc scale (Usero et al. 2015). The blue triangles and red dots are data for star forming galaxies and (U)LIRGs, respectively.. The equation indicates the power law fitting for data from Usero et al. (2015) (gray line), García-Burillo et al. (2012) (green line) and combined data (brown line). The yellow shaded region indicates the power law index of 1.0 with a factor of 2 scatter.

They find a uniform linear correlation between SFR and HCN luminosity for both normal spiral galaxies and U/LIRGs. Therefore, the superlinear correlation between between SFR and CO luminosity in the high $\Sigma_{\rm mol}$ regime is probably due to an increase in dense gas fraction. In this case, the relation between $\Sigma_{\rm SFR}$ and $\Sigma_{\rm mol}$ might be better described as a curve with continuously increasing power-law slope rather than a double power-law function. In contrast, $t_{\rm dep}$ for the dense gas stays relatively constant. This is consistent with the "fixed-density threshold" scenario (e.g. Lada et al. 2010, 2012; Evans et al. 2014), which suggests that SFR is determined by the mass of molecular gas above certain density threshold (generally $n > 10^4$ cm^{-3}). However, follow-up studies (e.g. Usero et al. 2015; Neumann et al. 2023, also see right panel of Fig. 1.8) show that there is a systematic variation in dense gas $t_{\rm dep}$ that depends on GMC properties.

An alternative model proposes that the threshold density for SFR is not fixed but depends on local gas properties, and is known as the "turbulence model" (e.g. Krumholz & McKee 2005; Krumholz & Thompson 2007). In this model, the probability density function (PDF) follows a log normal (or a log normal plus a power-law tail) distribution function, which is generally consistent with the column density PDF measured in Milky Way clouds (e.g. Heyer & Dame 2015; Lada et al. 2010, 2012; Schneider et al. 2011, 2015). The density threshold for stars to be formed is then determined by the GMC properties, specifically the virial parameter $\alpha_{\rm vir}$, and the Mach number M, in the form of (Krumholz & McKee 2005)

$$\frac{n_{\rm SF}}{n_0} = 0.82\alpha_{\rm vir}M^2 \tag{1.6}$$

where $n_{\rm SF}$ is the star formation threshold density and n_0 is the mean density of the GMC. For example, if gas M increases, then the threshold is higher and a smaller fraction of gas will form stars. Therefore, if we assume the HCN is emitted from gas above a fixed volume density (in reality HCN can also be subthermally excited in the low density regime), then the ratio between SFR and HCN will be affected by Mach number and $\alpha_{\rm vir}$ variations. Neumann et al. (2023) show that for PHANGS spiral galaxies, the HCN/CO and HCN/SFR ratio has a similar dependence on GMC $\Sigma_{\rm mol}$, σ_v and $\alpha_{\rm vir}$ as predicted from this simple model. However, another big uncertainty in using HCN to trace dense gas is the HCN-to-H$_2$ conversion factor ($\alpha_{\rm HCN}$), which is generally assumed to be constant in current studies. Barnes et al. (2020) compile a list of current α_{HCN} measurements for both Milky Way clouds and extra-galactic gas and the value spans a range of three orders of magnitudes, which suggests we need a unified and self-consistent method to measure this value.

1.5 Star Cluster Formation

1.5.1 Observations of young massive star clusters

Stars are formed through the collapse of GMCs (Lada et al. 1993) , which generally have mass of 10^5 – 10^7 $\mathrm{M}_{\odot}$ for nearby spiral galaxies (Rosolowsky et al. 2021). Therefore, we naturally expect stars are formed in clusters. Milky Way observations show that $\sim 70\%$ of O stars reside in young clusters or associations (Gies 1987) and $\sim 50\%$ of the remaining field population are run-away stars from the cluster environment (de Wit et al. 2005). In nearby starburst galaxies, ~ 20 – 100% of UV or Hα luminosities, which are related to the total SFR, comes from young star clusters (Meurer et al. 1995; Fall et al. 2005; Zepf et al. 1999). In our Milky Way, most young clusters are open clusters with mass smaller than 10^3 $\mathrm{M}_{\odot}$. However, there is still a small population (Portegies Zwart et al. 2010, $\sim 10\%$) of extremely Young Massive Clusters (YMCs) (age smaller than 100 Myr) found in the Milky Way halo with mass greater 10^4 $\mathrm{M}_{\odot}$, within the similar mass range of old Globular Clusters (GCs) in the Milky halo with age greater than 1 Gyr. Therefore, some literature suggests that these YMCs are progenitor of GCs and can help us understand the formation of GCs at early universe.

For star clusters in the Milky Way, the Magellanic Clouds and M 31, HST can resolve individual stars within the observed star clusters. Therefore, it is possible to place these individual stars in a Color Magnitude Diagram (CMD) and determine the main-sequence turn-off point, and hence measure the age of the star clusters. This method can achieve the highest measurement accuracy with uncertainty of $\sim 10\%$ (e.g. Glatt et al. 2010). However, for more distant galaxies, we cannot resolve individual stars due to the resolution limit of our instruments. These clusters are either identified based on apparent size (they are slightly more extended than isolated stars) or luminosity (Whitmore et al. 1993, generally brighter than most foreground stars). For unresolved clusters, the mass and age can be determined by matching observation with model tracks assuming a single stellar population in a two color diagram (e.g. Zackrisson et al. 2011). This technique can achieve an age measurement accuracy within a factor of 2 (Whitmore et al. 2010) in comparison with more accurate age measurements from spectroscopy. However, this technique suffers from the age-extinction degeneracy (e.g. Turner et al. 2021). Possible solutions include using high-resolution Hα images (Whitmore et al. 2020) or adding a log-normal Bayesian prior to the extinction (Ashworth et al. 2017). High resolution JWST images at mid- or far-infrared wavelength can also help with breaking the degeneracy.

There is still a significant fraction of young star clusters that are embedded in GMCs and not yet visible in optical wavelengths. Whitmore et al. (2010) suggest that about 16% of star clusters in the Antennae are hidden from view in the optical. This fraction can be even higher for star clusters in U/LIRGs. These embedded YMCs can be detected through radio continuum as it is unaffected by dust extinction (Murphy et al. 2011). The lower-frequency radio continuum (10 – 100 GHz) generally traces the free-free emission from the embedded H II region, which can be used to calculate the total stellar mass assuming a single stellar population. Cross-matching radio and optical clusters can help constrain the timescale of the embedded phase. Assuming the cluster formation rate is constant within a short timescale (e.g. $\sim$ 10 Myr), then the number ratio between these two objects reflects the timescale difference. These analyses generally give a very young age of $\sim$ 1 Myr for the radio detected YMCs (e.g. Johnson & Kobulnicky 2003; Whitmore et al. 2014).

1.5.2 Theory of Star Cluster Formation

In theory, star cluster formation involves a hierarchical collapse of molecular gas from GMC scale ($\sim$ 100 pc) down to dense gas clump scale (several pc). Therefore, we expect a strong link between the cluster mass function and the GMC and/or clump mass function. Observations of the Milky Way and nearby galaxies (Fig. 5 in Krumholz et al. 2019) show that the CMF follows a power-law function with a power-law index of $\sim$ 2, which is similar to the observed power-law index of GMCs (e.g. Rosolowsky et al. 2021) and dense clumps (e.g. Moore et al. 2015). The similar power-law index of 2 suggests a consistent scale-free distribution of the three types of objects and supports scale-free star formation theories (e.g. supersonic turbulence aided by gravity, Elmegreen & Scalo 2004). In contrast, the shape of the old GC mass function is better described as a log-normal distribution with a power-law tail (Brodie & Strader 2006, peak value of $\sim 2 \times 10^5$ M$_\odot$). A natural explanation is that

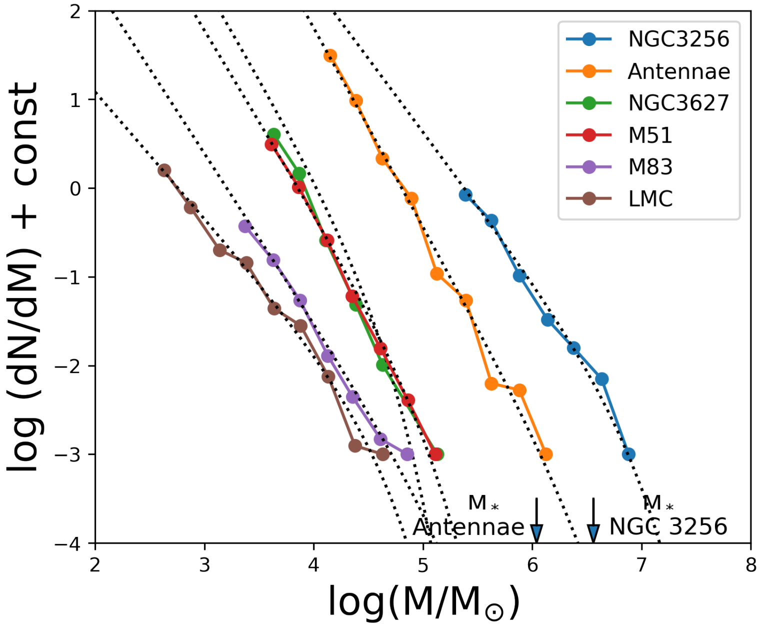

Figure 1.9: Mass functions of star clusters in nearby galaxies with age younger than 10 Myr (adapted from Mok et al. 2020). The mass functions for different galaxies are shifted by a different constant for a visual display. The dashed curves are the fitted Schechter function for each galaxy. (Bottom) The corresponding power-law slopes of the mass functions. The downward arrows indicate the Schechter truncation mass for the Antennae and NGC 3256.

only the more massive half of the log-normal distribution represents the initial mass spectrum right after star cluster formation while the less massive half is due to cluster destruction across cosmic time. However, this scenario still remains under debate.

At the higher mass end, the CMF is observed to be truncated with steeply decreasing power-law slope (Fig. 1.9). The mass function is hence better described with a Schechter function (Gieles et al. 2006a,b) in the form of

$$\frac{dN}{dM} \propto M^{-\beta} \exp -M/M_c, \tag{1.7}$$

where β is the power-law slope and M_c is the truncation mass. Extra-galactic observations (e.g. Johnson et al. 2017; Adamo et al. 2020a; Wainer et al. 2022) show a tight correlation between M_c and global SFR surface density, which suggests that starburst environments tend to form more massive clusters. Reina-Campos & Kruijssen (2017) propose a unified cluster formation model that predicts the maximal star cluster mass formed in each individual disk galaxy based on the gas surface density, the cluster formation efficiency (fraction of stars formed in clusters) and the Toomre Q. Their model naturally suggests that starburst galaxies with higher gas surface density (from Kennicutt-Schmidt relation) will form more massive GMCs with higher cluster formation efficiency (Kruijssen 2012), which naturally leads to a higher maximal cluster mass. The maximal cluster mass predicted in their model is consistent with the observed truncation mass within a factor of 2 (Kruijssen 2014; Wainer et al. 2022). However, some observers (e.g. Mok et al. 2019, 2020) argue that the truncation mass is not physically real and is mainly due to small statistics for clusters at higher mass end (not enough objects to sample the CMF at the higher mass end). In this case, the truncation mass should scale linearly with number of clusters in galaxies. They apply a maximal likelihood approach (Chapter 15.2 of Mo et al. 2010) to fit the Schechter mass function and find no statistical significance for the cutoff mass. So far, the existence of truncation mass is still under debate as the exact form of the function is sensitive to the uncertainty in cluster mass measurements (e.g. M 83 Adamo et al. 2015; Sun et al. 2016) and different statistical fitting methods adopted (Messa et al. 2018).

Another important quantity regarding cluster formation is the cluster formation efficiency (CFE) (Γ, also known as the cluster bound fraction), which measures what fraction of new stars are born in cluster environments. Kruijssen (2012) first suggested in their analytical star cluster formation model that galaxies with higher gas surface density, and hence higher SFR surface density, tend to have higher CFE. A simple fit to their analytical model gives

$$\Gamma = (1.15 + 0.6\Sigma_{\mathrm{SFR}}^{-0.4} + 0.05\Sigma_{\mathrm{SFR}}^{-1})^{-1} \tag{1.8}$$

Therefore, CFE will saturate at 70% – 80% when Σ_{SFR} reaches $\sim 10\ \mathrm{M}_\odot\ \mathrm{yr}^{-1}\ \mathrm{kpc}^{-2}$. In observations, CFE is generally measured by dividing the total mass of clusters younger than a certain age (generally $\sim$ 10 Myr) by the total SFR of the galaxy. Adamo et al. (2020b) show the CFE versus Σ_{SFR} for a compiled list of dwarf, spiral galaxies and U/LIRGs and find a general agreement between the observations and the analytical prediction, although with a large scatter. One caveat is that young clusters might not be gravitationally bound although appearing to be a compact source, and hence our measured CFE is generally an upper limit. Chandar et al. (2017) also point out that measured CFE can also be affected by the SFR tracer we use. For galaxies in the low Σ_{SFR} regime, the SFR tracer we use generally traces a timescale of 10 – 100 Myr while the SFR tracer for starburst galaxies traces the timescale of 1 – 10 Myr, which tends to overestimate the CFE since many clusters can be destroyed between the age of 10 – 100 Myr. Chandar et al. (2017) apply a consistent SFR tracer for this analysis and find a relatively constant CFE of 24%. Chandar et al. (2023) further show that with updated age estimates from Hα photometry, the CFE for starburst galaxies is also low even on timescales of 1 – 10 Myr, with a value of 15% – 39%. On the other hand, Adamo et al. (2020a) argue that the cluster identification method in Chandar et al. (2017) does not include a visual sanity check. Therefore, they might include a significant fraction of unbound stellar associations for galaxies with low Σ_{SFR}, and hence overestimate the CFE for these galaxies while the CFE for high Σ_{SFR} galaxies are less affected because the intrinsic fraction of clusters that are bound is high. From a simulation perspective, so far most simulations suggest a clear trend of CFE versus Σ_{SFR} relation (e.g. Pfeffer et al. 2019; Li et al. 2022).

1.5.3 Feedback mechanisms of young massive star clusters

Stellar feedback plays a central role in the star formation cycle by dispersing the star-forming gas and thus reducing the efficiency of star formation in galaxies. Observations show that starburst environments tend form stars in compact YMCs (e.g.

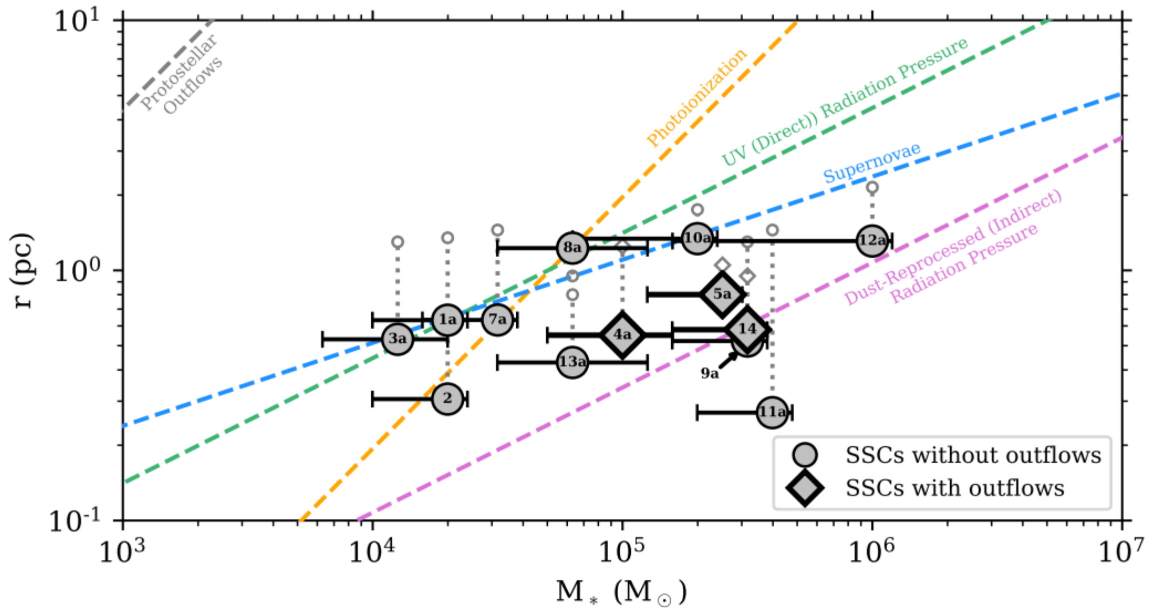

Figure 1.10: Size versus mass for YMCs in NGC 253 (Levy et al. 2021). The diamonds represent YMCs with P-Cygni profile outflow detection while the filled circles represent the rest of clusters. Dashed lines represent the limitation for different feedback mechanisms. Feedback effective regions are mostly to the left of the dashed line except for the IR radiation. There is a locus where none of the feedbacks is effective where most of the YMCs in the plot reside in.

Adamo et al. 2020b), which brings much stronger feedback (e.g. Keller et al. 2014) and can change the overall ISM budget in galaxies (Smith et al. 2021). Therefore, it is crucial to understand the timescales and relative strength of different feedback mechanisms to better understand the stellar feedback process.

Observations of YMCs at optical wavelength (Hollyhead et al. 2015; Grasha et al. 2018; Hannon et al. 2019) show that the timescale for YMCs to emerge from GMCs is $\sim 1 - 5$ Myr. Such a short feedback timescale suggests these YMCs have already cleared out the surrounding gas before the first supernovae (SNe) explosion (~ 3 Myr). Therefore, several alternative stellar feedback mechanisms have been proposed to be responsible for the gas dispersal, including protostellar outflow, photoionization, direct radiation pressure, dust-reprocessed infrared radiation pressure and hot stellar winds. Both observations (Nakamura & Li 2014) and theoretical works (e.g. Matzner & McKee 2000; Krumholz et al. 2012) show that protostellar outflow from individual stars plays a limited role due to the low ejection velocity that is not sufficient for gas to escape from the large-scale protocluster. Photon-ionization can heat gas up to 10^4 K, which generates outward momentum that can accelerate gas to the escape velocity. Theoretical works (e.g. Matzner 2002) suggest that photoionization can be effective for a 10^4 $M_\odot$ YMC to eject $\sim$ gas of 10 times its own mass in a few million years. However, the exact value of the escape velocity below which photoionization can be effective is still uncertain (Krumholz et al. 2019). Direct and indirect radiation from YMCs can also be strong enough to exceed the Eddington limit and hence push the surrounding gas away. The limiting factor for both mechanisms is the surface density of the gas but the criteria for the two mechanisms to be effective is different. Radiation pressure is typically effective for gas surface density below 340 $M_\odot$ pc^{-2} while the indirect radiation pressure is effective for gas surface density above 70,000 $M_\odot$ pc^{-2} (Krumholz et al. 2019). However, recent simulation work by Menon et al. (2022) shows that the indirect radiation is not as effective as we thought even for gas surface density above 10^5 $M_\odot$ pc^{-2} by applying a realistic temperature dependent dust opacity. Stellar winds are produced from the most massive stars in YMCs and can generate shocks with temperature above 10^7 K while in contact with the surrounding ISM. Simulations (e.g. Rogers & Pittard 2013; Mackey et al. 2015) show that stellar winds are subdominant compared to other feedback mechanisms but there has yet to be a comprehensive parameter study.

Based on the simple analytic model in Krumholz et al. (2019), we can determine whether a specific feedback mechanism is effective by putting the cluster in the mass-radius diagram (Fig. 1.10). YMCs are generally more compact than globular clusters (Krumholz et al. 2019). The expansion of clusters when it grows older can either be due to residual gas expulsion (Banerjee & Kroupa 2017) or internal two-body relaxation (Gieles et al. 2010). Fig. 1.10 also shows the feedback effective region for each feedback mechanism (to the right of the line for IR pressure and to the left of the line for other feedback mechanisms). There is a region enclosed by the orange, blue and purple dashed lines in the parameter space where none of the feedback mechanism is effective. Most old clusters reside in the parameter space where at least one feedback mechanism is effective (Krumholz et al. 2019). In contrast, YMCs are located in the white region where no stellar feedbacks are effective, which suggests they are still actively accreting gas and forming stars. Levy et al. (2021) find three YMCs in NGC 253 have outflow signatures ("P-Cygni profile") but locate within this non-feedback effective region, which suggests that the criteria for a certain feedback to be effective is more complex that we thought. They conclude that the outflow is most likely due to combination of IR radiation and stellar winds.

An alternative approach is to calculate the pressure from different feedback mechanisms and compare their relative strengths. Olivier et al. (2021) apply this approach to H II regions in the Milky Way combining radio, infrared and X-ray data and find that IR pressure is dominant for compact H II regions smaller than 3 pc. Barnes et al. (2021) apply a similar analysis to extragalactic H II regions using MUSE data and find that photoionization pressure, direct radiation pressure and stellar wind pressure have similar strength. They do not include analyses on IR pressure primarily due to lack of instruments with sufficient resolution at FIR wavelength. They also find that the sum of the three internal pressure is significantly higher than the external pressure, which suggests that these feedbacks are effective in further expanding the H II regions and pushing the gas away.

1.6 Outline of This Thesis

In this thesis, I aim to understand the interplay between the giant molecular clouds (GMCs) and star formation in nearby starburst galaxy mergers.

In chapter 2, I study the unique star formation products, young massive clusters (YMCs), in a typical starburst galaxy merger, the Antennae. I identify 6 compact sources that are likely to be extremely young YMCs (age of ~ 1 Myr) that are still embedded in GMCs in the Antennae overlap region with high-resolution ALMA radio continuum data at 100 GHz and 345 GHz. I further constrain the stellar mass, gas mass and virial mass of these YMCs with the radio continuum data and archival high-resolution ^{12}CO J=2-1 data, and find all of these detected sources are bound structures that are likely to be YMCs. I also cross match our detected YMCs with optical clusters identified using Hubble Space Telescope (HST) data and find a good correspondence in the total number of produced ionizing photon, but a significant position offsets between these two types of objects, which suggests these radio detected YMCs are just about to emerge from GMCs. I further compare our detected YMC stellar mass with the total stellar mass at GMC (giant molecular cloud) scale and find over 50% of star formation happens in these compact YMCs, which supports the argument that starburst environments tend to form stars in cluster environments. I also find a correlation between YMC total mass and GMC gas mass, which suggests that larger GMCs tend to form more massive YMCs.

I then approach the open question of the interplay between GMCs and star formation from the molecular gas side by quantifying GMC dynamical states and correlating these GMC quantities with the star formation rate (SFR). In chapter 3, I employ the idealized Feedback In Realistic Environment (FIRE) galaxy merger simulation, which contains both galaxy merger runs and control galaxy runs, to explore GMC evolution across different merging stages. I find the control galaxy run produces GMCs that follow the same trend in velocity dispersion versus GMC surface density as GMCs observed in the Physics at High Angular resolution in Nearby GalaxieS (PHANGS) survey, which suggests the success of the simulation to reproduce realistic GMCs. For the galaxy merger run, I find that the merging event will increase both the surface density and velocity dispersion of GMCs by a factor of $5-10$. I also measure the virial parameter of individual GMCs for the simulated merger run and find that most GMCs have virial parameters of $10-100$, ~ 10 times higher than that of normal spiral galaxies. Moreover, the virial parameter variation corresponds well with SFR variation, which suggests that starburst events are responsible for dispersing GMCs and making them less gravitationally bound. I also correlate GMC virial parameter with gas depletion time, which indicates how fast the star formation activity is able to to use up all the available gas, and find no correlation between these two quantities. Our results suggest that star formation activities are more complicated than we thought and large-scale environmental factors might be responsible for regulating star formation activities in starburst mergers.

One of biggest uncertainties in the comparison between simulation and observation in the previous project is the CO-to-H_2 conversion factor (α_{CO}) that converts CO intensity to physical molecular gas surface density. In chapter 4, I apply RADEX modeling using five CO and ^{13}CO line GMC-resolution observations to derive α_{CO} of each individual GMC and correlate α_{CO} with different GMC properties. I find that α_{CO} values in the Antennae are mostly close to the ULIRG values of 1.1 $M_\odot$ (K km s^{-1} $pc^2)^{-1}$ instead of 4.3 $M_\odot$ (K km s^{-1} $pc^2)^{-1}$ suggested by literature. The newly constrained α_{CO} values put most GMCs in the Antennae out of virial equilibrium, which confirms the simulation predictions from my previous project. I further correlate the measured α_{CO} with CO J=1-0 intensity and find a significant anti-correlation that is consistent with simulation prediction. I also find a tight correlation between α_{CO} and CO J=1-0 optical depth and ^{13}CO/^{12}CO ratio, which provides a potential tool to calibrate the spatial variation of α_{CO} within individual galaxies. I further test the scenario that α_{CO} varies in starburst mergers due to GMCs out of virial equilibrium and find a strong anti-correlation between α_{CO} and virial parameter that supports this scenario. My findings in general confirm the theoretical and simulation prediction that α_{CO} is closely related to GMC properties and provide potential calibration tools to measure α_{CO} spatial variation within individual galaxies.

I conclude this thesis with discussion in chapter 5.

In the Appendix, I include the published work from my ALMA internship project aiming to improve high-frequency flux calibration of ALMA telescope. I develop a new technique using water vapor data to continuously track the system temperature variation. This method is proved to be able to save 10% – 20% of ALMA observing time and improve flux measurement accuracy from 10% to 0.7% in some bad weather conditions.

Bibliography

Accurso, G., Saintonge, A., Catinella, B., et al. 2017, Monthly Notices of the Royal Astronomical Society, 470, 4750, doi: `10.1093/mnras/stx1556`

Adamo, A., Kruijssen, J. M. D., Bastian, N., Silva-Villa, E., & Ryon, J. 2015, Monthly

Notices of the Royal Astronomical Society, 452, 246, doi: `10.1093/mnras/stv1203`

Adamo, A., Zeidler, P., Kruijssen, J. M. D., et al. 2020a, Space Science Reviews, 216, 69, doi: `10.1007/s11214-020-00690-x`

Adamo, A., Hollyhead, K., Messa, M., et al. 2020b, Monthly Notices of the Royal Astronomical Society, 499, 3267, doi: `10.1093/mnras/staa2380`

Agertz, O., Renaud, F., Feltzing, S., et al. 2021, Monthly Notices of the Royal Astronomical Society, 503, 5826, doi: `10.1093/mnras/stab322`

Allen, M. L., & Kronberg, P. P. 1998, The Astrophysical Journal, 502, 218, doi: `10.1086/305894`

Ashworth, G., Fumagalli, M., Krumholz, M. R., et al. 2017, Monthly Notices of the Royal Astronomical Society, 469, 2464, doi: `10.1093/mnras/stx935`

Balser, D. S., Wenger, T. V., Anderson, L. D., & Bania, T. M. 2015, The Astrophysical Journal, 806, 199, doi: `10.1088/0004-637X/806/2/199`

Banerjee, S., & Kroupa, P. 2017, Astronomy and Astrophysics, 597, A28, doi: `10.1051/0004-6361/201526928`

Barcos-Muñoz, L., Leroy, A. K., Evans, A. S., et al. 2017, The Astrophysical Journal, 843, 117, doi: `10.3847/1538-4357/aa789a`

Barnes, A. T., Kauffmann, J., Bigiel, F., et al. 2020, Monthly Notices of the Royal Astronomical Society, 497, 1972, doi: `10.1093/mnras/staa1814`

Barnes, A. T., Glover, S. C. O., Kreckel, K., et al. 2021, Monthly Notices of the Royal Astronomical Society, 508, 5362, doi: `10.1093/mnras/stab2958`

Barnes, A. T., Chandar, R., Kreckel, K., et al. 2022, Astronomy and Astrophysics, 662, L6, doi: `10.1051/0004-6361/202243766`

Barnes, J. E., & Hernquist, L. 1996, The Astrophysical Journal, 471, 115, doi: `10.1086/177957`

Barnes, J. E., & Hernquist, L. E. 1991, The Astrophysical Journal, 370, L65, doi: `10.1086/185978`

Bellocchi, E., Pereira-Santaella, M., Colina, L., et al. 2022, A&A, 664, A60, doi: `10.1051/0004-6361/202142802`

Benincasa, S. M., Loebman, S. R., Wetzel, A., et al. 2020, Monthly Notices of the Royal Astronomical Society, 497, 3993, doi: `10.1093/mnras/staa2116`

Béthermin, M., De Breuck, C., Sargent, M., & Daddi, E. 2015, Astronomy and Astrophysics, 576, L9, doi: `10.1051/0004-6361/201525718`

Bigiel, F., Leroy, A., Walter, F., et al. 2008, The Astronomical Journal, 136, 2846, doi: `10.1088/0004-6256/136/6/2846`

Black, J. H., & Dalgarno, A. 1976, The Astrophysical Journal, 203, 132, doi: `10.1086/154055`

Black, J. H., & van Dishoeck, E. F. 1987, 115, 139

Bland-Hawthorn, J., & Gerhard, O. 2016, Annual Review of Astronomy and Astrophysics, 54, 529, doi: `10.1146/annurev-astro-081915-023441`

Blitz, L., & Rosolowsky, E. 2006, The Astrophysical Journal, 650, 933, doi: `10.1086/505417`

Bolatto, A. D., Leroy, A., Israel, F. P., & Jackson, J. M. 2003, The Astrophysical Journal, 595, 167, doi: `10.1086/377230`

Bolatto, A. D., Wolfire, M., & Leroy, A. K. 2013, Annual Review of Astronomy and Astrophysics, 51, 207, doi: `10.1146/annurev-astro-082812-140944`

Bournaud, F., Daddi, E., Weiß, A., et al. 2015, A&A, 575, A56, doi: `10.1051/0004-6361/201425078`

Braun, R., Thilker, D. A., Walterbos, R. A. M., & Corbelli, E. 2009, The Astrophysical Journal, 695, 937, doi: `10.1088/0004-637X/695/2/937`

Brodie, J. P., & Strader, J. 2006, Annu. Rev. Astron. Astrophys., 44, 193, doi: `10.1146/annurev.astro.44.051905.092441`

Brown, T., & Wilson, C. D. 2019, The Astrophysical Journal, 879, 17, doi: `10.3847/1538-4357/ab2246`

Brunetti, N. 2022, Thesis

Brunetti, N., & Wilson, C. D. 2022, Monthly Notices of the Royal Astronomical Society, 515, 2928, doi: `10.1093/mnras/stac1975`

Brunetti, N., Wilson, C. D., Sliwa, K., et al. 2020, Monthly Notices of the Royal Astronomical Society, 500, 4730, doi: `10.1093/mnras/staa3425`

Burkhart, B. 2018, The Astrophysical Journal, 863, 118, doi: `10.3847/1538-4357/aad002`

Buta, R. J., Sheth, K., Athanassoula, E., et al. 2015, The Astrophysical Journal Supplement Series, 217, 32, doi: `10.1088/0067-0049/217/2/32`

Calzetti, D., Kinney, A. L., & Storchi-Bergmann, T. 1996, The Astrophysical Journal, 458, 132, doi: `10.1086/176797`

Calzetti, D., Kennicutt, R. C., Engelbracht, C. W., et al. 2007, The Astrophysical Journal, 666, 870, doi: `10.1086/520082`

Carroll, B. W., & Ostlie, D. A. 2017, An Introduction to Modern Astrophysics, Second Edition

Cassata, P., Liu, D., Groves, B., et al. 2020, The Astrophysical Journal, 891, 83, doi: `10.3847/1538-4357/ab7452`

Chandar, R., Fall, S. M., Whitmore, B. C., & Mulia, A. J. 2017, The Astrophysical Journal, 849, 128, doi: `10.3847/1538-4357/aa92ce`

Chandar, R., Caputo, M., Mok, A., et al. 2023, The Astrophysical Journal, 949, 116, doi: `10.3847/1538-4357/acc93b`

Chown, R., Li, C., Athanassoula, E., et al. 2019, Monthly Notices of the Royal Astronomical Society, 484, 5192, doi: `10.1093/mnras/stz349`

Cleri, N. J., Trump, J. R., Backhaus, B. E., et al. 2021, arXiv:2009.00617 [astro-ph]. `http://ascl.net/2009.00617`

Colombo, D., Rosolowsky, E., Duarte-Cabral, A., et al. 2019, Monthly Notices of the Royal Astronomical Society, 483, 4291, doi: `10.1093/mnras/sty3283`

Comerón, S., Salo, H., Laurikainen, E., et al. 2014, Astronomy and Astrophysics, 562, A121, doi: `10.1051/0004-6361/201321633`

Condon, J. J., Huang, Z. P., Yin, Q. F., & Thuan, T. X. 1991, The Astrophysical Journal, 378, 65, doi: `10.1086/170407`

Condon, J. J., & Ransom, S. M. 2016, Essential Radio Astronomy

Cormier, D., Bigiel, F., Jiménez-Donaire, M. J., et al. 2018, Monthly Notices of the Royal Astronomical Society, 475, 3909, doi: `10.1093/mnras/sty059`

Cortés, F., Cortés, K., Reeves, R., Bustos, R., & Radford, S. 2020, Astronomy and Astrophysics, 640, A126, doi: `10.1051/0004-6361/202037784`

Costa, A. H., Johnson, K. E., Indebetouw, R., et al. 2021, ApJ, 918, 76, doi: `10.3847/1538-4357/ac0e93`

Cox, T. J., Jonsson, P., Somerville, R. S., Primack, J. R., & Dekel, A. 2008, Monthly Notices of the Royal Astronomical Society, 384, 386, doi: `10.1111/j.1365-2966.2007.12730.x`

Daddi, E., Elbaz, D., Walter, F., et al. 2010, The Astrophysical Journal, 714, L118, doi: `10.1088/2041-8205/714/1/L118`

Davé, R., Anglés-Alcázar, D., Narayanan, D., et al. 2019, Monthly Notices of the Royal Astronomical Society, 486, 2827, doi: `10.1093/mnras/stz937`

de Vaucouleurs, G. 1963, The Astrophysical Journal Supplement Series, 8, 31, doi: `10.1086/190084`

de Wit, W. J., Testi, L., Palla, F., & Zinnecker, H. 2005, Astronomy and Astrophysics, 437, 247, doi: `10.1051/0004-6361:20042489`

Dekel, A., Sari, R., & Ceverino, D. 2009, The Astrophysical Journal, 703, 785, doi: `10.1088/0004-637X/703/1/785`

Dessauges-Zavadsky, M., Richard, J., Combes, F., et al. 2019, Nat Astron, 3, 1115, doi: `10.1038/s41550-019-0874-0`

Díaz-Santos, T., Armus, L., Charmandaris, V., et al. 2017, The Astrophysical Journal, 846, 32, doi: `10.3847/1538-4357/aa81d7`

Dickinson, C. 2013, Advances in Astronomy, 2013, 162478, doi: `10.1155/2013/162478`

Downes, D., & Solomon, P. M. 1998, ApJ, 507, 615, doi: `10.1086/306339`

Downes, D., Solomon, P. M., & Radford, S. J. E. 1993, The Astrophysical Journal, 414, L13, doi: `10.1086/186984`

Draine, B. T. 2011, Physics of the Interstellar and Intergalactic Medium

Dubois, Y., Pichon, C., Welker, C., et al. 2014, Monthly Notices of the Royal Astronomical Society, 444, 1453, doi: `10.1093/mnras/stu1227`

Dunne, L., Maddox, S. J., Papadopoulos, P. P., Ivison, R. J., & Gomez, H. L. 2022, Monthly Notices of the Royal Astronomical Society, 517, 962, doi: `10.1093/mnras/stac2098`

Ellison, S. L., Wilkinson, S., Woo, J., et al. 2022, Monthly Notices of the Royal Astronomical Society, 517, L92, doi: `10.1093/mnrasl/slac109`

Elmegreen, B. G. 1993, The Astrophysical Journal, 411, 170, doi: `10.1086/172816`

Elmegreen, B. G., & Scalo, J. 2004, Annual Review of Astronomy and Astrophysics, 42, 211, doi: `10.1146/annurev.astro.41.011802.094859`

Elmegreen, D. M., Elmegreen, B. G., Kaufman, M., et al. 2017, The Astrophysical Journal, 841, 43, doi: `10.3847/1538-4357/aa6ba5`

Eskridge, P. B., Frogel, J. A., Pogge, R. W., et al. 2000, The Astronomical Journal, 119, 536, doi: `10.1086/301203`

Evans, A. S., Vavilkin, T., Pizagno, J., et al. 2008, The Astrophysical Journal, 675, L69, doi: `10.1086/533499`

Evans, II, N. J., Heiderman, A., & Vutisalchavakul, N. 2014, The Astrophysical Journal, 782, 114, doi: `10.1088/0004-637X/782/2/114`

Fall, S. M., Chandar, R., & Whitmore, B. C. 2005, The Astrophysical Journal, 631, L133, doi: `10.1086/496878`

Fensch, J., Renaud, F., Bournaud, F., et al. 2017, Monthly Notices of the Royal Astronomical Society, 465, 1934, doi: `10.1093/mnras/stw2920`

Finn, M. K., Indebetouw, R., Johnson, K. E., et al. 2022, The Astronomical Journal, 164, 64, doi: `10.3847/1538-3881/ac7aa1`

Fukui, Y., & Kawamura, A. 2010, Annu. Rev. Astron. Astrophys., 48, 547, doi: `10.1146/annurev-astro-081309-130854`

Fukui, Y., Kawamura, A., Minamidani, T., et al. 2008, The Astrophysical Journal Supplement Series, 178, 56, doi: `10.1086/589833`

Gao, Y., & Solomon, P. M. 2004, The Astrophysical Journal, 606, 271, doi: `10.1086/382999`

García-Burillo, S., Usero, A., Alonso-Herrero, A., et al. 2012, Astronomy and Astrophysics, 539, A8, doi: `10.1051/0004-6361/201117838`

Geach, J. E., Smail, I., Moran, S. M., et al. 2011, The Astrophysical Journal, 730, L19, doi: `10.1088/2041-8205/730/2/L19`

Gensior, J., Kruijssen, J. M. D., & Keller, B. W. 2020, Monthly Notices of the Royal Astronomical Society, 495, 199, doi: `10.1093/mnras/staa1184`

Genzel, R., Tacconi, L. J., Gracia-Carpio, J., et al. 2010, Monthly Notices of the Royal Astronomical Society, 407, 2091, doi: `10.1111/j.1365-2966.2010.16969.x`

Gerhard, O. 2002, Space Science Reviews, 100, 129, doi: `10.1023/A:1015818111633`

Gieles, M., Baumgardt, H., Heggie, D. C., & Lamers, H. J. G. L. M. 2010, Monthly Notices of the Royal Astronomical Society, 408, L16, doi: `10.1111/j.1745-3933.2010.00919.x`

Gies, D. R. 1987, The Astrophysical Journal Supplement Series, 64, 545, doi: `10.1086/191208`

Giménez-Arteaga, C., Brammer, G. B., Marchesini, D., et al. 2022, The Astrophysical Journal Supplement Series, 263, 17, doi: `10.3847/1538-4365/ac958c`

Ginsburg, A., Goss, W. M., Goddi, C., et al. 2016, Astronomy and Astrophysics, 595, A27, doi: `10.1051/0004-6361/201628318`

Glatt, K., Grebel, E. K., & Koch, A. 2010, Astronomy and Astrophysics, 517, A50, doi: `10.1051/0004-6361/201014187`

Glover, S. C. O. 2003, The Astrophysical Journal, 584, 331, doi: `10.1086/345684`

Goldsmith, P. F., & Langer, W. D. 1999, The Astrophysical Journal, 517, 209, doi: `10.1086/307195`

Gong, M., Ostriker, E. C., Kim, C.-G., & Kim, J.-G. 2020, The Astrophysical Journal, 903, 142, doi: `10.3847/1538-4357/abbdab`

Gordon, K. D., Roman-Duval, J., Bot, C., et al. 2014, The Astrophysical Journal, 797, 85, doi: `10.1088/0004-637X/797/2/85`

Grasha, K., Calzetti, D., Bittle, L., et al. 2018, Monthly Notices of the Royal Astronomical Society, 481, 1016, doi: `10.1093/mnras/sty2154`

Greve, T. R., Papadopoulos, P. P., Gao, Y., & Radford, S. J. 2009, Astrophysical Journal, 692, 1432, doi: `10.1088/0004-637X/692/2/1432`

Grudic, M. Y., Hopkins, P. F., Lee, E. J., et al. 2019, Monthly Notices of the Royal Astronomical Society, 488, 1501, doi: `10.1093/mnras/stz1758`

Haffner, L. M., Dettmar, R.-J., Beckman, J. E., et al. 2009, Rev. Mod. Phys., 81, 969, doi: `10.1103/RevModPhys.81.969`

Hannon, S., Lee, J. C., Whitmore, B. C., et al. 2019, Monthly Notices of the Royal Astronomical Society, 490, 4648, doi: `10.1093/mnras/stz2820`

Harrington, K. C., Weiss, A., Yun, M. S., et al. 2021, The Astrophysical Journal, 908, 95, doi: `10.3847/1538-4357/abcc01`

He, H., Wilson, C. D., Sliwa, K., Iono, D., & Saito, T. 2020, Monthly Notices of the Royal Astronomical Society, 496, 5243, doi: `10.1093/mnras/staa1826`

Heiles, C., & Troland, T. H. 2003, The Astrophysical Journal Supplement Series, 145, 329, doi: `10.1086/367785`

Hennebelle, P., & Chabrier, G. 2011, The Astrophysical Journal, 743, L29, doi: `10.1088/2041-8205/743/2/L29`

Hernquist, L. 1989, Nature, 340, 687, doi: 10.1038/340687a0

Heyer, M., & Dame, T. M. 2015, Annual Review of Astronomy and Astrophysics, vol. 53, p.583-629, 53, 583, doi: 10.1146/annurev-astro-082214-122324

Heyer, M. H., Carpenter, J. M., & Snell, R. L. 2001, The Astrophysical Journal, 551, 852, doi: 10.1086/320218

Hollyhead, K., Bastian, N., Adamo, A., et al. 2015, Monthly Notices of the Royal Astronomical Society, 449, 1106, doi: 10.1093/mnras/stv331

Hopkins, P. F., Wetzel, A., Kereš, D., et al. 2018, Monthly Notices of the Royal Astronomical Society, 480, 800, doi: 10.1093/mnras/sty1690

Howell, J. H., Armus, L., Mazzarella, J. M., et al. 2010, The Astrophysical Journal, 715, 572, doi: 10.1088/0004-637X/715/1/572

Hu, C.-Y., Schruba, A., Sternberg, A., & van Dishoeck, E. F. 2022, ApJ, 931, 28, doi: 10.3847/1538-4357/ac65fd

Hughes, A., Wong, T., Ott, J., et al. 2010, Monthly Notices of the Royal Astronomical Society, 406, 2065, doi: 10.1111/j.1365-2966.2010.16829.x

Iono, D., Yun, M. S., & Ho, P. T. P. 2005, The Astrophysical Journal Supplement Series, 158, 1, doi: 10.1086/429093

Israel, F. P., Tilanus, R. P. J., & Baas, F. 2006, Astronomy and Astrophysics, 445, 907, doi: 10.1051/0004-6361:20053096

Jameson, K. E., McClure-Griffiths, N. M., Liu, B., et al. 2019, The Astrophysical Journal Supplement Series, 244, 7, doi: 10.3847/1538-4365/ab3576

Jeffreson, S. M. R., Kruijssen, J. M. D., Keller, B. W., Chevance, M., & Glover, S. C. O. 2020, Monthly Notices of the Royal Astronomical Society, 498, 385, doi: 10.1093/mnras/staa2127

Jeffreson, S. M. R., Sun, J., & Wilson, C. D. 2022, Monthly Notices of the Royal Astronomical Society, 515, 1663, doi: 10.1093/mnras/stac1874

Jiao, Q., Zhao, Y., Lu, N., et al. 2019, The Astrophysical Journal, 880, 133, doi: 10.3847/1538-4357/ab29ed

Jiménez-Donaire, M. J., Bigiel, F., Leroy, A. K., et al. 2017, Monthly Notices of the Royal Astronomical Society, 466, 49, doi: `10.1093/mnras/stw2996`

Jiménez-Donaire, M. J., Usero, A., Bešlić, I., et al. 2023, Astronomy and Astrophysics, 676, L11, doi: `10.1051/0004-6361/202347050`

Johnson, K. E., & Kobulnicky, H. A. 2003, The Astrophysical Journal, 597, 923, doi: `10.1086/378585`

Johnson, L. C., Seth, A. C., Dalcanton, J. J., et al. 2017, The Astrophysical Journal, 839, 78, doi: `10.3847/1538-4357/aa6a1f`

Kamenetzky, J., Rangwala, N., & Glenn, J. 2017, Monthly Notices of the Royal Astronomical Society, 471, 2917, doi: `10.1093/mnras/stx1595`

Karl, S. J., Lunttila, T., Naab, T., et al. 2013, Monthly Notices of the Royal Astronomical Society, 434, 696, doi: `10.1093/mnras/stt1063`

Karl, S. J., Naab, T., Johansson, P. H., et al. 2010, The Astrophysical Journal, 715, L88, doi: `10.1088/2041-8205/715/2/L88`

Kaviraj, S. 2014a, Monthly Notices of the Royal Astronomical Society, 440, 2944, doi: `10.1093/mnras/stu338`

—. 2014b, Monthly Notices of the Royal Astronomical Society, 437, L41, doi: `10.1093/mnrasl/slt136`

Kazandjian, M. V., Meijerink, R., Pelupessy, I., Israel, F. P., & Spaans, M. 2015, Astronomy and Astrophysics, 574, A127, doi: `10.1051/0004-6361/201322805`

Keller, B. W., Wadsley, J., Benincasa, S. M., & Couchman, H. M. P. 2014, Monthly Notices of the Royal Astronomical Society, 442, 3013, doi: `10.1093/mnras/stu1058`

Kennicutt, Jr., R. C. 1998, The Astrophysical Journal, 498, 541, doi: `10.1086/305588`

Kennicutt, Jr., R. C., & De Los Reyes, M. A. C. 2021, The Astrophysical Journal, 908, 61, doi: `10.3847/1538-4357/abd3a2`

Kennicutt, Jr., R. C., Calzetti, D., Walter, F., et al. 2007, The Astrophysical Journal, 671, 333, doi: `10.1086/522300`

Khandai, N., Di Matteo, T., Croft, R., et al. 2015, Monthly Notices of the Royal Astronomical Society, 450, 1349, doi: `10.1093/mnras/stv627`

Knapen, J. H., Cisternas, M., & Querejeta, M. 2015, Monthly Notices of the Royal Astronomical Society, 454, 1742, doi: `10.1093/mnras/stv2135`

Koch, E. W., Rosolowsky, E. W., Leroy, A. K., et al. 2021, Monthly Notices of the Royal Astronomical Society, 504, 1801, doi: `10.1093/mnras/stab981`

Kreckel, K., Egorov, O. V., Belfiore, F., et al. 2022, Astronomy and Astrophysics, 667, A16, doi: `10.1051/0004-6361/202243858`

Kruijssen, J. M. D. 2012, Monthly Notices of the Royal Astronomical Society, 426, 3008, doi: `10.1111/j.1365-2966.2012.21923.x`

—. 2014, Classical and Quantum Gravity, 31, 244006, doi: `10.1088/0264-9381/31/24/244006`

Krumholz, M. R., Klein, R. I., & McKee, C. F. 2012, The Astrophysical Journal, 754, 71, doi: `10.1088/0004-637X/754/1/71`

Krumholz, M. R., & McKee, C. F. 2005, The Astrophysical Journal, 630, 250, doi: `10.1086/431734`

Krumholz, M. R., McKee, C. F., & Bland-Hawthorn, J. 2019, Annual Review of Astronomy and Astrophysics, vol. 57, p.227-303, 57, 227, doi: `10.1146/annurev-astro-091918-104430`

Krumholz, M. R., & Thompson, T. A. 2007, The Astrophysical Journal, 669, 289, doi: `10.1086/521642`

Lacy, J. H., Knacke, R., Geballe, T. R., & Tokunaga, A. T. 1994, The Astrophysical Journal, 428, L69, doi: `10.1086/187395`

Lada, C. J., & Dame, T. M. 2020, The Astrophysical Journal, 898, 3, doi: `10.3847/1538-4357/ab9bfb`

Lada, C. J., Forbrich, J., Lombardi, M., & Alves, J. F. 2012, The Astrophysical Journal, 745, 190, doi: `10.1088/0004-637X/745/2/19010.48550/arXiv.1112.4466`

Lada, C. J., Lombardi, M., & Alves, J. F. 2010, The Astrophysical Journal, 724, 687, doi: `10.1088/0004-637X/724/1/687`

Lada, E. A., Strom, K. M., & Myers, P. C. 1993, Environments of Star Formation - Relationship Between Molecular Clouds Dense Cores and Young Stars, 245

Langer, W. D., & Penzias, A. A. 1990, The Astrophysical Journal, 357, 477, doi: `10.1086/168935`

Larson, K. L., Sanders, D. B., Barnes, J. E., et al. 2016, The Astrophysical Journal, 825, 128, doi: `10.3847/0004-637x/825/2/128`

Larson, R. B. 1981, Monthly Notices of the Royal Astronomical Society, 194, 809, doi: `10.1093/mnras/194.4.809`

Lee, E. J., Miville-Deschênes, M.-A., & Murray, N. W. 2016, The Astrophysical Journal, 833, 229, doi: `10.3847/1538-4357/833/2/229`

Leitherer, C., Schaerer, D., Goldader, J. D., et al. 1999, The Astrophysical Journal Supplement Series, 123, 3, doi: `10.1086/313233`

Leroy, A. K., Walter, F., Brinks, E., et al. 2008, Astronomical Journal, 136, 2782, doi: `10.1088/0004-6256/136/6/2782`

Leroy, A. K., Bolatto, A., Gordon, K., et al. 2011, The Astrophysical Journal, 737, 12, doi: `10.1088/0004-637X/737/1/12`

Leroy, A. K., Hughes, A., Schruba, A., et al. 2016, The Astrophysical Journal, 831, 16, doi: `10.3847/0004-637X/831/1/16`

Leroy, A. K., Usero, A., Schruba, A., et al. 2017, The Astrophysical Journal, 835, 217, doi: `10.3847/1538-4357/835/2/217`

Leroy, A. K., Bolatto, A. D., Ostriker, E. C., et al. 2018, The Astrophysical Journal, 869, 126, doi: `10.3847/1538-4357/aaecd1`

Leroy, A. K., Schinnerer, E., Hughes, A., et al. 2021, ApJS, 257, 43, doi: `10.3847/1538-4365/ac17f3`

Levy, R. C., Bolatto, A. D., Leroy, A. K., et al. 2021, ApJ, 912, 4, doi: `10.3847/1538-4357/abec84`

Li, H., Vogelsberger, M., Bryan, G. L., et al. 2022, Monthly Notices of the Royal Astronomical Society, 514, 265, doi: `10.1093/mnras/stac1136`

Lofthouse, E. K., Kaviraj, S., Conselice, C. J., Mortlock, A., & Hartley, W. 2017, Monthly Notices of the Royal Astronomical Society, 465, 2895, doi: `10.1093/mnras/stw2895`

Lu, X., Zhang, Q., Kauffmann, J., et al. 2019, The Astrophysical Journal, 872, 171, doi: `10.3847/1538-4357/ab017d`

Mac Low, M.-M. 2013, Science, 340, 1229229, doi: `10.1126/science.1229229`

Mackey, J., Gvaramadze, V. V., Mohamed, S., & Langer, N. 2015, Astronomy and Astrophysics, 573, A10, doi: `10.1051/0004-6361/201424716`

Madau, P., Pozzetti, L., & Dickinson, M. 1998, The Astrophysical Journal, 498, 106, doi: `10.1086/305523`

Marinacci, F., Sales, L. V., Vogelsberger, M., Torrey, P., & Springel, V. 2019, Monthly Notices of the Royal Astronomical Society, 489, 4233, doi: `10.1093/mnras/stz2391`

Martig, M., Bournaud, F., Teyssier, R., & Dekel, A. 2009, The Astrophysical Journal, 707, 250, doi: `10.1088/0004-637X/707/1/250`

Martin, G., Kaviraj, S., Devriendt, J. E. G., et al. 2017, Monthly Notices of the Royal Astronomical Society, 472, L50, doi: `10.1093/mnrasl/slx136`

Masters, K. L., Nichol, R. C., Hoyle, B., et al. 2011, Monthly Notices of the Royal Astronomical Society, 411, 2026, doi: `10.1111/j.1365-2966.2010.17834.x`

Matsushita, S., Iono, D., Petitpas, G. R., et al. 2009, Astrophysical Journal, 693, 56, doi: `10.1088/0004-637X/693/1/56`

Matthews, A. M., Condon, J. J., Cotton, W. D., & Mauch, T. 2021, The Astrophysical Journal, 914, 126, doi: `10.3847/1538-4357/abfaf6`

Matzner, C. D. 2002, The Astrophysical Journal, 566, 302, doi: `10.1086/338030`

Matzner, C. D., & McKee, C. F. 2000, The Astrophysical Journal, 545, 364, doi: `10.1086/317785`

Meidt, S. E., Leroy, A. K., Rosolowsky, E., et al. 2018, The Astrophysical Journal, 854, 100, doi: `10.3847/1538-4357/aaa290`

Meier, D. S., & Turner, J. L. 2004, The Astronomical Journal, 127, 2069, doi: `10.1086/382904`

Menéndez-Delmestre, K., Sheth, K., Schinnerer, E., Jarrett, T. H., & Scoville, N. Z. 2007, The Astrophysical Journal, 657, 790, doi: `10.1086/511025`

Menon, S. H., Federrath, C., & Krumholz, M. R. 2022, Monthly Notices of the Royal Astronomical Society, 517, 1313, doi: `10.1093/mnras/stac2702`

Messa, M., Adamo, A., Östlin, G., et al. 2018, Monthly Notices of the Royal Astronomical Society, 473, 996, doi: `10.1093/mnras/stx2403`

Meurer, G. R., Heckman, T. M., Leitherer, C., et al. 1995, The Astronomical Journal, 110, 2665, doi: `10.1086/117721`

Michiyama, T., Saito, T., Tadaki, K.-i., et al. 2021, The Astrophysical Journal Supplement Series, 257, 28, doi: `10.3847/1538-4365/ac16df`

Mihos, J. C., & Hernquist, L. 1996, The Astrophysical Journal, 464, 641, doi: `10.1086/177353`

Miville-Deschênes, M.-A., Murray, N., & Lee, E. J. 2017, The Astrophysical Journal, 834, 57, doi: `10.3847/1538-4357/834/1/57`

Mizuno, N., Rubio, M., Mizuno, A., et al. 2001, Publications of the Astronomical Society of Japan, 53, L45, doi: `10.1093/pasj/53.6.L45`

Mo, H., van den Bosch, F. C., & White, S. 2010, Galaxy Formation and Evolution

Mok, A., Chandar, R., & Fall, S. M. 2019, The Astrophysical Journal, 872, 93, doi: `10.3847/1538-4357/aaf6ea`

—. 2020, The Astrophysical Journal, 893, 135, doi: `10.3847/1538-4357/ab7a14`

Montoya Arroyave, I., Cicone, C., Makroleivaditi, E., et al. 2023, Astronomy and Astrophysics, 673, A13, doi: `10.1051/0004-6361/202245046`

Moore, T. J. T., Plume, R., Thompson, M. A., et al. 2015, Monthly Notices of the Royal Astronomical Society, 453, 4264, doi: `10.1093/mnras/stv1833`

Moreno, J., Torrey, P., Ellison, S. L., et al. 2019, Monthly Notices of the Royal Astronomical Society, 485, 1320, doi: `10.1093/mnras/stz417`

Murphy, E. J., Condon, J. J., Schinnerer, E., et al. 2011, Astrophysical Journal, 737, doi: `10.1088/0004-637X/737/2/67`

Murray, C. E., Peek, J. E. G., Lee, M.-Y., & Stanimirović, S. 2018a, The Astrophysical Journal, 862, 131, doi: `10.3847/1538-4357/aaccfe`

Murray, C. E., Stanimirović, S., Goss, W. M., et al. 2018b, The Astrophysical Journal Supplement Series, 238, 14, doi: `10.3847/1538-4365/aad81a`

Mutch, S. J., Croton, D. J., & Poole, G. B. 2011, The Astrophysical Journal, 736, 84, doi: `10.1088/0004-637X/736/2/84`

Nakamura, F., & Li, Z.-Y. 2014, The Astrophysical Journal, 783, 115, doi: `10.1088/0004-637X/783/2/115`

Narayanan, D., Krumholz, M., Ostriker, E. C., & Hernquist, L. 2011, Monthly Notices of the Royal Astronomical Society, 418, 664, doi: `10.1111/j.1365-2966.2011.19516.x`

Narayanan, D., & Krumholz, M. R. 2014, Monthly Notices of the Royal Astronomical Society, 442, 1411, doi: `10.1093/mnras/stu834`

Narayanan, D., Krumholz, M. R., Ostriker, E. C., & Hernquist, L. 2012, Monthly Notices of the Royal Astronomical Society, 421, 3127, doi: `10.1111/j.1365-2966.2012.20536.x`

Neumann, L., Gallagher, M. J., Bigiel, F., et al. 2023, Monthly Notices of the Royal Astronomical Society, 521, 3348, doi: `10.1093/mnras/stad424`

Nishimura, A., Tokuda, K., Kimura, K., et al. 2015, ApJS, 216, 18, doi: `10.1088/0067-0049/216/1/18`

Oemler, Jr., A. 1974, The Astrophysical Journal, 194, 1, doi: `10.1086/153216`

Oka, T., Hasegawa, T., Sato, F., et al. 2001, The Astrophysical Journal, 562, 348, doi: 10.1086/322976

Olivier, G. M., Lopez, L. A., Rosen, A. L., et al. 2021, The Astrophysical Journal, 908, 68, doi: 10.3847/1538-4357/abd24a

Osterbrock, D. E., & Ferland, G. J. 2006, Astrophysics of Gaseous Nebulae and Active Galactic Nuclei

Padoan, P., & Nordlund, Å. 2011, The Astrophysical Journal, 730, 40, doi: 10.1088/0004-637X/730/1/40

Pan, H.-A., Lin, L., Hsieh, B.-C., et al. 2019, The Astrophysical Journal, 881, 119, doi: 10.3847/1538-4357/ab311c

Papadopoulos, P. P., & Seaquist, E. R. 1999, The Astrophysical Journal, 516, 114, doi: 10.1086/307090

Papadopoulos, P. P., van der Werf, P. P., Xilouris, E. M., et al. 2012, Monthly Notices of the Royal Astronomical Society, 426, 2601, doi: 10.1111/j.1365-2966.2012.21001.x

Papadopoulos, P. P., Zhang, Z.-Y., Xilouris, E. M., et al. 2014, The Astrophysical Journal, 788, 153, doi: 10.1088/0004-637X/788/2/153

Patton, D. R., Torrey, P., Ellison, S. L., Mendel, J. T., & Scudder, J. M. 2013, Monthly Notices of the Royal Astronomical Society, 433, L59, doi: 10.1093/mnrasl/slt058

Patton, D. R., Wilson, K. D., Metrow, C. J., et al. 2020, Monthly Notices of the Royal Astronomical Society, 494, 4969, doi: 10.1093/mnras/staa913

Pessa, I., Schinnerer, E., Belfiore, F., et al. 2021, Astronomy and Astrophysics, 650, A134, doi: 10.1051/0004-6361/202140733

Petric, A. O., Armus, L., Howell, J., et al. 2011, The Astrophysical Journal, 730, 28, doi: 10.1088/0004-637X/730/1/28

Pety, J., Guzmán, V. V., Orkisz, J. H., et al. 2017, Astronomy and Astrophysics, 599, A98, doi: 10.1051/0004-6361/201629862

Pfeffer, J., Bastian, N., Kruijssen, J. M. D., et al. 2019, Monthly Notices of the Royal Astronomical Society, 490, 1714, doi: `10.1093/mnras/stz2721`

Pillepich, A., Springel, V., Nelson, D., et al. 2018, Monthly Notices of the Royal Astronomical Society, 473, 4077, doi: `10.1093/mnras/stx2656`

Pineda, J. L., Goldsmith, P. F., Chapman, N., et al. 2010, The Astrophysical Journal, 721, 686, doi: `10.1088/0004-637X/721/1/686`

Pineda, J. L., Horiuchi, S., Anderson, L. D., et al. 2019, The Astrophysical Journal, 886, 1, doi: `10.3847/1538-4357/ab46c2`

Portegies Zwart, S. F., McMillan, S. L., & Gieles, M. 2010, Annu. Rev. Astron. Astrophys., 48, 431, doi: `10.1146/annurev-astro-081309-130834`

Privon, G. C., Barnes, J. E., Evans, A. S., et al. 2013, Astrophysical Journal, 771, doi: `10.1088/0004-637X/771/2/120`

Rangwala, N., Maloney, P. R., Glenn, J., et al. 2011, Astrophysical Journal, 743, doi: `10.1088/0004-637X/743/1/94`

Reina-Campos, M., & Kruijssen, J. M. D. 2017, Monthly Notices of the Royal Astronomical Society, 469, 1282, doi: `10.1093/mnras/stx790`

Renaud, F., Bournaud, F., Agertz, O., et al. 2019, Astronomy & Astrophysics, 625, A65, doi: `10.1051/0004-6361/201935222`

Renaud, F., Bournaud, F., & Duc, P.-A. 2015, Monthly Notices of the Royal Astronomical Society, 446, 2038, doi: `10.1093/mnras/stu2208`

Renaud, F., Bournaud, F., Kraljic, K., & Duc, P. A. 2014, Monthly Notices of the Royal Astronomical Society: Letters, 442, doi: `10.1093/mnrasl/slu050`

Rey, M. P., Agertz, O., Starkenburg, T. K., et al. 2022, VINTERGATAN-GM: The Cosmological Imprints of Early Mergers on Milky-Way-mass Galaxies

Rice, T. S., Goodman, A. A., Bergin, E. A., Beaumont, C., & Dame, T. M. 2016, The Astrophysical Journal, 822, 52, doi: `10.3847/0004-637X/822/1/52`

Rich, J., Aalto, S., Evans, A. S., et al. 2023, The Astrophysical Journal, 944, L50, doi: `10.3847/2041-8213/acb2b8`

Rico-Villas, F., Martin-Pintado, J., Gonzalez-Alfonso, E., Martin, S., & Rivilla, V. M. 2020, Monthly Notices of the Royal Astronomical Society, 491, 4573, doi: `10.1093/mnras/stz3347`

Robertson, B. E., & Kravtsov, A. V. 2008, The Astrophysical Journal, 680, 1083, doi: `10.1086/587796`

Rodighiero, G., Daddi, E., Baronchelli, I., et al. 2011, The Astrophysical Journal, 739, L40, doi: `10.1088/2041-8205/739/2/L40`

Rodríguez Montero, F., Davé, R., Wild, V., Anglés-Alcázar, D., & Narayanan, D. 2019, Monthly Notices of the Royal Astronomical Society, 490, 2139, doi: `10.1093/mnras/stz2580`

Rogers, H., & Pittard, J. M. 2013, Monthly Notices of the Royal Astronomical Society, 431, 1337, doi: `10.1093/mnras/stt255`

Rosolowsky, E., & Leroy, A. 2006, Publications of the Astronomical Society of the Pacific, 118, 590, doi: `10.1086/502982`

Rosolowsky, E., Hughes, A., Leroy, A. K., et al. 2021, Monthly Notices of the Royal Astronomical Society, 502, 1218, doi: `10.1093/mnras/stab085`

Rosolowsky, E. W., Pineda, J. E., Kauffmann, J., & Goodman, A. A. 2008, The Astrophysical Journal, 679, 1338, doi: `10.1086/587685`

Ryan, Jr., R. E., Cohen, S. H., Windhorst, R. A., & Silk, J. 2008, The Astrophysical Journal, 678, 751, doi: `10.1086/527463`

Salak, D., Nakai, N., Seta, M., & Miyamoto, Y. 2019, The Astrophysical Journal, 887, 143, doi: `10.3847/1538-4357/ab55dc`

Sánchez-García, M., Pereira-Santaella, M., García-Burillo, S., et al. 2022, Astronomy & Astrophysics, Volume 659, id.A102, <NUMPAGES>20</NUMPAGES> pp., 659, A102, doi: `10.1051/0004-6361/202141963`

Sanders, D. B., & Mirabel, I. F. 1996, Annual Review of Astronomy and Astrophysics, 34, 749, doi: `10.1146/annurev.astro.34.1.749`

Sanders, D. B., Soifer, B. T., Elias, J. H., et al. 1988, The Astrophysical Journal, 325, 74, doi: `10.1086/165983`

Sandstrom, K. M., Leroy, A. K., Walter, F., et al. 2013, The Astrophysical Journal, 777, 5, doi: `10.1088/0004-637X/777/1/5`

Schaye, J., Crain, R. A., Bower, R. G., et al. 2015, Monthly Notices of the Royal Astronomical Society, 446, 521, doi: `10.1093/mnras/stu2058`

Schaye, J., Kugel, R., Schaller, M., et al. 2023, Monthly Notices of the Royal Astronomical Society, doi: `10.1093/mnras/stad2419`

Schinnerer, E., Weiß, A., Aalto, S., & Scoville, N. Z. 2010, The Astrophysical Journal, 719, 1588, doi: `10.1088/0004-637X/719/2/1588`

Schinnerer, E., Meidt, S. E., Pety, J., et al. 2013, The Astrophysical Journal, 779, 42, doi: `10.1088/0004-637X/779/1/42`

Schneider, N., Bontemps, S., Simon, R., et al. 2011, Astronomy and Astrophysics, 529, A1, doi: `10.1051/0004-6361/200913884`

Schneider, N., Ossenkopf, V., Csengeri, T., et al. 2015, Astronomy and Astrophysics, 575, A79, doi: `10.1051/0004-6361/201423569`

Schruba, A., Leroy, A. K., Walter, F., et al. 2012, The Astronomical Journal, 143, 138, doi: `10.1088/0004-6256/143/6/138`

Scudder, J. M., Ellison, S. L., Momjian, E., et al. 2015, Monthly Notices of the Royal Astronomical Society, 449, 3719, doi: `10.1093/mnras/stv588`

Shimajiri, Y., Sakai, T., Tsukagoshi, T., et al. 2013, The Astrophysical Journal, 774, L20, doi: `10.1088/2041-8205/774/2/L20`

Shirley, Y. L. 2015, Publications of the Astronomical Society of the Pacific, 127, 299, doi: `10.1086/680342`

Sliwa, K., Wilson, C. D., Aalto, S., & Privon, G. C. 2017a, The Astrophysical Journal, 840, L11, doi: `10.3847/2041-8213/aa6ea4`

Sliwa, K., Wilson, C. D., Matsushita, S., et al. 2017b, The Astrophysical Journal, 840, 8, doi: `10.3847/1538-4357/aa689b`

Sliwa, K., Wilson, C. D., Petitpas, G. R., et al. 2012, Astrophysical Journal, 753, doi: `10.1088/0004-637X/753/1/46`

Smith, M. C., Bryan, G. L., Somerville, R. S., et al. 2021, Monthly Notices of the Royal Astronomical Society, 506, 3882, doi: `10.1093/mnras/stab1896`

Solomon, P. M., Rivolo, A. R., Barrett, J., & Yahil, A. 1987, The Astrophysical Journal, 319, 730, doi: `10.1086/165493`

Song, Y., Linden, S. T., Evans, A. S., et al. 2022, The Astrophysical Journal, 940, 52, doi: `10.3847/1538-4357/ac923b`

Sormani, M. C., Tress, R. G., Glover, S. C. O., et al. 2020, Monthly Notices of the Royal Astronomical Society, 497, 5024, doi: `10.1093/mnras/staa1999`

Springel, V., & Hernquist, L. 2005, The Astrophysical Journal, 622, L9, doi: `10.1086/429486`

Stahler, S. W., & Palla, F. 2004, The Formation of Stars

Stierwalt, S., Armus, L., Surace, J. A., et al. 2013, The Astrophysical Journal Supplement Series, 206, 1, doi: `10.1088/0067-0049/206/1/1`

Stott, J. P., Sobral, D., Smail, I., et al. 2013, Monthly Notices of the Royal Astronomical Society, 430, 1158, doi: `10.1093/mnras/sts684`

Strömgren, B. 1939, The Astrophysical Journal, 89, 526, doi: `10.1086/144074`

Stuber, S. K., Schinnerer, E., Williams, T. G., et al. 2023, Astronomy and Astrophysics, 676, A113, doi: `10.1051/0004-6361/202346318`

Sun, J., Leroy, A. K., Schruba, A., et al. 2018, The Astrophysical Journal, 860, 172, doi: `10.3847/1538-4357/aac326`

Sun, J., Leroy, A. K., Schinnerer, E., et al. 2020a, ApJL, 901, L8, doi: `10.3847/2041-8213/abb3be`

Sun, J., Leroy, A. K., Ostriker, E. C., et al. 2020b, ApJ, 892, 148, doi: `10.3847/1538-4357/ab781c`

Sun, J., Leroy, A. K., Rosolowsky, E., et al. 2022, The Astronomical Journal, 164, 43, doi: `10.3847/1538-3881/ac74bd`

Sun, J., Leroy, A. K., Ostriker, E. C., et al. 2023, Star Formation Laws and Efficiencies across 80 Nearby Galaxies, doi: `10.48550/arXiv.2302.12267`

Sun, W., de Grijs, R., Fan, Z., & Cameron, E. 2016, The Astrophysical Journal, 816, 9, doi: `10.3847/0004-637X/816/1/9`

Tacconi, L. J., Genzel, R., Neri, R., et al. 2010, Nature, 463, 781, doi: `10.1038/nature08773`

Teyssier, R., Chapon, D., & Bournaud, F. 2010, Astrophysical Journal Letters, 720, 149, doi: `10.1088/2041-8205/720/2/L149`

Thompson, T. A., Quataert, E., & Murray, N. 2005, The Astrophysical Journal, 630, 167, doi: `10.1086/431923`

Thorp, M. D., Ellison, S. L., Pan, H.-A., et al. 2022, Monthly Notices of the Royal Astronomical Society, 516, 1462, doi: `10.1093/mnras/stac2288`

Tielens, A. G. G. M. 2005, The Physics and Chemistry of the Interstellar Medium

Toomre, A. 1977, Mergers and Some Consequences, 401

Turner, J. A., Dale, D. A., Lee, J. C., et al. 2021, Monthly Notices of the Royal Astronomical Society, 502, 1366, doi: `10.1093/mnras/stab055`

U, V., Sanders, D. B., Mazzarella, J. M., et al. 2012, The Astrophysical Journal Supplement Series, 203, 9, doi: `10.1088/0067-0049/203/1/9`

Ueda, J., Iono, D., Petitpas, G., et al. 2012, The Astrophysical Journal, 745, 65, doi: `10.1088/0004-637X/745/1/65`

Usero, A., Leroy, A. K., Walter, F., et al. 2015, Astronomical Journal, 150, 115, doi: `10.1088/0004-6256/150/4/115`

Van Der Tak, F. F., Black, J. H., Schöier, F. L., Jansen, D. J., & Van Dishoeck, E. F. 2007, Astronomy and Astrophysics, 468, 627, doi: `10.1051/0004-6361:20066820`

Violino, G., Ellison, S. L., Sargent, M., et al. 2018, Monthly Notices of the Royal Astronomical Society, 476, 2591, doi: `10.1093/MNRAS/STY345`

Viti, S., García-Burillo, S., Fuente, A., et al. 2014, Astronomy and Astrophysics, 570, A28, doi: `10.1051/0004-6361/201424116`

Vogelsberger, M., Genel, S., Springel, V., et al. 2014, Monthly Notices of the Royal Astronomical Society, 444, 1518, doi: `10.1093/mnras/stu1536`

Wainer, T. M., Johnson, L. C., Seth, A. C., et al. 2022, The Astrophysical Journal, 928, 15, doi: `10.3847/1538-4357/ac51cf`

Watanabe, Y., Sorai, K., Kuno, N., & Habe, A. 2011, Monthly Notices of the Royal Astronomical Society, 411, 1409, doi: `10.1111/j.1365-2966.2010.17746.x`

Watson, D. M., Genzel, R., Townes, C. H., & Storey, J. W. V. 1985, The Astrophysical Journal, 298, 316, doi: `10.1086/163612`

Wei, L. H., Keto, E., & Ho, L. C. 2012, The Astrophysical Journal, 750, 136, doi: `10.1088/0004-637X/750/2/136`

Weilbacher, P. M., Monreal-Ibero, A., Verhamme, A., et al. 2018, Astronomy and Astrophysics, 611, A95, doi: `10.1051/0004-6361/201731669`

Wenger, T. V., Balser, D. S., Anderson, L. D., & Bania, T. M. 2019, The Astrophysical Journal, 887, 114, doi: `10.3847/1538-4357/ab53d3`

Whitmore, B. C., Schweizer, F., Leitherer, C., Borne, K., & Robert, C. 1993, The Astronomical Journal, 106, 1354, doi: `10.1086/116732`

Whitmore, B. C., Chandar, R., Schweizer, F., et al. 2010, Astronomical Journal, 140, 75, doi: `10.1088/0004-6256/140/1/75`

Whitmore, B. C., Brogan, C., Chandar, R., et al. 2014, ApJ, 795, 156, doi: `10.1088/0004-637X/795/2/156`

Whitmore, B. C., Chandar, R., Lee, J., et al. 2020, The Astrophysical Journal, 889, 154, doi: `10.3847/1538-4357/ab59e5`

Wilson, C. D., Elmegreen, B. G., Bemis, A., & Brunetti, N. 2019, The Astrophysical Journal, 882, 5, doi: `10.3847/1538-4357/ab31f3`

Wilson, C. D., Howe, J. E., & Balogh, M. L. 1999, The Astrophysical Journal, 517, 174, doi: `10.1086/307180`

Wilson, C. D., Walker, C. E., & Thornley, M. D. 1997, The Astrophysical Journal, 483, 210, doi: `10.1086/304216`

Wilson, C. D., Petitpas, G. R., Iono, D., et al. 2008, The Astrophysical Journal Supplement Series, 178, 189, doi: `10.1086/590910`

Wolfire, M. G., Hollenbach, D., & McKee, C. F. 2010, The Astrophysical Journal, 716, 1191, doi: `10.1088/0004-637X/716/2/1191`

Wong, T., & Blitz, L. 2002, The Astrophysical Journal, 569, 157, doi: `10.1086/339287`

Yamashita, T., Komugi, S., Matsuhara, H., et al. 2017, The Astrophysical Journal, 844, 96, doi: `10.3847/1538-4357/aa7af1`

Zackrisson, E., Rydberg, C.-E., Schaerer, D., Östlin, G., & Tuli, M. 2011, The Astrophysical Journal, 740, 13, doi: `10.1088/0004-637X/740/1/13`

Zepf, S. E., Ashman, K. M., English, J., Freeman, K. C., & Sharples, R. M. 1999, The Astronomical Journal, 118, 752, doi: `10.1086/300961`

Zhu, M., Seaquist, E. R., & Kuno, N. 2003, The Astrophysical Journal, 588, 243, doi: `10.1086/368353`

Chapter 2

Embedded Young Massive Star Clusters in the Antennae Merger

The content of this chapter has been published under the following citation:

He, H.; Wilson, C. D.; Brunetti, N.; Finn, M.; Bemis, A.; Johnson, K. 2022, “Embedded Young Massive Star Clusters in the Antennae Merger", ApJ, 928, 57

Embedded Young Massive Star Clusters in the Antennae Merger

Abstract

The properties of young massive clusters (YMCs) are key to understanding the star formation mechanism in starburst systems, especially mergers. We present ALMA high-resolution (∼10 pc) continuum (100 and 345 GHz) data of YMCs in the overlap region of the Antennae galaxy. We identify 6 sources in the overlap region, including two sources that lie in the same giant molecular cloud (GMC). These YMCs correspond well with radio sources in lower resolution continuum (100 and 220 GHz) images at GMC scales (∼60 pc). We find most of these YMCs are bound clusters through virial analysis. We estimate their ages to be ∼1 Myr and to be either embedded or just beginning to emerge from their parent cloud. We also compare each radio source with Paβ source and find they have consistent total ionizing photon numbers, which indicates they are tracing the same physical source. By comparing the free-free emission at ∼10 pc scale and ∼60 pc scale, we find that ∼50% of the free-free emission in GMCs actually comes from these YMCs. This indicates that roughly half of the stars in massive GMCs are formed in bound clusters. We further explore the mass correlation between YMCs and GMCs in the Antennae and find it generally agrees with the predictions of the star cluster simulations. The most massive YMC has a stellar mass that is 1% – 5% of its host GMC mass.

Keywords: *galaxies: individual (Antennae), galaxies: ISM, galaxies: starburst, galaxies: star clusters: general, galaxies: star formation*

2.1 Introduction

How massive star clusters form is one of the major unsolved problems in star formation. Massive cluster formation was ubiquitous in the early universe, as witnessed by the populations of old massive globular clusters found in galaxies of all masses and morphologies (Harris et al. 2013). Indeed, given that the fraction of stellar mass contained in globular clusters today may be 10% or less of their initial mass as protoclusters (Fall & Zhang 2001; Whitmore et al. 2007; Li & Gnedin 2014), massive clusters should have been one of the most important modes of star formation in the early universe. In addition, current theory suggests that star formation is caused by fragmentation of hierarchically collapsing giant molecular clouds (GMCs; e.g. McKee & Ostriker 2007), which naturally leads to the conclusion that stars tend to form together in bound clusters. Both theory (Kruijssen 2012) and observations (Adamo et al. 2020) suggest that for ultra/luminous infrared galaxies (U/LIRGs), more than 50% of stars are formed in bound clusters. Therefore, studying young massive star clusters (YMCs) will help us understand the star forming process in starburst systems.

Large populations of young massive star clusters are seen in a diverse range of interacting galaxies and merger remnants by the Hubble Space Telescope (HST), from the M51 system (Scoville et al. 2001) to the Antennae (Whitmore et al. 1999, 2010) to Arp 220 (Scoville et al. 2000; Zhang et al. 2001). Of all the systems studied so far, the Antennae stands out for its uniquely large population of young massive clusters (Scoville et al. 2000; Wilson et al. 2006) and massive molecular clouds (Wilson et al. 2003), while its proximity (22 Mpc Schweizer et al. 2008) allows us to obtain the highest possible spatial resolution. Multi-wavelength observations have mapped out the distribution of optically visible young clusters (Whitmore et al. 2010) as well as the far-infrared emission that traces buried star formation (Klaas et al. 2010). Much of the far-infrared emission is located in the "overlap region" (Stanford et al. 1990), a region that is also rich in molecular gas (Wilson et al. 2003; Whitmore et al. 2014; Schirm et al. 2016) and radio continuum emission (Neff & Ulvestad 2000). The overlap region also contains two bright water masers, which are a common indicator of massive star formation (Brogan et al. 2010). However, optical observations generally miss extremely young clusters (ages < few Myr, Johnson & Kobulnicky 2003; Johnson et al. 2004; Reines et al. 2008; Johnson et al. 2009; Hannon et al. 2019) that have high dust extinction. Whitmore et al. (2010) suggest that about 16% of star clusters in

Table 2.1: Summary of the ALMA continuum observations of the Antennae

Project Code	Central Frequency (GHz)	Beam (")	Arrays used	LAS [a] (")	RMS noise (mJy beam^{-1})
2018.1.00272.S	100	0.57 × 0.43	12m+7m	70	0.011
2018.1.00272.S	220	0.63 × 0.59	12m+7m	41	0.054
2016.1.00041.S	100	0.11 × 0.11	12m	4.1	0.016
2016.1.00041.S	345	0.11 × 0.11	12m	4.1	0.04

a. LAS stands for largest angular scale.

the Antennae are hidden from view in the optical. However, since radio observations are generally unaffected by dust extinction (Murphy et al. 2011), we can use radio frequencies to probe these extremely young YMCs.

In this paper, we measure YMC properties using ALMA continuum images at ~ 10 pc scale. We compare these images with continuum images at GMC scales ($\sim$60 pc) to explore various correlations between the YMCs and their host GMCs. In Section 2, we describe the observations and how we processed the data. In Section 3, we describe how we measure various quantities, such as free-free flux, dust flux, temperature and velocity dispersion. We then derive the stellar mass and gas mass based on those quantities. In Section 4, we use those quantities to explore the evolutionary stage and dynamical state of the YMCs. In Section 5, we compare various quantities, such as star formation rate (SFR) and total mass at YMC and GMC scales, to study the correlation between these two types of objects.

2.2 Observations and Data Reduction

2.2.1 Continuum at star cluster resolution

The continuum data at star cluster resolution is from ALMA project 2016.1.00041.S (PI: Christine Wilson). This project only has continuum observations from the 12m array and covers ALMA Bands 3 (100 GHz) and 7 (345 GHz). The total bandwidth for each spectral window is 2000 MHz. The spatial resolution for both frequency bands is about 0.1 arcsec (~ 10 pc). The largest angular scale is about 4.1 arcsec ($\sim$ 500 pc, Table 1)

The original reduction scripts were used to calibrate the raw data using CASA version 4.7.2. All of the imaging steps were carried out using CASA version 5.1.0-70.

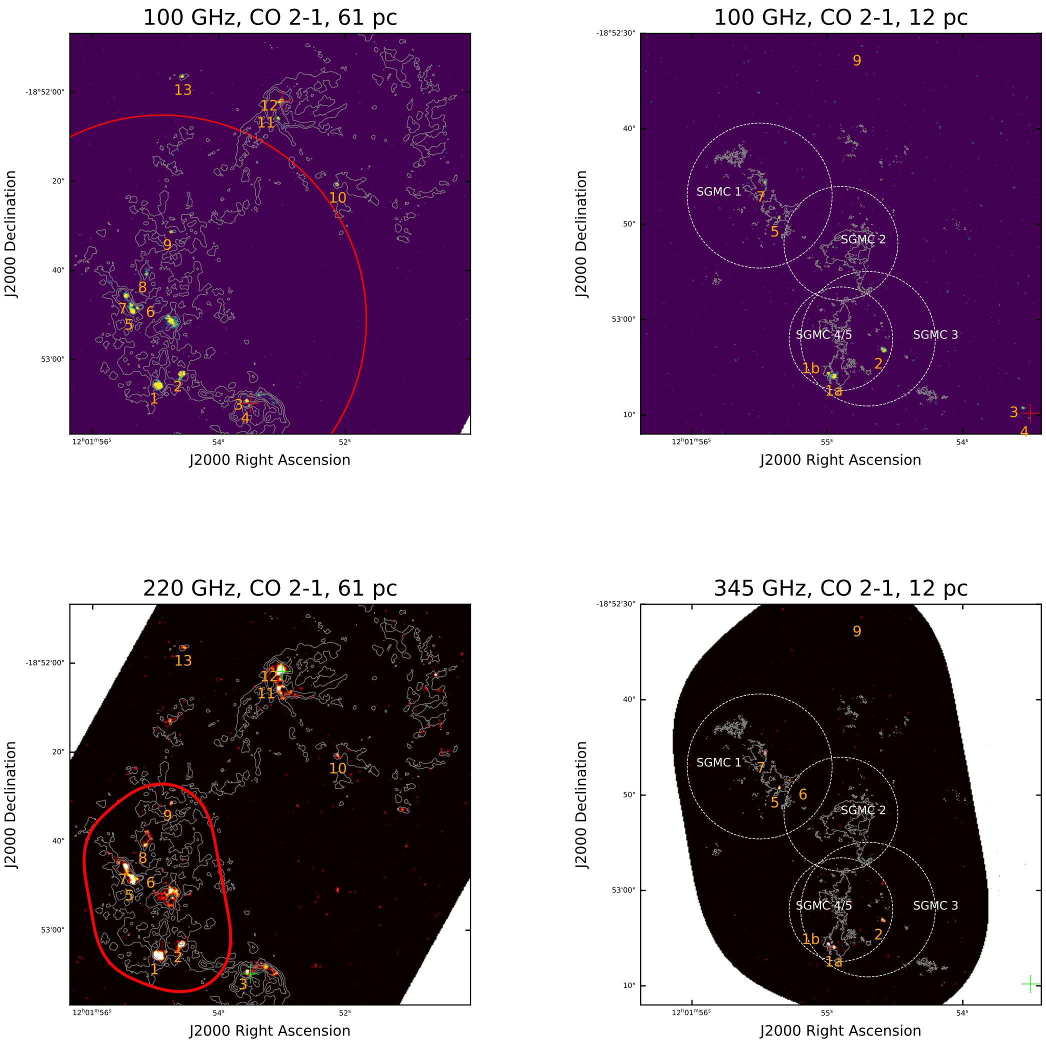

Figure 2.1: Continuum image of the Antennae at (Upper) 100 GHz, (Lower Left) 230 GHz and (Lower Right) 340 GHz. The continuum images in the left panels are from ALMA project 2018.1.00272.S with physical resolution of 61 pc. The contours are from the ^{12}CO J=2-1 moment 0 map from Brunetti et al. (in prep). Red apertures show the field of view of the high-resolution images shown in the right panels. The continuum images in the right panels are from ALMA project 2016.1.00041.S with physical resolution of 12 pc. Contours in the right panels are from the ^{12}CO J=2-1 moment 0 map from Finn et al. (2019). The dashed circles in the right panels show the location of the SGMCs identified in Wilson et al. (2000) with the diameters equal to those of the SGMCs. The red and green plus signs show the locations of two nuclei from Zhang et al. (2001).

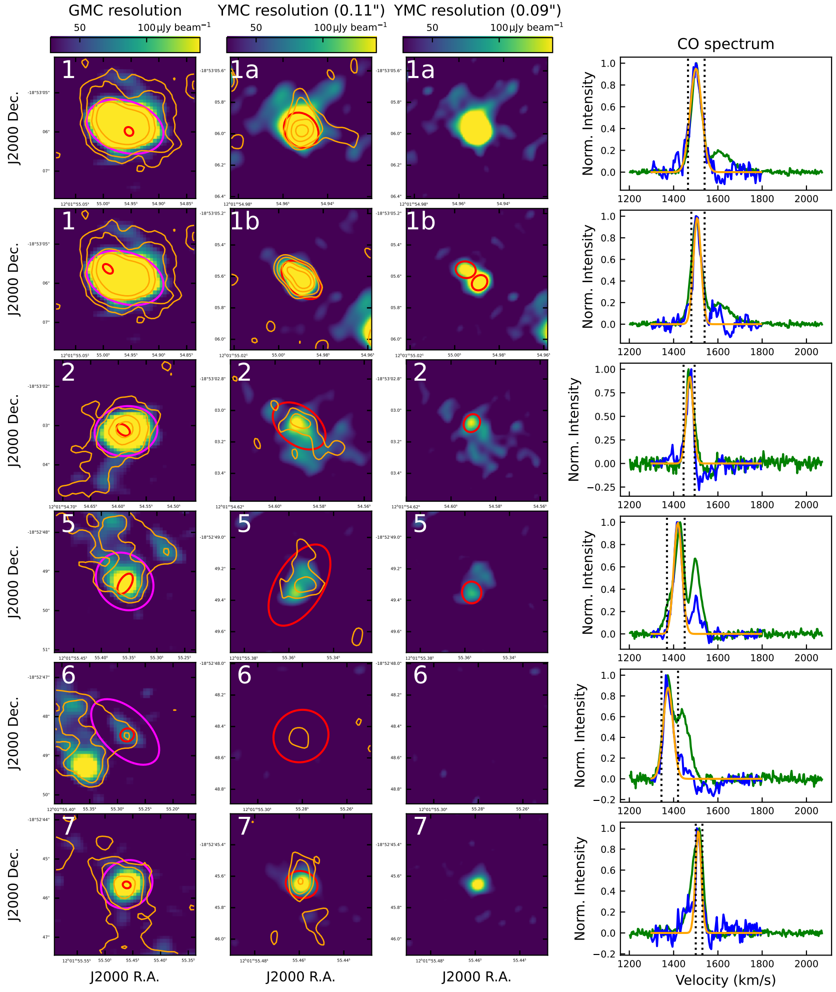

Figure 2.2: (Left) Continuum images and (Right) ^{12}CO J=2-1 spectra of individual YMCs. For the images, the left column shows the 100 GHz data at GMC resolution (61 pc). The orange contours are the 220 GHz data at similar resolution. Magenta apertures are the apertures used to measure the flux at GMC scales. Red apertures are the apertures used to measure the flux at YMC scales. The middle and right column show the 100 GHz data at YMC scales with slightly different resolution. The orange contours in the middle column are the 345 GHz data at the same resolution. Red apertures in the middle column are the same as the ones in the left column. The red apertures in the right column are the fitted Gaussian beam for substructures in some of the YMCs. The ^{12}CO J=2-1 spectra are normalized to the peak of the line emission measured in the magenta apertures in the left column (green spectrum)and the red apertures in the middle column (blue spectrum). The orange curves are the fitted Gaussian function to the measured spectrum (shown in blue). The vertical dotted lines specify the velocity ranges that we use to fit the Gaussian spectra.

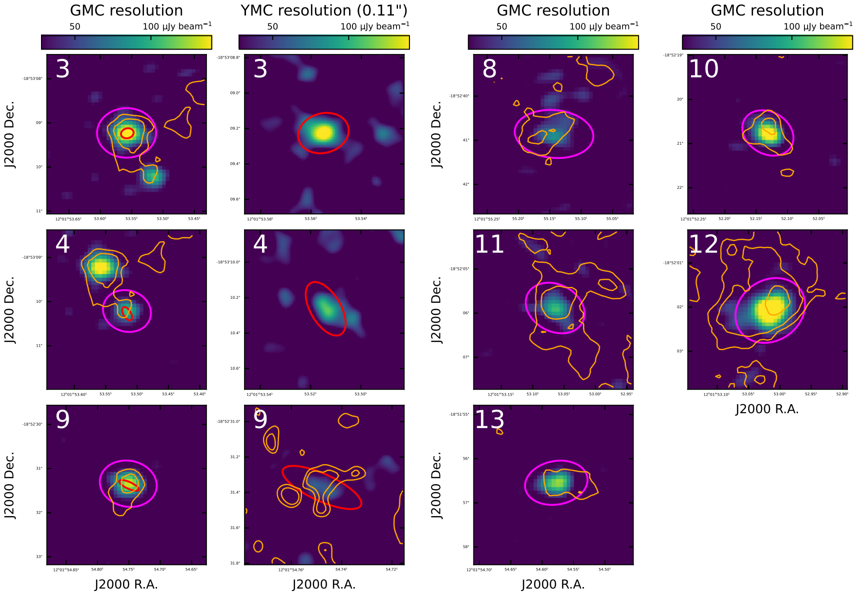

Figure 2.3: Images for YMCs that do not have ^{12}CO J=2-1 observations at 12 pc scale. (Left) the 3 sources that have 100 GHz images at YMC scale. (Right) The remaining sources that only have 100 GHz GMC resolution data. The orange contour in GMC-resolution images are the 220 GHz continuum and that in YMC-resolution images are the 345 GHz continuum. The magenta apertures are used to measure the GMC fluxes while the red apertures are used to measure the YMC fluxes.

Before imaging, we binned channels in the calibrated measurement set to a channel width of 125 MHz for Band 3 and 250 MHz for Band 7. We then ran `tclean` on the measurement set and did the clean interactively. To match the spatial scale of the Band 3 and Band 7 images, we set the lowest uvrange to be 50 kλ. We used a robust parameter of 0.5 for the `tclean` command. Finally, we used the CASA command `imsmooth` to smooth both images to a beam size of 0.11" × 0.11" (12 pc).

2.2.2 Continuum at GMC resolution

The continuum data at GMC resolution is acquired from project 2018.1.00272.S (PI: Christine Wilson). This project has observations with both the 7m array and 12m extended and compact configuration arrays and covers frequencies in ALMA Bands 3 (110 GHz) and 6 (220 GHz) with various spectral lines detected (Brunetti et al. in prep.). The total usable bandwidth for each of the spectral windows is 1875 MHz for the 12m array and 2000 MHz for the 7m array. The highest spectral resolution is 0.976 MHz (Table 1).

The original reduction scripts were used to calibrate the raw data using CASA version 5.4.0-70. We used CASA 5.6.1 to image the continuum in Band 3 and Band 6 using all of the spectral windows in each band. Before imaging, we flagged the channels with detected spectral lines and combined data from different arrays into a single measurement set. We also binned the channels to a channel width of 125 MHz to speed up the imaging process. Imaging used the CASA command `tclean` with the clean threshold set to be 2 times the RMS noise. We chose the specmode to be "mfs" and masking method to be 'auto-multithresh' (Kepley et al. 2020) to choose the clean regions automatically. The 'auto-multithresh' parameters were left as the default values. We applied the primary beam correction to the cleaned images.

2.2.3 CO line data at GMC resolution

The ^{12}CO J=2-1 data with GMC resolution is also from project 2018.1.00272.S (PI: Christine Wilson). The image cube was made with a modified version of PHANGS pipeline (Leroy et al. 2021, ; see details in Brunetti et al. in prep.). The beam size was rounded to 0.51" × 0.51" (54 pc). The velocity resolution is 2.65 km s^{-1}. The RMS is 2.6 K.

2.2.4 CO line data at star cluster resolution

The ^{12}CO J=2-1 data with star cluster resolution is from Finn et al. (2019). The beam size of the data is 0.12" × 0.09" (13 pc). The channel width of the cube is 5 km s^{-1}. The RMS of the cube is 1.2 mJy $beam^{-1}$.

2.2.5 HST Data

We use Paβ and I Band maps from Whitmore et al. (2014) for comparison with the radio continuum. Both images have resolution of $\sim$ 0.2". The I Band image has a pixel size of 0.04" while the Paβ image has a larger pixel size of 0.128". In Section 2.4.4 we use Paβ to calculate the total ionized photon number ($Q(H^0)$) and compare it with that derived from 100 GHz continuum.

For Paβ, we perform continuum subtraction using the HST J Band image. Since the wavelengths of the two filters are close to each other, we adopt a simple model that the intensity at J Band for background stars is the scaled version for that in Paβ image. Therefore, the Paβ intensity is

$$I_{\mathrm{Pa}\beta} = I_{\mathrm{F128N}} - \beta \cdot I_{\mathrm{F116W}} \tag{2.1}$$

where I_{F128N} is the Paβ intensity before continuum subtraction, I_{F116W} is the J Band intensity and $I_{\mathrm{Pa}\beta}$ is the intensity after the continuum subtraction. To calculate the β, we draw apertures around sources that are point like and not associated with any galaxy structures, which are likely background stars. We then measure the fluxes of these sources from F128N and F116W filters. We also measure the background fluxes by drawing apertures close to these background stars. We then plot the background-subtracted fluxes from the two filters and fit a proportional relation to get β. We calculate β = 0.03, which is close to β value in Kessler et al. (2020). We then reproject the J Band image to the Paβ and apply Eq. 2.1 to perform the continuum subtraction.

2.3 Measurements and Derived Quantities

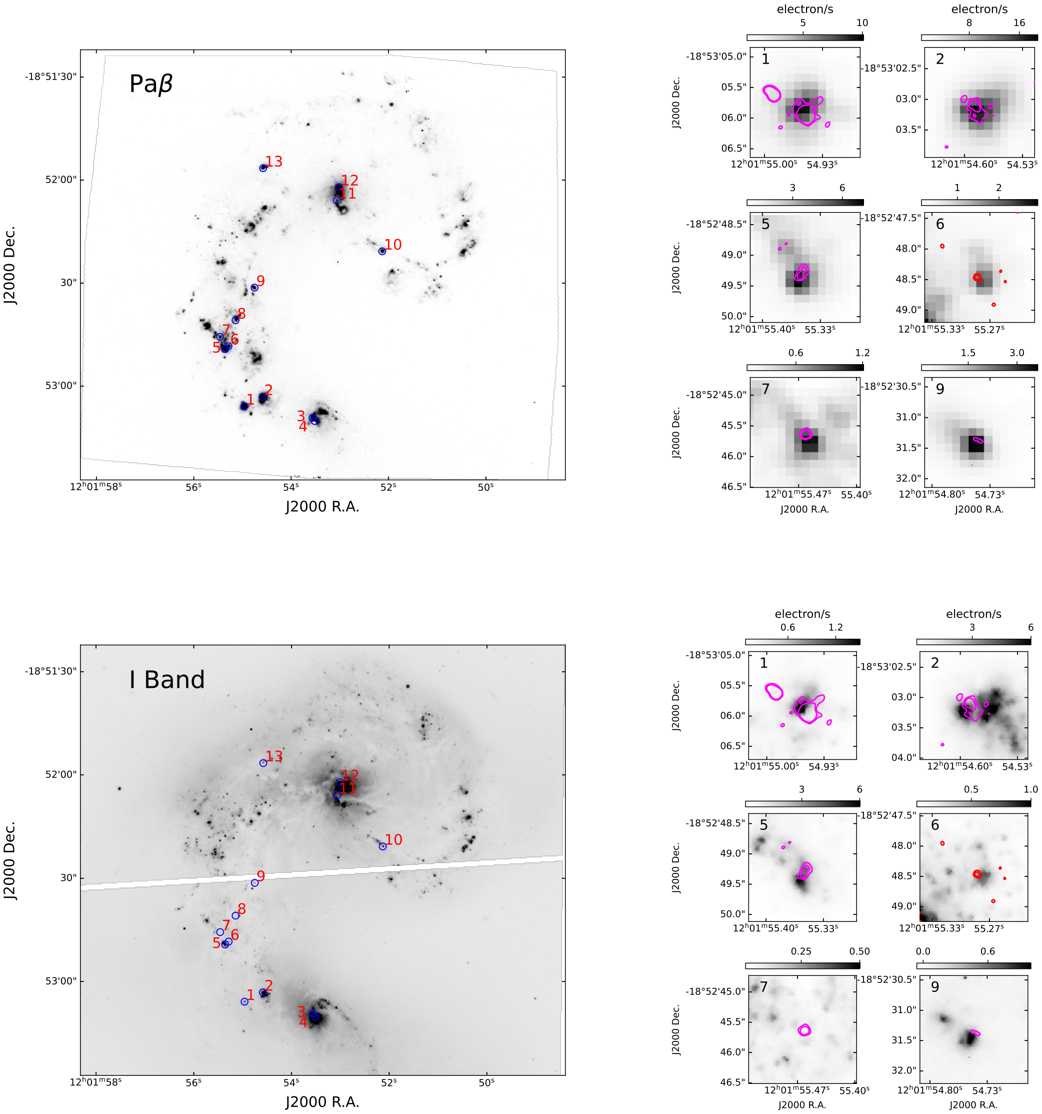

Figure 2.4: The Paschen β (upper) and I band (lower) maps of the Antennae. (Upper Left) The Paschen β map of the Antennae (Whitmore et al. 2014) with the positions of the radio continuum sources labeled as blue circles. (Upper Right) Zoom-in Paβ images for the individual YMCs. The magenta and red contours are 100 and 345 GHz continuum at 12 pc resolution. The typical offset between the Paβ and radio continuum sources is $\sim$ 11 pc. (Lower Left) The HST I Band image for the entire field of view of the Antennae. (Lower Right) Zoom-in I Band image for each YMC.

Table 2.2: Measured Quantities of YMCs in the Antennae

Index (1)	Coordinates (J2000) (2)	$S_{100\text{GHz}}$ (mJy) (3)	$S_{340\text{GHz,dust}}$ (mJy) (4)	σ_v (km/s) (5)	T_{kin} (K) (6)	d_{FWHM} (arcsec) (7)
1a	12h01m54.95s, -18d53m05.98s	1.2 ± 0.04	< 0.04	$< 26 \pm 1$	40 ± 2	0.085 ± 0.01
1b	12h01m54.99s, -18d53m05.62s	0.69 ± 0.04	0.89 ± 0.1	$< 19 \pm 1$	53 ± 2	0.12 ± 0.02
2	12h01m54.59s, -18d53m03.10s	0.41 ± 0.05	0.33 ± 0.1	$< 17 \pm 2$	42 ± 2	0.17 ± 0.04
3	12h01m53.55s, -18d53m09.23s	0.28 ± 0.07	–	–	–	0.12 ± 0.03
4	12h01m53.51s, -18d53m10.26s	0.19 ± 0.07	–	–	–	0.14 ± 0.05
5	12h01m53.51s, -18d53m10.26s	0.37 ± 0.07	0.67 ± 0.1	$< 19 \pm 1$	48 ± 2	0.28 ± 0.06
6	12h01m55.28s, -18d52m48.46s	< 0.081	0.32 ± 0.1	$< 23 \pm 2$	48 ± 2	0.14 ± 0.03
7	12h01m55.46s, -18d52m45.65s	0.23 ± 0.03	0.25 ± 0.07	$< 15 \pm 1$	38 ± 2	0.06 ± 0.02
9	12h01m54.75s, -18d52m31.37s	0.14 ± 0.06	0.19 ± 0.2	–	–	0.22 ± 0.09

(1) Source ID (2) Coordinates. (3) Fluxes at 100 GHz. (4) Estimated dust fluxes at 345 GHz. (5) ^{12}CO J=2-1 velocity dispersion. All values are upper limits (see Section 2.3.2.) (6) Kinetic temperature from LTE analysis. (7) Deconvolved FWHM of the source from CASA task `imfit`. At the distance of the Antennae (22 Mpc), 0.1" = 10.67 pc.

2.3.1 Source Identification

The continuum images from the two ALMA continuum projects are shown in Fig. 2.1. As we can see, the continuum images at GMC resolution have higher sensitivity. Therefore, we use the 100 GHz GMC-resolution map, which has the highest sensitivity among all the continuum data, as a guide to find sources in the higher resolution maps by eye. The identified sources are labeled in Fig. 2.1. As we can see, there are ~ 10 continuum sources that are likely to be YMCs. The reason we do not observe as many radio continuum sources as optical clusters is mainly due to the limited sensitivity of the radio data. As mentioned in Section 2.2, a continuum point source with S/N of 5 corresponds to a 7.2×10^5 $M_{\odot}$, which is greater than the masses of most star clusters in spiral galaxies. On the other hand, the lifetime of the radio clusters are also much lower than that of optical clusters (see Section 2.4.1 for detailed discussion), which also contributes to the limited number of sources we detected.

We then match the 100 GHz low-resolution image with the high-resolution image to check if the continuum source is still point-like in the high-resolution image. Source 8 is not detected in the high-resolution image and may be dominated by GMC-scale emission that is filtered out in the high-resolution image. Another interesting source is source 1, which is the brightest source in the continuum map. It separates into two sources in the higher resolution image. Furthermore, source 1b further divides into two sub-sources in our highest resolution image, as shown in Fig. 2.2. We can see source 1a and 1b have similar velocities (Fig. 2). This comparison suggests these two clusters are close to each other in 3D space and probably interacting with each other within a single GMC. Multiple YMCs within a single GMC have also been observed in NGC 253 (Leroy et al. 2015, 2018). Statistical studies (e.g. Grasha et al. 2018; Tsuge et al. 2019) also show that a significant fraction of GMCs will form more than one YMCs.

We further check the 220 GHz continuum image at GMC scale and the 345 GHz continuum image at star cluster scale. An interesting source is source 6, which is not seen in the 100 GHz continuum image but is seen in both 220 and 345 GHz continuum. Since 100 GHz continuum traces free-free emission from extremely young stars, it seems likely that this source is dominated by a clump of gas with stars yet to form.

Sources 1a, 1b, 2, 5, 6 and 7 have all been covered by high-resolution observations of 100 and 345 GHz continuum and the ^{12}CO J=2-1 line with high S/N detections.

Therefore, we will focus on these sources in the rest of this paper. Images for these sources are shown in Fig. 2.2, while the remaining sources are shown in Fig. 2.3. The measured properties of all sources are listed in Tables 2.2 and 2.3. The comparison between radio continuum and Paβ is shown in Fig. 2.4.

2.3.2 Size, Flux and Line Width Measurements

We determine the sizes of the YMCs using the CASA task `imfit` on the high-resolution 100 GHz data. This task fits a 2D Gaussian function for a selected encircled region. First, we draw an elliptical aperture around each identified source by eye. We then run the task `imfit` to get the major axis, minor axis and position angle of the fitted beam. We confirm the fitting results by comparing the half-maximum contour of the source with the fitted apertures on the map. The `imfit` command also gives us the Gaussian size deconvolved from the beam, which tells us the true source size. We list the major axis of the deconvolved Gaussian in Table 2.2. For source 6, since we do not have a detection in 100 GHz continuum, we use the 345 GHz continuum image to fit the source. Note that the beam size of 12 pc is larger than most YMCs in the literature, which have measured sizes of about 2 pc (Leroy et al. 2018). If the YMCs in the Antennae were to have a similar size, we would expect our derived sizes to be upper limits to the true source size.

We use an aperture with diameter equal to two times the fitted Gaussian FWHM to measure the flux. The flux uncertainty is calculated as

$$Err = \mathrm{RMS} \times \sqrt{N_{\mathrm{beam}}}/\mathrm{pbcor}$$

where RMS is the image noise, N_{beam} is the number beams in the aperture and pbcor is the value for the primary beam response.

We also measured the line width for the star clusters using the ^{12}CO J=2-1 map from Finn et al. (2019) and the same apertures used for the flux measurements. We export the spectrum for each source and then fit a Gaussian to get the velocity dispersion. Many spectra show an extra bump besides the major peak, which comes from gas outside the star cluster. Therefore, we manually set the upper and lower limit for the fitting range to only fit the Gaussian to the major peak. The fits are shown in Fig. 2.2. In addition, we apply the same method to draw the aperture on sources in the 100 GHz GMC map (see Section 2.5.1). We also overlay the GMC-scale ^{12}CO J=2-1 spectrum measured in those apertures in the right column of Fig. 2.2. As we can see, the velocity dispersions at YMC scale are almost the same as those at GMC scale. We suspect this is because the velocity dispersion as measured with ^{12}CO J=2-1 at YMC scale still traces the overall cloud motions. In this case, the measured velocity dispersion for YMC should be treated as upper limit.

2.3.3 Separating Dust Emission and Free-Free Emission

At 345 GHz, dust emission is usually expected to be dominant. However, there is still a significant fraction of free-free emission at this frequency for these YMCs. To calculate the dust mass, we need to separate the dust emission from the free-free emission. To begin with, we assume free-free emission dominates the total emission at 100 GHz. This assumption has been shown to hold for YMCs in the Henize 2-10 dwarf galaxy with similar resolution of ∼10 pc (Costa et al. 2021). Free-free emission scales with frequency as a power-law function with index of -0.1 (Ginsburg et al. 2016). Therefore, we can predict the free-free flux at 340 GHz using

$$S_{345\mathrm{GHz,ff}} = S_{100\mathrm{GHz}} \left(\frac{345\ \mathrm{GHz}}{100\ \mathrm{GHz}} \right)^{-0.1} \tag{2.2}$$

where $S_{100\mathrm{GHz}}$ is the continuum flux at 100 GHz. Then the dust flux is just

$$S_{345\mathrm{GHz,dust}} = S_{345\mathrm{GHz}} - S_{345\mathrm{GHz,ff}} \tag{2.3}$$

We will use the dust-only flux to calculate the dust and gas mass in the YMCs.

2.3.4 Gas Temperature

To calculate the dust mass from the dust flux, we need to assume a dust temperature. We assume the dust temperature is equal to the gas kinetic temperature. The gas temperature can then be constrained through the ^{12}CO J=2-1 observations (Finn et al. 2019) by assuming local thermal equilibrium (LTE). The basic formula to connect the peak brightness temperature and the gas temperature is

$$T_b = \left[\frac{h\nu/k}{\exp(h\nu/kT_{\mathrm{ex}}) - 1} - \frac{h\nu/k}{\exp(h\nu/kT_{\mathrm{bg}}) - 1} \right] \left(1 - e^{-\tau} \right) \tag{2.4}$$

where T_b is the peak brightness temperature, $T_{\rm ex}$ is the excitation temperature, $T_{\rm bg} = 2.73K$ is the background temperature, ν is the observed frequency of the line, τ is the optical depth, h is Planck's constant and k is the Boltzmann constant. For ^{12}CO J=2-1, $h\nu/k$ = 11.07 K. We also assume $\tau \to \infty$. Applying all these assumptions, we can express $T_{\rm kin}$ as

$$T_{\rm kin} = T_{\rm ex} = \frac{11.07}{\ln\left[1 + \frac{11.07}{T_b + 0.195}\right]} \tag{2.5}$$

The gas temperatures are shown in Table 2.2. We see that almost all the sources have $T_{\rm kin} \sim 40$ K. Rico-Villas et al. (2020) show that YMCs in NGC 253 have temperatures of 150 - 300 K based on line ratios of HC$_3$N. We note that our physical beam size (12 pc) is much larger than those for NGC 253 (1.9 pc). As discussed in Section 4.1, we probably overestimate the sizes of these YMCs. Therefore, our apertures probably include a large fraction of surrounding gas with lower temperatures.

2.3.5 Gas Mass

The gas mass is calculated from the dust emission after correcting for free-free contamination. We calculate the dust mass based on the equation in Wilson et al. (2008),

$$M_{\rm dust} = 74,220 S_{880} D^2 \frac{\left(e^{17/T} - 1\right)}{\kappa} \, (M_\odot) \tag{2.6}$$

where S_{880} is the flux from dust emission at 880 μm (345 GHz), D is the distance in Mpc, T is the dust temperature in Kelvin and κ is the dust emissivity in cm^2 g^{-1}. In this case we assume κ = 0.9 cm^2 g^{-1} (Wilson et al. 2008). The dust mass is highly dependent on the dust temperature. We assume the dust temperature is equal to the gas kinetic temperature (see Section 3.4)

From the dust mass, we then calculate the molecular gas mass based on the gas-to-dust mass ratio:

$$M_{\rm gas} = \frac{[\rm Gas]}{[\rm Dust]} \times M_{\rm dust} \tag{2.7}$$

We adopt a gas-to-dust mass ratio of 120 from Wilson et al. (2008). The gas masses are given in Table 2.3.

2.3.6 Extinction

From the gas mass we calculated, we can then derive the gas surface density which is directly related to the optical extinction A_V. We can compare A_V from the dust emission with that from optical data to see if they agree with each other. We adapt the equation in Draine (2003) to calculate the visual extinction A_V from the gas surface density,

$$A_V = 0.0491\Sigma_{\text{gas,YMC}} \tag{2.8}$$

where $\Sigma_{\text{gas,YMC}}$ is the YMC gas surface density derived from the dust continuum flux and deconvolved radius in $\text{M}_\odot\ \text{pc}^{-2}$. The A_V values (Table 2.3) show that these sources generally have visual extinctions of hundreds of magnitudes. These extinctions are much larger than the A_V values derived for the optical counterparts of these YMCs (Table 2.4). We will discuss this discrepancy in Section 2.4.4.

2.3.7 Total Ionizing Photon Number

We can use both the 100 GHz continuum and the Paβ line to calculate the total number of ionizing photons, $Q(H^0)$, since they both trace emission from the ionized gas. We compare the $Q(H^0)$ from two different data sets in Section 2.4.4. $Q(H^0)$ can also be used to calculate the stellar mass of young star clusters based on a few assumptions.

For 100 GHz continuum, we assume the emission is dominated by free-free emission. Therefore, we can calculate the total number of ionizing photons using the equation from Murphy et al. (2011),

$$\left[\frac{Q\left(H^0\right)}{\text{s}^{-1}}\right] = 6.3\times10^{25}\left(\frac{T_\text{e}}{10^4\ \text{K}}\right)^{-0.45}\left(\frac{v}{\text{GHz}}\right)^{0.1}\times\left(\frac{L_v^\text{T}}{\text{ergs}^{-1}\ \text{Hz}^{-1}}\right) \tag{2.9}$$

where $Q\left(H^0\right)$ is the total number of ionizing photons, T_e is the temperature of the HII region (generally 10^4 K), $\nu = 100$ GHz is the observed frequency and L_v^T is the luminosity of the free-free emission at the observed frequency.

For Paβ data, we use the equation to calculate $Q(H^0)$ from Hα (Murphy et al. 2011). Assume Hα/Paβ = 17.6 (Case B recombination, T=10^4 K, and $n_e = 10^4$ cm^{-3}; given by Osterbrock 1989; Cleri et al. 2020) and the equation to calculate

$Q(H^0)$ from Paβ is given by

$$Q_{\mathrm{Pa}\beta}(H^0) = 1.3 \times 10^{13}\ 10^{0.4A_{\mathrm{Pa}\beta}} L_{\mathrm{Pa}\beta} \tag{2.10}$$

where $L_{\mathrm{Pa}\beta}$ is the luminosity of Paβ in erg s^{-1} and $A_{\mathrm{Pa}\beta}$ is the extinction for the Paβ line in magnitude. $A_{\mathrm{Pa}\beta}$ can be derived from A_V based on the extinction curve in Calzetti et al. (2000) as

$$A_{\mathrm{Pa}\beta} = A_V \times \frac{k_{\mathrm{P}\beta}}{k_V} = 0.43 A_V \tag{2.11}$$

where $k_{\mathrm{P}\beta}$ and k_V are the values of reddening curve at the two wavelengths (Calzetti et al. 2000, Eq. 4).

2.3.8 Stellar Mass

From $Q\,(H^0)$, we can calculate the stellar mass using the equation from Leroy et al. (2018),

$$M_\star = \frac{Q\,(H^0)}{4 \times 10^{46}}\ M_\odot \tag{2.12}$$

This equation assumes a Kroupa initial mass function with maximum stellar mass of 100 $M_\odot$ and also assumes YMCs have a single stellar population (SSP). The stellar masses calculated from the 100 GHz fluxes in Table 2 are given in Table 3.

2.4 Star cluster properties

2.4.1 Ages of the YMCs

We can estimate the ages of the YMCs by comparing the number of clusters at optical wavelengths with the number observed in the radio. This method has been used previously for estimating ages of YMCs in the dwarf galaxy Henize 2-10 (Kobulnicky & Johnson 1999; Johnson & Kobulnicky 2003). The number ratio is roughly the age ratio of the two populations if we assume a constant SFR during this time period. Zhang et al. (2001) estimate there are about 1600 clusters with ages smaller than 16 Myr and masses greater than 10^4 M$_\odot$. For our 100 GHz GMC map, the S/N=5 cutoff is $\sim 7.2 \times 10^4$ M$_\odot$. To estimate the number of optical clusters with masses greater

Table 2.3: Derived Physical Properties of YMCs

Index (1)	$\log_{10} M_\star$ ($M_\odot$) (2)	$\log_{10} M_{\rm gas}$ ($M_\odot$) (3)	$\log_{10} M_{\rm vir}$ ($M_\odot$) (4)	$\log_{10} \Sigma_{\rm tot}$ ($M_\odot$ pc^{-2}) (5)	R_h (pc) (6)	A_V (10^2 mag) (7)
1a	6.2 ± 0.01	< 5.4	$< 6.8 \pm 0.06$	4.4 ± 0.2	4.5 ± 0.5	< 2
1b	6.0 ± 0.03	6.8 ± 0.05	$< 6.7 \pm 0.09$	4.7 ± 0.2	6.4 ± 1.1	22 ± 8
2	5.8 ± 0.05	6.4 ± 0.15	$< 6.8 \pm 0.13$	4.1 ± 0.2	9.1 ± 2.1	4.5 ± 2.6
5	5.7 ± 0.08	6.7 ± 0.08	$< 7.0 \pm 0.1$	3.9 ± 0.2	15 ± 3	3.2 ± 1.5
6	< 5.1	6.3 ± 0.15	$< 6.9 \pm 0.1$	4.1 ± 0.2	7.5 ± 1.6	6.1 ± 3.3
7	5.5 ± 0.05	6.3 ± 0.13	$< 6.3 \pm 0.2$	4.7 ± 0.3	3.2 ± 1.1	28 ± 20

(1) Source ID. (2) Stellar mass. (3) Dust mass. (3) Gas mass derived from dust continuum (see Section 3.5). (4) Virial mass as upper limit. (5) Total surface density (gas+star) of YMCs (6) Half-light radius (7) Optical extinction at V band

than that value, we assume the cluster mass function has a slope of -2 (Krumholz et al. 2019). In this case, we expect about 200 optical clusters with masses greater than 7.2×10^4 $M_\odot$ and ages less than 16 Myr. Our actual 100 GHz GMC map reveal 17 continuum sources greater than that value. Based on that number, we would expect the age of these radio YMCs to be $\sim$ 1 Myr. Various HST studies of YMCs have adopted similar statistical counting methods and find the time for star clusters to dissociate from their host GMCs is about 2–3 Myr (Hollyhead et al. 2015; Grasha et al. 2018; Hannon et al. 2019). If this timescale is also true for the Antennae, we would expect feedback has not been effective for most of our radio sources. Therefore, they should still be forming stars.

2.4.2 Size-Mass relation

We plot our measurements of the YMCs in the size-mass relation along with literature data from other galaxies (Fig 2.5). According to Leroy et al. (2018) and Levy et al. (2021), very young YMCs are generally very compact with radii of 1 $\sim$ 2 pc. However, from the fit to the size-mass relation in the LEGUS sample (Brown & Gnedin 2021), we would expect a radius of $\sim$ 5 pc for a YMC with stellar mass of 10^6 $M_\odot$. This radius is consistent with what we measured for some of the YMCs in the Antennae. Note that the Brown & Gnedin (2021) relation for young star clusters does not extend to 10^6 $M_\odot$.

We also plot dashed lines from Krumholz et al. (2019) to show regions where

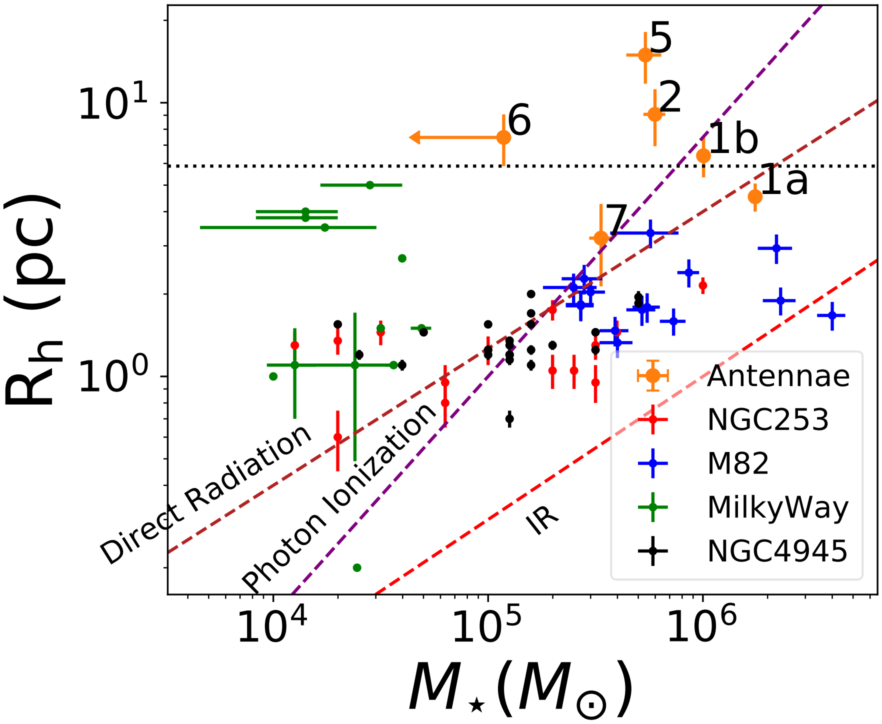

Figure 2.5: The half-light radius versus stellar mass for YMCs in the Antennae, NGC 253 (Leroy et al. 2018), M82 (McCrady & Graham 2007), Milky Way (Krumholz et al. 2019) and NGC 4945 (Emig et al. 2020). The horizontal dotted line marks our YMC resolution (0.11"). The diagonal dashed lines specify the area where the feedback from direct radiation (brown), photoionization (purple) and IR radiation (red) is effective for dispersing the surrounding gas (Krumholz et al. 2019). For direct radiation and photoionization, the effective area is leftward and for IR radiation, the effective area is rightward.

feedback is effective. As we can see, most of the YMCs lie in the area where direct radiation or photoionization feedback is effective. This suggests two possibilities. One is that feedback is actually effective for these YMCs. As shown in Table 2.3, most YMCs except for source 1a have gas fractions greater than 50%. According to various observations (Whitmore & Zhang 2002; Whitmore et al. 2014; Hannon et al. 2019; Chevance et al. 2020), the timescale for feedback to disperse the gas is around 1 – 3 Myr. As we have calculated, these YMCs should generally have ages of ~ 1 Myr. Therefore, although feedback is expected to play a role, it has not cleared all the gas surrounding the YMCs.

On the other hand, we might overestimate the sizes of these YMCs. As shown in Fig. 2.5, our resolution limit is higher than most of YMCs with similar masses. As an example, suppose the radii are overestimated by a factor of 4: cluster 1a would then fall on the line for IR radiation feedback to be effective, while the rest of the clusters would lie in the region where no feedback is effective. However, we note that the feedback region in the size-mass diagram is one projection of a complex process. In ?, they find outflows in YMCs which they do not expect to be experiencing feedback given their location in the size-mass diagram.

2.4.3 Virial Mass

We use the equation in Bolatto et al. (2013) to calculate the virial mass,

$$M_{\rm vir} = 1061\ R_h\ \sigma_v^2 \tag{2.13}$$

where $M_{\rm vir}$ is the virial mass in $\mathrm{M}_\odot$, R_h is the deconvolved half-light radius in pc and σ_v is the measured velocity dispersion in km s^{-1} of the source. This equation assumes uniform density.

Fig. 2.6 shows the comparison between virial mass and total mass. We can see that the virial masses for all the YMCs are smaller than $2 \times M_{\rm tot}$, which implies that these YMCs are likely gravitationally bound systems. We need to note that the virial masses of the YMCs should be treated as upper limits because our measured velocity dispersion is tracing the overall cloud motion instead of the dispersion inside the YMC. This further confirms that all these sources should be gravitationally bound system and may be virialized.

Although these YMC+gas systems are currently gravitationally bound, whether

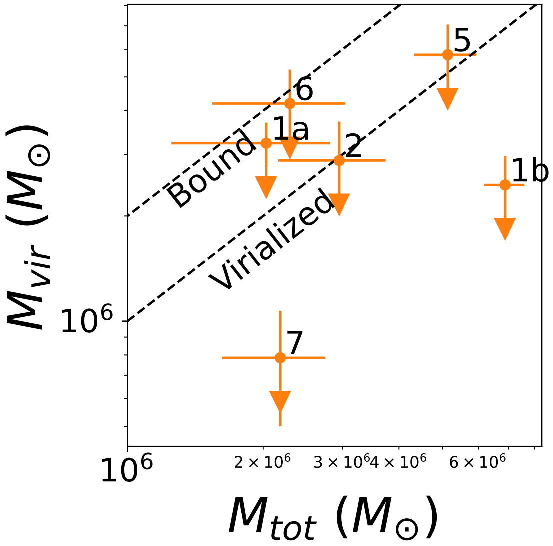

Figure 2.6: The comparison between the total mass and the virial mass. The two diagonal dashed lines mark the boundaries below which systems are bound or virialized. The offset between the dashed lines is a factor of 2. We can see that most of sources are bound systems.

the final star cluster will be gravitationally bound or not depends on the fraction of the gas mass that is eventually turned into stars. Thus, the boundedness of these very young embedded YMCs is not necessarily inconsistent with the results from Matthews et al. (2018), who found that only a small fraction of the optically visible young star clusters in the Antennae are likely to remain gravitationally bound.

2.4.4 Comparison with Optical Data

Table 2.4: Corresponding optical YMCs

Index (1)	Region (2)	HST ID (3)	$\log_{10} M_\star$ ($M_\odot$) (4)	Age (Myr) (5)	A_V (mag) (6)	$S_{\mathrm{Pa}\beta}$ (10^{-14} erg s^{-1}) (7)	$S_{\mathrm{100GHz,smooth}}$ (mJy) (8)	Cross ID (9)
1a	SGMC 4/5	14612	6.8	1.0	7.3	1.92	2.1 ± 0.05	B1
2	SGMC 4/5	15492	6.6	2.5	3.0	4.1	1.3 ± 0.07	B
5	SGMC 1	19330	5.5	1.0	1.0	0.84	0.4 ± 0.04	D
6	SGMC 1	19807	–	8	5.0	0.24	< 0.075	D1
7	SGMC 1	–	–	3.5	4.1	0.16	0.61 ± 0.05	D2
9	LT	3475	6.0	1.0	4.2	0.36	0.35 ± 0.07	E3

(1) Source ID from Table 2.2. (2) Regions defined in Whitmore et al. (2014) based on ^{12}CO J=3-2 map. (3) HST IDs for star clusters identified in Whitmore et al. (2010)(source 1a, 2, 5, 6) or Whitmore & Zhang (2002)(source 9). (4) Stellar mass of the star clusters from Whitmore et al. (2010) or Whitmore & Zhang (2002). (5) Age of the star clusters from Whitmore et al. (2014). (6) Extinction at V band from Whitmore et al. (2014). (7) The flux measured for Paβ sources. (8) The flux measured for 100 GHz radio sources smoothed to the resolution of 0.201". (9) Cross IDs of K Band sources identified in Gilbert & Graham (2007).

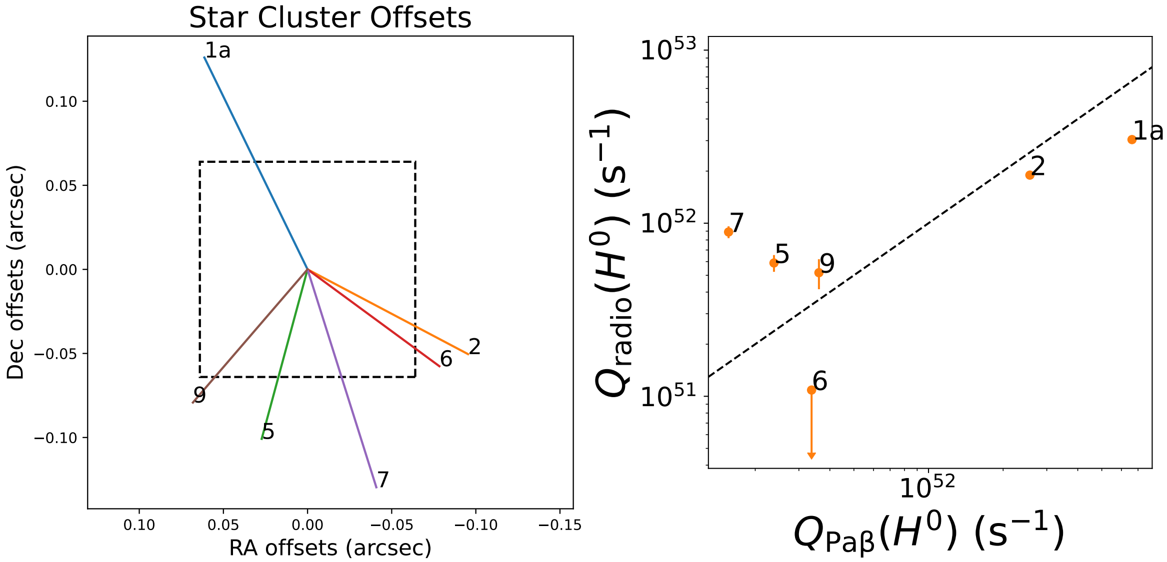

Figure 2.7: (Left) The coordinate offsets between Paβ sources and radio continuum sources. The dashed square shows the pixel size of the Paβ image (0.128"). (Right) The comparison of the total ionizing photon numbers derived from Paβ and 100 GHz images. The dashed line shows the 1-to-1 relation.

Based on the multi-wavelength comparison in Whitmore et al. (2014), we can see that most of our sources have optical counterparts. The properties of these optical YMCs are summarized in Table 2.4. As we mentioned in Section 2.3.6, the A_V derived from the optical data is $\sim$ 100 times smaller than that derived from the dust continuum. This difference suggests the optical source and radio source might just happen to be along the same line of sight. Furthermore, the radio continuum data used in Whitmore et al. (2014) only has a resolution of $\sim$ 0.5". With our new data, we can make a more precise comparison of the coordinates of the optical and radio sources. We use Paβ for this comparison since both 100 GHz radio continuum and Paβ trace emission from the ionized gas.

The Paβ and I Band maps for the Antennae and the individual sources are shown in Fig. 2.4. As we can see, the Paβ image looks quite similar to the I band image. The individual I band sources and Paβ sources also match and have consistent offsets from the radio sources except for source 7, which does not have I band detection which we hypothesis is due to the extinction. To make a more quantitative comparison between coordinates of radio sources and those of HST sources, we apply `imfit` on

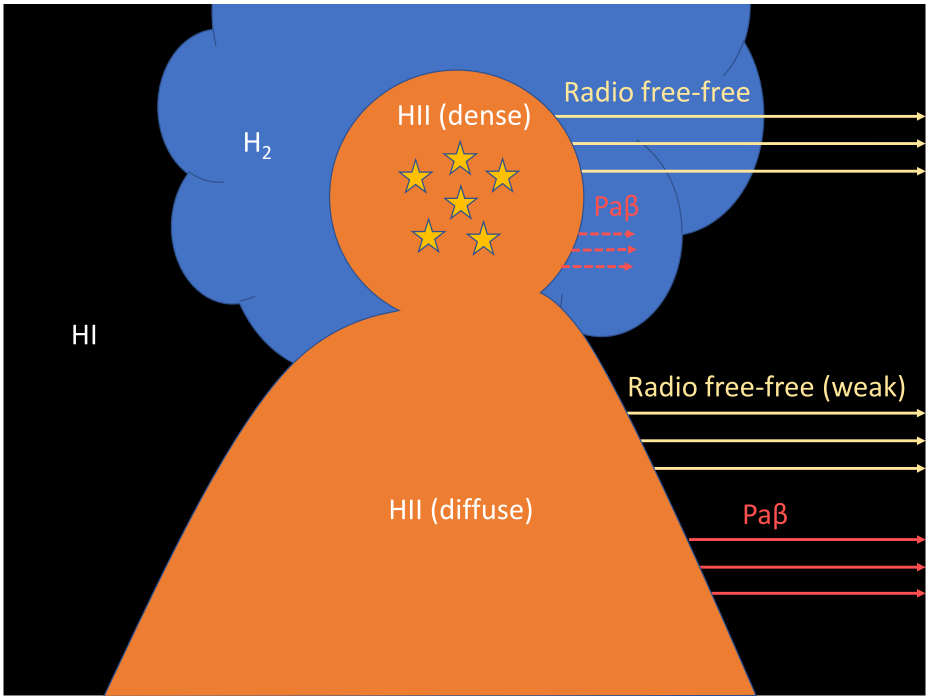

Figure 2.8: A schematic showing an HII region ionized by a star cluster that is at the edge of the cloud. In addition to the HII region inside the cloud, some photons leak out and ionize some of the HI gas outside of the cloud. The HII region inside the cloud is smaller than the HII region outside the cloud due to the higher gas pressure in the cloud. Both dense and diffuse HII regions produce radio free-free continuum and Paβ emission. We cannot see the Paβ emission from the HII region inside the cloud due to the high extinction. Outside the cloud, we can see both radio free-free emission and Paβ emission. However, the radio free-free emission might not be detectable due to the low density of the HII region.

Paβ sources to get the central coordinates and compare them with those derived from radio continuum. The offsets between the two central coordinates are shown in the left panel of Fig. 2.7. As we can see, these offsets are not in a consistent direction and so we cannot shift the coordinates of the Paβ image to align the peak of the Paβ sources with the radio sources. The offsets are generally larger than 0.1", which translates to a physical distance of 11 pc. In comparison, the offset between the 100 GHz and 345 GHz image is typically less than 0.03".

On the other hand, as mentioned in Section 2.3.7, we can use both images to calculate $Q(H^0)$. If the $Q(H^0)$ from the two sets of data agree with each other, then it seems likely that the Paβ emission and 100 GHz continuum are from the same physical source instead of from two sources that happen to lie along the same line of sight. We smooth the radio continuum image to a resolution of 0.21" to match the Paβ image and then use Eq. 2.9 and 2.10 to calculate the total number of ionizing photons from 100 GHz radio continuum and Paβ. As shown in the right panel of Fig. 2.7, the total numbers of ionizing photons derived from the two datasets generally agree with each other within a factor of 2. This agreement suggests the radio continuum and Paβ might actually trace the same physical source, despite the offset in their coordinates.

One possible explanation is that clumpiness or density gradients in the surrounding molecular cloud is allowing photons from the YMC to leak out of the cloud and ionize the surrounding HI gas (Fig. 2.8). This has been proposed as the 'blister' model (Israel 1978) to explain the spatial and velocity offset between CO clouds and HII regions in Milky Way. In this case, high extinction inside the cloud could prevent us from observing the Pa beta emission produced there, while the relatively low sensitivity of the radio continuum data could prevent us from detecting radio continuum emission from the HII region outside the cloud. It would explain the spatial offset between the peaks at different wavelengths and also why we have different A_V values from optical data and 345 GHz dust emission.

For source 6, the ionizing photon counts from Paβ are much higher than the upper limit derived from the 100 GHz radio continuum image. A possible scenario is that this source has already emerged from the cloud and heats the nearby GMC without ionizing much of the cloud. In this scenario, the detected 345 GHz continuum emission comes primarily from heated dust from the edge of the GMC, while any radio continuum emission from the ionized gas seen in Paβ is too faint to be detected. Another interesting object is source 7, which has lower $Q(H^0)$ derived from Paβ emission than source 6, but which is detected in 100 GHz continuum. Since this source does not have I band detection, we suspect this source is still quite embedded in the parent cloud and only has small amount of ionizing photons leaked out to generate the Paβ emission.

2.4.5 Missing Proto Star Cluster - Firecracker

Whitmore et al. (2014) identified a candidate of proto star cluster called the Firecracker in the SGMC 2 region. It is luminous and compact in ^{12}CO J=3-2 but without any associate radio counterpart at 3.6 cm (Johnson et al. 2015), which suggests it is at the very beginning stage of forming stars. Therefore, we do not expect the source to appear in our 100 GHz map. On the other hand, we do expect it to have strong dust emission at higher frequencies. However, as we see in 345 GHz map (Fig 2.1), there is no signal detected in SGMC 2 region.

Johnson et al. (2015) detected the Firecracker at 345 GHz with a resolution of 0.5" (53 pc). The peak intensity of the dust continuum reported is 9.8×10^{-4} Jy beam^{-1}. If we assume it is a perfect point source, the same peak intensity at 0.11" resolution would give us a S/N of 25, which is clearly not the case. On the other hand, if we assume the dust emission is uniformly distributed over the 53 pc area, we would expect a S/N of 1 for the emission peak, which agrees better with what we observe. This analyses clearly suggests that Firecracker has structure on GMC scales. Furthermore, we would expect the dust temperature to be quite cold throughout the whole area due to the lack of stellar radiation. Therefore, the dust would not be as luminous as our YMC candidates and thus the Firecracker would not appear as strong point source.

2.5 Comparison with GMC properties

Table 2.5: Measured properties of selected GMCs in the Antennae

Index (1)	Coordinates (J2000) (2)	$S_{100\mathrm{GHz}}$ (mJy) (3)	$S_{220\mathrm{GHz,dust}}$ (mJy) (4)	$S_{345\mathrm{GHz,dust}}$ (mJy) (5)	T_{kin} (K) (6)	$\log_{10} M_{\mathrm{gas}}$ ($\mathrm{M}_\odot$) (7)	$\log_{10} \Sigma_{\mathrm{gas}}$ ($\mathrm{M}_\odot$ pc^{-2}) (8)
1	12h01m54.96s, -18d53m05.86s	3.5 ± 0.04	1.5 ± 0.1	6.9 ± 0.5	21.5 ± 0.3	7.86 ± 0.03	3.90 ± 0.03
2	12h01m54.59s, -18d53m03.10s	1.2 ± 0.03	0.57 ± 0.09	2.6 ± 0.4	12.3 ± 0.4	7.69 ± 0.07	3.85 ± 0.07
3	12h01m53.55s, -18d53m09.23s	0.25 ± 0.03	0.42 ± 0.08	1.9 ± 0.4	16.8 ± 0.4	7.40 ± 0.09	3.68 ± 0.09
4	12h01m53.51s, -18d53m10.26s	0.12 ± 0.02	< 0.07	< 0.3	13.8 ± 0.4	< 6.71	< 3.17
5	12h01m53.51s, -18d53m10.26s	0.52 ± 0.03	0.57 ± 0.1	2.6 ± 0.4	22.8 ± 0.3	7.42 ± 0.07	3.55 ± 0.07
6	12h01m55.28s, -18d52m48.46s	0.21 ± 0.04	0.37 ± 0.1	1.7 ± 0.5	15.8 ± 0.4	7.37 ± 0.13	3.45 ± 0.12
7	12h01m55.46s, -18d52m45.65s	0.51 ± 0.03	0.71 ± 0.09	3.3 ± 0.4	17.6 ± 0.4	7.61 ± 0.05	3.87 ± 0.05
8	12h01m55.14s, -18d52m40.86s	0.18 ± 0.03	0.45 ± 0.09	2.1 ± 0.4	14.3 ± 0.4	7.51 ± 0.09	3.70 ± 0.09
9	12h01m54.75s, -18d52m31.37s	0.19 ± 0.03	0.21 ± 0.08	1.0 ± 0.4	9.9 ± 0.5	7.42 ± 0.16	3.83 ± 0.16
10	12h01m52.13s, -18d52m20.76s	0.19 ± 0.02	0.24 ± 0.07	1.1 ± 0.3	15.2 ± 0.4	7.21 ± 0.13	3.62 ± 0.13
11	12h01m53.06s, -18d52m05.88s	0.16 ± 0.03	0.54 ± 0.08	2.5 ± 0.4	19.0 ± 0.3	7.46 ± 0.07	3.76 ± 0.06
12	12h01m53.02s, -18d52m02.07s	0.46 ± 0.03	1.2 ± 0.1	5.7 ± 0.5	27.5 ± 0.3	7.70 ± 0.04	3.81 ± 0.03
13	12h01m54.58s, -18d51m56.55s	0.22 ± 0.03	0.43 ± 0.13	2.0 ± 0.6	13.1 ± 0.4	7.55 ± 0.13	3.87 ± 0.13

(1) Source ID. (2) Coordinates. (3) GMC fluxes at 100 GHz. (4) GMC dust fluxes at 220 GHz. (5) GMC dust fluxes at 345 GHz. (6) Peak gas kinetic temperature. (7) GMC gas mass derived from dust continuum. (see Section 5.1) (8) GMC surface density derived from dust continuum.

2.5.1 Flux at GMC scales

To measure the fluxes at GMC scales, we apply a similar procedure as described in Section 3.2 with the aperture determined through 2D Gaussian fitting to the 100 GHz GMC-scale continuum image. We use a similar procedure to split the free-free emission and dust emission as described in Section 3.2, although now we are calculating the dust flux at 220 GHz instead of 345 GHz. The free-free and dust emission at 220 GHz are calculated as

$$S_{\mathrm{220GHz,ff}} = S_{\mathrm{100GHz}} \left(\frac{220\ \mathrm{GHz}}{100\ \mathrm{GHz}}\right)^{-0.1} \tag{2.14}$$

$$S_{\mathrm{220GHz,dust}} = S_{\mathrm{220GHz}} - S_{\mathrm{220GHz,ff}} \tag{2.15}$$

Previous studies (e.g. Whitmore et al. 2010) have used continuum data with ∼ 60 pc resolution to study star clusters, which generally have diameters of several pc. This approach will potentially include emission from outside the star cluster. A comparison between our 61 pc and 12 pc resolution data will enable us to quantify this bias. In addition, the ratio between fluxes from the two spatial scales will tell us how concentrated the star formation is in each individual GMC. After we split the dust emission from the free-free emission, we can calculate the GMC gas mass based on Eq. 2.6 and 2.7 with the dust temperature calculated using equation 2.5. The GMC properties are summarized in Table 2.5.

To compare the dust emission at different scales, we need to extrapolate the dust flux at 220 GHz to the flux at 345 GHz. We assume the dust is still optically thin so that the grey-body dust spectrum is

$$S_{\nu,\mathrm{dust}} \propto \frac{\nu^{\beta+3}}{e^{h\nu/kT}-1} \propto \nu^{\beta+2} \tag{2.16}$$

(Casey 2012) where β is the dust emissivity index and we assume $\beta = 1.5$. The extrapolated flux at 345 GHz can be calculated as

$$S_{\mathrm{345GHz,dust}} = S_{\mathrm{220GHz,dust}} \left(\frac{345\mathrm{GHz}}{220\mathrm{GHz}}\right)^{3.5} \tag{2.17}$$

The flux ratios are shown in the left panel of Fig. 2.9. As we can see, the flux

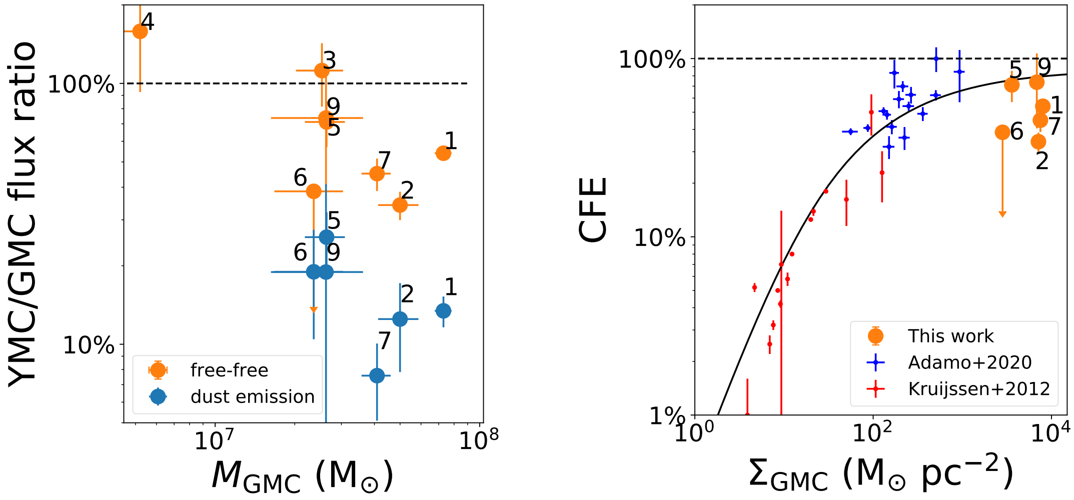

Figure 2.9: (Left) The ratio of flux at YMC scales to that at GMC scales versus the GMC mass. Flux ratios are shown for both free-free emission and dust emission. (Right) The YMC-to-GMC ratio for free-free emission, which is equivalent to the cluster formation efficiency (CFE) versus the gas surface density. The mean gas surface density for individual YMCs from the Antennae is taken to be the gas surface density at GMC scales (Table 2.5). The blue and red points are CFEs for individual galaxies compiled by Adamo et al. (2020) and Kruijssen (2012). The solid curve is the theoretical prediction of CFE from Kruijssen (2012). We can see that CFEs for individual GMCs in the Antennae generally agree with the observations and theoretical predictions for entire galaxies.

ratio for free-free emission is about 50% while the dust emission fraction is $\sim$20%. The free-free emission traces the ionized gas component, which lets us calculate the mass of the stellar component based on the SSP assumption, while the dust emission traces the gas component. Therefore, we can conclude that the stellar component is more concentrated in YMCs than is the gas component. We note that the gas in the YMCs is generally warmer than the gas outside the YMCs (Tables 2.2 and 2.5). As indicated by Eq. 2.16, warmer dust is more luminous. Hence the fraction of central gas over total GMC gas mass may be even lower than the observed luminosity ratio of 20 %. These results are consistent with simulations (Li et al. 2019) that show that the stellar component is more radially concentrated than the gas component in GMCs.

Fig. 2.9 also shows that sources 3 and 4 have flux ratios greater than 100%. If we increase the sensitivity of the image by using a robust parameter of 2.0 instead of 0.5, we recover even higher fluxes at YMC scales that exceed the allowed uncertainty range. Since our GMC-scale map has a LAS of $\sim$70", this difference is unlikely to be caused by missing flux at large scales. Because the YMC-resolution data were taken 2 years before the GMC-resolution data, it is possible that these two sources are time-variable sources with decreasing luminosity with time. As shown in Fig. 2.1, these two sources are close to the southern nucleus and so it is possible these sources are AGN or supernovae.

2.5.2 Cluster Formation Efficiency

The ratio of free-free emission at YMC scales compared to GMC scales basically characterizes what fraction of stars are formed in bound star clusters, which is equivalent to the cluster formation efficiency (CFE). We ignore the "cruel cradle factor" (Kruijssen 2012), which is the fraction of stars that remain bound after the cloud is dispersed. Kruijssen (2012) derived theoretical predictions for the global CFE of galaxies. Among all the factors, CFEs are most strongly dependent on the mean gas surface density of the galaxy. To compare with this theoretical prediction, we plot our free-free flux ratio versus the GMC surface density in the right panel of Fig. 2.9. The GMC surface density is derived from the dust flux at 220 GHz continuum. We also overlay the literature data (compiled by Kruijssen 2012; Adamo et al. 2020) for comparison; in these studies, each data point represents a measurement for a single galaxy. We can see our measurements for individual GMCs are close to but below

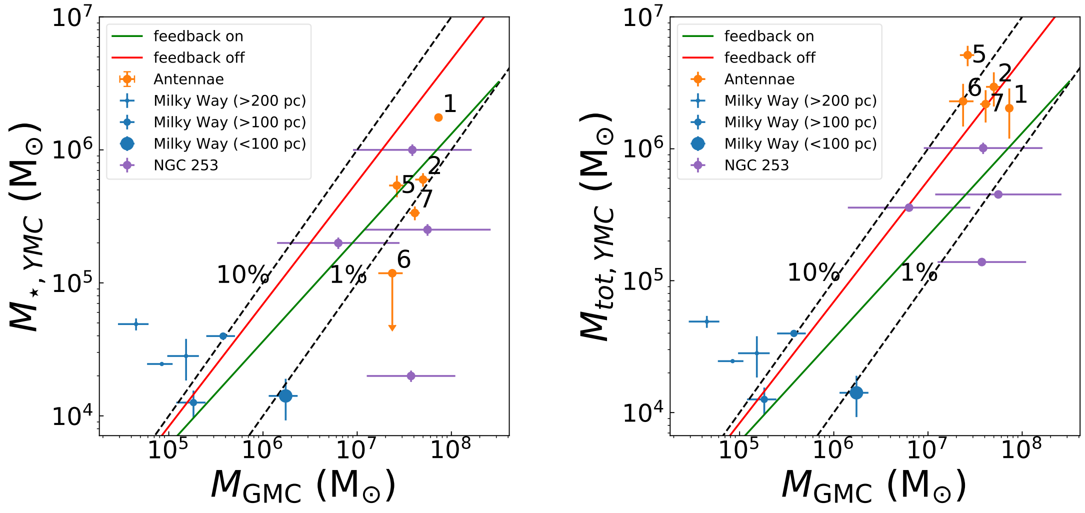

Figure 2.10: YMC stellar mass (Left) and total mass (Right) versus the host GMC mass. The red and green solid lines are simulations from Howard et al. (2018) with feedback off and on. The two dashed lines are constant ratios of 0.1 and 0.01. We can see the observational data generally agree with the simulation predictions.

the theoretical prediction. Since our data points are all at high gas surface density end, we cannot use our new data on its own to fit the whole trend and see if it agrees with the theoretical prediction.

We note that in the model of Kruijssen (2012), both CFE and gas surface density are global quantities for each individual galaxy. Here we are trying to apply this model to GMC scales. The major effect is that the model is averaging gas at much larger scales and so the gas surface density should be lower than the surface density for individual GMCs, which could bring the data points leftward.

2.5.3 Mass correlation between GMCs and YMCs

Clusters generally form in the densest parts of GMCs (Krumholz et al. 2019). As they form, feedback starts to take effect and eventually removes the gas, thereby limiting the star formation efficiency (SFE). It is known from observations that the mass functions of YMCs and GMCs have similar power-law slopes of -2.0, which suggests a relatively constant SFE (e.g. Mok et al. 2020). However, the statistical cutoff due to the rarity of GMCs and YMCs at the upper mass end makes it hard to study this relation for the massive clouds ($\sim 10^8$ M$_\odot$) that are common in LIRGs and ULIRGs. On the other hand, idealized simulations confirm a tight correlation between the maximal cluster mass and GMC mass (Howard et al. 2018) up to GMC masses of 10^6 M$_\odot$. Radio observations can probe the most massive YMCs ($\sim 10^6$ M$_\odot$) when they are still associated with clouds, thus enabling us to match these YMCs with their host GMCs.

In Fig. 2.10, we plot the stellar mass and total mass of YMCs versus GMC molecular gas mass for the Antennae, NGC 253 and Milky Way. For the Milky Way, the stellar masses of YMCs are from Krumholz et al. (2019). Since most of these YMCs are already outside the host molecular cloud, we assume the total masses of these clusters are the same as their stellar masses. We then match the Milky Way YMCs with their closest GMCs using the GMC catalog in Rice et al. (2016). We excluded matched clouds with a closest distance greater than 300 pc. If there are more than two clusters belong to the same cloud, we only show the cluster with the maximum stellar mass. For NGC 253, the YMC data is from Leroy et al. (2018) while the GMC data is from Leroy et al. (2015). We overlay the YMCs on Fig. 9 in Leroy et al. (2015) to spatially match each YMCs with its corresponding GMC. We then compare the central velocity of the YMCs with their matched GMCs to confirm this correspondence. If the central velocity does not match, we find the closest cloud that has a velocity range covering the YMC central velocity. The same rule that we only show the cluster with maximum stellar or total mass applies if we have more than 1 YMC corresponding a single GMC. We also plot the simulation predictions for the YMC-GMC mass relation from Howard et al. (2018) with feedback on and off. Note that this relation is between the GMC mass and maximum YMC mass within that GMC. The upper limit of the GMC mass in this simulation is 10^6 M$_\odot$ and so we must extrapolate the relation to higher masses of $\sim 10^8$ M$_\odot$.

From Fig. 2.10, we can see the data generally agrees with the correlations predicted by the simulation. For the Milky Way data points, we use symbols of different sizes to represent clusters within different distance ranges away from their matched GMCs. We can see that YMCs more than 200 pc away from their matched GMCs are all far above the simulation predictions. Since GMC diameters are generally smaller than 100 pc in Milky Way (Heyer & Dame 2015), we would expect those YMCs are outside their matched GMCs. A probable scenario is that those YMCs have already dispersed a significant amount of gas in their host GMCs and hence their matched

GMC mass is less than what we expect. In contrast, the YMC with distance less than 100 pc from its matched GMC shows a stellar masses less than what we expect. This YMC is probably still embedded in its matched GMC and may be continuing to form stars.

We can also see that YMCs in NGC 253 have a similar mass range as YMCs in the Antennae. For NGC 253, there is one data point significantly below the simulation predictions. We would expect that YMC is very young and lots of stars are yet to form. In the right panel of Fig. 2.10 where we plot the total YMC mass versus the GMC gas mass, we can see that data point is closer to the simulation predictions. YMCs in the Antennae show less scatter in the left panel and seem to agree better with the feedback-on relation from Howard et al. (2018). However, we note that those values may be lower limits since some of the YMCs are still going to form stars (see Section 4.1). If we plot the total mass versus the GMC mass, we can see those points are clustered around the feedback-off relation. However, as we discussed in Section 4.2, we probably include a lot of gas that is outside of the YMCs. Therefore, the data points in the right panel of Fig. 2.10 should be considered as upper limits. Also, due to our limited sample size and heterogeneous data sources, the results in this section should be considered to be illustrative, still in need of further investigation.

2.5.4 No Effect of YMCs on GMC temperatures

It is interesting to see if clouds with YMCs have different properties from clouds without YMCs. As we know, YMCs have strong free-free emission, which could heat the dust and make the clouds warmer. Therefore, we might expect a temperature difference between clouds with or without YMCs. We apply equation 2.5 to the ^{12}CO J=2-1 data at GMC resolution (Brunetti et al. in prep). To avoid effects from correlated pixels, we Nyquist sample the image by rebinning the pixels to half of the beam. Fig. 2.11 shows the calculated $T_{\rm kin}$ versus the surface density of the molecular gas. Note that in this plot, the gas surface density is calculated based on the GMC-resolution ^{12}CO J=2-1 cube since we do not have 220 GHz continuum detections for all ^{12}CO J=2-1 detected pixels. The gray points show all the detected pixels in the ^{12}CO J=2-1 map with peak brightness temperature greater than 10 times the rms noise. The orange points are the peak value of the pixels within our apertures used to measure the flux of the continuum point source at GMC scales. Those points represent the properties of the GMCs that host radio YMCs. We also divide the data

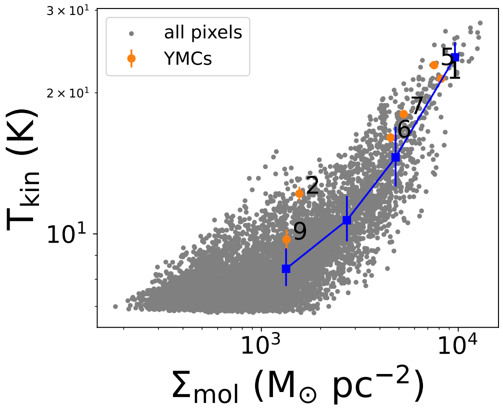

Figure 2.11: The GMC temperature derived from CO 2-1 observations at resolution of ∼60 pc versus the molecular gas surface density. We assume a ULIRG α_{CO} of 1.1 $M_\odot$ (K km s^{-1} pc^2)$^{-1}$. The gray points are all pixels detected in the ^{12}CO J=2-1 map. The orange points are pixels in the ^{12}CO J=2-1 map that coincide with peaks of the continuum source. The blue points and error bars represent the median and 25 and 75 percentile value at each given bin for the gas surface density. There is no strong evidence that the temperatures of GMCs that are forming YMCs are significantly higher than the temperatures of the remaining GMCs.

points into different bins based on the gas surface density values and calculate the median for each bin (blue points; error bars show the value of 1st and 3rd quartile of each bin).

From the plot, we can see the orange points are generally above the blue points. However, at the high surface end (5000 – 10000 $\mathrm{M_\odot\ pc^{-2}}$), 3 of 4 YMCs have temperatures lower than the first quartile values, which indicates their temperature is not significantly different from the rest of pixels. On the other hand, we see the 2 orange points are above the first quartile values at the low surface density end ($\sim 1000\ \mathrm{M_\odot\ pc^{-2}}$). However, in this surface density regime, we are hitting the sensitivity limit of the 100 GHz YMC-resolution continuum. Source 9 is barely detected in our high-resolution continuum image so we can consider it to mark the lower detection limit. Therefore, our methods to identify YMCs bias towards sources with high peak brightness temperatures at low mass surface densities. Overall, we see no clear evidence that the feedback from YMCs has increased the temperature of the host GMCs yet. However, since we only have a limited number of radio sources, our results cannot conclusively show whether YMC feedback has affected GMCs yet. In the future, we will consider to add young optical star clusters to this type of analysis.

2.6 Conclusions

In this paper, we have presented new, high-resolution continuum data for YMCs in the Antennae. We combine these data with CO and continuum data at GMC scales to explore the correlation of properties between the YMCs and their host GMCs. Our main conclusions are summarized below.

- These YMCs have stellar masses of $\sim 10^5$–$10^6\ \mathrm{M_\odot}$ and radius of $\sim$ 3–15 pc. For sources 1b, 2 and 5, we can observe substructures in higher-resolution images, which suggest we might overestimate their radii by including some surrounding diffuse emission. Source 1a and 7 still look compact at the highest resolution.

- Based on statistical counts, we estimate the lifespan of these YMCs to be about 1 Myr. This is consistent with estimates of embedded YMC lifetimes. However, all these sources have Paβ counterparts. By comparing the coordinates and fluxes between 100 GHz and Paβ sources, we think these YMCs have partly emerged and have already ionized some diffuse medium outside the cloud.

- A virial analysis of these YMCs suggests the majority are bound systems. This further suggests that they may appear as young globular clusters after the gas is dispersed.
- More than 50% of the free-free emission at GMC scales comes from compact YMCs inside those GMCs. This fraction is equivalent to the cluster formation efficiency (CFE). We compare this fraction with the theoretical prediction from Kruijssen (2012) and literature data for galaxies from Adamo et al. (2020) and see a quite good agreement.
- We explore the correlation between the YMC mass and its host GMC mass. We also compare this correlation in the Antennae with those in NGC 253 and the Milky Way. We find the data generally agree with the predicted correlation from simulations (Howard et al. 2018).
- When comparing the gas temperature in regions with and without YMCs, we find no significant difference between those two populations of clouds. We see no clear evidence that YMC feedback has increased the cloud temperature at GMC scales.

Bibliography

Adamo, A., Hollyhead, K., Messa, M., et al. 2020, MNRAS, 499, 3267, doi: `10.1093/mnras/staa2380`

Bolatto, A. D., Wolfire, M., & Leroy, A. K. 2013, Annual Review of Astronomy and Astrophysics, 51, 207, doi: `10.1146/annurev-astro-082812-140944`

Brogan, C., Johnson, K., & Darling, J. 2010, ApJL, 716, L51, doi: `10.1088/2041-8205/716/1/L51`

Brown, G., & Gnedin, O. Y. 2021, MNRAS, 508, 5935, doi: `10.1093/mnras/stab2907`

Calzetti, D., Armus, L., Bohlin, R. C., et al. 2000, ApJ, 533, 682, doi: `10.1086/308692`

Casey, C. M. 2012, MNRAS, 425, 3094, doi: `10.1111/j.1365-2966.2012.21455.x`

Chevance, M., Kruijssen, J. M. D., Vazquez-Semadeni, E., et al. 2020, SSRv, 216, 50, doi: `10.1007/s11214-020-00674-x`

Cleri, N. J., Trump, J. R., Backhaus, B. E., et al. 2020, arXiv e-prints, arXiv:2009.00617. `https://arxiv.org/abs/2009.00617`

Costa, A. H., Johnson, K. E., Indebetouw, R., et al. 2021, ApJ, 918, 76, doi: `10.3847/1538-4357/ac0e93`

Draine, B. T. 2003, ARA&A, 41, 241, doi: `10.1146/annurev.astro.41.011802.094840`

Emig, K. L., Bolatto, A. D., Leroy, A. K., et al. 2020, ApJ, 903, 50, doi: `10.3847/1538-4357/abb67d`

Fall, S. M., & Zhang, Q. 2001, ApJ, 561, 751, doi: `10.1086/323358`

Finn, M. K., Johnson, K. E., Brogan, C. L., et al. 2019, ApJ, 874, 120, doi: `10.3847/1538-4357/ab0d1e`

Gilbert, A. M., & Graham, J. R. 2007, ApJ, 668, 168, doi: `10.1086/520910`

Ginsburg, A., Goss, W. M., Goddi, C., et al. 2016, A&A, 595, A27, doi: `10.1051/0004-6361/201628318`

Grasha, K., Calzetti, D., Bittle, L., et al. 2018, MNRAS, 481, 1016, doi: `10.1093/mnras/sty2154`

Hannon, S., Lee, J. C., Whitmore, B. C., et al. 2019, MNRAS, 490, 4648, doi: `10.1093/mnras/stz2820`

Harris, W. E., Harris, G. L. H., & Alessi, M. 2013, ApJ, 772, 82, doi: `10.1088/0004-637X/772/2/82`

Heyer, M., & Dame, T. M. 2015, ARA&A, 53, 583, doi: `10.1146/annurev-astro-082214-122324`

Hollyhead, K., Bastian, N., Adamo, A., et al. 2015, MNRAS, 449, 1106, doi: `10.1093/mnras/stv331`

Howard, C. S., Pudritz, R. E., & Harris, W. E. 2018, Nature Astronomy, 2, 725, doi: `10.1038/s41550-018-0506-0`

Israel, F. P. 1978, A&A, 70, 769

Johnson, K. E., Hunt, L. K., & Reines, A. E. 2009, AJ, 137, 3788, doi: `10.1088/0004-6256/137/4/3788`

Johnson, K. E., Indebetouw, R., Watson, C., & Kobulnicky, H. A. 2004, AJ, 128, 610, doi: `10.1086/422017`

Johnson, K. E., & Kobulnicky, H. A. 2003, ApJ, 597, 923, doi: `10.1086/378585`

Johnson, K. E., Leroy, A. K., Indebetouw, R., et al. 2015, ApJ, 806, 35, doi: `10.1088/0004-637X/806/1/35`

Kepley, A. A., Tsutsumi, T., Brogan, C. L., et al. 2020, PASP, 132, 024505, doi: `10.1088/1538-3873/ab5e14`

Kessler, S., Leroy, A., Querejeta, M., et al. 2020, ApJ, 892, 23, doi: `10.3847/1538-4357/ab77a8`

Klaas, U., Nielbock, M., Haas, M., Krause, O., & Schreiber, J. 2010, A&A, 518, L44, doi: `10.1051/0004-6361/201014670`

Kobulnicky, H. A., & Johnson, K. E. 1999, ApJ, 527, 154, doi: `10.1086/308075`

Kruijssen, J. M. D. 2012, MNRAS, 426, 3008, doi: `10.1111/j.1365-2966.2012.21923.x`

Krumholz, M. R., McKee, C. F., & Bland-Hawthorn, J. 2019, ARA&A, 57, 227, doi: `10.1146/annurev-astro-091918-104430`

Leroy, A. K., Bolatto, A. D., Ostriker, E. C., et al. 2015, ApJ, 801, 25, doi: `10.1088/0004-637X/801/1/25`

—. 2018, ApJ, 869, 126, doi: `10.3847/1538-4357/aaecd1`

Leroy, A. K., Hughes, A., Liu, D., et al. 2021, ApJS, 255, 19, doi: `10.3847/1538-4365/abec80`

Levy, R. C., Bolatto, A. D., Leroy, A. K., et al. 2021, ApJ, 912, 4, doi: `10.3847/1538-4357/abec84`

Li, H., & Gnedin, O. Y. 2014, ApJ, 796, 10, doi: `10.1088/0004-637X/796/1/10`

Li, H., Vogelsberger, M., Marinacci, F., & Gnedin, O. Y. 2019, MNRAS, 487, 364, doi: `10.1093/mnras/stz1271`

Matthews, A. M., Johnson, K. E., Whitmore, B. C., et al. 2018, ApJ, 862, 147, doi: `10.3847/1538-4357/aac958`

McCrady, N., & Graham, J. R. 2007, ApJ, 663, 844, doi: `10.1086/518357`

McKee, C. F., & Ostriker, E. C. 2007, ARA&A, 45, 565, doi: `10.1146/annurev.astro.45.051806.110602`

Mok, A., Chandar, R., & Fall, S. M. 2020, ApJ, 893, 135, doi: `10.3847/1538-4357/ab7a14`

Murphy, E. J., Condon, J. J., Schinnerer, E., et al. 2011, ApJ, 737, 67, doi: `10.1088/0004-637X/737/2/67`

Neff, S. G., & Ulvestad, J. S. 2000, AJ, 120, 670, doi: `10.1086/301503`

Osterbrock, D. E. 1989, Astrophysics of gaseous nebulae and active galactic nuclei

Reines, A. E., Johnson, K. E., & Goss, W. M. 2008, AJ, 135, 2222, doi: `10.1088/0004-6256/135/6/2222`

Rice, T. S., Goodman, A. A., Bergin, E. A., Beaumont, C., & Dame, T. M. 2016, ApJ, 822, 52, doi: `10.3847/0004-637X/822/1/52`

Rico-Villas, F., Martín-Pintado, J., González-Alfonso, E., Martín, S., & Rivilla, V. M. 2020, MNRAS, 491, 4573, doi: `10.1093/mnras/stz3347`

Schirm, M. R. P., Wilson, C. D., Madden, S. C., & Clements, D. L. 2016, ApJ, 823, 87, doi: `10.3847/0004-637X/823/2/87`

Schweizer, F., Burns, C. R., Madore, B. F., et al. 2008, AJ, 136, 1482, doi: `10.1088/0004-6256/136/4/1482`

Scoville, N. Z., Polletta, M., Ewald, S., et al. 2001, AJ, 122, 3017, doi: `10.1086/323445`

Scoville, N. Z., Evans, A. S., Thompson, R., et al. 2000, AJ, 119, 991, doi: `10.1086/301248`

Stanford, S. A., Sargent, A. I., Sanders, D. B., & Scoville, N. Z. 1990, ApJ, 349, 492, doi: `10.1086/168334`

Tsuge, K., Sano, H., Tachihara, K., et al. 2019, ApJ, 871, 44, doi: `10.3847/1538-4357/aaf4fb`

Whitmore, B. C., Chandar, R., & Fall, S. M. 2007, AJ, 133, 1067, doi: `10.1086/510288`

Whitmore, B. C., & Zhang, Q. 2002, AJ, 124, 1418, doi: `10.1086/341822`

Whitmore, B. C., Zhang, Q., Leitherer, C., et al. 1999, AJ, 118, 1551, doi: `10.1086/301041`

Whitmore, B. C., Chandar, R., Schweizer, F., et al. 2010, AJ, 140, 75, doi: `10.1088/0004-6256/140/1/75`

Whitmore, B. C., Brogan, C., Chandar, R., et al. 2014, ApJ, 795, 156, doi: `10.1088/0004-637X/795/2/156`

Wilson, C. D., Harris, W. E., Longden, R., & Scoville, N. Z. 2006, ApJ, 641, 763, doi: `10.1086/500577`

Wilson, C. D., Scoville, N., Madden, S. C., & Charmandaris, V. 2000, ApJ, 542, 120, doi: `10.1086/309504`

—. 2003, ApJ, 599, 1049, doi: `10.1086/379344`

Wilson, C. D., Petitpas, G. R., Iono, D., et al. 2008, The Astrophysical Journal Supplement Series, 178, 189, doi: `10.1086/590910`

Zhang, Q., Fall, S. M., & Whitmore, B. C. 2001, ApJ, 561, 727, doi: `10.1086/322278`

Chapter 3

Molecular Gas and Star Formation in Nearby Starburst Mergers

The content of this chapter is a second revision of the manuscript text for publication under the following citation:

He, H.; Bottrell, C.; Wilson, C.D.; Moreno, J.; Burkhart, B.; Hayward.C.C; Herquist, L.; Twum, A. 2023, “Molecular Gas and Star Formation in Nearby Starburst Mergers", ApJ, 950, 56

Molecular Gas and Star Formation in Nearby Starburst Mergers

Abstract

We employ the Feedback In Realistic Environments (FIRE-2) physics model to study how the properties of giant molecular clouds (GMCs) evolve during galaxy mergers. We conduct a pixel-by-pixel analysis of molecular gas properties in both the simulated control galaxies and galaxy major mergers. The simulated GMC-pixels in the control galaxies follow a similar trend in a diagram of velocity dispersion (σ_v) versus gas surface density ($\Sigma_{\rm mol}$) to the one observed in local spiral galaxies in the Physics at High Angular resolution in Nearby GalaxieS (PHANGS) survey. For GMC-pixels in simulated mergers, we see a significant increase of factor of 5 – 10 in both $\Sigma_{\rm mol}$ and σ_v, which puts these pixels above the trend of PHANGS galaxies in the σ_v vs $\Sigma_{\rm mol}$ diagram. This deviation may indicate that GMCs in the simulated mergers are much less gravitationally bound compared with simulated control galaxies with virial parameter ($\alpha_{\rm vir}$) reaching 10 – 100. Furthermore, we find that the increase in $\alpha_{\rm vir}$ happens at the same time as the increase in global star formation rate (SFR), which suggests stellar feedback is responsible for dispersing the gas. We also find that the gas depletion time is significantly lower for high $\alpha_{\rm vir}$ GMCs during a starburst event. This is in contrast to the simple physical picture that low $\alpha_{\rm vir}$ GMCs are easier to collapse and form stars on shorter depletion times. This might suggest that some other physical mechanisms besides self-gravity are helping the GMCs in starbursting mergers collapse and form stars.

Keywords: *ISM: clouds, ISM: kinematics and dynamics, ISM: structure, galaxies: interactions, galaxies: starburst, galaxies: star formation*

3.1 Introduction

Despite the diversity of galaxy morphology and environment, giant molecular clouds (GMCs) are the sites of star formation across cosmic time (Krumholz et al. 2019; Chevance et al. 2020). As one of the most promising star formation model, the turbulence model (Krumholz & McKee 2005; Hennebelle & Chabrier 2011) suggest a relatively uniform star formation efficiency per freefall time ($\epsilon_{\rm ff}$) for individual GMCs. They predict that the observed scatter in $\epsilon_{\rm ff}$ could be account for by the diversity in GMC properties (e.g.virial parameter $\alpha_{\rm vir}$ and Mach number). However, Lee et al. (2016) show that the observed scatter is larger than these early theoretical predictions expected and updated models suggest that cloud evolution, in addition to initial conditions such as Mach number and $\alpha_{\rm vir}$, should be accounted for (see Burkhart 2018; Mocz & Burkhart 2018; Burkhart & Mocz 2019). Furthermore, Grudić et al. (2018) show in their simulation that GMCs in starburst galaxies can have different $\epsilon_{\rm ff}$ in normal spiral galaxies. Hence, to understand the links between GMCs and star formation in galaxies, it is essential to study various GMC properties in a broad range of environments.

However, modeling of GMCs starting from the scales of galaxies and cosmological zoom-ins is complicated by challenges in capturing the structure of the coldest and densest gas, which is heavily affected by various numerical choices, such as resolution (e.g. Bournaud et al. 2008; Teyssier et al. 2010) and the treatment of feedback (Fall et al. 2010; Murray et al. 2010; Dale et al. 2014; Myers et al. 2014; Raskutti et al. 2016; Kim et al. 2017; Grudić et al. 2018; Smith et al. 2021). Most resolved GMC simulations focus on the evolution of individual GMCs (e.g. Burkhart et al. 2015; Howard et al. 2018; Li et al. 2019; Decataldo et al. 2020; Burkhart et al. 2020) and ignore the wider environment. Only a handful of galaxy simulations have the ability to model GMC populations inside Milky-Way-like galaxies (Jeffreson & Kruijssen 2018; Benincasa et al. 2020) and mergers (Renaud et al. 2019a; Li et al. 2022).

High-resolution CO observations have successfully characterized GMCs in the Milky Way (e.g. Rice et al. 2016; Rico-Villas et al. 2020; Miville-Deschênes et al. 2017; Colombo et al. 2019; Lada & Dame 2020) and nearby galaxies (e.g. Donovan Meyer et al. 2013; Hughes et al. 2013; Colombo et al. 2014; Leroy et al. 2016; Schruba et al. 2019). In particular, the recently completed PHANGS-ALMA survey (Leroy et al. 2021) has expanded these observations across a complete sample of nearby spiral galaxies, providing direct measurements of molecular gas surface density $\Sigma_{\rm mol}$, velocity dispersion σ_v and size of GMCs, which are key quantities for determining the physical state of GMCs (Larson 1981). Observations show that the correlation between σ_v^2/R and $\Sigma_{\rm mol}$ is nearly linear (e.g., Heyer & Dame 2015; Sun et al. 2018, 2020), which is consistent with the theoretical prediction that most clouds follows the Larson's second law (Larson 1981), which indicates a constant ratio between clouds' kinetic energy and gravitational potential energy. This universal correlation provides us with a starting point to study how other galactic environmental factors (e.g., external pressure, stellar potential) influence the dynamical state of GMCs.

Unlike studies targeting isolated galaxies, GMCs in starburst galaxy mergers are less well studied. On the observational side, the scarcity of nearby mergers means that we have only a handful of systems with GMC resolution data (Wei et al. 2012; Ueda et al. 2012; Whitmore et al. 2014; Elmegreen et al. 2017; Brunetti et al. 2020; Brunetti 2022; Sánchez-García et al. 2022; Bellocchi et al. 2022). These studies show that GMCs in mergers have significantly higher gas surface densities and are less gravitationally bound compared to GMCs in normal spirals. However, it is difficult to draw statistically robust conclusions on how GMC properties evolve across various merging stages based on these limited number of local galaxy mergers. On the simulation front, only a handful of studies (e.g., Teyssier et al. 2010; Renaud et al. 2014; Fensch et al. 2017) have the ability to probe the cold gas at ∼pc scale starting from cosmological scales. Using a comprehensive library of idealized galaxy merger simulations based on the FIRE-2 physics model, Moreno et al. (2019) show that SFR enhancement is accompanied by an increase in the cold dense gas reservoir. This simulation suite thus provides us with the ideal tool to properly examine GMC evolution along the entire merging sequence.

This paper explores how GMC properties evolve during the starburst merging event using the FIRE-2 merger suite from Moreno et al. (2019) and performs comparisons with observations to test the simulation model. In Section 2, we describe this simulation suite and the observational data used for comparison. Section 3 compares the $\sigma_v - \Sigma_{\rm mol}$ relation between control simulated galaxies and normal spirals in the PHANGS-ALMA sample. Section 4 examines the $\sigma_v - \Sigma_{\rm mol}$ relation for mergers in both observations and simulations. In Section 5, we discuss and interpret various aspects of the comparison between observations and simulations.

3.2 Data Processing

3.2.1 Simulated data

The FIRE-2 Model

We use the FIRE-2 model (Hopkins et al. 2018), which employs the hydrodynamic code GIZMO (Hopkins 2015, 2017). Compared with the previous version, FIRE-2 adopts the updated meshless finite-mass (MFM) magnetohydrodynamics (MHD) solver, which is designed to capture the advantages of both grid-based and particle-based methods. We refer the reader to Hopkins (2015) and Hopkins et al. (2018) for details. The model includes treatment of radiative heating and cooling from free-free, photo-ionization/recombination, Compton, photoelectric, dust-collisional, cosmic ray, molecular, metal line, and fine-structure processes. Star formation occurs in gas that is self-gravitating (3D $\alpha_{\rm vir} < 1$ at the resolution scale), self-shielded, and denser than 1000 cm^{-3} (see Appendix C of Hopkins et al. 2018). Stellar feedback mechanisms include (i) mass, metal, energy, and momentum flux from supernovae type Ia & II; (ii) continuous stellar mass-loss through OB/AGB winds; (iii) photoionization and photoelectric heating; and (iv) radiation pressure. Each stellar particle is treated as a single stellar population. Mass, age, metallicity, luminosity, energy, mass-loss rate, and stellar feedback event rate for each stellar particle are calculated using the STARBURST99 stellar population synthesis model (Leitherer et al. 1999). The model does not account for feedback generated via accretion of gas onto a supermassive black hole (SMBH).

Our FIRE-2 galaxy suite

Moreno et al. (2019) present a suite of idealized galaxy merger simulations (Initial conditions are manually set instead of from cosmological simulations; see also Bottrell et al. 2019; Moreno et al. 2021; McElroy et al. 2022) covering a range of orbital parameters and mass ratios between 4 disc galaxies (G1, G2, G3 and G4, in order of increasing total stellar mass of (0.21, 1.24, 2.97 and 5.5×10^{10} M$_\odot$), along with separate runs for each disk galaxy in isolation (the control runs). Their orbit settings contain 3 orbital spin directions, 3 impact parameters and 3 impact velocities (see Fig. 3 in Moreno et al. 2019). For these simulations, the highest gas density and spatial resolution are 5.8×10^5 cm^{-3} and 1.1 pc, respectively. The gravitational softening lengths are 10 pc for the dark matter and stellar components and 1 pc for the gaseous component. The mass resolution for a gas particle is 1.4 $\times 10^4$ $M_\odot$. The time resolution of a typical snapshot is 5 Myr (See further details in Moreno et al. 2019).

Table 3.1: Orbital Parameter of 'e1' and 'e2' orbit

	e1	e2
Apo. Dist. (kpc)^a	60	120
Peri. Dist. (kpc)^a	15.5	9.3

[a] First apocentric distance between the centers of two galaxies.
[b] Second pericentric distance between the centers of two galaxies.

For our analysis, we focus on the simulation run of isolated G2 and G3 galaxies along with one of G2&G3 merger suites. The detailed information of G2 and G3 galaxies is in Moreno et al. (2019, Table 2). The G2&G3 merger suites have a mass ratio of 1:2.5 and hence are similar to major mergers such as the Antennae and NGC 3256 for which we have observational data. In addition, G2 and G3 have stellar masses within the range of the PHANGS sample (10^{10}–10^{11} $M_\odot$; Leroy et al. 2021). We choose the 'e' orbit (Robertson et al. 2006, roughly prograde), which is expected to maximally enhance the star formation rate. In most of our analyses, we focus on the 'e2' orbit since this is the fiducial run in Moreno et al. (2019). We use the 'e1' orbit as a comparison in some cases as it has smaller impact parameter and is more similar to the orbit of the Antennae merger (Privon et al. 2013), for which we have GMC observational data. The pericentric distance of 'e1' and 'e2' orbit is listed in Table 3.1.

Molecular gas

We follow the scheme in Moreno et al. (2019) to separate the ISM of our simulated galaxy mergers into 4 components based on temperature and density: hot, warm, cool, and cold-dense gas, which roughly correspond to the hot, ionized, atomic, and molecular gas in observations (see Table 4 in Moreno et al. 2019). The components that are most important for this work are the cool (temperatures below 8000 K and densities above 0.1 cm^{-3}) and the cold-dense gas (temperatures below 300 K and densities above 10 cm^{-3}), which corresponds to H I and H$_2$. This choice captures HI and H$_2$ gas reasonably well (Orr et al. 2018). Orr et al. (2018) also demonstrate that using this threshold to separate H$_2$ and HI yields reasonable agreement with the observed Kennicutt-Schmidt law (Kennicutt 1998; Kennicutt & Evans 2012). In the following, we refer to total gas as the sum of the gas in the cool and cold-dense phases (simulations) or in the atomic and molecular phases (observations).

We adopt the same definition of molecular gas as in Moreno et al. (2019) (temperature below 300 K and density above 10 cm^{-3}). Guszejnov et al. (2017) demonstrate that the model successfully reproduces the GMC mass function in the Milky Way (Rice et al. 2016) and the size-linewidth relation (e.g., the Larson scaling relationship, Larson 1981) in our Galaxy (Heyer et al. 2009; Heyer & Dame 2015) and in nearby galaxies (Bolatto et al. 2008; Fukui et al. 2008; Muraoka et al. 2009; Roman-Duval et al. 2010; Colombo et al. 2014; Tosaki et al. 2017). Given the density cut of 10 cm^{-3} and mass resolution of 1.4 $\times 10^4$ M$_\odot$, the lower limit of our spatial resolution ($\sqrt[3]{M/\rho}$, where M is the mass resolution and ρ is the mass volume density) is $\sim$ 40 pc, which is smaller than the typical scale of observed GMCs (40 – 100 pc, Rosolowsky et al. 2021). In addition, GMC mass function peaks at 10^5 – 10^6 M$_\odot$ in Milky Way (Rice et al. 2016), which is significantly larger than our mass resolution. Therefore, we would generally expect more than 1 gas particle is included for molecular gas in each GMC-scale pixel.

For generating different components of the ISM, the simulations start with a homogeneous ISM with a temperature of 10^4 K and solar metallicity. The multi-phase ISM then emerges quickly as a result of cooling and feedback from star formation. The initial gas mass for the simulation is set to match the median HI mass from the xCOLDGASS survey (Catinella et al. 2018).

Data cubes

We first convert the FIRE-2 molecular gas data into mass-weighted position-position-velocity (p-p-v) data cubes to match the format of the CO data from radio observations (McMullin et al. 2007). We adopt the cube construction method created for Bottrell et al. (2022) and Bottrell & Hani (2022) and then adapted to the FIRE-2 merger suite by McElroy et al. (2022). Kinematic cubes are produced along four lines-of-sight (labeled as 'v0', 'v1', 'v2', 'v3'), defined by the vertices of a tetrahedron centered at the primary galaxy (G3 in this work). For the isolated galaxy simulations, we generate p-p-v data cubes at different inclination angles (10 – 80 degrees). We adopt a pixel size of 100 pc and velocity resolution of 2 km s^{-1}, which is similar to PHANGS choice (Sun et al. 2020). The field of view (FOV) for the data cube is set to be 25 kpc.

Then we create zeroth-moment maps of the gas surface density $\Sigma_{\rm mol}$ and second-moment maps of the velocity dispersion σ_v. We do not set any thresholds on these moment maps since we argue that every gas particle in the simulated cube should be treated as a real signal, rather than observational noise. However, in later analyses, when we display σ_v versus $\Sigma_{\rm mol}$ for the simulated data, we select pixels with $\Sigma_{\rm mol}$ greater than 1 $M_\odot$ pc^{-2}, which approximates the lower limit of the molecular gas detection threshold in the observational data (Sun et al. 2018). We also exclude pixels detected in fewer than two velocity channels in the simulated cube to exclude inaccurate measurements of σ_v.

To characterize clouds, we use a pixel-based analysis (Leroy et al. 2016), which treats each pixel as an individual GMC, rather than identifying each individual cloud from the data cube. This approach has been widely applied to GMC analyses for PHANGS galaxies (Sun et al. 2018, 2020). Compared to the traditional cube-based approach, this new method requires minimal assumptions and can be easily applied to many datasets in a uniform way, while still giving us the essential GMC properties (e.g., molecular gas surface density $\Sigma_{\rm mol}$, gas velocity dispersion σ_v). On the other hand, the pixel-based method has a major disadvantage of not able to decompose different cloud components along the same line of sight. Several observational studies (e.g. Brunetti & Wilson 2022; Sun et al. 2022) have compared this new approach with the traditional approach and found good agreement on cloud properties between two methods for both normal spiral galaxies and starburst mergers, especially for clouds in galaxy disks. These comparisons show pixel-based analysis should be valid for capturing individual cloud properties, especially for galaxy disks which generally have single-layer of GMCs (see Section 3.5.1 for detailed discussion about the projection effect). In this work, we adopt this approach to match the method in Brunetti et al. (2020) and Brunetti (2022). We also note that since we treat each pixel as a GMC, these GMCs do not necessarily represent independent ISM structures. In fact, given the mass resolution of 1.4 $\times 10^4$ $M_\odot$, we can barely resolve the internal structure of most massive GMCs of $\sim 10^6$ $M_\odot$ (100 elements). We refer to them as GMCs in this paper to be consistent with similar observational analyses (e.g. Sun et al. 2018, 2020).

3.2.2 Star Formation Rate Maps

To further explore how the GMC properties at 100 pc scale affect the star formation, we also make SFR maps with the same resolution of 100 pc for the simulated mergers at different times. We create these maps using a method similar to the one used to create the gas cubes. We include all the stellar particles with age younger than 10 Myr and create p-p-v data cubes for these stellar particles. The mass-weighted cubes are integrated along the velocity axis to produce 2D maps of stellar mass formed within the last 10 Myr. These surface-density mass maps are subsequently divided by 10 Myr to obtain the average star-formation rates over the last 10 Myr.

3.2.3 Observational Data

We use several sets of observations for comparison with our simulations.

Spiral galaxies: PHANGS data

For isolated galaxies, we mainly use the PHANGS data from Sun et al. (2020) with resolution of 90 pc, which is comparable to our pixel size choice of 100 pc. Sun et al. (2020) apply the pixel-based method for statistical analyses of GMC properties for 70 galaxies in the PHANGS sample. We also include GMC data for M31 from Sun et al. (2018) at resolution of 120 pc. M31 is identified as a green-valley galaxy, similar to our own Milky Way, and hence has a lower total gas fraction than normal spiral galaxies (Mutch et al. 2011). Both M31 and the Milky Way seem to be in a transition from blue spiral galaxies to quenched galaxies via depletion of their cold gas (Bland-Hawthorn & Gerhard 2016). M31 has stellar mass of 10^{11} $M_\odot$ (Sick et al. 2015), H_2 mass of 3.6×10^8 $M_\odot$ and HI mass of 4.8×10^9 $M_\odot$ (Nieten et al. 2006).

Galaxy mergers: the Antennae and NGC 3256

We use the ^{12}CO J=2-1 data for NGC 3256 (Brunetti et al. 2020) and the Antennae (Brunetti (2022, Brunetti et al. in prep)) at resolutions of 90 and 80 pc, respectively. The GMC measurements use the same pixel-based approach as in Sun et al. (2018, 2020). Both NGC 3256 and the Antennae are identified as late-stage major mergers that have been through their second perigalactic passage (Privon et al. 2013). NGC 3256 has stellar mass of 1.1×10^{11} $M_\odot$, total molecular gas of 8×10^9 $M_\odot$ (cal-

Table 3.2: Information about the observed mergers in this work

	Antennae	NGC 3256	#References
$M_\star$ (10^{10} $M_\odot$)^a	4.5	11.4	(1); (2)
$M_{\rm mol}$ (10^{10} $M_\odot$)^b	1.2	0.8	(3); this work
SFR ($M_\odot$yr^{-1})	8.5	50	(1); (4)
Sep. (kpc)^c	7.3	1.1	(5); (4)
$t_{\rm now}$ (Myr)^d	40	···	(6)
mass ratio^f	1:1	···	(6)
Peri. Sep (kpc)^g	10.4	···	(6)

Notes: *a.* Stellar mass. *b.* Molecular gas mass. *c.* Current separation between two nuclei. *d.* Current time since the second passage. *e.* Mass ratio of the two progenitor galaxies. *g.* Pericentric distance of two nuclei from the simulation model.

References: (1) Seillé et al. (2022) (2) Howell et al. (2010) (3) Wilson et al. (2000) (4) Sakamoto et al. (2014) (5) Zhang et al. (2001) (6) Karl et al. (2010)

culated based on ^{12}CO J=2-1 map in Brunetti & Wilson (2022), assuming $\alpha_{\rm CO}$ of 1.1 $M_\odot$ (K km s^{-1} pc^2)$^{-1}$ and ^{12}CO J=2-1/1-0 ratio of 0.8) and SFR of 50 $M_\odot$yr^{-1} (Sakamoto et al. 2014). In contrast, the Antennae has a stellar mass of 4.5 × 10^{10} $M_\odot$ and SFR of 8.5 $M_\odot$yr^{-1} (Seillé et al. 2022). NGC 3256 currently has a more intense starburst, perhaps because it is at different evolutionary stage in the merging process. The detailed information is in Table 3.2.

To convert the ^{12}CO J=2-1 emission to molecular gas mass requires the assumption of a CO-to-H$_2$ conversion factor ($\alpha_{\rm CO}$). The exact value of $\alpha_{\rm CO}$ has large uncertainties and varies significantly among different types of galaxies, especially for starburst galaxies. Downes & Solomon (1998) find that for starburst U/LIRGs, the $\alpha_{\rm CO}$ value is generally 4 times smaller than that in our Milky Way. The major method for direct measurement of $\alpha_{\rm CO}$ is through large velocity gradient (LVG) radiative transfer modeling of multiple CO and its isotope lines. For $\alpha_{\rm CO}$ in the Antennae, various LVG modeling (e.g. Zhu et al. 2003; Schirm et al. 2014) suggests that the Antennae has $\alpha_{\rm CO}$ close to the Milky Way value of 4.3 $M_\odot$ (K km s^{-1} pc^2)$^{-1}$. This is also supported by the galaxy simulation that specifically matches the Antennae (Renaud et al. 2019a). For NGC 3256, we do not have a direct measurement of $\alpha_{\rm CO}$. We therefore adopt the treatment from Sargent et al. (2014) to determine the $\alpha_{\rm CO}$ for an individual galaxy as

$$\alpha_{\mathrm{CO}} = (1 - f_{\mathrm{SB}}) \times \alpha_{\mathrm{CO,MS}} + f_{\mathrm{SB}} \times \alpha_{\mathrm{CO,SB}}, \tag{3.1}$$

where $\alpha_{\mathrm{CO,MS}}$ and $\alpha_{\mathrm{CO,SB}}$ are the conversion factors for the Milky Way (4.3 $\mathrm{M}_\odot$ (K km s^{-1} $\mathrm{pc}^2)^{-1}$) and U/LIRGs (1.1 $\mathrm{M}_\odot$ (K km s^{-1} $\mathrm{pc}^2)^{-1}$, including helium), and f_{SB} is the probability for a galaxy to be a starburst galaxy, which is determined by its deviation from the star-forming main sequence. We adopt the star-forming main sequence relation from Catinella et al. (2018),

$$\log \mathrm{sSFR}_{\mathrm{MS}} = -0.344(\log M_\star - 9) - 9.822, \tag{3.2}$$

where sSFR = SFR / $M_\star$ is the specific star formation rate. NGC 3256 has an $\mathrm{sSFR}/\mathrm{sSFR}_{\mathrm{MS}}$ ratio of 15 (Brunetti et al. 2020), which suggests NGC 3256 should have α_{CO} close to the U/LIRG value of 1.1 $\mathrm{M}_\odot$ (K km s^{-1} $\mathrm{pc}^2)^{-1}$. Therefore, in the following analyses, we will adopt α_{CO} of 4.3 $\mathrm{M}_\odot$ (K km s^{-1} $\mathrm{pc}^2)^{-1}$ for the Antennae and 1.1 $\mathrm{M}_\odot$ (K km s^{-1} $\mathrm{pc}^2)^{-1}$ for NGC 3256.

3.3 Control (Isolated) Galaxies

To test if the simulation successfully reproduces observed GMCs, Figure 3.1 shows the well-known correlation between σ_v and Σ_{mol} for isolated simulated galaxies and PHANGS-ALMA spiral galaxies. We show σ_v versus Σ_{mol} contours for G2 and G3 galaxies at an inclination angle of 30 degrees, compared with that of observed galaxies. The two simulated galaxies exhibit similar properties (black and dark red solid contours) and generally lie on the trend followed by the PHANGS galaxies. We also plot a red dashed line indicating GMCs with constant virial parameter α_{vir} of 3.1. For the pixel-based analysis, α_{vir} is calculated as (Sun et al. 2018)

$$\begin{aligned}\alpha_{\mathrm{vir}} &= \frac{9\ln 2}{2\pi G}\frac{\sigma_v^2}{\Sigma_{\mathrm{mol}} R} \\ &= 5.77\left(\frac{\sigma_v}{\mathrm{km\ s^{-1}}}\right)^2\left(\frac{\Sigma_{\mathrm{mol}}}{\mathrm{M_\odot pc^{-2}}}\right)^{-1}\left(\frac{R}{40\mathrm{pc}}\right)^{-1},\end{aligned} \tag{3.3}$$

where R is the GMC radius. In Sun et al. (2018), R is set to be the radius of the beam in the image, as each beam is treated as an independent GMC. We can see both our simulated galaxies and observed PHANGS galaxies follow the trend of the constant

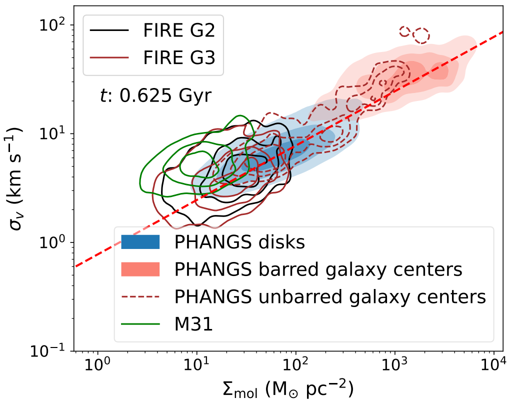

Figure 3.1: Velocity dispersion versus gas surface density for the G2 (black solid contour) and G3 (brown solid contour) simulated galaxies at 0.625 Gyr with inclination angle of 30 degrees compared to the PHANGS galaxy sample. The contours are mass-weighted and set to include 20%, 50% and 80% of the data. The density contours of PHANGS galaxies (Sun et al. 2020) show the distribution of measurements in galaxy disks (blue shaded contours), the centers of barred galaxies (salmon shaded contours) and the centers of unbarred galaxies (brown dashed contours) with a resolution of 90 pc. The red dashed line marks the position of the median values of $\alpha_{\rm vir}$ for PHANGS galaxies of 3.1 (Sun et al. 2020). We also show the data for M31 (green solid contour) at 120 pc resolution from Sun et al. (2018). *We can see that the FIRE-2 spiral galaxies follow the same* σ_v*-* $\Sigma_{\rm mol}$ *relation as the PHANGS galaxies.*

$\alpha_{\rm vir}$, which yields the relation of $\sigma_v^2 \propto \Sigma_{\rm mol}$ that suggests the simulations reproduce GMCs similar to the observations. However, we can see that the two galaxies lie at the low surface-density end of the PHANGS distribution and thus their gas properties are more similar to those of M31 than a typical PHANGS galaxy. Indeed, the molecular and total gas properties of the simulated galaxies are similar to those of M 31, perhaps due to the choice of initial gas mass in the simulations.

3.4 Merging galaxies

3.4.1 GMC linewidth and surface density

We performed a similar σ_v versus $\Sigma_{\rm mol}$ analysis for our suite of galaxy merger simulations. Since we are particularly interested in how the starburst activity influences GMC properties, we focus on the period right before and after the second passage where we can see the largest contrast in SFR. In Fig. 3.2 we show some example snapshots of σ_v versus Σ_{mol} for different merger stages during the second passage, along with Σ_{mol} and α_{vir} maps at each snapshot. Note that the datacube is centered on the primary galaxy G3. At the time of first snapshot (2.54 Gyr), right before the start of the second perigalactic passage, the simulated mergers still have Σ_{mol} and σ_v that are similar the isolated galaxies. Then the molecular gas quickly transitions to a more turbulent state with much higher σ_v after the second passage along with a dramatic increase in global SFR, as shown in the snapshot for 2.66 Gyr (middle panel of Fig. 3.2). The merger at this time still shows two separate nuclei in the zeroth moment map; this is similar to our observed mergers, the Antennae and NGC 3256. At this time, the σ_v versus Σ_{mol} contours for the simulated merger lie above the trend seen for the PHANGS galaxies, similar to NGC 3256, but in contrast to the Antennae, which still lies along the trend of the PHANGS galaxies. The larger deviation above the PHANGS trend implies higher α_{vir}. We note that different α_{CO} choices will affect the position of the contours. If we choose the ULIRG α_{CO} instead of the Milky Way value, the Antennae would have α_{vir} similar to that of NGC 3256 and our G2&G3 merger. The uncertainty in the correct α_{CO} value to use makes it difficult to interpret the data for the Antennae in this context.

The bottom panel of Fig. 3.2 shows the snapshot at 2.87 Gyr, which marks the post-merger stage after the final coalescence of two nuclei (defined here as the time at which the two central supermassive black holes are at a distance of 500 pc for the last time). This is the time when both Σ_{mol} and σ_v reach their highest values. We can see that most of the molecular gas is concentrated in the central 1 kpc region, with Σ_{mol} reaching 1000 $\mathrm{M}_\odot$ pc^{-2}. σ_v reaches 200 km s^{-1}, which is even higher than the σ_v observed in NGC 3256, which is in an earlier merging stage when the two nuclei have not yet coalesced.

To better quantify the variation of Σ_{mol} and σ_v during the second passage, we plot the 16th, 50th and 84th percentile of the mass-weighted values for all pixels of each snapshot during the second passage in Fig. 3.3. We also normalize both the median Σ_{mol} and σ_v to the median values of the isolated G3 galaxy at 0.625 Gyr (Fig. 3.1) to show how the merging event affects the GMC properties during the second passage. Both Σ_{mol} and σ_v increase significantly during the merger, with a maximum increase of a factor of 10. The increase in σ_v and Σ_{mol} is roughly of the same order. Eq. 3.3 shows that a constant α_{vir} requires $\sigma_v^2 \propto \Sigma_{\mathrm{mol}}$. These results imply that our simulated merger will have higher $\alpha_{\rm vir}$ compared to PHANGS galaxies.

3.4.2 The virial parameters of GMCs

During the second passage, we see that the σ_v vs $\Sigma_{\rm mol}$ distribution for our simulated merger lies above the trend observed for the PHANGS galaxies. A higher σ_v for a given $\Sigma_{\rm mol}$ means the GMCs in these mergers are more turbulent and less gravitationally bound than in normal spiral galaxies.

We adopt the same approach as in observations to calculate $\alpha_{\rm vir}$ for pixel-based GMC pixels using Eq. 3.3. Since the simulation data do not have a telescope "beam" and each pixel in this analysis is treated as an independent GMC, we set R to be half the size of each pixel (50 pc). With constant R, $\alpha_{\rm vir}$ depends only on σ_v and $\Sigma_{\rm mol}$. Higher σ_v at a similar $\Sigma_{\rm mol}$ thus implies that $\alpha_{\rm vir}$ values for GMCs in simulated mergers are higher than the values for PHANGS or simulated isolated galaxies. Higher values for $\alpha_{\rm vir}$ are also found for NGC 3256 (Brunetti et al. 2020; Brunetti & Wilson 2022) and the Antennae (Brunetti 2022).

Fig. 3.4 shows $\alpha_{\rm vir}$ as a function of time during the period near the second pericentric passage for the merger simulations with "e2" and "e1" orbits and viewed from "v0" angle. $\alpha_{\rm vir}$ stays low before the second passage and suddenly rises after the passage along with a sudden increase in SFR. The peak of median $\alpha_{\rm vir}$ can reach $\sim$100. After the second passage, $\alpha_{\rm vir}$ gradually dies down as the SFR also decreases. During the entire merging process, we generally see a good correspondence between the SFR and $\alpha_{\rm vir}$ peaks, which suggests that the $\alpha_{\rm vir}$ value is either regulated by feedback from star formation or that both SFR and $\alpha_{\rm vir}$ increase together as a result of the merger.

$\alpha_{\rm vir}$ for our fiducial 'e2' orbit is generally higher than that of the 'e1' orbit and stays at higher values for a significantly longer time. The 'e2' orbit has a higher impact parameter than the 'e1' orbit (Section 3.2.1). Therefore, we would expect more gravitational potential energy transferred to the kinetic energy of individual GMCs, potentially making these GMCs less gravitationally bound. The $\alpha_{\rm vir}$ values for the 'e1' orbit are more similar to the $\alpha_{\rm vir}$ of NGC 3256 and the Antennae and the 'e1' orbit is more similar to the orbit of the Antennae. We note that both the Antennae and NGC 3256 are at the very start of their second passages (Privon et al. 2013; Renaud et al. 2019a). At this stage, there are significant variations in $\alpha_{\rm vir}$, which makes it difficult to pick the exact snapshot that matches the observation. If we use the U/LIRG α_{CO} instead of the Milky Way value, α_{vir} for the Antennae would be similar to that of NGC 3256. We will discuss our α_{CO} choices further in Section 3.5.2.

3.4.3 Molecular Gas in the central 1 kpc region

From the moment 0 maps in Fig. 3.2, we can see that most molecular gas is concentrated in the center during the post-merger phase after 2.83 Gyr. This is consistent with the traditional scenario that the central starburst activity is caused by the inflow of molecular gas due to the loss of angular momentum (Hernquist 1989; Barnes & Hernquist 1991; Mihos & Hernquist 1994, 1996; Barnes & Hernquist 1996; Moreno et al. 2015). To quantify how much of the molecular gas is concentrated in the center, Fig. 3.5 shows the molecular gas mass within the central 1 kpc, and the ratio between this value and total molecular gas mass. The fraction of molecular gas concentrated in the center reaches as high as 80% for a significant period of time ($\sim$ 500 Myr) around the final coalescence. On the other hand, Moreno et al. (2019) shows that the total molecular gas mass decreases during the second passage. Therefore, the overall high Σ_{mol} values of GMCs across our simulated merger compared to isolated galaxies are mostly due to the central gas concentration.

Fig. 3.6 shows the σ_v versus Σ_{mol} distribution for pixels in the central kpc region of the G2&G3 merger at 2.87 Gyr (red aperture in Fig. 3.2), along with pixels in the center of PHANGS galaxies, the Antennae and NGC 3256. We can see the pixels in the center of the G2&G3 merger have a larger deviation from the PHANGS trend than NGC 3256, which indicates that the G2&G3 merger has GMCs with larger α_{vir} in the center. We also show the mass weighted median α_{vir} for the entire and central region of G2&G3 merger as a function of time (Fig. 3.6 right). α_{vir} in the center is generally higher than for the entire region, which indicates that GMCs in the center are more perturbed and less gravitationally bound. At the time right after the second passage, we see dramatic fluctuations of α_{vir} for both the center and the entire galaxy, which is probably due to the complex and constantly varying gas morphology during this period. Moreover, we might see two GMCs that are far apart in 3D space but lie along the same line of sight, which cause large measured α_{vir} value, but in a short time they no longer lie along the same line of sight, which causes a sudden drop of α_{vir}. At the post-merger phase, α_{vir} values are more stable. However, we see that α_{vir} of the disk region gradually settles down while the central α_{vir} keeps increasing.

This might indicate that GMCs in the central region take more time to settle down to their normal states, which may be due to the starburst activity in the center. We also see high $\alpha_{\rm vir}$ for the center at the very start (2.54 Gyr), which probably means GMCs in the center at this time have not recovered from the starburst event that occured during the first peri-galactic passage.

3.4.4 Correlation between the central SFR and GMC Properties

The driving mechanism behind the SFR enhancement in mergers is of great interest to the study of star formation and galaxy evolution. One approach to tackle this problem is to decompose the SFR into the following 2 terms

$$\mathrm{SFR} = \frac{M_{\rm mol}}{t_{\rm dep}}, \tag{3.4}$$

where $t_{\rm dep}$ is the depletion time, defined as the time for star formation to consume the available molecular gas. This approach makes it clearer that the rise in SFR could be either due to a larger amount of molecular gas “fuel driven") or shorter depletion time (“efficiency driven"). The simulations (e.g. Moreno et al. 2021) and observations (e.g. Thorp et al. 2022) indicate that both terms contribute to the SFR enhancement at kpc scales. Moreover, many studies of the Kennicutt-Schmidt relation in U/LIRGs at kpc scales show that these starburst mergers have relatively short $t_{\rm dep}$ of $\sim 10^8$ yr compared to normal spiral galaxies of $\sim 10^9$ yr (e.g. Daddi et al. 2010), which confirms the role of efficiency driving in mergers. With our simulations being able to probe the molecular gas at GMC scales, we can explore how $t_{\rm dep}$ is correlated with GMC populations in different regions.

For this analysis, we focus on the molecular gas and star formation in the central 1 kpc region since most gas is concentrated here during the second passage (see Section 3.4.3). We measure the mass-weighted median $\alpha_{\rm vir}$ in this central region as a metric for GMC dynamical state in the center. Fig. 3.7 shows $\Sigma_{\rm mol}$ and $\Sigma_{\rm SFR}$ color-coded by $\alpha_{\rm vir}$ for the central region as a function of time. We calculate the average $\Sigma_{\rm mol}$ and $\Sigma_{\rm SFR}$ by dividing the total $M_{\rm mol}$ or SFR in the central region by the aperture size. We show the data points within the period of 2.54 – 2.61 Gyr (before the second passage) and 2.73 – 3.47 Gyr (after the second passage) for comparison. We exclude the data points between the start of the second passage (2.62 Gyr) and the time when the central/total gas fraction starts to reach 50% (2.73 Gyr) because data points from this period show a large deviation from the major trend in $\Sigma_{\rm SFR}$ vs $\Sigma_{\rm mol}$ diagram. The large deviation is probably because the limited amount of molecular gas is highly perturbed in the central region. Gas is either quickly consumed without being replenished in time, or just concentrated and has not formed stars yet, which causes the large scatter in the $\Sigma_{\rm SFR}$ vs $\Sigma_{\rm mol}$ relation. On the other hand, before and after this period, the central region is in a relatively stable state when the molecular gas is constantly replenished to fuel star formation activity.

In the left panel of Fig. 3.7, we can see that $t_{\rm dep}$ becomes shorter as $\Sigma_{\rm mol}$ and $\Sigma_{\rm SFR}$ increase. The points at the lower left end of the $\Sigma_{\rm mol}$ correspond to the times before the second passage, which also have relatively low $\alpha_{\rm vir}$. In contrast, the $\alpha_{\rm vir}$ after the second passage is significantly higher. We also note that $t_{\rm dep}$ even before the second passage ($\sim 10^8$ yr) is quite shorter than that of normal spiral galaxies (10^9 yr). The difference could be due to different dynamical timescales of simulated and observed galaxies. At this time, we can see $\alpha_{\rm vir}$ for the central region is already ~ 10 which indicates the molecular gas in the central region has already been disturbed.

There is no significant correlation between $t_{\rm dep}$ and $\alpha_{\rm vir}$, with Spearman coefficient of -0.08 for all data points and of 0.18 for data after the second passage, which is against our expectation that low $\alpha_{\rm vir}$ gas form stars more quickly. We can also clearly see a distinction between $\alpha_{\rm vir}$ before and after the second passage. The $\alpha_{\rm vir}$ before the second passage is relatively small and corresponds to larger $t_{\rm dep}$ while the $\alpha_{\rm vir}$ after the second passage is significantly larger but corresponds to shorter $t_{\rm dep}$. This again is inconsistent with our expectation that low $\alpha_{\rm vir}$ GMCs should form stars more easily. Other physical mechanisms rather than self-gravity of individual GMCs may be needed to help the molecular gas to collapse (see detailed discussion in Section 3.5.1).

On the other hand, we see an anti-correlation between $t_{\rm dep}$ and $\Sigma_{\rm mol}$. This relation is similar to the global Kennicutt-Schmidt relation where the gas rich U/LIRGs have the shorter $t_{\rm dep}$ (Daddi et al. 2010). One explanation for this trend is that the fraction of dense gas (traced by HCN) that are actually forming stars (i.e. traces the self-gravitating gas fraction) is increasing as $\Sigma_{\rm mol}$ increases (e.g. Gao & Solomon 2004; Bemis & Wilson 2023). If we assume $\Sigma_{\rm mol}$ is proportional to the mean volume density of molecular gas in the central region, we would expect larger fraction of molecular gas above the dense gas threshold ($n > 10^4$ cm^{-3}) in FIRE-2 simulation (Hopkins 2015), which leads to faster star formation and shorter $t_{\rm dep}$.

3.5 Discussion

3.5.1 How can high $\alpha_{\rm vir}$ gas form stars in simulated mergers?

As shown in Section 3.4.2, $\alpha_{\rm vir}$ generally stays above 10 during the second passage for the G2&G3 merger. If we assume star formation occurs in individual GMCs and is driven by the collapse of the clouds due to self-gravity , we would expect star forming GMCs to have $\alpha_{\rm vir}$ below 1. The combination of high $\alpha_{\rm vir}$ values and starburst activity is inconsistent with this expectation, unless the velocity dispersion is being driven to higher values by infall motion. Furthermore, we find no correlation between $\alpha_{\rm vir}$ and $t_{\rm dep}$ (Section 3.4.4), which suggests low $\alpha_{\rm vir}$ values do not strongly affect the depletion time in our simulations. However, we need to note that our measurement of $\alpha_{\rm vir}$ from pixel-based method might not reflect the real $\alpha_{\rm vir}$ of individual GMC components, especially for the post-second-passage phase when molecular gas is concentrated in the center. Although observations (Brunetti & Wilson 2022; Sun et al. 2020) show that cloud properties extracted from a pixel-based approach is generally consistent with the traditional cloud-based approach, they also show the pixel-based approach gives higher σ_v and $\alpha_{\rm vir}$ for molecular gas in galaxy centers. This is likely due to the superimposition of different GMC components along the same line of sight in gas-concentrated galaxy centers. Sun et al. (2022) find that $\alpha_{\rm vir}$ from pixel-based approach is ~ 3 times higher than the cloud-based approach for galaxy centers. If we assume the same degree of overestimate in our simulation data for the merger center, we would expect the real $\alpha_{\rm vir}$ to be ~ 10 during the second passage, still significantly higher than the critical value of 1 when clouds reach the self-collapsing criterion. We also note that even the observational cloud-based approach by extracting different GMC components from p-p-v data cube might still suffer from the projection effects. Beaumont et al. (2013) find that $\alpha_{\rm vir}$ from p-p-p and p-p-v cubes have a factor of 2 difference for substructures in their cloud simulation due to a mismatch of substructures from these two data cubes. Therefore, one of our next steps is to perform cloud-finding algorithm (Burkhart et al. 2013) on both p-p-p and p-p-v simulation data cubes to fully understand how GMCs evolve during the merging events.

A possible explanation for large α_{vir} is that GMCs that satisfy the self-collapsing criterion have already formed stars and become unbound or destroyed due to the stellar feedback. However, if this is the case, we would expect α_{vir} to fluctuate around the critical value of 1. Furthermore, according to Benincasa et al. (2020), GMCs with high α_{vir} (>10) have significantly shorter lifetimes ($\sim$2 Myr) than GMCs with low α_{vir} ($\sim$1; lifetime of $\sim$10 Myr). If we assume all GMCs are of the same population but at different evolutionary stages, we would expect GMCs to stay at low α_{vir} state for a longer time and hence we should be more likely to catch these low α_{vir} GMCs in our simulation snapshots. Instead, we see α_{vir} constantly higher than 10 during the starburst activity (Fig. 3.4), which is inconsistent with this scenario.

It is perhaps likely that the explanation is that these GMCs are experiencing compression from the large-scale gravitational potential. This compression could add additional potential energy to balance the kinetic energy. Furthermore, they can trigger inflow of gas into GMCs and bring radial velocity (V_r) component into our σ_v measurement. Ganguly et al. (2022) find in their simulation that v_r could be an important factor to produce high measured α_{vir} clouds. For GMCs in normal spiral galaxies and galaxy pairs (e.g., M 51), Meidt et al. (2018) show that the large-scale stellar potential could be responsible for holding individual GMCs in energy equipartition state. Compared to galaxies in their study, the starburst mergers in our study undergo more dramatic morphological changes, which could generate complicated gravitational tidal fields. Renaud et al. (2009) show in their simulation that major mergers can produce fully compressive tidal fields that concentrate molecular gas and trigger starburst activities. These compressive tidal fields are believed to be responsible for creating the off-nuclei gas concentration region in the ULIRG, Arp 220 (Downes & Solomon 1998). In our next step to test this scenario, we will need to calculate tidal deformation timescale (as in Ganguly et al. 2022) for each individual GMC and compare it with GMC free-fall and crossing timescales to see how important the external tidal field is compared to GMC self-gravity.

Another possible explanation is that molecular gas is smoothly distributed rather than clumped into individual GMCs during the starburst activities. If this is the case, the star formation is regulated by the entire molecular disk rather than individual GMC components (Krumholz et al. 2018). Wilson et al. (2019) propose that the star formation in U/LIRGs is regulated by the hydrodynamic pressure of the molecular disk with a constant scale height. In observation, one way to test the smoothness of gas distribution is by comparing average gas surface density at different observing resolutions (Leroy et al. 2017). Brunetti et al. (2020) show that molecular gas in the LIRG, NGC 3256, is smoothly distributed based on this method. For our simulated merger, gas might be smoothly distributed during the second passage when most gas is concentrated in the center (e.g. at 2.87 Gyr, Fig. 3.2. We could test this scenario by changing the pixel size in our p-p-v cubes and compare the average gas surface densities in the central region at different pixel resolutions.

3.5.2 Comparison with observations

As shown in Section 3.4, our simulated merger generally has lower $\Sigma_{\rm mol}$ and higher σ_v and $\alpha_{\rm vir}$ compared to the two observed mergers, the Antennae and NGC 3256. We note that this simulation is not set to match the exact condition of the observed mergers, so some discrepancy between observations and simulations would be expected. From the observational side, the biggest uncertainty that comes into the measurement is the value of $\alpha_{\rm CO}$. As mentioned in Section 3.4.1, if we adopt the ULIRG $\alpha_{\rm CO}$ instead of the Milky Way value for the Antennae, we would find the Antennae to have similar $\Sigma_{\rm mol}$ and $\alpha_{\rm vir}$ as NGC 3256. In contrast, if we assume an even smaller $\alpha_{\rm CO}$ for NGC 3256, that might bring the contours of the observations further away from the PHANGS trend and hence more similar to the simulation contours. However, various LVG modelings (Papadopoulos et al. 2012; Harrington et al. 2021) show that local U/LIRGs and high-z starburst galaxies generally have $\alpha_{\rm CO}$ above 0.8 $M_\odot$ (K km s^{-1} pc^2)$^{-1}$. In fact, a recent study by Dunne et al. (2022) concludes that these starburst galaxies might actually have $\alpha_{\rm CO}$ equal to the Milky Way value by cross-correlating the CO luminosity with dust and CI luminosity. Therefore, a factor of 3 discrepancy in $\alpha_{\rm vir}$ between simulated mergers and NGC 3256 is probably real rather than due to measurement uncertainties.

For the comparison between observations and simulations, we also note that the two observed mergers are both in an early stage after the second passage since we can still identify two separate nuclei. In this stage, $\alpha_{\rm vir}$ is quite time-sensitive and it is difficult to match the exact same stage between the simulated and observed galaxies. Therefore, it is possible that both NGC 3256 and Antennae are caught at a specific merger stage with a lower $\alpha_{\rm vir}$ (although in the case of NGC 3256, still enhanced relative to PHANGS galaxies). In comparison, $\alpha_{\rm vir}$ in the simulations is relatively stable in the post-merger stage. This stability suggests that a comparison between simulations and observations of post-merger galaxies could be a useful next step. Moreover, post-mergers have a rather simple morphology, which simplifies the task of making quantitative comparisons.

It would also be interesting to compare the simulation results with starburst galaxies at high redshift. Recent works (e.g. Dessauges-Zavadsky et al. 2019; Meštrić et al. 2022) show that we can probe GMC-scale star-forming clumps in gravitationally lensed objects at high redshift. These star-forming clumps generally show a similar $\alpha_{\rm vir}$ to GMCs of normal spiral galaxies in our local Universe despite using different $\alpha_{\rm CO}$, and therefore lower than what we see in the simulations. However, these high-z targets likely live in a completely different environment than our idealized mergers. Specifically, high-z galaxies tend to have a much higher gas fraction, and thus can form self-gravitating clumps with low $\alpha_{\rm vir}$ more easily (Fensch & Bournaud 2021).

3.5.3 Comparison with other simulations

In this work, we use the non-cosmological simulations from Moreno et al. (2019) to compare GMC properties in mergers and normal spiral galaxies. Two major advantages of this simulation suite are that it has a resolution of 1.1 pc (which is much smaller than typical GMC sizes) and it can model the ISM down to low temperatures ($\sim$ 10 K), both of which allow us to match the molecular gas in simulations with CO observations. Various cosmological simulations show that mergers are responsible for enhancing gas fractions and triggering starburst activity (Scudder et al. 2015; Knapen et al. 2015; Patton et al. 2013; Martin et al. 2017; Rodríguez Montero et al. 2019; Patton et al. 2020, e.g.,). However, these simulations can only model gas with temperatures down to 10^4 K and hence are incapable of capturing the turbulent multi-phase structure of the ISM. An alternative approach is to compare observations with cosmological zoom-in simulations, which allows for higher resolution, more realistic feedback star formation thresholds, and more realistic modeling of the multiphase ISM. Various authors have explored GMC properties, mostly in Milky-Way-like galaxies (e.g. Guedes et al. 2011; Ceverino et al. 2014; Sawala et al. 2014; Benincasa et al. 2020; Orr et al. 2021), and they generally reproduce the GMC mass function in our Milky Way. However, only a handful of work (e.g. Rey et al. 2022) has been done for GMCs in mergers. Also, the Milky Way is identified as a green-valley galaxy (Mutch et al. 2011) with lower SFR than typical spiral galaxies in the local universe. Therefore, due to the lack of zoom-in cosmological simulations on local mergers, we have adopted idealized simulations for this study. Furthermore, idealized simulations allow us to compare GMCs of control galaxies with those of mergers to directly study the impact of the merging event.

Several idealized simulations have been performed to study molecular gas and GMC properties in mergers. Karl et al. (2013) perform a merger simulation closely matched to the Antennae and find a great match on CO distributions between simulation and observations, which suggests insufficient stellar feedback efficiencies in the Antennae. Li et al. (2022) perform a study of GMCs and young massive star clusters (YMCs) in Antennae-like mergers. They find that GMC mass functions for mergers have similar power-law slopes to normal spirals during the second coalescence but with much higher mass values. Narayanan et al. (2011) compare the α_{CO} in mergers and normal spiral galaxies and find that the low α_{CO} in mergers is mostly due to the high temperature and α_{vir} of GMCs in the merger. They predict there is a transition stage with α_{CO} between U/LIRG and Milky Way values and that α_{vir} is tightly anti-correlated with α_{CO}. In contrast, Renaud et al. (2019b) show that α_{CO} values drop quickly during each coalescence between two galaxies. We find similar behavior for α_{vir} during the second coalescence, which might imply a similar drop in α_{CO} (Narayanan et al. 2011).

3.6 Conclusions

We summarize our main conclusions below:

- Our pixel-by-pixel analysis shows that the FIRE-2 simulation by Moreno et al. (2019) successfully reproduces the σ_v vs Σ_{mol} relation for GMC-scale pixels measured for galaxies in the PHANGS survey.
- The simulated mergers show a significant increase in both Σ_{mol} and σ_v for GMC-pixels by a factor of 5 – 10 during the second passage when SFR peaks, which brings these pixels above PHANGS-trend in the σ_v vs Σ_{mol} diagram. This may indicate GMCs in these mergers are less gravitationally bound. We quantify this deviation by the virial parameter α_{vir} and find that our simulated mergers have α_{vir} of $10-100$, which is even higher than the observed α_{vir} in NGC 3256. However, this discrepancy could be partly due to the high impact parameter in the initial set-up of the simulated mergers. Furthermore, we see a good

correspondence between the increase in SFR and α_{vir}, which suggest either the starburst feedback is responsible for dispersing the gas or the correlation is in response to gas compression.

- Our simulated mergers show a clear gas concentration in the center during the second passage, with up to 80% of molecular gas in the central 1 kpc region. Therefore, the GMC-pixels in the central region tend to have the highest Σ_{mol}. We also find these pixels tend to have the highest σ_v and α_{vir}, which could be caused by the starburst feedback and the inflow of gas.

- We explore if α_{vir} at GMC scales is responsible for the varying depletion time (t_{dep}) in observed mergers. While we do not find a significant correlation between t_{dep} and α_{vir}, we see a clear distinction before (small α_{vir}, long t_{dep}) and after (large α_{vir}, short t_{dep}) the second passage. This could be due to projection effects (multiple GMCs along the same line of sight) during the second passage when most of the molecular gas is concentrated in the central 1 kpc region. The next step is to run a cloud-identification algorithm on the data to disentangle this factor. We also suspect there might be some other mechanism, such as the stellar potential and inflow of gas, that helps the GMCs in starburst mergers to collapse and form stars. We also find that t_{dep} has a significant anti-correlation with Σ_{mol} for the central region. This may be due to higher Σ_{mol} leading to a higher fraction of dense gas, which shortens t_{dep}.

In the future, we would like to expand our comparison to more observed and simulated mergers. From the observational side, we need larger samples of galaxy mergers spanning different evolutionary stages in order to understand how GMCs evolve throughout the merging. In addition, it is easier to compare the observations with simulations in the post-merger stage since the morphology is simpler and easier to quantify. The ALMA archive contains $\sim$ 40 U/LIRGs with GMC resolution CO 2-1 observations that can be used to build a more complete sample of GMCs in mergers at different stages. From the simulation side, it would be helpful to have simulations that better match the observed galaxies. The Antennae has been widely studied and matched by non-cosmological simulations (e.g. Renaud et al. 2019a; Li et al. 2022) but NGC 3256 is less well studied. Besides comparing with these non-cosmological simulations, we could also compare observation with cosmological simulations, such as FIREBox (Feldmann et al. 2022), that include local mergers.

Data Availability

The datasets generated during and/or analysed during the current study are available from the corresponding author on reasonable request, contingent on approval by the FIRE Collaboration on a case-by-case basis. The scripts and data to generate the animation are stored in the repository `10.5281/zenodo.7796593`.

Bibliography

Barnes, J. E., & Hernquist, L. 1996, The Astrophysical Journal, 471, 115, doi: `10.1086/177957`

Barnes, J. E., & Hernquist, L. E. 1991, The Astrophysical Journal, 370, L65, doi: `10.1086/185978`

Beaumont, C. N., Offner, S. S. R., Shetty, R., Glover, S. C. O., & Goodman, A. A. 2013, The Astrophysical Journal, 777, 173, doi: `10.1088/0004-637X/777/2/173`

Bellocchi, E., Pereira-Santaella, M., Colina, L., et al. 2022, A&A, 664, A60, doi: `10.1051/0004-6361/202142802`

Bemis, A. R., & Wilson, C. D. 2023, arXiv e-prints, arXiv:2301.06478. `https://arxiv.org/abs/2301.06478`

Benincasa, S. M., Loebman, S. R., Wetzel, A., et al. 2020, Monthly Notices of the Royal Astronomical Society, 497, 3993, doi: `10.1093/mnras/staa2116`

Bolatto, A. D., Leroy, A. K., Rosolowsky, E., Walter, F., & Blitz, L. 2008, The Astrophysical Journal, 686, 948, doi: `10.1086/591513`

Bottrell, C., & Hani, M. H. 2022, Monthly Notices of the Royal Astronomical Society, 514, 2821, doi: `10.1093/mnras/stac1532`

Bottrell, C., Hani, M. H., Teimoorinia, H., Patton, D. R., & Ellison, S. L. 2022, Monthly Notices of the Royal Astronomical Society, 511, 100, doi: `10.1093/mnras/stab3717`

Bottrell, C., Hani, M. H., Teimoorinia, H., et al. 2019, Monthly Notices of the Royal Astronomical Society, 490, 5390, doi: `10.1093/mnras/stz2934`

Bournaud, F., Duc, P. A., & Emsellem, E. 2008, Monthly Notices of the Royal Astronomical Society, 389, L8, doi: `10.1111/j.1745-3933.2008.00511.x`

Brunetti, N. 2022, Thesis

Brunetti, N., & Wilson, C. D. 2022, Monthly Notices of the Royal Astronomical Society, 515, 2928, doi: `10.1093/mnras/stac1975`

Brunetti, N., Wilson, C. D., Sliwa, K., et al. 2020, Monthly Notices of the Royal Astronomical Society, 500, 4730, doi: `10.1093/mnras/staa3425`

Burkhart, B. 2018, ApJ, 863, 118, doi: `10.3847/1538-4357/aad002`

Burkhart, B., Collins, D. C., & Lazarian, A. 2015, The Astrophysical Journal, 808, 48, doi: `10.1088/0004-637X/808/1/48`

Burkhart, B., Lazarian, A., Goodman, A., & Rosolowsky, E. 2013, ApJ, 770, 141, doi: `10.1088/0004-637X/770/2/141`

Burkhart, B., & Mocz, P. 2019, ApJ, 879, 129, doi: `10.3847/1538-4357/ab25ed`

Burkhart, B., Appel, S. M., Bialy, S., et al. 2020, The Astrophysical Journal, 905, 14, doi: `10.3847/1538-4357/abc484`

Catinella, B., Saintonge, A., Janowiecki, S., et al. 2018, Monthly Notices of the Royal Astronomical Society, 476, 875, doi: `10.1093/mnras/sty089`

Ceverino, D., Klypin, A., Klimek, E. S., et al. 2014, Monthly Notices of the Royal Astronomical Society, 442, 1545, doi: `10.1093/mnras/stu956`

Chevance, M., Kruijssen, J. M. D., Hygate, A. P. S., et al. 2020, Monthly Notices of the Royal Astronomical Society, 493, 2872, doi: `10.1093/mnras/stz3525`

Colombo, D., Hughes, A., Schinnerer, E., et al. 2014, The Astrophysical Journal, 784, 3, doi: `10.1088/0004-637X/784/1/3`

Colombo, D., Rosolowsky, E., Duarte-Cabral, A., et al. 2019, Monthly Notices of the Royal Astronomical Society, 483, 4291, doi: `10.1093/mnras/sty3283`

Daddi, E., Elbaz, D., Walter, F., et al. 2010, The Astrophysical Journal, 714, L118, doi: `10.1088/2041-8205/714/1/L118`

Dale, J. E., Ngoumou, J., Ercolano, B., & Bonnell, I. A. 2014, Monthly Notices of the Royal Astronomical Society, 442, 694, doi: `10.1093/mnras/stu816`

Decataldo, D., Lupi, A., Ferrara, A., Pallottini, A., & Fumagalli, M. 2020, Monthly Notices of the Royal Astronomical Society, 497, 4718, doi: `10.1093/mnras/staa2326`

Dessauges-Zavadsky, M., Richard, J., Combes, F., et al. 2019, Nat Astron, 3, 1115, doi: `10.1038/s41550-019-0874-0`

Donovan Meyer, J., Koda, J., Momose, R., et al. 2013, The Astrophysical Journal, 772, 107, doi: `10.1088/0004-637X/772/2/107`

Downes, D., & Solomon, P. M. 1998, ApJ, 507, 615, doi: `10.1086/306339`

Dunne, L., Maddox, S. J., Papadopoulos, P. P., Ivison, R. J., & Gomez, H. L. 2022, Monthly Notices of the Royal Astronomical Society, 517, 962, doi: `10.1093/mnras/stac2098`

Elmegreen, D. M., Elmegreen, B. G., Kaufman, M., et al. 2017, The Astrophysical Journal, 841, 43, doi: `10.3847/1538-4357/aa6ba5`

Fall, S. M., Krumholz, M. R., & Matzner, C. D. 2010, Astrophysical Journal Letters, 710, 142, doi: `10.1088/2041-8205/710/2/L142`

Feldmann, R., Quataert, E., Faucher-Giguère, C.-A., et al. 2022, FIREbox: Simulating Galaxies at High Dynamic Range in a Cosmological Volume

Fensch, J., & Bournaud, F. 2021, Monthly Notices of the Royal Astronomical Society, 505, 3579, doi: `10.1093/mnras/stab1489`

Fensch, J., Renaud, F., Bournaud, F., et al. 2017, Monthly Notices of the Royal Astronomical Society, 465, 1934, doi: `10.1093/mnras/stw2920`

Fukui, Y., Kawamura, A., Minamidani, T., et al. 2008, The Astrophysical Journal Supplement Series, 178, 56, doi: `10.1086/589833`

Ganguly, S., Walch, S., Clarke, S. D., & Seifried, D. 2022, SILCC-Zoom: The Dynamic Balance in Molecular Cloud Substructures

Gao, Y., & Solomon, P. M. 2004, The Astrophysical Journal, 606, 271, doi: `10.1086/382999`

Grudić, M. Y., Hopkins, P. F., Faucher-Giguère, C. A., et al. 2018, Monthly Notices of the Royal Astronomical Society, 475, 3511, doi: `10.1093/MNRAS/STY035`

Guedes, J., Callegari, S., Madau, P., & Mayer, L. 2011, The Astrophysical Journal, 742, 76, doi: `10.1088/0004-637X/742/2/76`

Guszejnov, D., Hopkins, P. F., & Ma, X. 2017, Monthly Notices of the Royal Astronomical Society, 472, 2107, doi: `10.1093/mnras/stx2067`

Harrington, K. C., Weiss, A., Yun, M. S., et al. 2021, The Astrophysical Journal, 908, 95, doi: `10.3847/1538-4357/abcc01`

Hennebelle, P., & Chabrier, G. 2011, The Astrophysical Journal, 743, L29, doi: `10.1088/2041-8205/743/2/L29`

Hernquist, L. 1989, Nature, 340, 687, doi: `10.1038/340687a0`

Heyer, M., & Dame, T. M. 2015, Annual Review of Astronomy and Astrophysics, vol. 53, p.583-629, 53, 583, doi: `10.1146/annurev-astro-082214-122324`

Heyer, M., Krawczyk, C., Duval, J., & Jackson, J. M. 2009, The Astrophysical Journal, 699, 1092, doi: `10.1088/0004-637X/699/2/1092`

Hopkins, P. F. 2015, Monthly Notices of the Royal Astronomical Society, 450, 53, doi: `10.1093/mnras/stv195`

—. 2017, A New Public Release of the GIZMO Code

Hopkins, P. F., Wetzel, A., Kereš, D., et al. 2018, Monthly Notices of the Royal Astronomical Society, 480, 800, doi: `10.1093/mnras/sty1690`

Howard, C. S., Pudritz, R. E., & Harris, W. E. 2018, Nature Astronomy, 2, 725, doi: `10.1038/s41550-018-0506-0`

Howell, J. H., Armus, L., Mazzarella, J. M., et al. 2010, The Astrophysical Journal, 715, 572, doi: `10.1088/0004-637X/715/1/572`

Hughes, A., Meidt, S. E., Colombo, D., et al. 2013, The Astrophysical Journal, 779, 46, doi: `10.1088/0004-637X/779/1/46`

Jeffreson, S. M. R., & Kruijssen, J. M. D. 2018, Monthly Notices of the Royal Astronomical Society, 28, 1, doi: `10.1093/mnras/sty594`

Karl, S. J., Lunttila, T., Naab, T., et al. 2013, Monthly Notices of the Royal Astronomical Society, 434, 696, doi: `10.1093/mnras/stt1063`

Karl, S. J., Naab, T., Johansson, P. H., et al. 2010, The Astrophysical Journal, 715, L88, doi: `10.1088/2041-8205/715/2/L88`

Kennicutt, R. C., & Evans, N. J. 2012, Annual Review of Astronomy and Astrophysics, 50, 531, doi: `10.1146/annurev-astro-081811-125610`

Kennicutt, Jr., R. C. 1998, The Astrophysical Journal, 498, 541, doi: `10.1086/305588`

Kim, C.-G., Ostriker, E. C., & Raileanu, R. 2017, The Astrophysical Journal, 834, 25, doi: `10.3847/1538-4357/834/1/25`

Knapen, J. H., Cisternas, M., & Querejeta, M. 2015, Monthly Notices of the Royal Astronomical Society, 454, 1742, doi: `10.1093/mnras/stv2135`

Krumholz, M. R., Burkhart, B., Forbes, J. C., & Crocker, R. M. 2018, MNRAS, 477, 2716, doi: `10.1093/mnras/sty852`

Krumholz, M. R., & McKee, C. F. 2005, The Astrophysical Journal, 630, 250, doi: `10.1086/431734`

Krumholz, M. R., McKee, C. F., & Bland-Hawthorn, J. 2019, Annual Review of Astronomy and Astrophysics, vol. 57, p.227-303, 57, 227, doi: `10.1146/annurev-astro-091918-104430`

Lada, C. J., & Dame, T. M. 2020, The Astrophysical Journal, 898, 3, doi: `10.3847/1538-4357/ab9bfb`

Larson, R. B. 1981, Monthly Notices of the Royal Astronomical Society, 194, 809, doi: `10.1093/mnras/194.4.809`

Lee, E. J., Miville-Deschênes, M.-A., & Murray, N. W. 2016, The Astrophysical Journal, 833, 229, doi: `10.3847/1538-4357/833/2/229`

Leitherer, C., Schaerer, D., Goldader, J. D., et al. 1999, The Astrophysical Journal Supplement Series, 123, 3, doi: `10.1086/313233`

Leroy, A. K., Hughes, A., Schruba, A., et al. 2016, The Astrophysical Journal, 831, 16, doi: `10.3847/0004-637X/831/1/16`

Leroy, A. K., Usero, A., Schruba, A., et al. 2017, The Astrophysical Journal, 835, 217, doi: `10.3847/1538-4357/835/2/217`

Leroy, A. K., Schinnerer, E., Hughes, A., et al. 2021, ApJS, 257, 43, doi: `10.3847/1538-4365/ac17f3`

Li, H., Vogelsberger, M., Bryan, G. L., et al. 2022, Monthly Notices of the Royal Astronomical Society, 514, 265, doi: `10.1093/mnras/stac1136`

Li, H., Vogelsberger, M., Marinacci, F., & Gnedin, O. Y. 2019, Monthly Notices of the Royal Astronomical Society, 487, 364, doi: `10.1093/mnras/stz1271`

Martin, G., Kaviraj, S., Devriendt, J. E. G., et al. 2017, Monthly Notices of the Royal Astronomical Society, 472, L50, doi: `10.1093/mnrasl/slx136`

McElroy, R., Bottrell, C., Hani, M. H., et al. 2022, Monthly Notices of the Royal Astronomical Society, 515, 3406, doi: `10.1093/mnras/stac1715`

McMullin, J. P., Waters, B., Schiebel, D., Young, W., & Golap, K. 2007, 376, 127

Meidt, S. E., Leroy, A. K., Rosolowsky, E., et al. 2018, The Astrophysical Journal, 854, 100, doi: `10.3847/1538-4357/aaa290`

Meštrić, U., Vanzella, E., Zanella, A., et al. 2022, Monthly Notices of the Royal Astronomical Society, 516, 3532, doi: `10.1093/mnras/stac230910.48550/arXiv.2202.09377`

Mihos, J. C., & Hernquist, L. 1994, The Astrophysical Journal, 431, L9, doi: `10.1086/187460`

—. 1996, The Astrophysical Journal, 464, 641, doi: `10.1086/177353`

Miville-Deschênes, M.-A., Murray, N., & Lee, E. J. 2017, The Astrophysical Journal, 834, 57, doi: `10.3847/1538-4357/834/1/57`

Mocz, P., & Burkhart, B. 2018, MNRAS, 480, 3916, doi: `10.1093/mnras/sty1976`

Moreno, J., Torrey, P., Ellison, S. L., et al. 2015, Monthly Notices of the Royal Astronomical Society, 448, 1107, doi: `10.1093/mnras/stv094`

—. 2019, Monthly Notices of the Royal Astronomical Society, 485, 1320, doi: `10.1093/mnras/stz417`

—. 2021, Monthly Notices of the Royal Astronomical Society, 503, 3113, doi: `10.1093/mnras/staa2952`

Muraoka, K., Kohno, K., Tosaki, T., et al. 2009, The Astrophysical Journal, 706, 1213, doi: `10.1088/0004-637X/706/2/1213`

Murray, N., Quataert, E., & Thompson, T. A. 2010, The Astrophysical Journal, 709, 191, doi: `10.1088/0004-637X/709/1/191`

Mutch, S. J., Croton, D. J., & Poole, G. B. 2011, The Astrophysical Journal, 736, 84, doi: `10.1088/0004-637X/736/2/84`

Myers, A. T., Klein, R. I., Krumholz, M. R., & McKee, C. F. 2014, Monthly Notices of the Royal Astronomical Society, 439, 3420, doi: `10.1093/mnras/stu190`

Narayanan, D., Krumholz, M., Ostriker, E. C., & Hernquist, L. 2011, Monthly Notices of the Royal Astronomical Society, 418, 664, doi: `10.1111/j.1365-2966.2011.19516.x`

Nieten, C., Neininger, N., Guélin, M., et al. 2006, Astronomy and Astrophysics, Volume 453, Issue 2, July II 2006, pp.459-475, 453, 459, doi: `10.1051/0004-6361:20035672`

Orr, M. E., Hayward, C. C., Hopkins, P. F., et al. 2018, Monthly Notices of the Royal Astronomical Society, 478, 3653, doi: `10.1093/mnras/sty1241`

Orr, M. E., Hatchfield, H. P., Battersby, C., et al. 2021, The Astrophysical Journal, 908, L31, doi: `10.3847/2041-8213/abdebd`

Papadopoulos, P. P., van der Werf, P. P., Xilouris, E. M., et al. 2012, Monthly Notices of the Royal Astronomical Society, 426, 2601, doi: `10.1111/j.1365-2966.2012.21001.x`

Patton, D. R., Torrey, P., Ellison, S. L., Mendel, J. T., & Scudder, J. M. 2013, Monthly Notices of the Royal Astronomical Society, 433, L59, doi: `10.1093/mnrasl/slt058`

Patton, D. R., Wilson, K. D., Metrow, C. J., et al. 2020, Monthly Notices of the Royal Astronomical Society, 494, 4969, doi: `10.1093/mnras/staa913`

Privon, G. C., Barnes, J. E., Evans, A. S., et al. 2013, Astrophysical Journal, 771, doi: `10.1088/0004-637X/771/2/120`

Raskutti, S., Ostriker, E. C., & Skinner, M. A. 2016, The Astrophysical Journal, 829, 130, doi: `10.3847/0004-637X/829/2/130`

Renaud, F., Boily, C. M., Naab, T., & Theis, C. 2009, Astrophysical Journal, 706, 67, doi: `10.1088/0004-637X/706/1/67`

Renaud, F., Bournaud, F., Agertz, O., et al. 2019a, Astronomy & Astrophysics, 625, A65, doi: `10.1051/0004-6361/201935222`

Renaud, F., Bournaud, F., Daddi, E., & Weiß, A. 2019b, Astronomy & Astrophysics, Volume 621, id.A104, <NUMPAGES>5</NUMPAGES> pp., 621, A104, doi: `10.1051/0004-6361/201834397`

Renaud, F., Bournaud, F., Kraljic, K., & Duc, P. A. 2014, Monthly Notices of the Royal Astronomical Society: Letters, 442, doi: `10.1093/mnrasl/slu050`

Rey, M. P., Agertz, O., Starkenburg, T. K., et al. 2022, VINTERGATAN-GM: The Cosmological Imprints of Early Mergers on Milky-Way-mass Galaxies

Rice, T. S., Goodman, A. A., Bergin, E. A., Beaumont, C., & Dame, T. M. 2016, The Astrophysical Journal, 822, 52, doi: `10.3847/0004-637X/822/1/52`

Rico-Villas, F., Martin-Pintado, J., Gonzalez-Alfonso, E., Martin, S., & Rivilla, V. M. 2020, Monthly Notices of the Royal Astronomical Society, 491, 4573, doi: `10.1093/mnras/stz3347`

Robertson, B., Bullock, J. S., Cox, T. J., et al. 2006, The Astrophysical Journal, 645, 986, doi: `10.1086/504412`

Rodríguez Montero, F., Davé, R., Wild, V., Anglés-Alcázar, D., & Narayanan, D. 2019, Monthly Notices of the Royal Astronomical Society, 490, 2139, doi: `10.1093/mnras/stz2580`

Roman-Duval, J., Jackson, J. M., Heyer, M., Rathborne, J., & Simon, R. 2010, The Astrophysical Journal, 723, 492, doi: `10.1088/0004-637X/723/1/492`

Rosolowsky, E., Hughes, A., Leroy, A. K., et al. 2021, Monthly Notices of the Royal Astronomical Society, 502, 1218, doi: `10.1093/mnras/stab085`

Sakamoto, K., Aalto, S., Combes, F., Evans, A., & Peck, A. 2014, The Astrophysical Journal, 797, 90, doi: `10.1088/0004-637X/797/2/90`

Sánchez-García, M., Pereira-Santaella, M., García-Burillo, S., et al. 2022, Astronomy & Astrophysics, Volume 659, id.A102, <NUMPAGES>20</NUMPAGES> pp., 659, A102, doi: `10.1051/0004-6361/202141963`

Sargent, M. T., Daddi, E., Béthermin, M., et al. 2014, Astrophysical Journal, 793, doi: `10.1088/0004-637X/793/1/19`

Sawala, T., Frenk, C. S., Fattahi, A., et al. 2014, Local Group Galaxies Emerge from the Dark

Schirm, M. R. P., Wilson, C. D., Parkin, T. J., et al. 2014, The Astrophysical Journal, 781, 101, doi: `10.1088/0004-637X/781/2/101`

Schruba, A., Kruijssen, J. M. D., & Leroy, A. K. 2019, The Astrophysical Journal, 883, 2, doi: `10.3847/1538-4357/ab3a43`

Scudder, J. M., Ellison, S. L., Momjian, E., et al. 2015, Monthly Notices of the Royal Astronomical Society, 449, 3719, doi: `10.1093/mnras/stv588`

Seillé, L. M., Buat, V., Haddad, W., et al. 2022, Spatial Disconnection between Stellar and Dust Emissions: The Test of the Antennae Galaxies (Arp 244)

Sick, J., Courteau, S., Cuillandre, J.-C., et al. 2015, 311, 82, doi: `10.1017/S1743921315003440`

Smith, M. C., Bryan, G. L., Somerville, R. S., et al. 2021, Monthly Notices of the Royal Astronomical Society, 506, 3882, doi: `10.1093/mnras/stab1896`

Sun, J., Leroy, A. K., Schruba, A., et al. 2018, The Astrophysical Journal, 860, 172, doi: `10.3847/1538-4357/aac326`

Sun, J., Leroy, A. K., Schinnerer, E., et al. 2020, ApJL, 901, L8, doi: `10.3847/2041-8213/abb3be`

Sun, J., Leroy, A. K., Rosolowsky, E., et al. 2022, The Astronomical Journal, 164, 43, doi: `10.3847/1538-3881/ac74bd`

Teyssier, R., Chapon, D., & Bournaud, F. 2010, Astrophysical Journal Letters, 720, 149, doi: `10.1088/2041-8205/720/2/L149`

Thorp, M. D., Ellison, S. L., Pan, H.-A., et al. 2022, Monthly Notices of the Royal Astronomical Society, 516, 1462, doi: `10.1093/mnras/stac2288`

Tosaki, T., Kohno, K., Harada, N., et al. 2017, Publications of the Astronomical Society of Japan, 69, 18, doi: `10.1093/pasj/psw122`

Ueda, J., Iono, D., Petitpas, G., et al. 2012, The Astrophysical Journal, 745, 65, doi: `10.1088/0004-637X/745/1/65`

Wei, L. H., Keto, E., & Ho, L. C. 2012, The Astrophysical Journal, 750, 136, doi: `10.1088/0004-637X/750/2/136`

Whitmore, B. C., Brogan, C., Chandar, R., et al. 2014, ApJ, 795, 156, doi: `10.1088/0004-637X/795/2/156`

Wilson, C. D., Elmegreen, B. G., Bemis, A., & Brunetti, N. 2019, The Astrophysical Journal, 882, 5, doi: `10.3847/1538-4357/ab31f3`

Wilson, C. D., Scoville, N., Madden, S. C., & Charmandaris, V. 2000, The Astrophysical Journal, 542, 120, doi: `10.1086/309504`

Zhang, Q., Fall, S. M., & Whitmore, B. C. 2001, Observatory, 10

Zhu, M., Seaquist, E. R., & Kuno, N. 2003, The Astrophysical Journal, 588, 243, doi: `10.1086/368353`

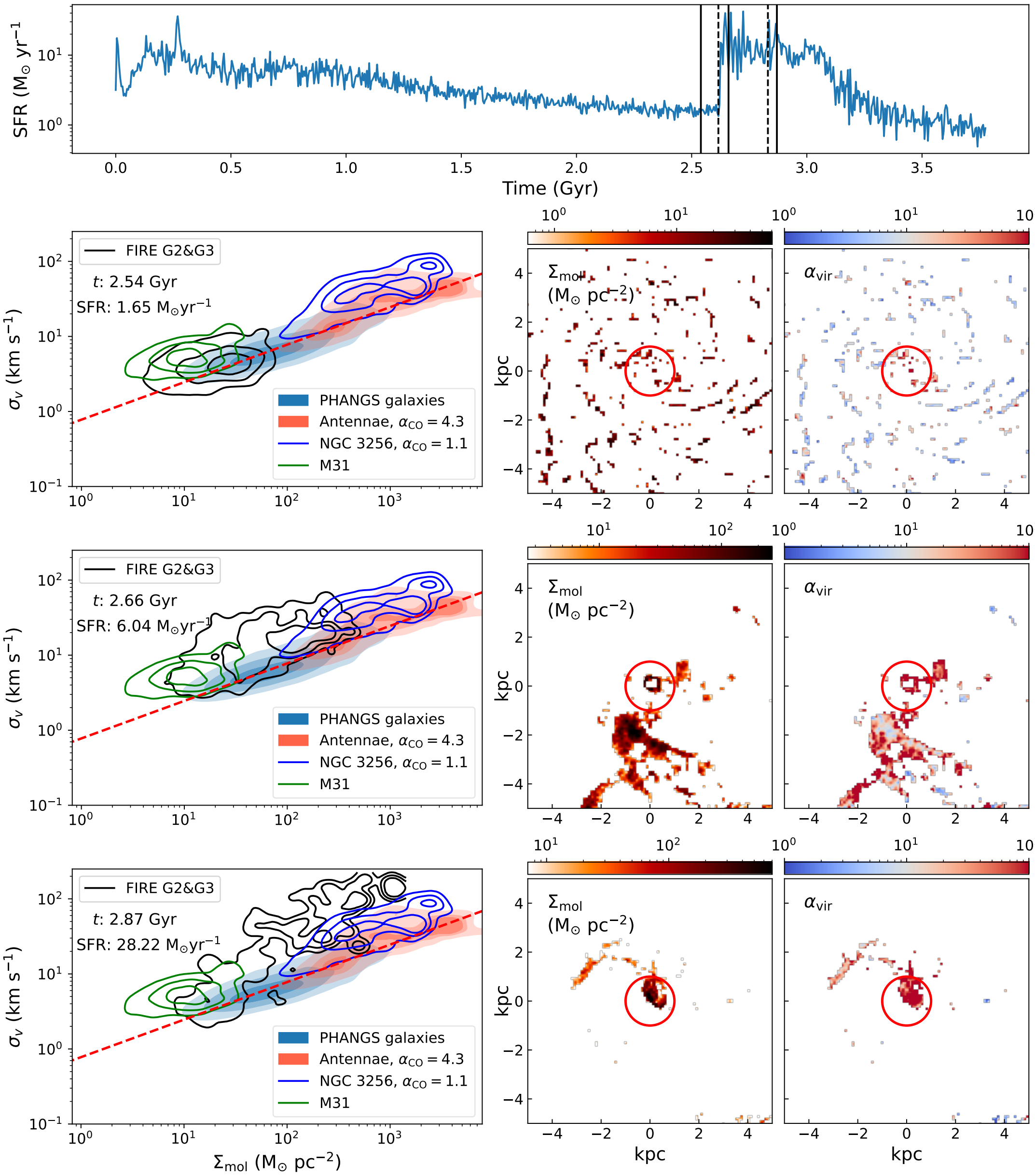

Figure 3.2: (*Top*) SFR history for the G2&G3 merger with 'e2' orbit with viewing angle of 'v0'. The 3 solid black vertical lines indicate the time for each snapshot displayed below. The two dashed lines indicate the times at the start of second merging and the final coalesce of two nuclei. (*Bottom*) Three snapshots. For each snapshot, the left panel shows the σ_v versus $\Sigma_{\rm mol}$ mass-weighted contour with the same setting as Fig. 3.1. The right two panels show the $\Sigma_{\rm mol}$ and $\alpha_{\rm vir}$ maps of inner 5 kpc regions where we have most of our detected pixels. We can see that the properties of the GMCs right before the second passage still resemble those of normal spiral galaxies, while GMCs after the second passage lie above the PHANGS trend in the σ_v vs $\Sigma_{\rm mol}$ plot and show significantly higher $\alpha_{\rm vir}$.

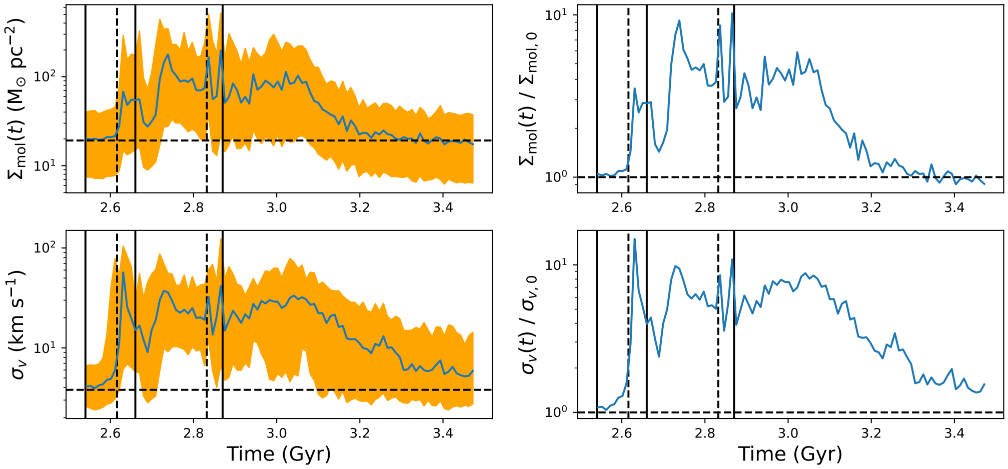

Figure 3.3: The $\Sigma_{\rm mol}$ and σ_v variation across the second passage and final coalescence of the G2&G3 merger at 'e2' orbit with viewing angle of 'v0'. The two dashed vertical lines indicate the times when the simulated merger begin the second passage and experience final coalescence. The three solid vertical lines correspond to the 3 snapshots shown in Fig, 3.2. The horizontal dashed lines indicate the median value of the isolated G3 galaxy at time of 0.625 Gyr (Fig. 3.1) as a baseline for comparison. (*Upper left*) $\Sigma_{\rm mol}$ vs time. Blue lines shows the mass weighted median $\Sigma_{\rm mol}$ of the entire merger while the orange filled area indicates $\Sigma_{\rm mol}$ range between 16th and 84th percentile. The two dashed lines indicate the time for the start of the second passage and the final coalesce of the two nuclei. (*Upper right*) The ratio between median $\Sigma_{\rm mol}$ at given time and the median value $\Sigma_{\rm mol,0}$ for the isolated G3 galaxy at 0.625 Gyr. (*Lower left*) The mass-weighted median σ_v versus time. (*Lower right*) The ratio between the median σ_v and the value $\sigma_{v,0}$ for isolated G3 galaxies at 0.625 Gyr. We can see both $\Sigma_{\rm mol}$ and σ_v increase dramatically during the second passage when the extreme starburst happens.

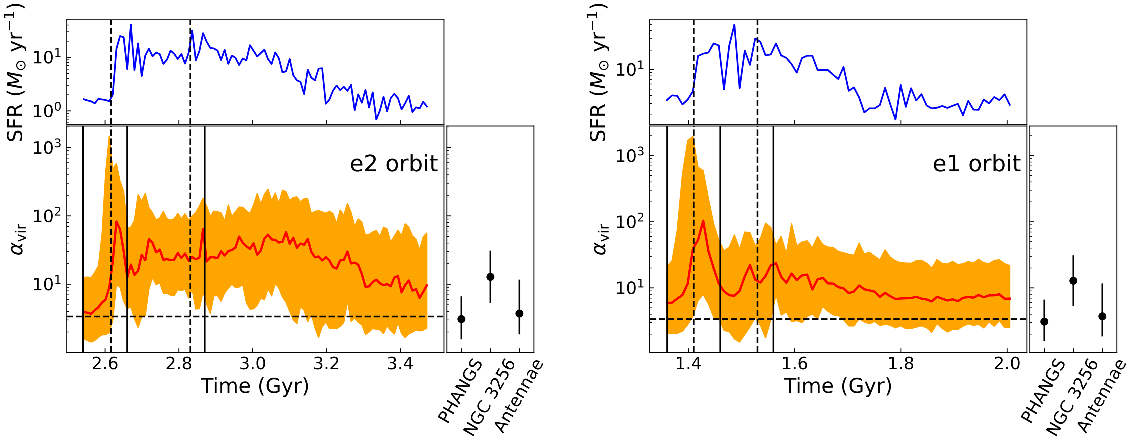

Figure 3.4: $\alpha_{\rm vir}$ versus time for the G2&G3 mergers in (left) the e2 orbit and (right) the e1 orbit viewed from 'v0' angle during the final coalescence. (*Left*) The red line is the mass-weighted median for $\alpha_{\rm vir}$ from the simulation. The orange shaded region includes data within the 16th and 84th quantile of $\alpha_{\rm vir}$ values. The dashed lines correspond to the start of the second passage and the final coalescence of the two nuclei. The three solid lines correspond to the merger times shown in Fig. 3.2. The horizontal dashed line indicates the median $\alpha_{\rm vir}$ for the isolated G3 galaxy at 0.625 Gyr (Fig . 3.1) as a baseline for comparison. The upper panel shows SFR versus time for the second coalescence and the right panel shows the 16th, 50th and 84th quantile of $\alpha_{\rm vir}$ for PHANGS, NGC 3256 and the Antennae from the observations. In calculating $\alpha_{\rm vir}$, we use the U/LIRG $\alpha_{\rm CO}$ for NGC 3256 and the Milky Way value for PHANGS and the Antennae. (*Right*) Same plot for G2&G3 merger in the 'e1' orbit during the final coalescence. The 3 solid lines correspond to 3 snapshots in Fig. 3.2. The 'e1' orbit has a smaller impact parameter than the 'e2' orbit. We can see the global $\alpha_{\rm vir}$ increases dramatically right after the second passage as SFR rises. The peak SFR also roughly corresponds with the peak $\alpha_{\rm vir}$, which suggests the high $\alpha_{\rm vir}$ might be caused by the feedback from the starburst.

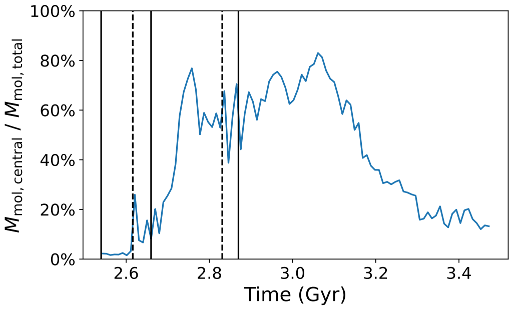

Figure 3.5: The ratio between molecular gas mass within the central 1 kpc radius circle of the G3 galaxy and total molecular gas inside our FOV of 25 kpc. During the second coalescence between 2.7 Gyr and 3.2 Gyr, more than 50% of molecular gas is concentrated within the central 1 kpc region, which indicates the $\Sigma_{\rm mol}$ increase we see in the simulated merger during the second passage is probably due to this gas concentration.

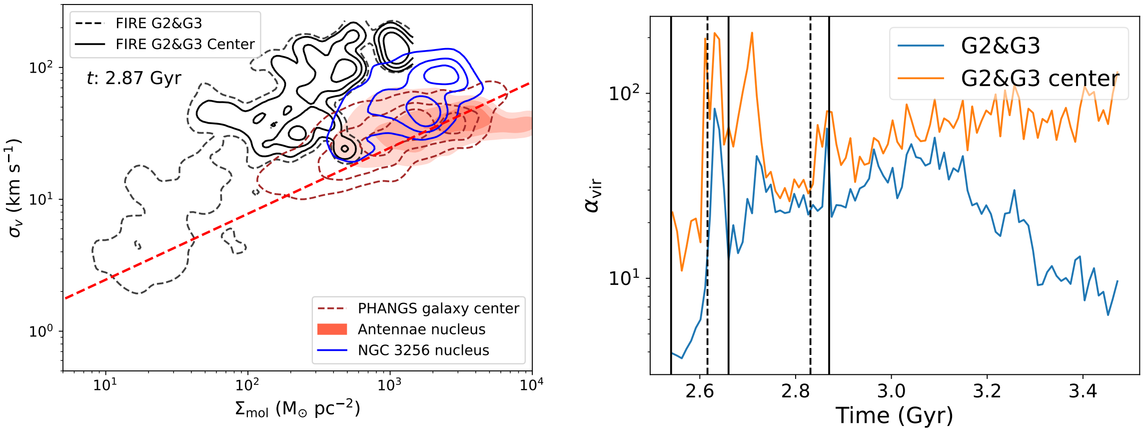

Figure 3.6: (*Left*) The σ_v versus $\Sigma_{\rm mol}$ contour for the entire (dashed contour) and central 1 kpc region (solid contour) of the G2&G3 merger at 2.87 Gyr viewed from the 'v0' angle. We also show contours for the centers of PHANGS galaxies (brown dashed contours), the Antennae (orange shaded contours) and NGC 3256 (blue contours). We can see the central region in our simulated merger generally has the highest σ_v and $\alpha_{\rm vir}$. (*Right*) The mass weighted median $\alpha_{\rm vir}$ for molecular gas in the entire (blue) and central (orange) region of G2&G3 merger viewed from 'v0' angle. We see that $\alpha_{\rm vir}$ for the entire disk gradually settles back to the original low value, while that for the central region keeps a high value until the end of the simulation.

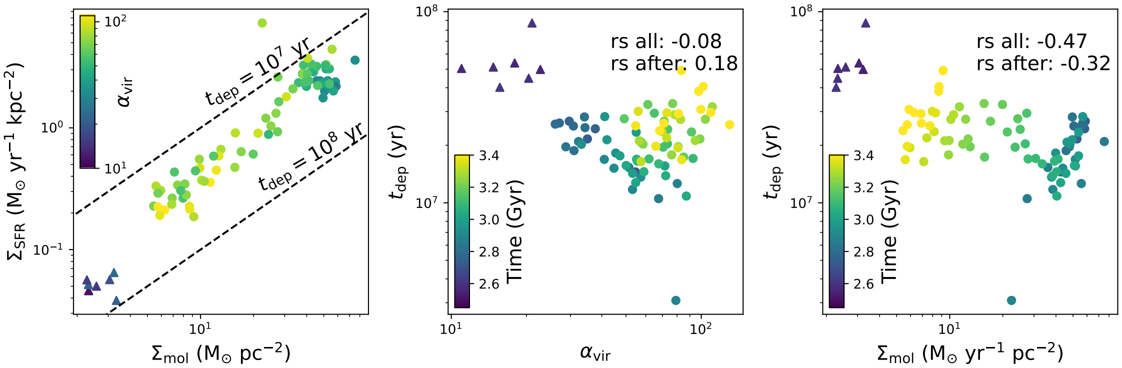

Figure 3.7: (*Left*) SFR surface density $\Sigma_{\rm SFR}$ versus $\Sigma_{\rm mol}$ color coded by the mass-weighted median $\alpha_{\rm vir}$ for the central 1 kpc region of the the G2&G3 merger during the second passage of the 'e2' orbit viewed from 'v0' orientation. We include simulated data points within 2.54 – 2.61 Gyr (before the second passage; trangle) and 2.73 – 3.47 Gyr (after the second passage; circle). Both $\Sigma_{\rm SFR}$ and $\Sigma_{\rm mol}$ are calculated as total central SFR or $M_{\rm mol}$ within 1 kpc radius divided by the aperture size, while $\alpha_{\rm vir}$ is the mass weighted median of pixels inside the aperture. The two dashed line indicate constant depletion times ($t_{\rm dep} = \Sigma_{\rm mol}/\Sigma_{\rm SFR}$) of 10^7 and 10^8 years. (*Middle*) $t_{\rm dep}$ versus $\alpha_{\rm vir}$ for the central 1 kpc. (*Right*) $t_{\rm dep}$ versus $\Sigma_{\rm mol}$ for the central region. The label "rs all" shows the Spearman coefficient between $t_{\rm dep}$ and $\alpha_{\rm vir}$ and $\Sigma_{\rm mol}$ for all data points while "rs after" shows the Spearman coefficient only for data after the second passage. We can see there is no significant correlation between $\alpha_{\rm vir}$ and $t_{\rm dep}$, which is against our expectation that low $\alpha_{\rm vir}$ clouds will consume molecular gas at faster rate.

Chapter 4

Constraining Spatial Variation of CO-to-H_2 Conversion Factor in the Antennae

The content of this chapter is a draft manuscript to be submitted to ApJ.

Constraining Spatial Variation of CO-to-H_2 Conversion Factor in the Antennae

Abstract

CO line emission has been widely used as a tracer of molecular gas mass. However, it has been a long-standing issue to accurately constrain the CO-to-H2 conversion factor (α_{CO}) that transforms CO luminosity to molecular gas mass, especially in starburst galaxy mergers. We present the first resolved α_{CO} modeling results with multiple ALMA CO and ^{13}CO observations at both giant molecular cloud (GMC) and kpc scales for one of the closest starburst mergers, the Antennae. By combining our CO modeling results and dust continuum measurements, we find that most GMCs in the Antennae have α_{CO} values $\sim$ 4 times smaller than the commonly adopted Milky Way value of 4.3. We find α_{CO} at GMC scales shows a strong dependence on CO intensity, ^{13}CO/CO ratio and GMC virial parameter, which is consistent with various theoretical and simulation predictions. Specifically, we suggest that ^{13}CO/CO ratio and the virial parameter can be used to calibrate α_{CO} in starburst regions. By applying our modeled α_{CO} to the GMC surface density calculation, we find that GMCs in the Antennae are less gravitationally bound than in normal spiral galaxies, which is more consistent with GMC dynamical states predicted by merger simulations. At kpc scale, we find that our modeled α_{CO} values are consistent with those at GMC scales, which is consistent with theory predictions that α_{CO} is a scale-free parameter. We also find a similar correlation of α_{CO} and CO intensity at kpc scale to that at GMC scale. We further explore the metallicity dependence of α_{CO} at kpc scale and find no significant correlation, which is probably due to limited metallicity range of the Antennae.

Keywords: *Molecular gas (1073), Molecular clouds (1072), CO line emission (262), Starburst galaxies (1570), Galaxy mergers (608)*

4.1 Introduction

The cold and dense molecular gas in the interstellar medium (ISM) is the direct fuel for current and future star formation. Measuring the amount and properties of the molecular gas is crucial for understanding star formation, the ISM, and their relations with galaxy evolution. Although H_2 is the dominant component of molecular gas, it is not normally observable due to the high excitation temperature ($T_{\rm ex}$) of its lines. Instead, the CO J=1-0 line (hereafter ^{12}CO J=1-0) is the most commonly used tracer for measuring the molecular gas mass via the CO-to-H2 conversion factor $\alpha_{\rm CO}$. This $\alpha_{\rm CO}$ is commonly defined for the J = 1-0 line as the ratio of total molecular gas to ($M_{\rm mol}$ in $\rm M_\odot$) to the ^{12}CO J=1-0 luminosity ($L_{\rm CO(1-0)}$ in K km s^{-1} pc^2) , or equivalently, the ratio of molecular gas surface density ($\Sigma_{\rm mol}$ in $\rm M_\odot$ pc^{-2}) to the ^{12}CO J=1-0 intensity ($I_{\rm CO(1-0)}$ in K km s^{-1}):

$$\alpha_{\rm CO} = \frac{M_{\rm mol}}{L_{\rm CO(1-0)}} = \frac{\Sigma_{\rm mol}}{I_{\rm CO(1-0)}} \left[\frac{\rm M_\odot}{\rm K\ km\ s^{-1}}\right] \tag{4.1}$$

Given that CO is so straightforwardly observable, a concrete prescription for $\alpha_{\rm CO}$ as a function of local ISM properties has been a longstanding goal.

$\alpha_{\rm CO}$ was first calibrated for individual giant molecular clouds (GMCs) in our Milky Way based on virial methods (e.g. Solomon et al. 1987; Scoville et al. 1987; Scoville & Good 1989; Maloney 1990; Young & Scoville 1991), optically thin tracers such as dust continuum (Boulanger et al. 1996; Dame et al. 2001; Planck Collaboration et al. 2011), CO isotopologue lines (Goldsmith et al. 2008) and gamma-ray observations (e.g. Strong & Mattox 1996; Grenier et al. 2005; Abdo et al. 2010). These studies found a relatively constant $\alpha_{\rm CO}$ around 4.3 $\rm M_\odot$ (K km s^{-1} pc^2)$^{-1}$ (Bolatto et al. 2013, and references therein) with scatter of 0.3 dex. However, systematic variations of $\alpha_{\rm CO}$ have been found in the Milky Way, specifically for GMCs in the central molecular zone (CMZs) where $\alpha_{\rm CO}$ can be 3 – 10 times lower than the average value (Bolatto et al. 2013, and references therein). Furthermore, extra-galactic observations have found systematic variations of $\alpha_{\rm CO}$ up to one or two orders of magnitude across different galactic environments (e.g. Bolatto et al. 2008; Donovan Meyer et al. 2012; Rebolledo et al. 2012; Sandstrom et al. 2013). This issue is further complicated by the fact that different calibration methods can lead to vastly discrepant estimates of $\alpha_{\rm CO}$ values (e.g. SMC Bolatto et al. 2003; Leroy et al. 2011). Therefore, assuming a constant $\alpha_{\rm CO}$

can introduce systematic bias in calculating molecular gas mass and surface density and related quantities, such as molecular gas depletion time, the cloud free-fall time, the virial parameter and the turbulent pressure (Sun et al. 2022, 2023).

Theoretical models and simulations suggest that $\alpha_{\rm CO}$ can be dependent on both small-scale GMC properties, such as temperature, volume and surface density (Gong et al. 2020, and references therein), and kpc-scale environmental properties, such as metallicity, galactic disk surface density and velocity dispersion (e.g. Wolfire et al. 2010; Narayanan et al. 2012; Kazandjian et al. 2015; Renaud et al. 2019a; Gong et al. 2020; Hu et al. 2022). Recently, a lot of progress has been made in calibrating metallicity dependence of $\alpha_{\rm CO}$ (e.g. Schruba et al. 2012; Amorín et al. 2016; Accurso et al. 2017), which has been applied to several recent works (e.g. Sun et al. 2020a,b; Pessa et al. 2021; Sun et al. 2023). However, we still lack a general $\alpha_{\rm CO}$ prescription that incorporates all the related physical quantities at different scales.

In particular, $\alpha_{\rm CO}$ in starburst systems, such as ultra/ luminous infrared galaxies (U/LIRGs), is poorly constrained. Early studies (e.g. Downes et al. 1993; Bryant & Scoville 1996, 1999; Solomon et al. 1997; Downes & Solomon 1998) find that $\alpha_{\rm CO}$ in U/LIRGs generally needs to be ~ 4 times lower than the Milky Way value to give a reasonable molecular gas mass values within the dynamical mass range. Studies on a large sample of U/LIRGs using multi-CO line large velocity gradient (LVG) radiative transfer modeling (e.g. Solomon & Vanden Bout 2005; Downes & Solomon 1998; Papadopoulos et al. 2012) find consistent average $\alpha_{\rm CO}$ values around $1.1\ {\rm M}_\odot\ ({\rm K\ km\ s^{-1}\ pc^2})^{-1}$ (Downes & Solomon 1998, with helium contribution). Therefore, a discrete bimodal $\alpha_{\rm CO}$ prescription or a modified version accounting for the deviation from the star-forming main sequence (e.g. Magnelli et al. 2012; Sargent et al. 2014) is generally applied in observed normal spiral and starburst galaxies. However, there is likely a large galaxy-to-galaxy $\alpha_{\rm CO}$ variation for different U/LIRGs (Papadopoulos et al. 2012; Sliwa et al. 2017a; Carleton et al. 2017), which is not captured by those $\alpha_{\rm CO}$ prescriptions. This problem is further complicated by recent works using optically thin tracers (e.g. Dunne et al. 2022), which suggest a Milky-Way like $\alpha_{\rm CO}$ value for these U/LIRGs.

Besides galaxy-to-galaxy variation, theoretical works (Narayanan et al. 2012; Bolatto et al. 2013) also suggest that $\alpha_{\rm CO}$ could vary within galaxies depending on the local environment. Therefore, it is crucial to understand the physical driver of the low $\alpha_{\rm CO}$ in these starburst systems. Narayanan et al. (2011) suggest that the low

$\alpha_{\rm CO}$ is caused by the increase in GMC temperature (partly through thermal coupling with dust heated by UV radiation Magnelli et al. 2012; Olsen et al. 2016) and/or velocity dispersion (out of self-gravity Papadopoulos et al. 2012), which makes CO emission over-luminous. Recent galaxy merger observations (e.g. Papadopoulos et al. 2012) and simulations (e.g. Bournaud et al. 2015) seem to favor the increase in velocity dispersion to play the major role. However, Renaud et al. (2019b) show in their simulation the $\alpha_{\rm CO}$ is not a sole function of velocity dispersion and is also dependent on different merging stages. To disentangle these factors, it is crucial to constrain the GMC physical properties and dynamical states in observed starburst mergers among different stages.

In order to diagnose GMCs physical states and reasons for $\alpha_{\rm CO}$ variation, it is necessary to observe multiple CO and other molecular lines (specifically optically thin lines) at GMC resolution ($\sim$ 100 pc) to perform comprehensive LVG modeling. However, due to the limited sensitivity and resolution of current instruments, most LVG studies on individual starburst mergers (e.g. Papadopoulos et al. 2012; Sliwa et al. 2012, 2013, 2014; He et al. 2020) can only probe a limited number of gas-rich regions at kpc resolution, making it hard to extract any $\alpha_{\rm CO}$ dependence on GMC properties and local environments. As one of the closest starburst mergers, NGC 4038/9 (the Antennae) is an ideal target for this study. At a distance of 22 Mpc (Schweizer et al. 2008), ALMA can readily resolve molecular gas at GMC scales. The total SFR of the Antennae is between 11 $\rm M_\odot yr^{-1}$ (estimated from UV and 24 µm probing $\sim$ 1 to 400 Myr Bemis & Wilson 2019) and 20 $\rm M_\odot yr^{-1}$ (estimated from extinction corrected Hα probing $\sim$ 1 to 10 Myr Chandar et al. 2017). Although the Antennae is technically not a LIRG based on its total infrared luminosity, the higher SFR value traced by Hα is comparable to those of LIRGs, which suggests a starburst event that was just triggered recently several tens of Myr ago. As a typical major merger between two gas-rich galaxies, the Antennae has been well-studied in both simulations and observations. Most simulations (e.g. Karl et al. 2010; Privon et al. 2013; Renaud et al. 2019a) suggest that the Antennae has just passed its second pericentric passage $\sim$ 40 Myr ago. Its central region hosts the two progenitor nuclei, still separated by about 7 kpc (Zhang et al. 2001). As a starburst merger, it also hosts a large number ($\sim 10^4$) of young massive star clusters exceeding 10^4 $\rm M_\odot$, with maximal mass reaching 10^6 $\rm M_\odot$ (Whitmore et al. 2014; Mok et al. 2020; He et al. 2022). The extreme number of YMCs will provide much stronger stellar feedback

(Keller et al. 2014) that will disperse molecular gas and significantly reduce the α_{CO} values (Renaud et al. 2019a).

In this paper, we perform LVG modeling on high-resolution ($\sim$ 150 pc) CO and ^{13}CO molecular lines from ALMA observations of the Antennae to constrain the physical properties of the molecular gas and α_{CO} at both GMC and kpc scales. In Section 2, we describe the observations and how we processed the data. In Section 3, we describe the RADEX modeling method that we used to derive gas physical quantities (e.g. temperature, volume density and CO column density) and α_{CO}. In Section 4, we present our modeled gas physical properties (e.g. kinetic temperature, volume density and CO column density) and their connection with different line ratios. In Section 5, we present our modeled α_{CO} at GMC scale and compare its dependence on various GMC observational and physical quantities with theoretical and simulation predictions. We also apply our modeled α_{CO} in calculation of GMC surface density and virial equilibrium states. In Section 6, we present modeled α_{CO} at kpc scales and its comparison with α_{CO} at GMC scales. We also explore α_{CO} dependence on kpc-scale gas properties (e.g. gas surface density, velocity dispersion and metallicity). The conclusions are summarized in Section 7.

4.2 Observations and Data Processing

4.2.1 ALMA Spectral Lines

Table 4.1: ALMA CO data products

Lines (1)	ALMA Band (2)	Native Resolution (3)	LAS (4)	Velocity Resolution (5)	$\mathrm{RMS_{native}}$ (6)	$\mathrm{RMS_{150pc}}$ (7)
^{12}CO J=1-0	3	0.84″, 90 pc	14.5′, 93 kpc	2.54 km $\mathrm{s^{-1}}$	0.09 K	0.05 K
^{12}CO J=2-1	6	0.51″, 54 pc	6.9′, 44 kpc	2.54 km $\mathrm{s^{-1}}$	0.24 K	0.11 K
^{12}CO J=3-2	7	0.67″, 71 pc	4.5′, 29 kpc	3.4 km $\mathrm{s^{-1}}$	0.09 K	0.04 K
^{13}CO J=1-0	3	1.41″, 150 pc	15′, 96 kpc	2.7 km $\mathrm{s^{-1}}$	0.04 K	0.04 K
^{13}CO J=2-1	6	0.71″, 76 pc	6.9′, 44 kpc	5.3 km $\mathrm{s^{-1}}$	0.09 K	0.04 K

Columns: (1) CO spectral lines. (2) ALMA observing frequency bands (3) Native resolution for the smallest round beam. (4) Largest angular scale. (5) Velocity resolution. (6) Noise of the image cubes at the native resolution (7) Noise of the image cubes after smoothing to the resolution of 150 pc.

We use multiple CO lines (^{12}CO J=1-0, 2-1, 3-2 and ^{13}CO J=1-0, 2-1) from the Atacama Large Millimeter/Submillimeter Array (ALMA) to determine the physical properties of the gas in the Antennae at 150 pc scale. We obtained ALMA Band 3, 6 and 7 observations from cycle 5 project 2018.1.00272.S and cycle 8 project 2021.00439.S to capture multiple CO and ^{13}CO lines to perform the RADEX modeling. Our Band 3 observations on ^{12}CO J=1-0 (from project 2018.1.00272.S) employ configurations of C43-5, C43-2 and ACA, which cover scales from 870 arcsec down to 0.55 arcsec. The spectral resolution is 2.54 km s^{-1}. Our Band 3 observations on ^{13}CO J=1-0 (from project 2021.1.00439.S) employ configurations of C43-4, C43-1 and ACA, which cover scales from 900 arcsec down to 1 arcsec. The spectral resolution is 2.7 km s^{-1}. We also observed C^{18}O J=1-0 in the same frequency tuning. Our Band 6 observations on CO and ^{13}CO J=2-1 (from project 2021.1.00439.S) employ configurations of C43-4, C43-1 and ACA, which covers spatial scales from 415 arcsec down to 0.26 arcsec. The spectral resolution is 2.54 km s^{-1} We also observed C^{18}O J=2-1 in the same spectral tuning. Our Band 7 observations on ^{12}CO J=3-2 (from project 2021.1.00439.S) employ configurations C43-5 and ACA, which cover spatial scales from 270 arcsec down to 0.37 arcsec. The velocity resolution is 3.4 km s^{-1}. A summary of the data information is in Table 1.

We calibrate the raw visibility data with the observatory-supplied calibration scripts and the appropriate version of the CASA pipeline. From the calibrated measurement sets, we extract and image a relevant subset of visibility data for each molecular line using a modified version of the PHANGS–ALMA imaging pipeline (Leroy et al. 2021). Before imaging lines, we performed continuum subtraction by subtracting the 1st-order fit modeling on line-free channels. We then combine the 12m and 7m measurement set together and perform the imaging. The imaging steps generally follow the PHANGS imaging scheme (Leroy et al. 2021). We first run a shallow, multi-scale cleaning to pick up regions with S/N of 4 detection. We then run a deep single-scale cleaning down to the threshold of 2 × RMS. The single-scale cleaning is restricted to regions that are picked out in the multi-scale cleaning. For the weighting of the visibility data, we adopt the the *Briggs* method with robustness parameter of 0.5. After the cleaning, we then feather the cleaned image product with TP data and apply the primary beam correction to get final image cubes for each line. We also smooth all the images to the smallest round beam. In the final step, we convert all the image cubes to units of Kelvin (K).

We then perform post-processing steps to homogenize all 5 CO lines. We smooth all five image cubes to the resolution of 150 pc (1.41 arcsec) and match all their spatial grids to the ^{12}CO J=1-0 line. We then produced a set of moment maps and effective width (σ_v) maps for all five lines at this common resolution. Specifically, the effective width is measured as the ratio between moment 0 and moment 8 maps, which is

$$\sigma_v = \frac{I}{\sqrt{2\pi} T_{\rm peak}} \tag{4.2}$$

For a perfect Gaussian line profile, the effective width is identical to the traditionally used moment 2 measurements. We adopt this alternative method because it gives a better estimate on velocity dispersion within clouds, specifically if two or more clouds are along the same line of sight (see Heyer et al. 2001; Sun et al. 2018, for more details). To make moment maps, we start with generating masks adopting the scheme of the PHANGS-ALMA pipeline, which starts from a high-confidence mask including at least two consecutive channels with S/N above 5 and then expand the mask to include pixels with S/N above 2 for at least two consecutive channels. We run this scheme for each line and combine all the mask together to create a "combo" mask. We then apply this common "combo" mask to all the five line data cubes to make moment maps and their corresponding error maps. We also apply a S/N of 3 cut to the moment 0 maps of each line to exclude noisy pixels in weak line maps.In the final steps, we nyquist-sample the moment and effective width maps for all the lines to remove the spatial correlation between different pixels. Some representative moment maps are shown in Fig. 4.1 and 4.2.

4.2.2 ALMA continuum

We also make the ALMA Band 7 continuum image in order to calculate the dust and gas mass. After the calibration of the Band 7 data, we use the PHANGS-ALMA pipeline (Leroy et al. 2021) to combine the 12m and 7m measurement sets and extract the line-free channels from the combined measurement set for the continuum imaging. We also collapse each spectral window into a single channel in order speed up the continuum imaging process. We then use the `auto-multithresh` algorithm to clean the continuum data down to threshold of 2 × RMS. After imaging, we smooth the dust continuum map to the resolution of 150 pc and regrid the map to the nyquist-sampled CO images.

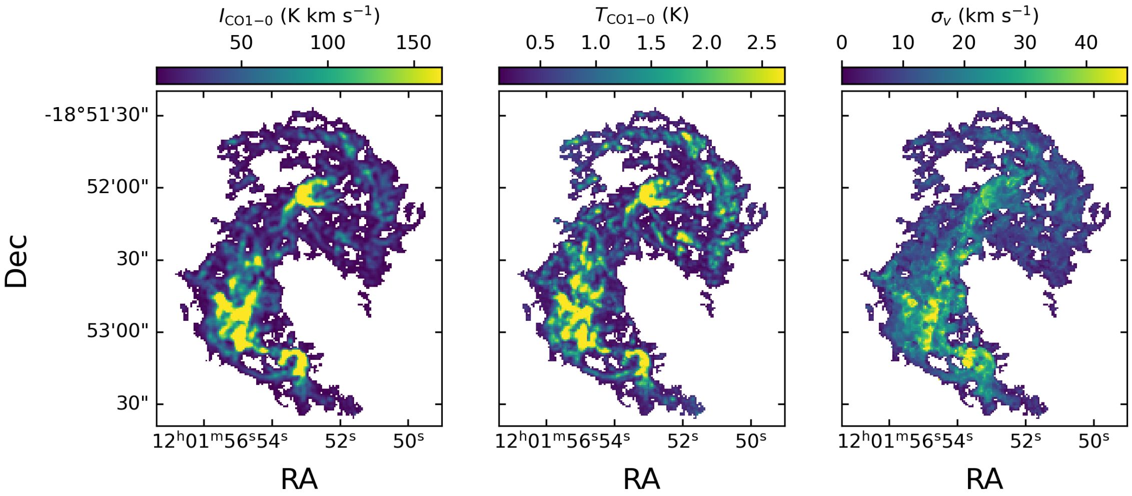

Figure 4.1: (*Left*) Integrated intensity, (*Middle*) peak brightness temperature and (*Right*) velocity dispersion of the ^{12}CO J=1-0 observations at 150 pc resolution.

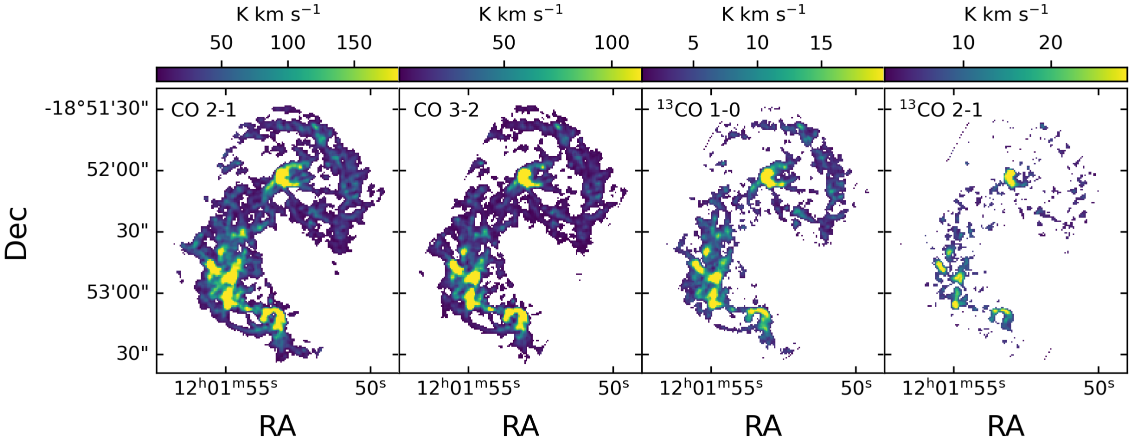

Figure 4.2: Integrated intensity maps for ^{12}CO J=2-1, 3-2 and ^{13}CO J=1-0 and 2-1 lines at 150 pc resolution. Pixels with S/N smaller than 3 are masked (see text).

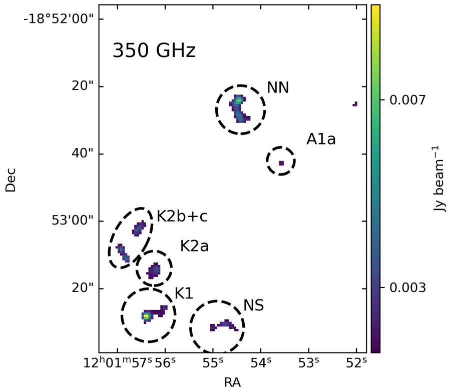

Figure 4.3: 350 GHz dust continuum map of the Antennae. Pixels with S/N < 4 are masked. Dashed circles corresponds to knots in the Herschel 70 μm map identified in Klaas et al. (2010).

4.3 RADEX Modeling

4.3.1 General Modeling Procedure

We adapt the code from Teng et al. (2022) to perform non-LTE radiative transfer modeling for each pixel with all five CO and ^{13}CO lines detected at 150 pc. We briefly summarize the code and our adaptation below (please refer to Teng et al. 2022, 2023, for more details). This code runs RADEX (Van Der Tak et al. 2007) modeling, which assumes a homogeneous medium and uses radiative transfer equations based on the escape probability formalism to find a converged solution for the excitation temperature and level population. We adopt the one-component RADEX modeling to generate 5D grids of integrated line intensities for the five lines under combinations of varying H$_2$ volume density (n), kinetic temperature ($T_{\rm kin}$), CO column density ($N_{^{12}\rm CO}$), CO/^{13}CO abundance ratio ($X_{12/13}$) and beam filling factor ($\Phi_{\rm bf}$). Note that the model assumes the same $\Phi_{\rm bf}$ for all 5 lines. We assume a linewidth Δv of 15 km s^{-1} ($\Delta v = 2.35\sigma_v$) in the modeling. Note that the radiative transfer calculation in RADEX (Van Der Tak et al. 2007) depends on $N_{\rm CO}/\Delta v$ instead of $N_{^{12}\rm CO}$ alone. Therefore, we can set an arbitrary Δv and then scale the modeled $N_{^{12}\rm CO}$ by multiplying the ratio between measured velocity dispersion and our adopted value of 15 km s^{-1}. We also assume the CO/H$_2$ abundance ratio ($x_{\rm co}$) of 3×10^{-4}. We will discuss our $x_{\rm co}$ choice in Section 4.5.2. Our input parameters are summarized in Table 2.

We then follow the Bayesian likelihood analyses in Teng et al. (2022) to characterize the probability density function (PDF) for the five varying parameters. For each

Table 4.2: RADEX Input Parameters

Parameter	Range	Step
log (n) (cm^{-3})	2 – 5.1	0.2
log ($T_{\rm kin}$) (K)	1 – 2.4	0.1
log ($N_{^{12}\rm CO}$) (cm^{-2})	16 – 21	0.2
$X_{12/13}$	10 – 400	10
$\Phi_{\rm bf}$	0.05 – 1	0.05
Δv (km s^{-1})	15	–
[CO]/[H$_2$]	3×10^{-4}	–

pixel, the code calculates the χ^2 by comparing the modeled line intensities with the measured line intensities. Note that in Teng et al. (2022), they compare modeled and measured integrated line intensities. This introduces the issue that the fixed velocity FWHM (15 km s^{-1}) in the modeling is inconsistent with varying velocity FWHMs measured for different pixels in the observations. Therefore, we rescale the measured intensity by the ratio of measured linewidth to the assumed linewidth of 15 km s^{-1}. Then we calculate the χ^2 matrix as

$$\chi^2(\vec{\theta}) = \sum_{i=1}^{N=5} \frac{I_i^{\rm mod}(\vec{\theta}) - I_i^{\rm obs,scaled}}{\sigma_i^2} \tag{4.3}$$

where $\vec{\theta}$ represents each modeled parameter set of $(n_{\rm H_2}, T_{\rm kin}, N_{\rm CO}/\Delta v, X_{12/13}, \Phi_{\rm bf})$, $I_i^{\rm mod}$ represents the modeled integrated intensity for each line and $I_i^{\rm obs,scaled} = I_i^{\rm obs}\frac{15{\rm kms}^{-1}}{\Delta v}$ represents the scaled integrated intensities from observations, σ_i the measurement uncertainty for $I_i^{\rm obs,scaled}$ of each line and N specify the number of lines used for the modeling. For each pixel value, we calculate the posterior probability distribution function across the 5D model parameter space as

$$P(\vec{\theta}|\vec{I}_{\rm obs}) = \frac{1}{Q}\exp(-\chi^2/2) \tag{4.4}$$

where $Q^2 = \prod_i 2\pi\sigma_i$ is the normalization coefficient. From the 5D distribution, we can calculate the 'Bestfit' set of modeled parameters with maximal $P(\vec{\theta}|\vec{I}_{\rm obs})$. We can also calculate the marginalized 1D probability distribution for each individual modeled parameter by integrating the 5D $P(\vec{\theta}|\vec{I}_{\rm obs})$ over the rest of parameter space.

Table 4.3: Solutions for the Modeled Parameter

Solution	Condition
Bestfit	$P(\vec{\theta}_{\mathrm{Bestfit}}\vert\vec{I}_{\mathrm{obs}}) = \max P(\vec{\theta}\vert\vec{I}_{\mathrm{obs}})$
1DMax	$P(\theta_{i,\mathrm{1DMax}}\vert\vec{I}_{\mathrm{obs}}) = \max P(\theta_i\vert\vec{I}_{\mathrm{obs}})$
Neg1Sig	$\int^{\theta_{i,\mathrm{Neg1Sig}}} d\theta_i P(\theta_i\vert\vec{I}_{\mathrm{obs}}) = 0.16$
Median	$\int^{\theta_{i,\mathrm{Median}}} d\theta_i P(\theta_i\vert\vec{I}_{\mathrm{obs}}) = 0.5$
Pos1Sig	$\int^{\theta_{i,\mathrm{Pos1Sig}}} d\theta_i P(\theta_i\vert\vec{I}_{\mathrm{obs}}) = 0.84$

The equation for the 1D marginalized distribution is

$$P(\theta_i|\vec{I}_{\mathrm{obs}}) = \underbrace{\int \cdots \int}_{j\neq i} d\theta_j P(\vec{\theta}|\vec{I}_{\mathrm{obs}}) \tag{4.5}$$

where θ_i is the one modeled parameter that we want to calculate the 1D marginalized distribution and θ_j are the rest of modeled parameters. From the 1D marginalized distribution, we can calculate the '1DMax' solution for each modeled parameter with largest $P(\theta_i|\vec{I}_{\mathrm{obs}})$. We can also calculate the 16th, 50th and 84th percentile of the cumulative 1D distributions as -1σ, median and +1σ values. We have summarized the statistical quantities from our modeling in Table 4.3.

4.3.2 Modeling of CO-to-H_2 conversion factor

The CO-to-H_2 conversion factor α_{CO} is calculated (Teng et al. 2022) as

$$\begin{aligned}\alpha_{\mathrm{CO}} &= \frac{\Sigma_{\mathrm{mol}}}{I_{\mathrm{CO(1-0)}}}\left[\frac{\mathrm{M}_\odot}{\mathrm{K\ km\ s^{-1}}}\right]\\ &= \frac{1.36 m_{\mathrm{H_2}} N_{\mathrm{CO}} \Phi_{\mathrm{bf}}}{x_{\mathrm{co}} I_{\mathrm{CO(1-0)}}}\\ &= \frac{1}{4.5\times10^{19}}\frac{N_{\mathrm{CO}}[\mathrm{cm^{-2}}]\Phi_{\mathrm{bf}}}{x_{\mathrm{co}} I_{\mathrm{CO(1-0)}}[\mathrm{K\ km\ s^{-1}}]},\end{aligned} \tag{4.6}$$

where x_{co} is the [CO]/[H_2] abundance ratio. This equation has the correction coefficient of 1.36 for helium contribution. This equation shows the key modeling parameters to constrain α_{CO} are the CO column density $N_{^{12}\mathrm{CO}}$, beam filling factor Φ_{bf} and [CO]/[H_2] abundance ratio. Therefore, we can calculate α_{CO} 1D distribution by summing up all the probabilities of parameters in 5D space that yield a given α_{CO}

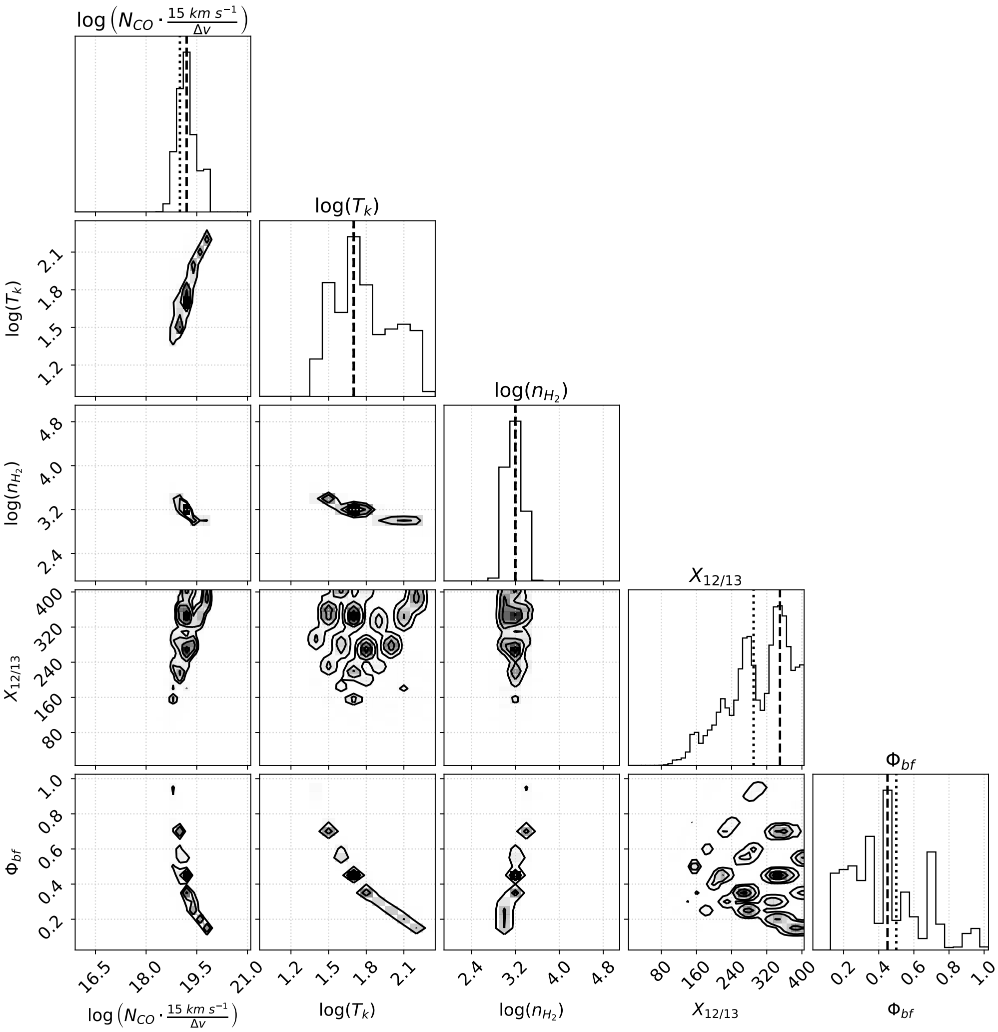

Figure 4.4: Corner plot of modeled RADEX physical properties for one pixel at the northern nuleius (pixel coordinates, (87, 138)). From the left to right is the scaled CO column density (cm^{-2}), kinetic temperature (K), hydrogen volume density (cm^{-3}), [CO]/[^{13}CO] abundance ratio and beam filling factor. The dashed and dotted lines mark the maximal and median of the 1D distribution for each quantity.

value, which is

$$\begin{aligned} P_{\rm biased}(\alpha_{\rm CO}|\vec{I}_{\rm obs}) &= P_{\rm biased}(\frac{N_{\rm CO}\Phi_{\rm bf}}{x_{\rm co}I^{\rm mod}_{\rm CO(1-0)}}|\vec{I}_{\rm obs}) \\ &= \int\limits_{f(\vec{\theta})=\alpha_{\rm CO}} d\vec{\theta}P(\vec{\theta}|\vec{I}_{\rm obs}) \end{aligned} \tag{4.7}$$

where $f(\vec{\theta}) \equiv \frac{N_{\rm CO}\Phi_{\rm bf}}{x_{\rm co}I^{\rm mod}_{\rm CO(1-0)}}$. However, we need to note that $\alpha_{\rm CO}$ is not uniformly sampled in our 5D parameter space. To get the unbiased PDF, we calculate the normalized ratio of our biased $\alpha_{\rm CO}$ probability to the $\alpha_{\rm CO}$ prior probability in our sampling space, which is

$$P(\alpha_{\rm CO}|\vec{I}_{\rm obs}) = \left[\frac{P_{\rm biased}(\alpha_{\rm CO}|\vec{I}_{\rm obs})}{P_{\rm prior}(\alpha_{\rm CO})}\right]_{\rm norm} \tag{4.8}$$

An example on the 3 $\alpha_{\rm CO}$ PDFs for one pixel is shown in Fig. 4.5.

Note that our derived $\alpha_{\rm CO}$ is dependent on our assumed $x_{\rm co}$ value. In Section 4.5.2, we will discuss reasonable $x_{\rm co}$ choice. The equation to convert our derived $\alpha_{\rm CO}$ to the real $\alpha_{\rm CO}$ with known $x_{\rm co}$ value is

$$\alpha^{\rm real}_{\rm CO} = \frac{3\times 10^{-4}}{x_{\rm CO}}\alpha^{\rm derived}_{\rm CO} \tag{4.9}$$

4.4 Modeled GMC physical properties

4.4.1 Line Ratios

The brightness temperature ratios of different lines can be used to probe differences in molecular gas properties among different regions. The line ratio maps are shown in Fig.4.6 and 4.7. For all the ratio maps, we apply a S/N > 3 cut to the ^{13}CO J=1-0 and 2-1 moment 0 maps to exclude pixels with ^{13}CO non-detections.

The ^{12}CO J=3-2/1-0 and ^{12}CO J=2-1/1-0 ratios are indicators of the CO excitation, which is directly related to the molecular gas temperature and/or volume density Leroy et al. (2017). Fig. 4.6 shows the two ratio maps along with their dependencies on ^{12}CO J=1-0 brightness temperature. We can see that the ^{12}CO J=2-1/1-0 ratio is generally uniform with values close to 1 across the entire molecular gas detected region. This uniformity suggests that both ^{12}CO J=1-0 and 2-1 are thermally excited,

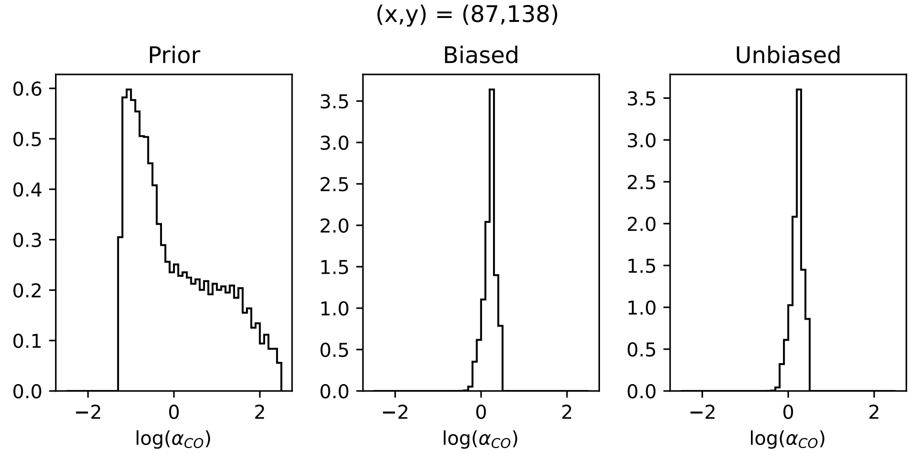

Figure 4.5: Marginalized $\alpha_{\rm CO}$ distribution. (*Left*) The prior distribution of $\alpha_{\rm CO}$ calculated by attributing uniform weighting to every set of parameters. (*Middle*) The histogram of $\alpha_{\rm CO}$ posterior distribution without sampling bias correction. (*Right*) The histogram of $\alpha_{\rm CO}$ posterior distribution after correcting for the sampling bias.

which generally holds for warm, dense and CO optically thick environments (Salak et al. 2019) that are typical in starburst systems (e.g. Sliwa et al. 2017b). Simulations also predict that the low-J CO lines are mostly thermalized for typical starburst mergers (e.g. Bournaud et al. 2015). The ^{12}CO J=2-1/1-0 ratio in the Antennae is also larger than those of normal spiral galaxies of $\sim$ 0.7 (Leroy et al. 2021), which is the commonly used ratio value to convert between ^{12}CO J=2-1 and ^{12}CO J=1-0 brightness temperature. On the other hand, this ratio value is consistent with what measured in starburst U/LIRGs (Montoya Arroyave et al. 2023). Since most GMC observations for starburst mergers (e.g. Brunetti et al. 2020; Brunetti & Wilson 2022) are done using ^{12}CO J=2-1 line due to its higher resolution and sensitivity, it is important to assume an appropriate ^{12}CO J=2-1/1-0 ratio for the gas mass calculation. Our study shows that a typical starburst merger should have ^{12}CO J=2-1/1-0 ratio values close to 1 instead of the commonly adopted 0.7.

On the other hand, the ^{12}CO J=3-2/1-0 ratio shows a clear spatial variation among different regions. In particular, the ratio is high in the gas concentrated regions, such as the two nuclei and the overlap region. We can also see a clear trend that the ^{12}CO J=3-2/1-0 ratio increases as the ^{12}CO J=1-0 intensity (or gas surface density) increases (Fig. 4.6, lower-right panel). This trend suggests that gas in these gas-concentrated regions is either denser and/or warmer than the rest of regions. The average ^{12}CO J=3-2/1-0 ratio is $\sim 0.4 - 0.7$ (Fig. 4.6, lower right panel), which is much higher than those of normal spiral galaxies of ~ 0.2 (e.g. NGLS survey, Wilson et al. 2012). Instead, this ratio value is close to that of the centers of normal spiral galaxies of ~ 0.8, such as M 31 (Li et al. 2020) and M 51 (Vlahakis et al. 2013), which suggests that the physical states of molecular gas in starburst systems are similar to that of central region of normal spiral galaxies. Compared to starburst U/LIRGs, our measured ratio is also slightly higher. Wilson et al. (2008) measured an average ^{12}CO J=3-2/1-0 ratio of 0.5 for a large sample of U/LIRGs, which generally have higher molecular gas and SFR surface density than the Antennae. A possible explanation is that we are probing much denser gas at GMC scales with ^{13}CO detections while the ratio measured in Wilson et al. (2008) is at kpc scales which can include a lot of diffuse gas where ^{12}CO J=3-2 is less excited. We also note there is a discrepancy between our measured ^{12}CO J=3-2/1-0 ratio and the literature values of 0.25 (Ueda et al. 2012; Bigiel et al. 2015) for the Antennae, which is probably due to the same resolution effect.

We also make ^{13}CO/^{12}CO J=1-0 and ^{13}CO/^{12}CO J=2-1 ratio maps for the Antennae (Fig. 4.7), which can be used to probe the [^{13}CO]/[CO] abundance ratio and the optical depth (e.g. Jiménez-Donaire et al. 2017). Due to CO being optically thick, it is hard to disentangle all these factors without comprehensive LVG modeling. To demonstrate this degeneracy, we first consider a simple case where both CO and ^{13}CO lines are thermally excited, which should not be far off from the real situation as discussed above. We use CO and ^{13}CO J=1-0 lines for the demonstration but we would expect this also applies to CO and ^{13}CO J=2-1 lines. Under the local thermal equilibrium (LTE) condition, we would expect the ^{13}CO/CO line ratio to be

$$\begin{aligned} R_{^{13}\mathrm{CO/CO1-0}} &= \frac{T^{\mathrm{peak}}_{^{13}\mathrm{CO1-0}}}{T^{\mathrm{peak}}_{\mathrm{CO1-0}}} \\ &= \frac{\Phi_{\mathrm{bf}} T_{\mathrm{kin}} \left[1-\exp(-\tau_{^{13}\mathrm{CO1-0}})\right]}{\Phi_{\mathrm{bf}} T_{\mathrm{kin}} \left[1-\exp(-\tau_{\mathrm{CO1-0}})\right]} \\ &\approx \tau_{^{13}\mathrm{CO1-0}}, \ (\tau_{^{13}\mathrm{CO1-0}} \ll 1 \ll \tau_{\mathrm{CO1-0}}) \end{aligned} \tag{4.10}$$

Since the ^{13}CO J=1-0 optical depth can be simply expressed as the ^{12}CO J=1-0 optical depth divided by the [CO]/[^{13}CO] abundance ratio ($X_{12/13}$), the ^{13}CO/^{12}CO

J=1-0 ratio can be further expressed as

$$R_{^{13}\mathrm{CO/CO1-0}} \approx \tau_{^{13}\mathrm{CO1-0}} = \tau_{\mathrm{CO1-0}}/X_{12/13} \qquad (4.11)$$

Therefore, if we observe a higher $R_{^{13}\mathrm{CO/CO1-0}}$, it can be either due to higher CO optical depth (and hence higher column density) and/or lower $X_{12/13}$ abundance ratio. We need to note that our simple derivation assumes both CO and ^{13}CO J=1-0 lines are thermally excited and share the same beam filling factor Φ_{bf}. In the real case, since ^{12}CO J=1-0 is generally optically thick while ^{13}CO J=1-0 is optically thin, the effective critical density of ^{12}CO J=1-0 is lower than that of ^{13}CO J=1-0 due to the line trapping effects. This will lead to lower beam filling factor and excitation temperature for ^{13}CO J=1-0 line and hence lower $R_{^{13}\mathrm{CO/CO1-0}}$ value, specifically for lower-density regions (Jiménez-Donaire et al. 2017, see detailed discussion in). Therefore, we would also expect higher $R_{^{13}\mathrm{CO/CO1-0}}$ in regions with higher gas volume density.

We can see both $R_{^{13}\mathrm{CO/CO1-0}}$ and $R_{^{13}\mathrm{CO/CO2-1}}$ have similar values of ~ 0.1. This ratio is similar to the typical $R_{^{13}\mathrm{CO/CO1-0}}$ ratio of 0.1 for normal spiral galaxies (e.g. Cormier et al. 2018). On the other hand, this ratio is much higher than typical ratio of starburst U/LIRGs ($\sim$ 0.02 Brown & Wilson 2019). However, this does not necessarily mean that molecular gas properties in the Antennae are more similar to normal spiral galaxies than to the U/LIRGs. As discussed above, the higher $R_{^{13}\mathrm{CO/CO}}$ can be either caused by higher gas surface density or to lower $X_{12/13}$, It is more likely that the lower $R_{^{13}\mathrm{CO/CO}}$ in other U/LIRGs is caused by the higher $X_{12/13}$ values, which could be due to more intense starburst activities that generates higher [^{12}C]/[^{13}C] ratio (e.g. Matsushita et al. 2009; Sliwa & Downes 2017). For the comparison with normal spiral galaxies, we can see in Section 4.5.1 that the $X_{12/13}$ values in the Antennae are factor of 2–3 higher than that in normal spiral galaxies ($\sim$ 80, Langer & Penzias 1990; Milam et al. 2005; Sliwa et al. 2017a). On the other hand, the higher gas surface density in the Antennae compared to normal spirals may increase the $R_{^{13}\mathrm{CO/CO}}$. These two factors might compensate each other and give us $R_{^{13}\mathrm{CO/CO}}$ values in the Antennae that are similar to other normal spiral galaxies.

We also note that both $R_{^{13}\mathrm{CO/CO1-0}}$ and $R_{^{13}\mathrm{CO/CO2-1}}$ decrease as the CO intensity increases until $I_{\mathrm{CO(1-0)}} \approx 200$ K kms^{-1} (Fig. 4.7, upper and lower right panel). Under LTE condition, this means that the ^{13}CO optical depth is lower in regions with higher gas surface density, which is against our expectations. We note that these higher surface density regions might also have higher velocity dispersions, which could in turn reduce the optical depth of the ^{13}CO lines.

4.4.2 Modeling results and their connection to the line ratios

We show the maps of our derived physical quantities in Fig. 4.8. We can see that most quantities show clear spatial variations among different regions. If we use the CO column density map as a guide, we can see that regions with higher gas surface densities, such as the two nuclei and the overlap region, generally have higher kinetic temperatures, beam filling factors and [CO]/[^{13}CO] abundance ratios. On the other hand, the volume density distributions are more uniform throughout the entire galaxy. We note that we only include pixels with ^{13}CO line detections. Therefore, we would expect these regions to have volume density above ^{13}CO line critical density (650 cm^{-3} Jiménez-Donaire et al. 2017). For regions with only CO detections, we might expect smaller volume densities.

The spatial variations of these quantities are also closely related the line ratio maps. We can see that the kinetic temperature map looks similar to the ^{12}CO J=3-2/1-0 ratio maps. This is consistent with our expectations that ^{12}CO J=3-2 is more excited in warmer regions. As we previously discussed, the higher ^{12}CO J=3-2/1-0 ratio could either be caused by higher temperature or density. Since the volume density does not have as much spatial variation as the kinetic temperature, it seems the major driver for the ^{12}CO J=3-2/1-0 ratio variation is temperature. We have also discussed that the ^{12}CO J=2-1/1-0 ratio map looks uniformly close to 1, which suggests both lines are thermalized. Under this condition, we would expect the excitation temperature of these two lines are equal to the kinetic temperature. In Fig. 4.9 (upper left and middle panel), we compare the excitation temperature of ^{12}CO J=2-1 and 1-0 lines with the kinetic temperature. We can see both lines have excitation temperatures close to the one-to-one lines, which further confirms they are thermalized. Simulations (e.g. Hu et al. 2022) suggest that the LTE condition is generally satisfied when kinetic temperature is above 10 K and volume density above 10^3 cm^{-3}. As we can see from the temperature and volume density maps (Fig. 4.8), most of regions satisfy this condition.

On the other hand, most ^{13}CO J=1-0 emission is not thermally excited, hence has excitation temperature lower than the kinetic temperature. However, we expect that

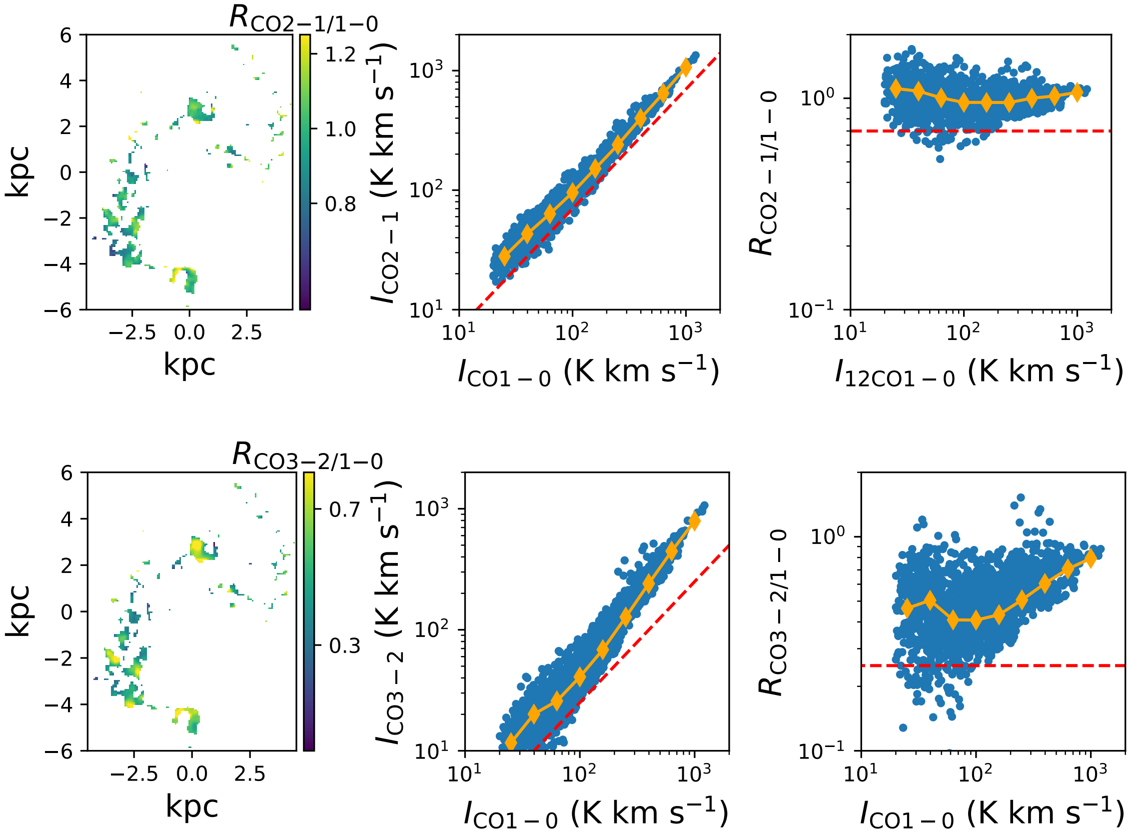

Figure 4.6: Line ratios of (*upper*) CO 2-1/1-0 and (*lower*) CO 3-2/1-0. Orange diamonds specify the median for each CO 1-0 bin. The red dashed lines are the literature ratio values ($R_{\mathrm{CO2-1/1-0}} = 0.7$ and $R_{\mathrm{CO2-1/1-0}} = 0.25$, Sun et al. 2018). We can see the line ratios in the Antennae are significantly higher than the literature values, which could be due to higher temperature or density of GMCs in starburst systems. The $R_{\mathrm{CO2-1/1-0}}$ values in the Antennae are uniformly close to 1, which suggests both ^{12}CO J=2-1 and 1-0 are thermally excited. On the other hand, $R_{\mathrm{CO3-2/1-0}}$ is significantly higher for regions with higher surface density, which could be either due to high gas temperature and/or volume density in these regions.

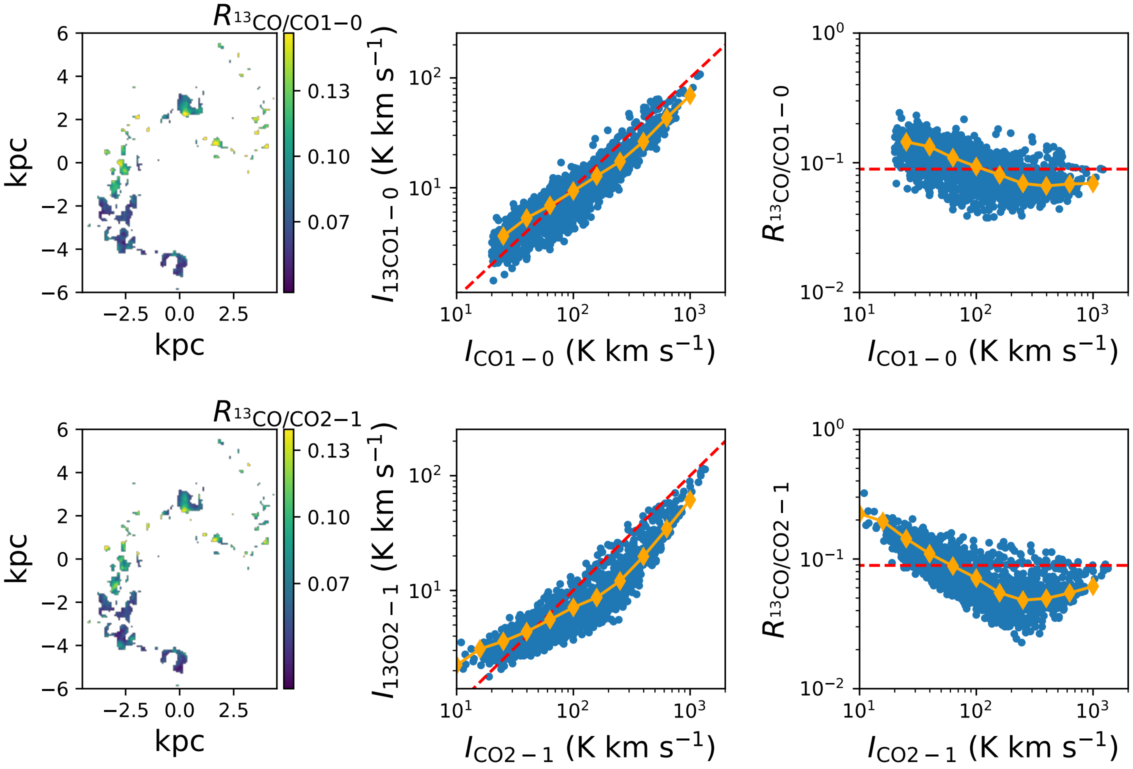

Figure 4.7: Line ratios of ^{13}CO/CO 1-0 (*upper*) and 2-1 (*lower*). The red dashed lines are the literature ratio values ($R_{^{13}\mathrm{CO/CO1-0}} = 0.09$ Cormier et al. 2018).We can see that both $R_{^{13}\mathrm{CO/CO1-0}}$ and $R_{^{13}\mathrm{CO/CO2-1}}$ have a significant anti-correlation with ^{12}CO J=1-0 and 2-1 intensity for CO intensities smaller than 100 K km s^{-1}. This could either be due to low optical depth of CO or high $X_{12/13}$ abundance ratio in high surface density region (see text for detailed discussion).

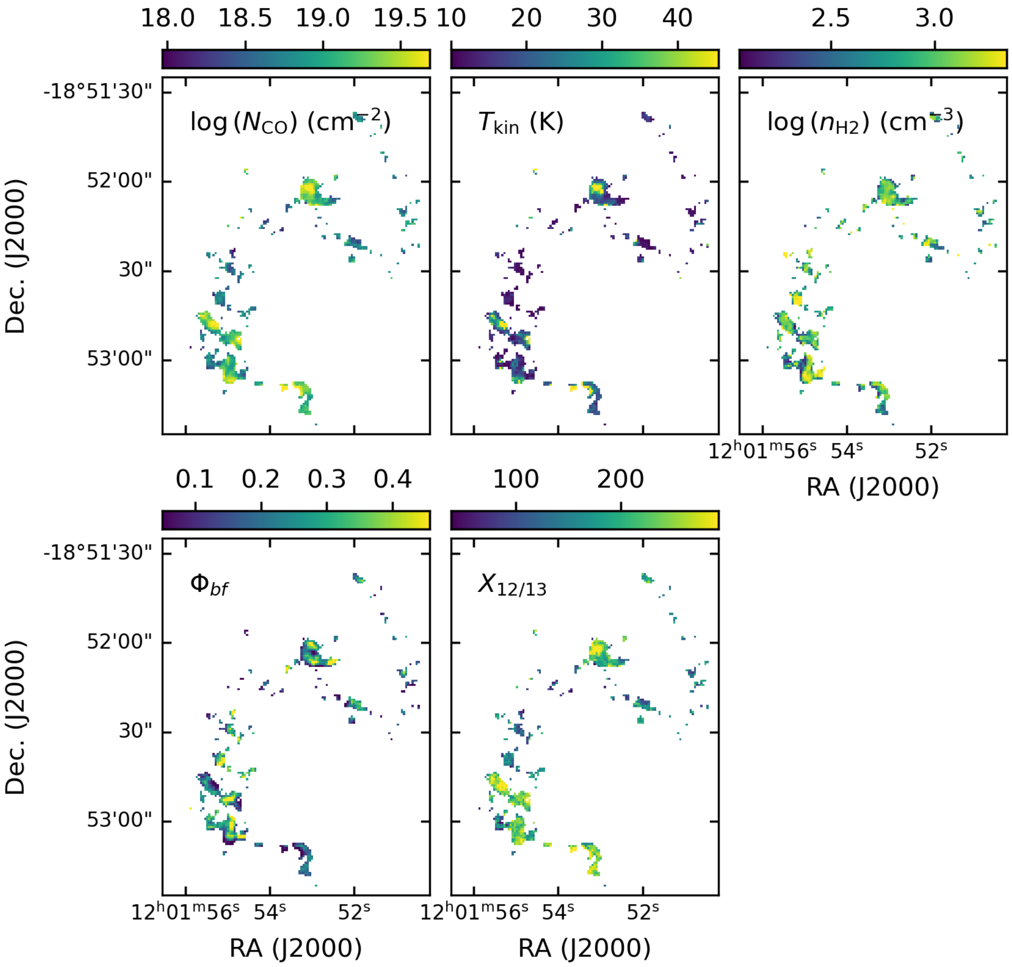

Figure 4.8: Maps of RADEX derived physical properties of the Antennae. The top row shows, from left to right, CO column density, kinetic temperature and molecular gas volume density. The bottom row shows the beam filling factor on the left and the [CO]/[^{13}CO] abundance ratio on the right. The maximal values for the color bars for all the quantities are set to be 95 percentile values.

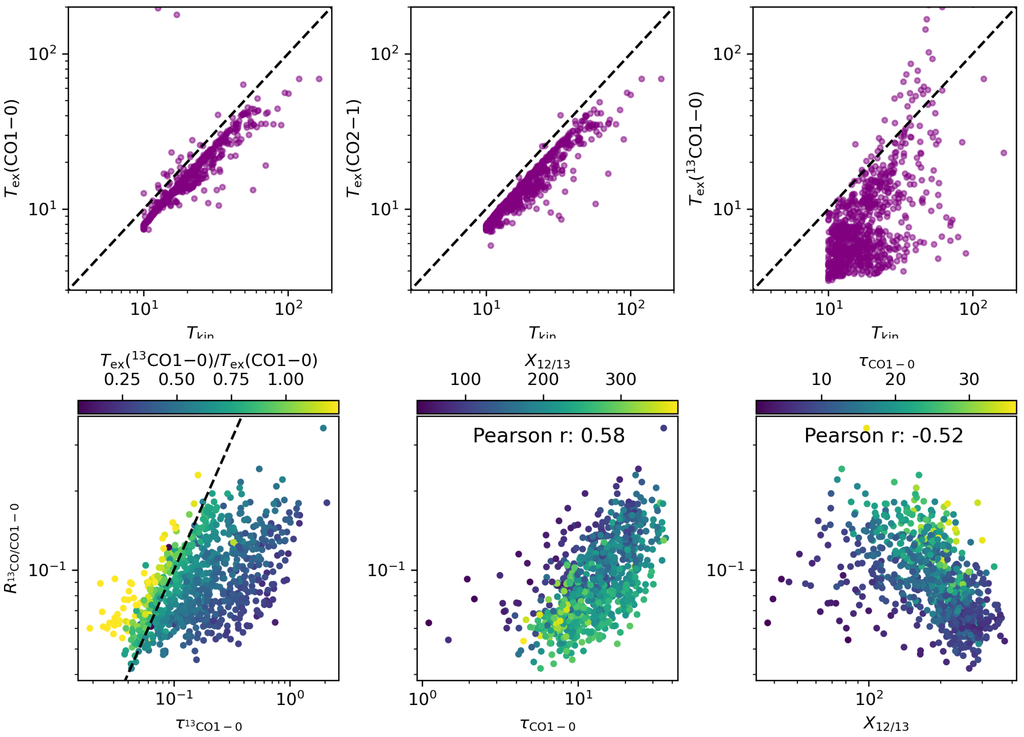

Figure 4.9: (*Upper*) The excitation temperature of ^{12}CO J=1-0, 2-1 and ^{13}CO J=1-0 versus the kinetic temperature. We can see both ^{12}CO J=1-0 and ^{12}CO J=2-1 emissions are thermally excited. On the other hand, most ^{13}CO J=1-0 emission is subthermally excited. (*Lower left*) The $R_{^{13}\mathrm{CO/CO1-0}}$ ratio versus ^{13}CO J=1-0 optical depth. We can see when ^{13}CO J=1-0 is thermally excited ($T_{\mathrm{ex}}(^{13}\mathrm{CO1}-0)/T_{\mathrm{ex}}(\mathrm{CO1}-0) \approx 1$). $R_{^{13}\mathrm{CO/CO1-0}}$ ratio is roughly equal to the ^{13}CO J=1-0 optical depth (dashed line), as expected. (*Lower middle*) $R_{^{13}\mathrm{CO/CO1-0}}$ versus $\tau_{\mathrm{CO1-0}}$ and (*lower right*) $X_{12/13}$ abundance ratio. We can see $R_{^{13}\mathrm{CO/CO1-0}}$ has strong correlation with both quantities.

most regions should have volume density above the ^{13}CO J=1-0 critical density (650 cm^{-3} Jiménez-Donaire et al. 2017) and hence be thermally excited as ^{12}CO J=1-0. We note that in our model, we assume ^{13}CO J=1-0 has the same beam filling factor as the ^{12}CO J=1-0 emission. In reality, ^{13}CO J=1-0 might have smaller beam filling factor compared to ^{12}CO J=1-0 as it mostly come from denser regions. In this case, we might overestimate the actual size of the ^{13}CO J=1-0 emission and hence underestimate the actual excitation temperature of ^{13}CO J=1-0 emission. As we have discussed before, under the LTE condition, we would expect ^{13}CO/^{12}CO J=1-0 ratio to be equivalent to the ^{13}CO J=1-0 optical depth. As shown in the lower-left panel of Fig. 4.9,when LTE condition holds for ^{13}CO J=1-0 ($T_{\mathrm{ex}}(^{13}\mathrm{CO1}-0) \approx T_{\mathrm{ex}}(\mathrm{CO1}-0)$), we see good 1-to-1 correspondence between the ratio and the optical depth. However, since most regions have ^{13}CO J=1-0 emission subthermally excited according to our modeling, we can see that the ratio in those regions is generally smaller than the actual ^{13}CO J=1-0 optical depth. As we have discussed in Section 4.4.1, the two major drivers for ^{13}CO/^{12}CO J=1-0 ratio variation are the ^{12}CO J=1-0 optical depth and $X_{12/13}$ abundance ratio. Since ^{13}CO J=1-0 might not satisfy LTE condition, we test if the ^{13}CO/^{12}CO J=1-0 ratio are still affected by those two factors using our RADEX modeling results. As shown in bottom middle and left panel of Fig. 4.9, our RADEX modeling results suggest that $R_{^{13}\mathrm{CO/CO1}-0}$ still has strong correlations with both quantities. We also perform a two-variable power-law fit between $R_{^{13}\mathrm{CO/CO1}-0}$ and $\tau_{\mathrm{CO1}-0}$ and $X_{12/13}$ and obtain

$$\log R_{^{13}\mathrm{CO/CO1}-0} = 0.43 \log \tau_{\mathrm{CO1}-0} - 0.5 \log X_{12/13} - 0.4 \tag{4.12}$$

We also note that there is a clear spatial variation of $X_{12/13}$ that corresponds well with T_{kin} and $N_{^{12}\mathrm{CO}}$ variation (Fig. 4.8). Regions with higher CO column density and kinetic temperature generally have higher $X_{12/13}$. In theory, the high $X_{12/13}$ value could be caused by starburst activity that generates large amounts of ^{12}C at short timescales ($\sim$ 10 Myr Vigroux et al. 1976) by massive stars while ^{13}C will only be released by intermediate-mass stars after $\sim$ 1 Gyr. This scenario is consistent with our expectation since regions with higher gas temperature and surface densities are generally where starburst events happen. In Section 4.4.1, we have also discussed the negative correlation between $R_{^{13}\mathrm{CO/CO1}-0}$ and ^{12}CO J=1-0 intensity. The low $R_{^{13}\mathrm{CO/CO1}-0}$ in high surface density regions could be potentially due to high $X_{12/13}$ in these regions. We also find most regions have $X_{12/13}$ values between 100 – 300. This value is more similar to the $X_{12/13}$ in starburst mergers (125 in Arp 220, 250 in NGC 2623 Sliwa & Downes 2017; Sliwa et al. 2017b) and significantly higher than that in the Milky Way center of ~ 30 (e.g. Langer & Penzias 1990; Milam et al. 2005). This is also consistent with the scenario that starburst events boost the $X_{12/13}$ ratio.

4.5 Modeled CO-to-H_2 conversion factor at GMC scales

4.5.1 CO-to-H_2 conversion factor dependence on observables

Dependence on ^{12}CO J=1-0 intensity

Various simulations (e.g. Narayanan et al. 2012) have proposed that the bimodal distribution of $\alpha_{\rm CO}$ across normal spiral galaxies and U/LIRGs can be accounted for by an $\alpha_{\rm CO}$ dependence on ^{12}CO J=1-0 intensity ($I_{\rm CO\ 1\text{-}0}$) at kpc scales. Recent simulations (e.g. Gong et al. 2020) have further pushed this dependence down to GMC spatial scales. However, it is hard to test this dependence at GMC scales in observations due to limited resolution and sensitivity of current instruments. Our study hence provides the first direct test of this dependence in starburst mergers. As shown in the left panel of Fig. 4.10, we see a significant anti-correlation between $\alpha_{\rm CO}$ and $I_{\rm CO\ 1\text{-}0}$. Our fit power-law relation is

$$\log \alpha_{\rm CO} = 0.61 - 0.25 \log I_{\rm CO1-0} \tag{4.13}$$

Our power-law slope is slightly steeper than the prediction (-0.14) in Gong et al. (2020) but in a relatively good agreement with the prediction in Hu et al. (2022). In general, our fit power-law relation agrees with the simulation prediction within tolerance of different simulation set-ups. We note that both Gong et al. (2020) and Hu et al. (2022) simulate a kpc-size box of a normal spiral galaxy, which has much lower gas content than starburst mergers like the Antennae and only has maximal $I_{\rm CO\ 1\text{-}0}$ barely reaching 100 K km s^{-1}. Therefore, we do not expect our results to fully agree with the simulation prediction. We also note that our modeled $\alpha_{\rm CO}$ values are slightly below the simulation prediction. Besides the environmental differences between normal spiral galaxies and starburst mergers, our choice of $x_{\rm co}$ could also

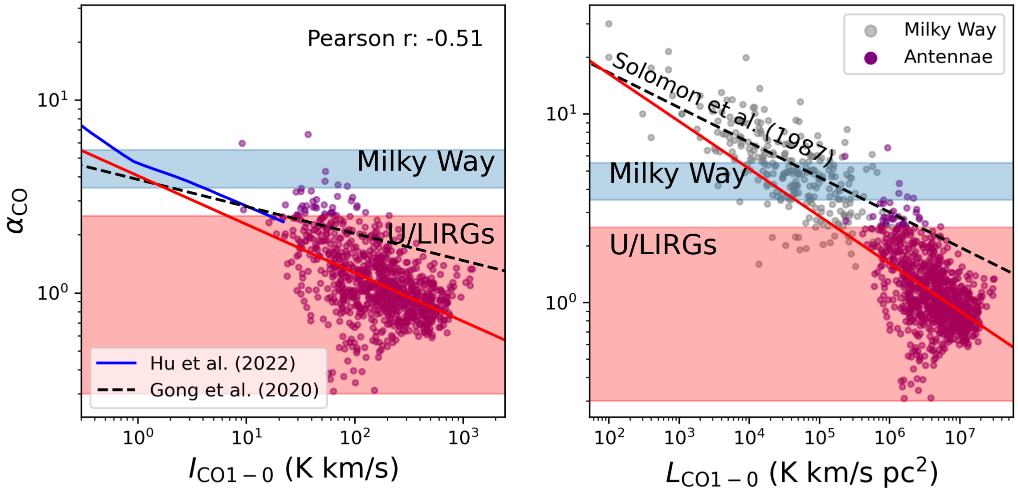

Figure 4.10: (*Left*) Modeled $\alpha_{\rm CO}$ versus ^{12}CO J=1-0 integrated intensity $I_{\rm CO(1-0)}$. The red solid line is the fit to $\alpha_{\rm CO}$ versus $I_{\rm CO(1-0)}$ using data in this work. The dashed line is the simulation prediction from Gong et al. (2020) at a resolution of 128 pc and the blue solid line is the simulation prediction from Hu et al. (2022) at a resolution of 125 pc. (*Right*) Modeled $\alpha_{\rm CO}$ versus the total ^{12}CO J=1-0 luminosity of individual GMCs for the Antennae (purple) and Milky Way (gray, Solomon et al. 1987). The dashed line is the power-law fit for the Milky Way data points (Solomon et al. 1987) while the red solid line is the power-law fit to the Antennae data from this work. We can see a significant anti-correlation between $\alpha_{\rm CO}$ and $I_{\rm CO(1-0)}$ as suggested by the literature with similar power-law slope. The difference in the power-law relations might be due to the fact that molecular gas in the Antennae is in a higher gas surface density regime.

cause the discrepancy in the absolute values. If we adopt $x_{\rm co} = 2 \times 10^{-4}$, it will bring our modeled results align with simulation prediction.

A similar anti-correlation between $\alpha_{\rm CO}$ and total ^{12}CO J=1-0 luminosity ($L_{\rm CO\ 1\text{-}0}$) has been found for GMCs in the Milky Way with power law slope of -0.185 (Solomon et al. 1987). We can further explore if this correlation extends to the high GMC surface density regime in the Antennae. Since we adopt the pixel-based approach to study GMCs in the Antennae, we would expect each pixel represents a single GMC with total luminosity calculated as

$$L_{\rm CO\ 1\text{-}0} = 1.1331 B_{\rm fwhm}^2 I_{\rm CO\ 1\text{-}0} \tag{4.14}$$

where $B_{\rm fwhm} = 150$ pc is the working resolution of our data cubes. The comparison between $\alpha_{\rm CO}$ and $L_{\rm CO\ 1\text{-}0}$ is shown in Fig. 4.10. Since each pixel has a fixed size, we have $L_{\rm CO\ 1\text{-}0} \propto I_{\rm CO\ 1\text{-}0}$ and hence the $\alpha_{\rm CO}$ versus $L_{\rm CO\ 1\text{-}0}$ relation has the same power law slope as $\alpha_{\rm CO}$ versus $I_{\rm CO\ 1\text{-}0}$ with power-law index of -0.25. The data points of the Antennae join nicely with those of the Milky Way. However, $\alpha_{\rm CO}$ versus $L_{\rm CO\ 1\text{-}0}$ in the Antennae has a much steeper slope. We note that $\alpha_{\rm CO}$ in Solomon et al. (1987) is calculated as the ratio of virial mass to the ^{12}CO J=1-0 luminosity under the assumption of virial equilibrium. However, the virial equilibrium itself might not hold, especially for GMCs in starburst mergers (e.g. He et al. 2023). For the Antennae, high $\alpha_{\rm vir}$ GMCs generally reside in the overlap region and the two nuclei, which also have the highest $I_{\rm CO\ 1\text{-}0}$ values. If the positive correlation between $\Sigma_{\rm mol}$ and $\alpha_{\rm vir}$ exists, we would expect the additional increase in $\alpha_{\rm vir}$ will make $\alpha_{\rm CO}$ drop more rapidly (see detailed discussion in Section 4.5.1).

Dependence on CO 1-0 optical depth and ^{13}CO/CO ratio

Recent GMC LVG modeling in normal spiral galaxies (Teng et al. 2022, 2023) suggests that $\alpha_{\rm CO}$ has a tight proportional correlation with the ^{12}CO J=1-0 optical depth ($\tau_{\rm CO1-0}$) when $\tau_{\rm CO(1-0)} > 1$. This is relation is consistent with our LVG modeling expectation. Under the LVG assumption, we have

$$\tau_{\rm CO1-0} \propto N_{\rm CO}/\Delta v \tag{4.15}$$

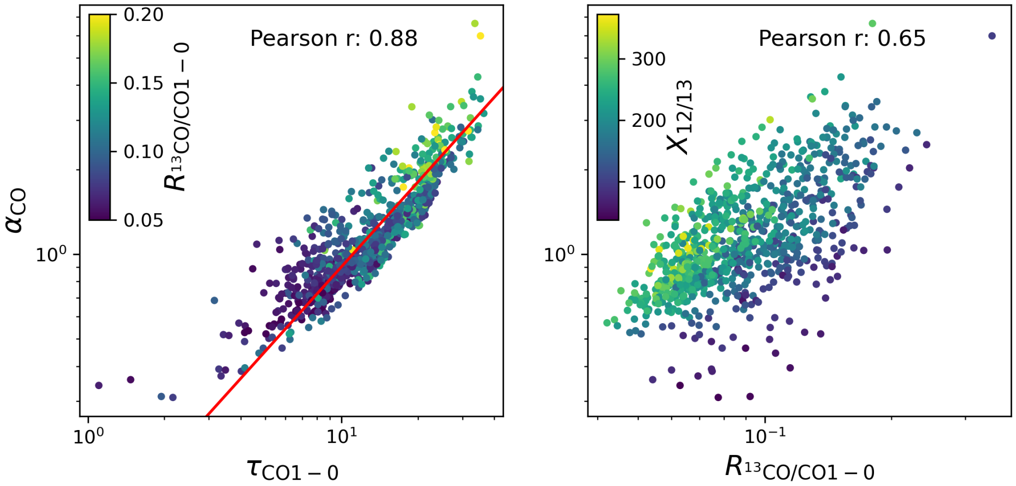

Figure 4.11: (*Left*) The modeled $\alpha_{\rm CO}$ versus the modeled $\tau_{\rm CO(1-0)}$ color coded by ^{13}CO/^{12}CO J=1-0 ratio ($R_{^{13}{\rm CO/CO1-0}}$). The red line is a proportional fit (power law slope of 1) to data points. (*Right*) Modeled $\alpha_{\rm CO}$ versus $R_{^{13}{\rm CO/CO1-0}}$ color coded by [CO]/[^{13}CO] abundance ratio $X_{12/13}$. We can see there is a tight linear correlation between $\alpha_{\rm CO}$ and $\tau_{\rm CO1-0}$ for the Antennae, which is consistent with results of Teng et al. (2022, 2023). We can also see a strong correlation between $\alpha_{\rm CO}$ and $R_{^{13}{\rm CO/CO1-0}}$, which suggests $R_{^{13}{\rm CO/CO1-0}}$ can be potentially used as an $\alpha_{\rm CO}$ tracer.

As shown in Section 4.4.1, most ^{12}CO J=1-0 emission is thermally excited with $R_{\rm CO2-1/1-0} \sim 1$. Based on the LTE assumption, we have

$$\begin{aligned} T_{\rm peak} &= \Phi_{\rm bf} T_{\rm exc}\left[1-\exp(-\tau_{\rm CO1-0})\right] \\ &\approx \Phi_{\rm bf} T_{\rm kin}\left[1-\exp(-\tau_{\rm CO1-0})\right] \end{aligned} \tag{4.16}$$

Substituting these two equations into Eq. 4.6, we have

$$\begin{aligned} \alpha_{\rm CO} &= \frac{N_{\rm CO}\Phi_{\rm bf}}{x_{\rm co} I_{\rm CO(1-0)}} = \frac{N_{\rm CO}/\Delta v}{x_{\rm co} T_{\rm peak}}\Phi_{\rm bf} \\ &\propto \frac{\tau_{\rm CO1-0}}{1-\exp(-\tau_{\rm CO1-0})}, \quad (x_{\rm CO}, T_{\rm kin} = {\rm const}) \\ &\propto \tau_{\rm CO1-0}, \quad (\tau_{\rm CO1-0} \gg 1) \end{aligned} \tag{4.17}$$

In the left panel of Fig. 4.11, we can see a tight linear correlation between $\alpha_{\rm CO}$ and $\tau_{\rm CO1-0}$, which is consistent with this theoretical expectation. The red solid line is the proportional fit to the relation, which is

$$\log \alpha_{\rm CO} = \log \tau_{\rm CO1-0} - 1.05 \tag{4.18}$$

In real observations, $\tau_{\mathrm{CO1-0}}$ is hard to measure and generally requires multi-CO transition radiative transfer modeling. Various studies (e.g. Jiménez-Donaire et al. 2017) have proposed to use the ^{13}CO/CO line ratio ($R_{^{13}\mathrm{CO/CO}}$) to trace the optical depth of optically thick ^{12}CO J=1-0 line. Based on Eq. 4.11, we would expect $R_{^{13}\mathrm{CO/CO1-0}} \propto \tau_{\mathrm{CO1-0}}$ if the $X_{12/13}$ abundance ratio is fixed. As shown in the right panel of Fig. 4.11, we can see a strong correlation between α_{CO} and $R_{^{13}\mathrm{CO/CO1-0}}$. However, this correlation has significantly larger scatter compared to the α_{CO} versus $\tau_{\mathrm{CO1-0}}$ relation. As discussed in Section 4.4.2, $R_{^{13}\mathrm{CO/CO1-0}}$ is determined by both $\tau_{\mathrm{CO1-0}}$ and $X_{12/13}$. Therefore, the scatter in α_{CO} versus $R_{^{13}\mathrm{CO/CO1-0}}$ can be caused by different $X_{12/13}$ values in different regions. We therefore color code the α_{CO} versus $R_{^{13}\mathrm{CO/CO1-0}}$ plot with $X_{12/13}$ values (Fig. 4.11, right panel). As we can see, there is a clear trend that the larger α_{CO} becomes, the higher $X_{12/13}$ values the data points have. This confirms that the scatter in α_{CO} versus $R_{^{13}\mathrm{CO/CO1-0}}$ relation mainly comes from $X_{12/13}$ variation. Combining Eq. 4.12 and 4.18, we have

$$\log \alpha_{\mathrm{CO}} = 2.33 \log R_{^{13}\mathrm{CO/CO1-0}} + 1.16 \log X_{12/13} + 0.93 \tag{4.19}$$

Therefore, if we know the $X_{12/13}$ values, we can derive α_{CO} from measured $R_{^{13}\mathrm{CO/CO1-0}}$ values.

Dependence on GMC dynamical states

As an optically thick line, ^{12}CO J=1-0 is often used as a molecular gas tracer based on the fact that the ^{12}CO J=1-0 luminosity is proportional to virial mass for individual GMCs in both the Milky Way and nearby galaxies (references in Bolatto et al. 2013). However, GMCs in starburst systems might be less gravitationally bound and hence the virial mass could actually be an overestimate of the actual molecular gas mass. Early theoretical works (e.g. Downes et al. 1993) suggested that for starburst systems, CO instead trace the geometric mean of molecular gas mass and virial mass (i.e. $L_{\mathrm{CO}} \propto T_{\mathrm{B,0}} \left(M_{\mathrm{gas}} M_{\mathrm{vir}} / \rho_{\mathrm{gas}}\right)^{1/2}$, see discussions in Shetty et al. 2011). However, it was hard to test these scaling relations due to the limited resolution of instruments at that time which made it hard to resolve individual GMCs. Papadopoulos et al. (2012) infer the dynamical states of GMCs in starburst U/LIRGs based on the LVG modeled volume density and velocity gradient and their results support the argument that α_{CO} is lower in starburst systems due to GMCs being out of equilibrium. However, with this indirect method, it is hard to capture the $\alpha_{\rm CO}$ variation within individual galaxies. Recent high-resolution ALMA observations (e.g. Brunetti et al. 2020; Brunetti 2022) and merger simulations (e.g. He et al. 2023) suggest that most GMCs in starburst mergers are out of virial equilibrium with a wide range of virial parameters across different regions (e.g. center versus outskirts). Therefore, $\alpha_{\rm vir}$ variations could be a major driver of $\alpha_{\rm CO}$ variations. The virial parameter of each individual GMC can be calculated as (Sun et al. 2018)

$$\begin{aligned}\alpha_{\rm vir} &= 5.77\left(\frac{\sigma_v}{\rm kms^{-1}}\right)^2\left(\frac{\Sigma_{\rm mol}}{M_\odot {\rm pc}^{-2}}\right)^{-1}\left(\frac{R}{40{\rm pc}}\right)^{-1} \\ &\propto \frac{\sigma_v^2}{\Sigma_{\rm mol}R}\end{aligned} \tag{4.20}$$

For GMCs with fixed $\Sigma_{\rm mol}$, a higher velocity dispersion σ_v can lead to a higher $\alpha_{\rm vir}$. At the same time, higher σ_v at a fixed CO column density leads to lower $\alpha_{\rm CO}$ according to Eq.4.18. In the left panel of Fig. 4.12, we see a significant anti-correlation between $\alpha_{\rm CO}$ and σ_v, which is consistent with our modeling expectation.

We can also build a more quantitative correlation between $\alpha_{\rm CO}$ and $\alpha_{\rm vir}$. For each individual GMC, we have

$$\begin{aligned}\alpha_{\rm CO} &= \frac{\Sigma_{\rm mol}}{I_{\rm CO}} = \frac{\Sigma_{\rm mol}}{T_{\rm peak}\Delta v} \\ &\propto \frac{\rho_{\rm mol}R}{T_{\rm peak}\sigma_v},\end{aligned} \tag{4.21}$$

where $\rho_{\rm mol}$ is mass volume density of molecular gas and R is the GMC radius. By combining Eq. 4.20 and 4.21, we can get the relation

$$\begin{aligned}\alpha_{\rm CO} &\propto \frac{1}{\sqrt{\alpha_{\rm vir}}}\frac{\sqrt{\rho_{\rm mol}}}{T_{\rm peak}} \\ &\propto \frac{1}{\sqrt{\alpha_{\rm vir}}} \quad (\rho_{\rm mol}, T_{\rm peak} = {\rm const})\end{aligned} \tag{4.22}$$

In the right panel, we plot $\alpha_{\rm CO}$ versus $\alpha_{\rm vir}$. Since we are using the pixel-based approach to study individual GMCs, the GMC radius R is set to be the half of the beam major axis (75 pc). We also note that $\alpha_{\rm vir}$ calculation in Eq. 4.20 involves $\Sigma_{\rm mol}$, which is derived based on our modeling $\alpha_{\rm CO}$ results. As we can see, the $\alpha_{\rm CO}$ vs $\alpha_{\rm vir}$ correlation is stronger than the $\alpha_{\rm CO}$ vs σ_v correlation, which suggests that $\alpha_{\rm CO}$

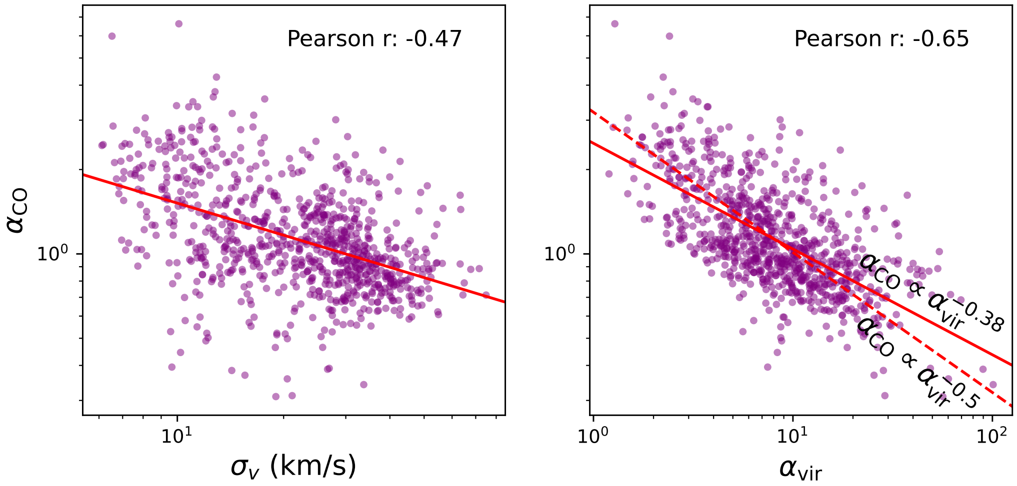

Figure 4.12: α_{CO} versus (*Left*) velocity dispersion σ_v and (*Right*) virial parameter α_{vir}. The red solid line is the power-law fit of both relations. The red dashed line is the power-law fit with fixed slope of -0.5 from theoretical predictions (see Section 4.5.1 for detailed discussion). We can see a strong anti-correlation between α_{CO} and both quantities, which suggests that the α_{CO} variation in the Antennae is caused by GMCs being turbulent and out of virial equilibrium.

variation might be driven by dynamical states of individual GMCs. We also perform a power-law fit to the α_{CO} versus α_{vir} relation, which is

$$\log \alpha_{CO} = 0.4 - 0.38 \log \alpha_{vir} \tag{4.23}$$

As we can see, the power-law slope of -0.45 is quite close to the theoretical expectation of -0.5. Therefore, α_{vir} can also be potentially used as a tracer of α_{CO} variations within a system. However, we note that the α_{vir} calculation itself requires an α_{CO} value to be given in advance to convert ^{12}CO J=1-0 intensity to gas surface density. A possible solution is to iteratively solve α_{vir} and α_{CO} until they converge to a correlation with power slope of -0.5.

Dependence on CO line ratios

It has been proposed recently by Gong et al. (2020) that the ^{12}CO J=2-1/1-0 ratio $R_{CO2-1/1-0}$ can be used as a tracer of α_{CO}. For individual GMCs in virial equilibrium,

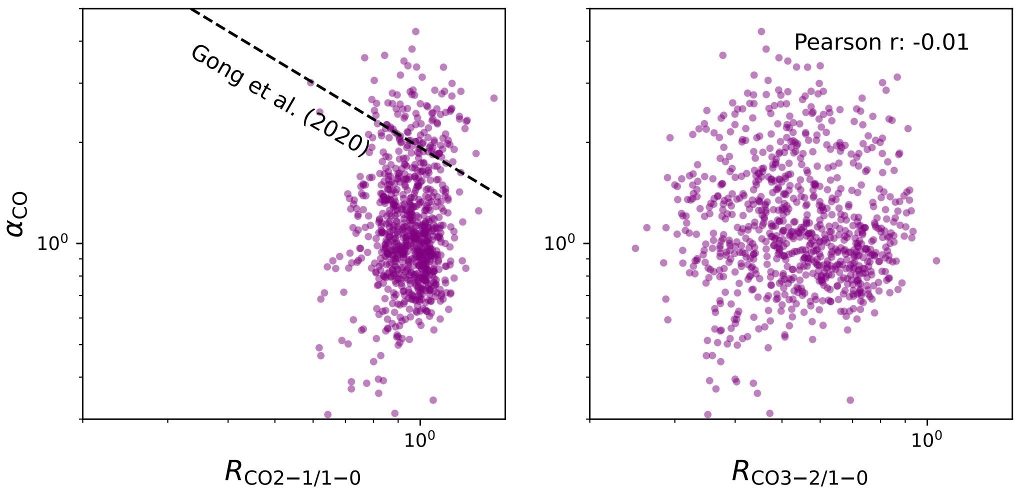

Figure 4.13: $\alpha_{\rm CO}$ versus ^{12}CO J=2-1/1-0 ratio $R_{\rm CO2-1/1-0}$ (*left*) and ^{12}CO J=3-2/1-0 ratio $R_{\rm CO3-2/1-0}$ (*right*) . The dashed line is the simulation fitting results from Gong et al. (2020). We can see there is no correlation between $\alpha_{\rm CO}$ and $R_{\rm CO2-1/1-0}$ due to ^{12}CO J=2-1 being thermalized, which saturates the ratio at values close to 1. We also do not see a significant anti-correlation between $\alpha_{\rm CO}$ and $R_{\rm CO3-2/1-0}$, which suggests that CO line ratios are generally not a good tracer of $\alpha_{\rm CO}$ variation in starburst systems with large gas surface densities.

we would expect the relation (Gong et al. 2020)

$$\alpha_{\rm CO} \propto \begin{cases} T_{\rm exc}^{-1/2}, & \text{low density} \\ \frac{\sqrt{n}}{T_{\rm kin}}, & \text{high density,} \end{cases} \tag{4.24}$$

where $T_{\rm exc}$ is the ^{12}CO J=1-0 excitation temperature, $T_{\rm kin}$ is the gas kinetic temperature and n is the gas volume density. In the low volume density regime, we have an anti-correlation between $\alpha_{\rm CO}$ and $T_{\rm exc}$. Since higher $T_{\rm exc}$ will directly lead higher $R_{\rm CO2-1/1-0}$ ratio, we would expect an anti-correlation between $\alpha_{\rm CO}$ and $R_{\rm CO2-1/1-0}$. In Fig. 4.13, we see no correlation between these two quantities, which is probably due to our limited range of $R_{\rm CO2-1/1-0}$ values (Fig. 4.6). Furthermore, as discussed in Section 4.4.1, the $R_{\rm CO2-1/1-0}$ ratio of GMCs in the Antennae is close to 1, which suggests they are in LTE condition with high gas volume density. In this case, we no longer expect an anti-correlation between $\alpha_{\rm CO}$ and $R_{\rm CO2-1/1-0}$.

Since $R_{\rm CO2-1/1-0}$ saturates to $\sim$ 1, it is likely the CO excitation condition is traced by ratios between higher-J CO lines, such as ^{12}CO J=3-2, and ^{12}CO J=1-0.

We therefore also test how $\alpha_{\rm CO}$ correlates with $R_{\rm CO3-2/1-0}$. As we can see, $R_{\rm CO3-2/1-0}$ shows a significantly larger range of values than $R_{\rm CO2-1/1-0}$. However, we still do not see a significant anti-correlation between $\alpha_{\rm CO}$ and $R_{\rm CO3-2/1-0}$, which suggests that excitation condition does not play a major role in $\alpha_{\rm CO}$ variation within starburst mergers. Bournaud et al. (2015) also find in their merger simulation that $\alpha_{\rm CO}$ has weak or no correlation with high-J CO to ^{12}CO J=1-0 line ratios. They further match the temperature between different types of galaxies and still find similar $\alpha_{\rm CO}$ differences between different types of galaxies. Instead, they find that the major difference that causes $\alpha_{\rm CO}$ variations among different types of galaxies is the turbulent velocity dispersion. This result further supports our argument that the $\alpha_{\rm CO}$ variation in starburst merger is caused by the variation in GMC dynamical states rather gas excitation conditions.

We can also see from Fig. 4.13 that our modeled $\alpha_{\rm CO}$ is slightly below the simulation prediction from Gong et al. (2020). One explanation would be that our chosen $x_{\rm co}$ value is slightly higher than the true value. If we reduce our $x_{\rm co}$ by a factor of 2, we would expect a better alignment between our modeled $\alpha_{\rm CO}$ and simulation prediction. However, as discussed in Section 4.5.2, this reduced $x_{\rm co}$ value will give us gas-to-dust ratio (GDR) close to 200. An alternative explanation is that the discrepancy is caused by other environmental factors. For example, the simulation set-up in Gong et al. (2020) has a maximum GMC surface density of 100 $\rm M_\odot$ pc^{-2}. In the Antennae, our highest GMC $\Sigma_{\rm mol}$ is above 1000 $\rm M_\odot$ pc^{-2}. As discussed in Section 4.5.1, the higher ^{12}CO J=1-0 intensity corresponds to lower $\alpha_{\rm CO}$ values. Therefore, we would expect most of our high $\Sigma_{\rm mol}$ GMCs to have lower $\alpha_{\rm CO}$ than the simulation prediction.

Summary

The $\alpha_{\rm CO}$ map is shown in Fig. 4.14. As we show in previous sections, $\alpha_{\rm CO}$ is tightly correlated with ^{12}CO J=1-0 optical depth ($\tau_{\rm CO1-0}$) and virial parameter ($\alpha_{\rm vir}$). Therefore, we also show the maps of those two quantities in Fig. 4.14. We note that high optical depth pixels generally have smaller gas surface densities, which is the other way as what we expect. We note that the optical depth in RADEX modeling is proportional to the $\Sigma_{\rm mol}/\sigma_v$. Therefore, it is likely that these regions have higher velocity dispersion, which results in lower optical depth in these high gas surface density regions. These gas concentration regions also tend to have higher $\alpha_{\rm vir}$ due to the large

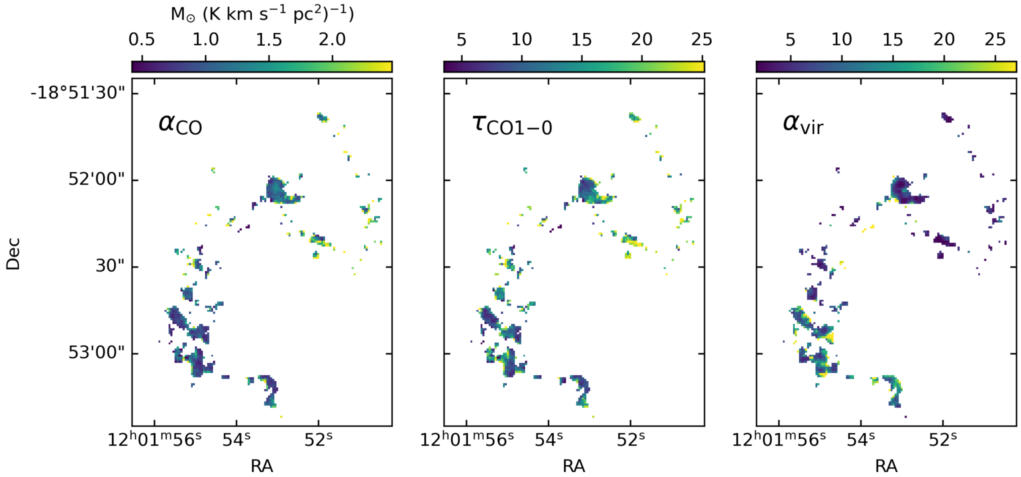

Figure 4.14: The derived maps of (*left*) $\alpha_{\rm CO}$, (*middle*) $\tau_{\rm CO1-0}$ and (*right*) $\alpha_{\rm vir}$ for the Antennae. As shown in Section 4.5.1, $\tau_{\rm CO1-0}$ and $\alpha_{\rm vir}$ has the strongest correlation with $\alpha_{\rm CO}$.

velocity dispersion, as $\alpha_{\rm vir} \propto \sigma_v^2/\Sigma_{\rm mol}$.

4.5.2 Constrain $x_{\rm co}$ abundance ratio with dust continuum

From the dust continuum map, we can then calculate the dust mass as (Wilson et al. 2008)

$$M_{\rm dust} = 74220 S_{880} D^2 \frac{\exp(17/T_{\rm dust})}{\kappa} \tag{4.25}$$

where S_{880} is the flux in Jy, D is the distance in Mpc, $T_{\rm dust}$ is the dust temperature in Kelvin and κ is the dust opacity in g^{-1} cm^2. We chose 0.9 g^{-1} cm^2 as the fiducial value for κ (Wilson et al. 2008) but note that κ can be a factor of 2 higher in starburst systems (Wilson et al. 2014). The dust surface density for a given pixel can then be calculated as

$$\begin{aligned}\Sigma_{\rm dust} &= M_{\rm dust}/(1.1331 B_{\rm FWHM}^2)\\ &= 2.9 I_{880} D^2 \frac{\exp(17/T_{\rm dust})}{\kappa}\left(\frac{B_{\rm FWHM}}{150{\rm pc}}\right)^{-2}\end{aligned} \tag{4.26}$$

where I_{880} is the intensity in Jy/beam and $B_{\rm FWHM}$ is the FWHM of the round beam in pc. One of the major uncertainties in the dust mass calculation comes from the unconstrained dust temperature. We adopt the dust temperature from Klaas et al.

(2010) for pixels in each defined subregion (Fig. 4.3). For subregion A1a which does not have a temperature measurement, we assume the temperature to be the same as the overall dust temperature derived from the integrated fluxes of the entire galaxy. The comparison of Σ_{mol} and Σ_{dust} is shown in the left panel of Fig. 4.15. We can see that a high x_{CO} value is favored in order to get a reasonable gas-to-dust ratio (GDR) below 200. Furthermore, since our modeling is targeting the most dense GMCs, we would expect them to have GDR values closer to dense gas values of 50 – 100 instead of most diffuse medium values of 200 (Remy et al. 2017). Instead, if we assume a constant Milky Way α_{CO} value, we will get GDR values of 300 – 400 (consistent with GDR values in Klaas et al. 2010, adopting the Milky Way α_{CO}).

An alternative explanation is that the Antennae might actually have a high GDR values due to low metallicity. According to Sandstrom et al. (2013), α_{CO} has an almost linear correlation with the inverse of GDR values in spiral galaxies, which suggests a constant fraction of heavy elements reside in dust grains. Therefore, low metallicity could lead to low heavy elements in dust grains, and hence increase the GDR values. However, as shown in Section 4.6.3, most of regions in the Antennae have solar metallicity. Therefore, we would not expect the Antennae to have abnormally high GDR values.

However, we also note that the dust mass we calculate is also affected by systematic uncertainties from other free parameters, such as dust temperature (T_{dust}) and opacity (κ). Specifically, the actual κ can be two times higher than our assumed standard value in starburst systems (Wilson et al. 2014). To explore how x_{co}, T_{dust} and κ work together to determine our measured gas-to-dust ratio, we calculated the median GDR from different combination of these three quantities (Fig. 4.15, middle and right panel). If we assume a standard κ value of 0.9 $\mathrm{g}^{-1}\ \mathrm{cm}^2$, we need to keep x_{co} greater than 2.5×10^{-4} even for very low dust temperatures (~ 20 K) to keep the GDR value around 100. If we increase the dust temperature, we will even need higher x_{co} values to keep the GDR at the same value. We note the typical [C]/[H] abundance in the Milky Way is 1.5×10^{-4} (Sofia et al. 2004), which sets the upper limit of $[\mathrm{CO}]/[\mathrm{H}_2]$ to be 3×10^{-4} (note that it requires two hydrogen atoms combined to make one hydrogen molecule which causes the factor of 2 difference in those two values). If we increase κ by a factor of 2 as found in some starburst systems, the dust will become more luminous and hence the actual dust mass will be lower, which gives us even higher GDR values. Therefore, we find that our assumed x_{co} of 3×10^{-4} is a reasonable

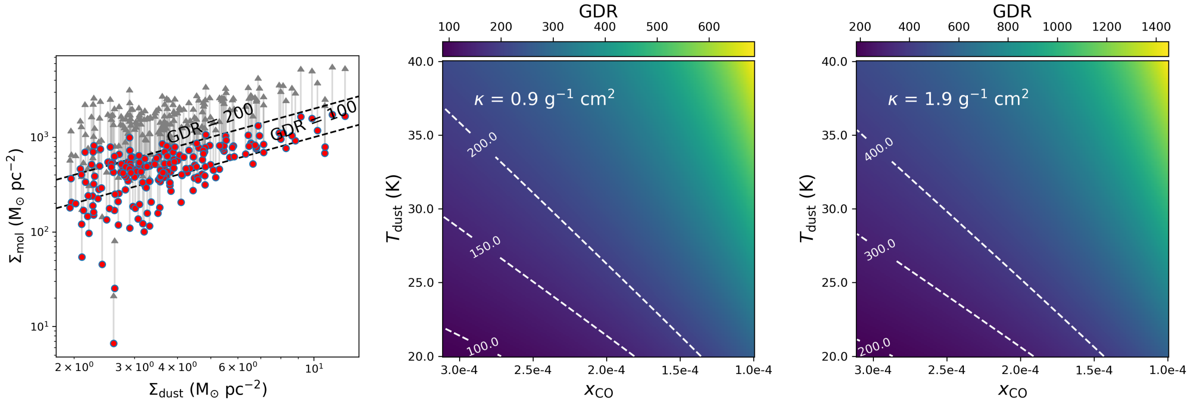

Figure 4.15: (*Left*) Molecular gas versus dust surface density. $\Sigma_{\rm mol}$ is calculated using our modeled $\alpha_{\rm CO}$ values. Red circles and gray arrows indicate $\Sigma_{\rm mol}$ calculated assuming $x_{\rm co}$ = 3e-4 and 1e-4 respectively. The dashed lines indicate constant gas-to-dust ratio (GDR). We can see that $x_{\rm co} = 3 \quad \times \quad 10^{-4}$ gives us more realistic GDR values. (*Middle*) Median GDR distribution in the $T_{\rm dust}$ vs $x_{\rm CO}$ plane assuming $\kappa = 0.9$ g^{-1} cm^2. The dashed line indicate constant GDR values. (*Right*) Same as middle panel but assuming $\kappa = 1.9$ g^{-1} cm^2. We can see that a high $x_{\rm CO}$ value is favored in order to get a GDR below 200.

choice, which suggests that most carbon in GMCs has gone into CO molecules. This is also consistent with several simulation predictions. Hu et al. (2022) shows that $x_{\rm co}$ saturates at its maximal when the CO column density is greater than 10^{18} cm^{-2}, which is generally the case for our modeled regions (Fig. 4.8).

4.5.3 GMC dynamical states in the Antennae

As discussed in He et al. (2023), the variation of $\alpha_{\rm CO}$ can lead to an uncertainty of a factor of 4 for GMC virial parameter ($\alpha_{\rm vir}$) measurements, hence affecting our judgement on GMC dynamical states in galaxy mergers. With our modeled $\alpha_{\rm CO}$, we can put a more accurate constraint on GMC dynamical states in the Antennae. Although the absolute values of our modeled $\alpha_{\rm CO}$ depend our $x_{\rm co}$ choice, we have found in Section 4.5.2 that $x_{\rm CO} = 3\times10^{-4}$ is a reasonable assumption to give us realistic GDR values. With $x_{\rm CO} = 3 \times 10^{-4}$, most of our modeled $\alpha_{\rm CO}$ are closer to U/LIRG values of 1.1 M$_\odot$ (K km s^{-1} pc^2)$^{-1}$, which is different from previous works that suggest that the Antennae should have a Milky Way $\alpha_{\rm CO}$ of 4.3 M$_\odot$ (K km s^{-1} pc^2)$^{-1}$ (e.g. Zhu et al. 2003; Schirm et al. 2014). This conclusion in general will bring up the $\alpha_{\rm vir}$ of the Antennae, which suggests GMCs in the Antennae are less gravitationally bound

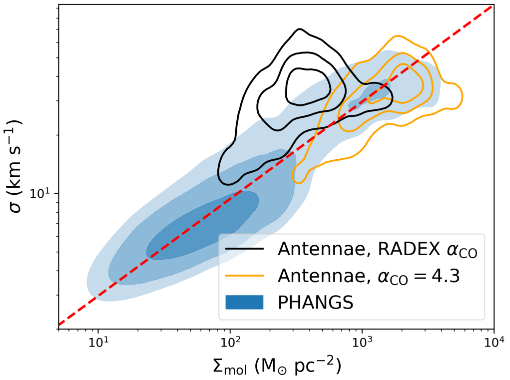

Figure 4.16: Velocity dispersion versus gas surface density contours for PHANGS galaxies (blue shaded) and the Antennae using varying α_{CO} from this work (black) and a constant Milky Way α_{CO} value (orange). The red dashed line marks the position of the median value of α_{vir} for PHANGS galaxies of 2.7 (Sun et al. 2020a). Our modeled α_{CO} results suggest that GMCs in the Antennae are less gravitationally bound than GMCs in the PHANGS galaxies.

than we might expect. As shown Fig. 4.16, our modeled α_{CO} results suggest GMCs in the Antennae are more turbulent, which is consistent with the simulation prediction from He et al. (2023).

We can also see that in spite of occupying a different parameter space, our modeled α_{CO} gives a similar contour shape as adopting a constant Milky Way α_{CO} (Fig. 4.16). This similarity suggests that the absolute value of global α_{CO} matters more than the relative α_{CO} variation within the galaxy. We note that most past literature studies suggest a Milky Way α_{CO} in the Antennae. (Wilson et al. 2003) first suggested this value based on comparison between virial mass and ^{12}CO J=1-0 luminosity. However, as we have discussed above, GMCs in starburst systems are not necessarily in virial equilibrium. Schirm et al. (2014) also suggest a typical α_{CO} value of ~ 7 M$_\odot$ (K km s^{-1} pc^2)$^{-1}$ based on two-component LVG modeling assuming $x_{CO} = 3 \times 10^{-5}$. They choose this value so that the hot component of gas from CO LVG modeling is comparable to the mass derived from H$_2$ emission. However, Harrington et al. (2021) suggest that the high-J CO transition fluxes that are used to constrain the second component might come from cold dense gas instead of hot diffuse gas, and hence not necessarily trace the same gas component as H$_2$ emission. If we adopt our preferred x_{co} value of 3×10^{-4}, the α_{CO} derived from Schirm et al. (2014) is consistent with our results.

4.6 Modeled CO-to-H_2 conversion factor at kpc scales

4.6.1 $\alpha_{\rm CO}$ comparison at GMC and kpc scales

Most previous studies on constraining the $\alpha_{\rm CO}$ have been done at kpc scales (e.g. Papadopoulos et al. 2012). Previous simulations (e.g Narayanan et al. 2012) argue that $\alpha_{\rm CO}$ should be a scale-free parameter down to cloud scale. However, there has been no observational evidence to test this statement yet due to limited resolution and sensitivity. In the Antennae, we have enough resolution elements and detections at both kpc and GMC scales to be able to perform this comparison.

We generate the $\alpha_{\rm CO}$ map at kpc scale by applying the same procedure as in Section 4.3 using the combo masked CO moment maps at 1 kpc resolution generated from the PHANGS-ALMA pipeline. To match the $\alpha_{\rm CO}$ maps at 150 pc and 1 kpc resolution, we regrid the 150 pc map to have the same pixel size as that of the 1 kpc map. For each regridded 150 pc map pixel, $\alpha_{\rm CO}$ is calculated as the ^{12}CO J=1-0 intensity averaged value of the smaller pixels that are associated with the regridded pixel,

$$\langle \alpha_{\rm CO,150pc} \rangle_{\rm 1kpc} = \frac{\sum \alpha_{\rm CO,150pc} I_{\rm CO(1-0)}}{\sum I_{\rm CO(1-0)}} \tag{4.27}$$

The comparison between $\alpha_{\rm CO}$ at both scales is shown in the upper panels of Fig. 4.17. We can see that $\alpha_{\rm CO}$ at kpc scale is generally consistent with $\alpha_{\rm CO}$ at GMC scale but with $\sim 20\%$ lower values. This result is generally what we expect since kpc-scale ^{12}CO J=1-0 emission might also include some diffuse component of molecular gas, which is warmer and more luminous and hence would have lower $\alpha_{\rm CO}$ values (Schirm et al. 2014; Kamenetzky et al. 2017). To quantify this effect, we also calculate the fraction of the emission at kpc scale that comes from dense GMCs. For each kpc-scale pixel, the total flux of GMC emission is calculated by summing up fluxes of all pixels in the 150 pc resolution map associated with the kpc-scale pixel and with valid $\alpha_{\rm CO}$ values. Then the fraction is calculated as

$$f_{\rm GMC} = \frac{\sum F^{\rm 150pc}_{\rm CO(1-0)}}{F^{\rm 1kpc}_{\rm CO(1-0)}} \tag{4.28}$$

where $F^{\rm 150pc}_{\rm CO(1-0)}$ and $F^{\rm 1kpc}_{\rm CO(1-0)}$ are the ^{12}CO J=1-0 flux of each pixel at GMC scale and kpc scale respectively. As shown in the upper left panel of Fig. 4.17, data points with high fraction ($\sim 100\%$) are closer to the 1-to-1 line, which is consistent with our expectation. We also split the data into two categories with $f_{\rm GMC}$ greater or smaller than 50% (Fig. 4.17, upper middle and right panel). As we can see, for pixels with $f_{\rm GMC} > 50\%$, $\alpha_{\rm CO}$ values at GMC and kpc scales are more consistent while for $f_{\rm GMC} < 50\%$, $\alpha_{\rm CO}$ at kpc scale is significantly lower. This comparison suggests that the lower $\alpha_{\rm CO}$ at kpc scales might be due to a diffuse molecular medium which is not detected in GMC-resolution data.

However, it is still under debate whether the diffuse component of molecular gas has higher or lower $\alpha_{\rm CO}$ compared to cold dense gas in GMCs. Liszt, Pety & Lucas (2010) show that $\alpha_{\rm CO}$ is relatively constant among different molecular gas components in our Milky Way. They suggest this constant $\alpha_{\rm CO}$ should be attributed to the offsetting effects of lower CO abundances with respect to $\rm H_2$ ($x_{\rm co}$) and a large $I_{\rm CO}/N_{^{12}\rm CO}$ ratio in low extinction gas. Recent studies by Ramambason et al. (2023) further suggest that the abundance factor plays a more dominant role and hence actually increases $\alpha_{\rm CO}$ in diffuse molecular gas. We note that our modeling does not have the ability to constrain $x_{\rm co}$. Therefore, the $\alpha_{\rm CO}$ we modeled is proportional to the $N_{^{12}\rm CO}/I_{\rm CO}$ ratio and hence does not reflect any $\alpha_{\rm CO}$ change due to CO abundance variation. For example, if the diffuse gas actually has lower $x_{\rm co}$, we would expect the actual $\alpha_{\rm CO}$ at kpc scale to be higher than our modeled values. We also note that our modeled $\alpha_{\rm CO}$ is higher in low surface density regions at GMC scales (Fig. 4.10), which seems to be contradictory to the conclusion that a diffuse component has lower $\alpha_{\rm CO}$. However, we note that all our modeled regions have ^{13}CO line detections and probably have higher gas densities than the diffuse gas component we refer to this section. Furthermore, as shown in Fig. 4.14, these low surface density regions actually have higher CO optical depths than the higher surface density regions while the diffuse gas here might actually have much lower optical depth.

4.6.2 $\alpha_{\rm CO}$ dependence at kpc scale

Due to limited resolution and sensitivity, previous studies are mostly focused on the kpc-scale $\alpha_{\rm CO}$ calibrations (e.g. Narayanan et al. 2012; Bolatto et al. 2013). These $\alpha_{\rm CO}$ prescriptions are widely applied to nearby galaxies (e.g. Sun et al. 2023). While these prescriptions generally catch the galaxy-to-galaxy variation, they are less well tested for $\alpha_{\rm CO}$ variation within individual galaxies. Our observations of the Antennae

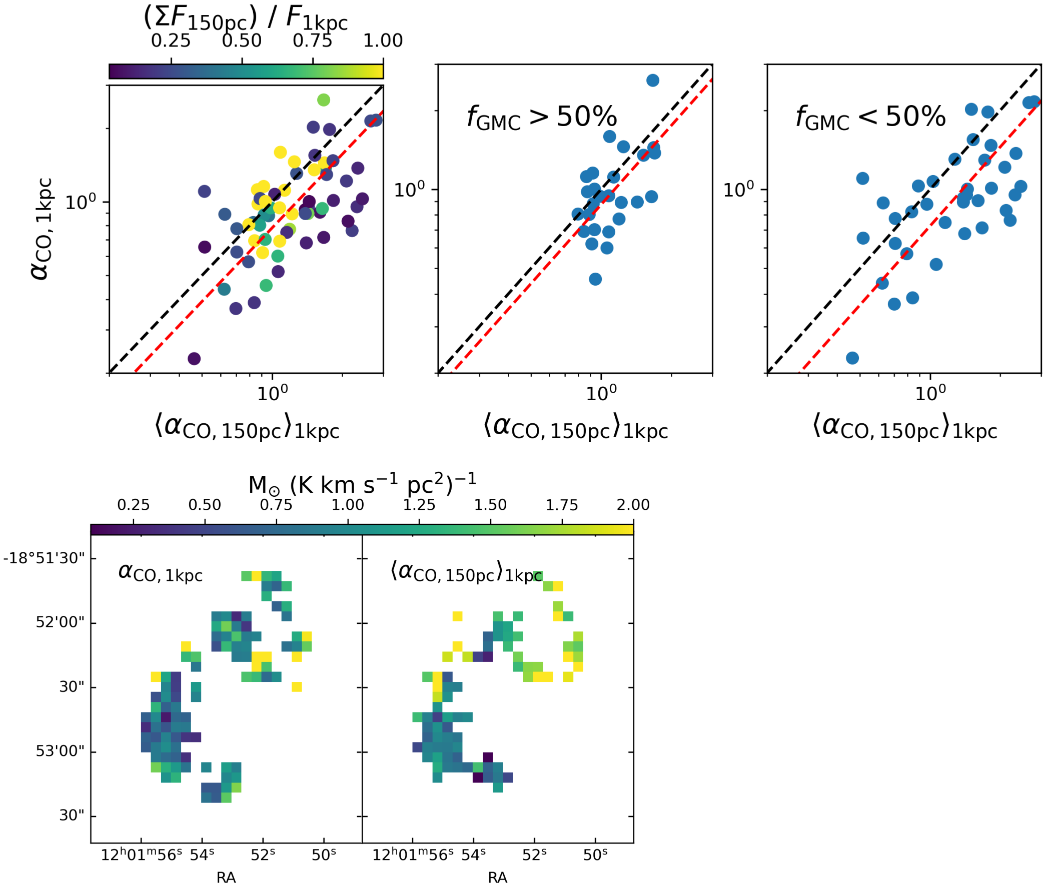

Figure 4.17: (*Top*) The comparison between α_{CO} at kpc scale ($\alpha_{CO,1kpc}$) and α_{CO} at 150 pc scale intensity averaged over kpc scale pixels ($\langle\alpha_{CO,150pc}\rangle_{1kpc}$). Pixels are color coded by the fraction of ^{12}CO J=1-0 emission at kpc scale that comes from GMC scales for each pixel (f_{GMC}, see text for detailed description). The middle and right panels show the data points with f_{GMC} greater and smaller than 50%, respectively. The black dashed line is the one-to-one while the red dashed line is the proportional fit to the data. We see that values of α_{CO} at kpc scales are generally consistent with averaged values of α_{CO} at GMC scales, especially if all the kpc CO emission comes from individual GMCs within the pixel. We can see that the RADEX derived α_{CO} at kpc scale is generally slightly smaller than the averaged GMC α_{CO}, which could be due to a diffuse component of molecular gas at kpc scales that has lower α_{CO} values. (*Bottom*) Maps of $\alpha_{CO,1kpc}$ and $\langle\alpha_{CO,150pc}\rangle_{1kpc}$.

provide an ideal test ground for kpc-scale α_{CO} variation within galaxies, specifically starburst systems. Besides metallicity dependence which we will discuss in Section 4.6.3, α_{CO} is also found to be dependent on ^{12}CO J=1-0 intensity (Narayanan et al. 2012) and total (stellar+gas) surface density (Bolatto et al. 2013). Therefore, we test these two dependencies in the Antennae (Fig. 4.18).

In the left panel of Fig. 4.18, we show α_{CO} versus $I_{\mathrm{CO1-0}}$ in comparison with simulation predictions. We can see a negative correlation between these two quantities with slope close to the two simulation predictions. We also see offsets between observed and simulation predicted absolute values. We note that the simulation by Hu et al. (2022) is focused on a typical kpc-size disk region in the Milky Way with a maximum $I_{\mathrm{CO1-0}}$ of 1 K km s^{-1} at kpc scales. Our observed $I_{\mathrm{CO1-0}}$ is clearly out of this range. We also note that our α_{CO} versus $I_{\mathrm{CO1-0}}$ correlation at GMC scale is in relatively good agreement with Hu et al. (2022) prediction. Therefore, the discrepancy in the kpc-scale α_{CO} versus $I_{\mathrm{CO1-0}}$ correlation might be caused by difference in GMC beam filling factor at kpc scales. If the number of GMCs inside the simulated kpc box were increased, we would expect higher kpc-scale $I_{\mathrm{CO1-0}}$ for a given α_{CO}, which would bring the simulation predicted relation rightward to become more aligned with our observed α_{CO}. On the other hand, the simulation from Narayanan et al. (2012) gives larger α_{CO} than our modeled results. It is possible that the true x_{co} is slightly lower than 3×10^{-4} and the actual α_{CO} in the Antennae might be higher than our derived values.

In the right panel of Fig. 4.18, we show α_{CO} versus the total surface density and compare it with the empirical relation by Bolatto et al. (2013). The absolute α_{CO} values occupy the right parameter space and are consistent with the theoretical expectation. However, we do not see a significant correlation between these two quantities for the Antennae alone (Pearson coefficient of -0.004) or the Antennae and other U/LIRGs combined (Pearson coefficient of -0.14). Therefore, it is possible that α_{CO} just has a bimodal distribution among normal spirals and U/LIRGs instead of a continuous dependence on the total surface densities. We also note that the α_{CO} derived in Sandstrom et al. (2013) uses the gas-to-dust ratio while the α_{CO} derived in the Antennae and U/LIRGs are based on LVG modeling; these different approaches can introduce some systematic uncertainties in α_{CO} comparison.

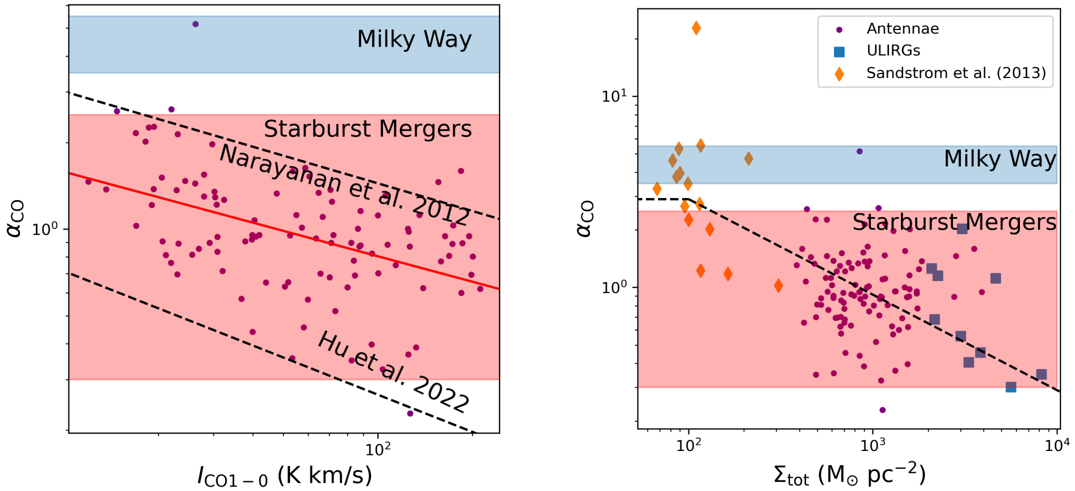

Figure 4.18: (*Left*) Modeled $\alpha_{\rm CO}$ versus ^{12}CO J=1-0 integrated intensity $I_{\rm CO(1-0)}$ at 1 kpc resolution. The red solid line is the power law fit to the data while the dashed lines are the simulation predicted relations from Narayanan et al. (2012) and Hu et al. (2022), respectively. We can see our fit relation has similar slope as the simulation predictions. (*Right*) Modeled $\alpha_{\rm CO}$ versus total surface density for the Antennae (purple), normal spiral galaxies (orange diamonds) and ULIRGs (blue squares). The dashed line is the prescription from Bolatto et al. (2013). We can see that the absolute value of $\alpha_{\rm CO}$ in the Antennae is generally consistent with the prediction of this prescription. However, we do not see a significant correlation between $\alpha_{\rm CO}$ and the total surface density for the Antennae alone.

4.6.3 α_{CO} dependence on metallicity

Various studies (e.g. Bolatto et al. 2013; Gong et al. 2020) suggest a primary driver for α_{CO} variation is metallicity. Therefore, we would expect the observed α_{CO} variation within the Antennae could also be caused by metallicity variations. To explore this α_{CO} dependence, we make metallicity measurements of each kpc-scale pixel using the HII region catalog in Gunawardhana et al. (2020). In their catalog, the metallicity of each H II region is derived by fitting the H II spectrum with an evolutionary population synthesis model, which is considered to be more accurate than deriving metallicity based on strong line ratios (e.g. Pagel et al. 1979). At GMC scale, HII regions are not necessarily associated with their closest GMC due to projection effect and different time evolutionary stages (Kruijssen et al. 2018; Pan et al. 2022), which could introduce large scatter in the α_{CO} vs metallicity relation. Therefore, it is better to average metallicities of H II regions and compare them with α_{CO} at kpc scale.

As shown in Fig. 4.19, we see no significant correlation between α_{CO} and metallicity. The primary reason is that the LVG modeling we applied cannot constrain x_{co}. The physical explanation behind the α_{CO} dependence on the metallicity is that gas with less metallicity is lacking in dust to shield the UV photon from dissociate CO molecules into neutral or ionized carbon (see Bolatto et al. 2013). This process will change x_{co}, which is not constrained in our LVG modeling. For example, the two low-metallicity kpc pixels might actually have lower x_{co} than our assumed value of 3×10^{-4}. However, we can see most regions in the Antennae have gas of solar metallicity. Therefore, we do not expect a large variation of x_{co} across the Antennae.

4.7 Conclusions

In this paper, we have constrained the spatial variation of the CO-to-H$_2$ conversion, α_{CO}, in the Antennae merger at both GMC and kpc scales based on high-resolution ALMA CO and ^{13}CO lines. Our main conclusions are summarized below.

- The ^{12}CO J=2-1/1-0 (~ 1) and ^{12}CO J=3-2/1-0 (~ 0.7) ratios in the Antennae are significantly higher than the commonly observed ratio in normal spiral galaxies (Leroy et al. 2021; Wilson et al. 2012). These large ratios suggest that molecular gas in this starburst system has higher volume density and/or kinetic temperature compared to normal spiral galaxies. In contrast, the ^{13}CO/^{12}CO

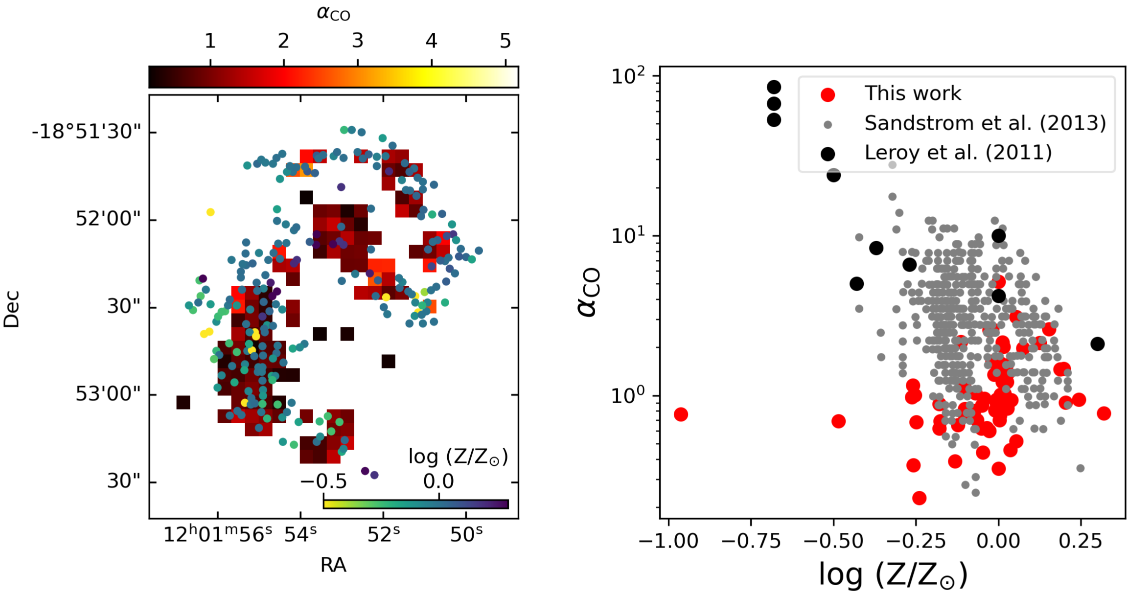

Figure 4.19: (*Left*) Modeled α_{CO} map at kpc scale overlaid by H II regions from Gunawardhana et al. (2020) The H II regions are color coded by the metallicity. (*Right*) α_{CO} versus metallicity for each kpc-scale pixel. The gray and black points are literature values for nearby spiral galaxies from Sandstrom et al. (2013) and Leroy et al. (2011). We can see there is no significant correlation between α_{CO} and metallicity within the Antennae.

J=1-0 and ^{13}CO/^{12}CO J=2-1 ratios (~ 0.1) in the Antennae are similar to those in normal spiral galaxies (Cormier et al. 2018). However, the two ratio values are probably resulted from compensation effect from larger CO optical depth and $X_{12/13}$ of the Antennae than those of normal spiral galaxies.

- Our modeling shows that α_{CO} is well constrained. We find that α_{CO} has a significant anti-correlation with GMC integrated intensity, $I_{\mathrm{CO1-0}}$, which is consistent with simulation predictions (Gong et al. 2020; Hu et al. 2022). This supports the argument that α_{CO} has a continuous dependence on $I_{\mathrm{CO1-0}}$ instead of a bimodal distribution among normal spiral and starburst galaxies.

- We find that α_{CO} has a strong tight linear correlation with the CO optical depth, which suggests that α_{CO} variations in starburst systems are mainly driven by optical depth variations rather than kinetic temperature variation. We also find a relatively tight correlation between α_{CO} and the ^{13}CO/^{12}CO J=1-0 ratio. This correlation is consistent with our expectation that the ^{13}CO/^{12}CO J=1-0 ratio can be a probe to the molecular gas optical depth. The scatter in the α_{CO} versus ^{13}CO/^{12}CO J=1-0 ratio is mainly driven by the varying [CO]/[^{13}CO] abundance ratio.

- We find that α_{CO} is also tightly related to the GMC dynamical state and shows strong anti-correlations with GMC velocity dispersion and virial parameter. In particular, the strong anti-correlation between α_{CO} and α_{vir} has a slope consistent with theoretical prediction of -0.5. This result is consistent with previous LVG studies on U/LIRGs (e.g. Papadopoulos et al. 2012), which suggested that the low α_{CO} in these systems are mainly caused by GMCs out of virial equilibrium.

- We compare our modeled gas surface density with 345 GHz dust continuum. Our comparison shows that our chosen CO-to-H$_2$ abundance ratio $x_{\mathrm{CO}} = 3 \times 10^{-4}$ gives us reasonable gas-to-dust ratios of ~ 100. Given this abundance ratio choice, we would expect most α_{CO} values in the Antennae are close to the typical U/LIRG value of 1.1 $\mathrm{M}_\odot$ (K km s^{-1} pc^2)$^{-1}$. This α_{CO} will put most GMCs in the Antennae out of virial equilibrium, which is consistent with simulation prediction of GMCs in starburst mergers (He et al. 2023).

- We compare luminosity weighted GMC-scale α_{CO} averaged at kpc resolution with the α_{CO} that are directly derived from kpc-resolution data. Our comparison shows that kpc-scale α_{CO} from LVG modeling is generally consistent with but slightly lower than the averaged values of α_{CO} at GMC scales. We suspect that the low α_{CO} values at kpc scales are mainly due to the additional large-scale component in velocity dispersion measurements.
- We also explore the dependence of modeled α_{CO} at kpc scales on various observables. We find that the kpc-scale α_{CO} shows a similar anti-correlation with CO intensity as predicted by simulations (e.g. Narayanan et al. 2012; Hu et al. 2022). We also tested the anti-correlation between α_{CO} and total surface density, Σ_{tot}, as suggested in Bolatto et al. (2013). We find α_{CO} of the Antennae lies along the trend with normal spiral galaxies and U/LIRGs. However, we do not see a significant correlation between α_{CO} and Σ_{tot}, especially for the Antennae alone or the Antennae and other U/LIRGs combined.
- We explore the dependence of kpc-scale α_{CO} on metallicity and do not find a significant anti-correlation. We suspect this is due to the limitation of our LVG modeling that are unable to constrain the CO-to-H_2 abundance ratio, which is affected by the metallicity. However, we find that most regions in the Antennae have metallicity values close to the solar metallicity. Therefore, we would expect the assumption of a constant CO-to-H_2 abundance ratio in the LVG modeling is an appropriate approximation.

Bibliography

Abdo, A. A., Ackermann, M., Ajello, M., et al. 2010, The Astrophysical Journal, 710, 133, doi: `10.1088/0004-637X/710/1/133`

Accurso, G., Saintonge, A., Catinella, B., et al. 2017, Monthly Notices of the Royal Astronomical Society, 470, 4750, doi: `10.1093/mnras/stx1556`

Amorín, R., Muñoz-Tuñón, C., Aguerri, J. A. L., & Planesas, P. 2016, Astronomy and Astrophysics, 588, A23, doi: `10.1051/0004-6361/201526397`

Bemis, A., & Wilson, C. D. 2019, The Astronomical Journal, 157, 131, doi: `10.3847/1538-3881/ab041d`

Bigiel, F., Leroy, A. K., Blitz, L., et al. 2015, The Astrophysical Journal, 815, 103, doi: `10.1088/0004-637X/815/2/103`

Bolatto, A. D., Leroy, A., Israel, F. P., & Jackson, J. M. 2003, The Astrophysical Journal, 595, 167, doi: `10.1086/377230`

Bolatto, A. D., Leroy, A. K., Rosolowsky, E., Walter, F., & Blitz, L. 2008, The Astrophysical Journal, 686, 948, doi: `10.1086/591513`

Bolatto, A. D., Wolfire, M., & Leroy, A. K. 2013, Annual Review of Astronomy and Astrophysics, 51, 207, doi: `10.1146/annurev-astro-082812-140944`

Boulanger, F., Abergel, A., Bernard, J. P., et al. 1996, Astronomy and Astrophysics, 312, 256

Bournaud, F., Daddi, E., Weiß, A., et al. 2015, A&A, 575, A56, doi: `10.1051/0004-6361/201425078`

Brown, T., & Wilson, C. D. 2019, The Astrophysical Journal, 879, 17, doi: `10.3847/1538-4357/ab2246`

Brunetti, N. 2022, Thesis

Brunetti, N., & Wilson, C. D. 2022, Monthly Notices of the Royal Astronomical Society, 515, 2928, doi: `10.1093/mnras/stac1975`

Brunetti, N., Wilson, C. D., Sliwa, K., et al. 2020, Monthly Notices of the Royal Astronomical Society, 500, 4730, doi: `10.1093/mnras/staa3425`

Bryant, P. M., & Scoville, N. Z. 1996, The Astrophysical Journal, 457, 678, doi: `10.1086/176763`

—. 1999, The Astronomical Journal, 117, 2632, doi: `10.1086/300879`

Carleton, T., Cooper, M. C., Bolatto, A. D., et al. 2017, Monthly Notices of the Royal Astronomical Society, 467, 4886, doi: `10.1093/mnras/stx390`

Chandar, R., Fall, S. M., Whitmore, B. C., & Mulia, A. J. 2017, The Astrophysical Journal, 849, 128, doi: `10.3847/1538-4357/aa92ce`

Cormier, D., Bigiel, F., Jiménez-Donaire, M. J., et al. 2018, Monthly Notices of the Royal Astronomical Society, 475, 3909, doi: `10.1093/mnras/sty059`

Dame, T. M., Hartmann, D., & Thaddeus, P. 2001, The Astrophysical Journal, 547, 792, doi: `10.1086/318388`

Donovan Meyer, J., Koda, J., Momose, R., et al. 2012, The Astrophysical Journal, 744, 42, doi: `10.1088/0004-637X/744/1/42`

Downes, D., & Solomon, P. M. 1998, ApJ, 507, 615, doi: `10.1086/306339`

Downes, D., Solomon, P. M., & Radford, S. J. E. 1993, The Astrophysical Journal, 414, L13, doi: `10.1086/186984`

Dunne, L., Maddox, S. J., Papadopoulos, P. P., Ivison, R. J., & Gomez, H. L. 2022, Monthly Notices of the Royal Astronomical Society, 517, 962, doi: `10.1093/mnras/stac2098`

Goldsmith, P. F., Heyer, M., Narayanan, G., et al. 2008, The Astrophysical Journal, 680, 428, doi: `10.1086/587166`

Gong, M., Ostriker, E. C., Kim, C.-G., & Kim, J.-G. 2020, The Astrophysical Journal, 903, 142, doi: `10.3847/1538-4357/abbdab`

Grenier, I. A., Casandjian, J.-M., & Terrier, R. 2005, Science, 307, 1292, doi: `10.1126/science.1106924`

Gunawardhana, M. L. P., Brinchmann, J., Weilbacher, P. M., et al. 2020, Monthly Notices of the Royal Astronomical Society, 497, 3860, doi: `10.1093/mnras/staa2158`

Harrington, K. C., Weiss, A., Yun, M. S., et al. 2021, The Astrophysical Journal, 908, 95, doi: `10.3847/1538-4357/abcc01`

He, H., Bottrell, C., Wilson, C., et al. 2023, Molecular Gas and Star Formation in Nearby Starburst Galaxy Mergers, doi: `10.48550/arXiv.2301.13250`

He, H., Wilson, C., Brunetti, N., et al. 2022, The Astrophysical Journal, 928, 57, doi: `10.3847/1538-4357/ac5628`

He, H., Wilson, C. D., Sliwa, K., Iono, D., & Saito, T. 2020, Monthly Notices of the Royal Astronomical Society, 496, 5243, doi: `10.1093/mnras/staa1826`

Heyer, M. H., Carpenter, J. M., & Snell, R. L. 2001, The Astrophysical Journal, 551, 852, doi: 10.1086/320218

Hu, C.-Y., Schruba, A., Sternberg, A., & van Dishoeck, E. F. 2022, ApJ, 931, 28, doi: 10.3847/1538-4357/ac65fd

Jiménez-Donaire, M. J., Bigiel, F., Leroy, A. K., et al. 2017, Monthly Notices of the Royal Astronomical Society, 466, 49, doi: 10.1093/mnras/stw2996

Kamenetzky, J., Rangwala, N., & Glenn, J. 2017, Monthly Notices of the Royal Astronomical Society, 471, 2917, doi: 10.1093/mnras/stx1595

Karl, S. J., Naab, T., Johansson, P. H., et al. 2010, The Astrophysical Journal, 715, L88, doi: 10.1088/2041-8205/715/2/L88

Kazandjian, M. V., Meijerink, R., Pelupessy, I., Israel, F. P., & Spaans, M. 2015, Astronomy and Astrophysics, 574, A127, doi: 10.1051/0004-6361/201322805

Keller, B. W., Wadsley, J., Benincasa, S. M., & Couchman, H. M. P. 2014, Monthly Notices of the Royal Astronomical Society, 442, 3013, doi: 10.1093/mnras/stu1058

Klaas, U., Nielbock, M., Haas, M., Krause, O., & Schreiber, J. 2010, Astronomy and Astrophysics, 518, L44, doi: 10.1051/0004-6361/201014670

Kruijssen, J. M. D., Schruba, A., Hygate, A. P. S., et al. 2018, Monthly Notices of the Royal Astronomical Society, 479, 1866, doi: 10.1093/mnras/sty1128

Langer, W. D., & Penzias, A. A. 1990, The Astrophysical Journal, 357, 477, doi: 10.1086/168935

Leroy, A. K., Bolatto, A., Gordon, K., et al. 2011, The Astrophysical Journal, 737, 12, doi: 10.1088/0004-637X/737/1/12

Leroy, A. K., Usero, A., Schruba, A., et al. 2017, The Astrophysical Journal, 835, 217, doi: 10.3847/1538-4357/835/2/217

Leroy, A. K., Schinnerer, E., Hughes, A., et al. 2021, ApJS, 257, 43, doi: 10.3847/1538-4365/ac17f3

Li, Z., Li, Z., Smith, M. W. L., et al. 2020, Monthly Notices of the Royal Astronomical Society, 492, 195, doi: 10.1093/mnras/stz3409

Magnelli, B., Saintonge, A., Lutz, D., et al. 2012, Astronomy and Astrophysics, 548, A22, doi: 10.1051/0004-6361/201220074

Maloney, P. 1990, The Astrophysical Journal, 348, L9, doi: 10.1086/185618

Matsushita, S., Iono, D., Petitpas, G. R., et al. 2009, The Astrophysical Journal, 693, 56, doi: 10.1088/0004-637X/693/1/56

Milam, S. N., Savage, C., Brewster, M. A., Ziurys, L. M., & Wyckoff, S. 2005, The Astrophysical Journal, 634, 1126, doi: 10.1086/497123

Mok, A., Chandar, R., & Fall, S. M. 2020, The Astrophysical Journal, 893, 135, doi: 10.3847/1538-4357/ab7a14

Montoya Arroyave, I., Cicone, C., Makroleivaditi, E., et al. 2023, Astronomy and Astrophysics, 673, A13, doi: 10.1051/0004-6361/202245046

Narayanan, D., Krumholz, M., Ostriker, E. C., & Hernquist, L. 2011, Monthly Notices of the Royal Astronomical Society, 418, 664, doi: 10.1111/j.1365-2966.2011.19516.x

Narayanan, D., Krumholz, M. R., Ostriker, E. C., & Hernquist, L. 2012, Monthly Notices of the Royal Astronomical Society, 421, 3127, doi: 10.1111/j.1365-2966.2012.20536.x

Olsen, K. P., Greve, T. R., Brinch, C., et al. 2016, Monthly Notices of the Royal Astronomical Society, 457, 3306, doi: 10.1093/mnras/stw162

Pagel, B. E. J., Edmunds, M. G., Blackwell, D. E., Chun, M. S., & Smith, G. 1979, Monthly Notices of the Royal Astronomical Society, 189, 95, doi: 10.1093/mnras/189.1.95

Pan, H.-A., Schinnerer, E., Hughes, A., et al. 2022, The Astrophysical Journal, 927, 9, doi: 10.3847/1538-4357/ac474f

Papadopoulos, P. P., van der Werf, P. P., Xilouris, E. M., et al. 2012, Monthly Notices of the Royal Astronomical Society, 426, 2601, doi: 10.1111/j.1365-2966.2012.21001.x

Pessa, I., Schinnerer, E., Belfiore, F., et al. 2021, Astronomy and Astrophysics, 650, A134, doi: `10.1051/0004-6361/202140733`

Planck Collaboration, Ade, P. A. R., Aghanim, N., et al. 2011, Astronomy and Astrophysics, 536, A19, doi: `10.1051/0004-6361/201116479`

Privon, G. C., Barnes, J. E., Evans, A. S., et al. 2013, Astrophysical Journal, 771, doi: `10.1088/0004-637X/771/2/120`

Ramambason, L., Lebouteiller, V., Madden, S. C., et al. 2023, Molecular Gas Distribution and CO-to-H2 Conversion Factors in CO-faint Low-Metallicity Dwarf Galaxies, doi: `10.48550/arXiv.2306.14881`

Rebolledo, D., Wong, T., Leroy, A., Koda, J., & Donovan Meyer, J. 2012, The Astrophysical Journal, 757, 155, doi: `10.1088/0004-637X/757/2/155`

Remy, Q., Grenier, I. A., Marshall, D. J., & Casandjian, J. M. 2017, Astronomy and Astrophysics, 601, A78, doi: `10.1051/0004-6361/201629632`

Renaud, F., Bournaud, F., Agertz, O., et al. 2019a, Astronomy & Astrophysics, 625, A65, doi: `10.1051/0004-6361/201935222`

Renaud, F., Bournaud, F., Daddi, E., & Weiß, A. 2019b, Astronomy & Astrophysics, Volume 621, id.A104, <NUMPAGES>5</NUMPAGES> pp., 621, A104, doi: `10.1051/0004-6361/201834397`

Salak, D., Nakai, N., Seta, M., & Miyamoto, Y. 2019, The Astrophysical Journal, 887, 143, doi: `10.3847/1538-4357/ab55dc`

Sandstrom, K. M., Leroy, A. K., Walter, F., et al. 2013, The Astrophysical Journal, 777, 5, doi: `10.1088/0004-637X/777/1/5`

Sargent, M. T., Daddi, E., Béthermin, M., et al. 2014, Astrophysical Journal, 793, doi: `10.1088/0004-637X/793/1/19`

Schirm, M. R. P., Wilson, C. D., Parkin, T. J., et al. 2014, The Astrophysical Journal, 781, 101, doi: `10.1088/0004-637X/781/2/101`

Schruba, A., Leroy, A. K., Walter, F., et al. 2012, The Astronomical Journal, 143, 138, doi: `10.1088/0004-6256/143/6/138`

Schweizer, F., Burns, C. R., Madore, B. F., et al. 2008, The Astronomical Journal, 136, 1482, doi: `10.1088/0004-6256/136/4/1482`

Scoville, N. Z., & Good, J. C. 1989, The Astrophysical Journal, 339, 149, doi: `10.1086/167283`

Scoville, N. Z., Yun, M. S., Clemens, D. P., Sanders, D. B., & Waller, W. H. 1987, The Astrophysical Journal Supplement Series, 63, 821, doi: `10.1086/191185`

Shetty, R., Glover, S. C., Dullemond, C. P., et al. 2011, Monthly Notices of the Royal Astronomical Society, 415, 3253, doi: `10.1111/j.1365-2966.2011.18937.x`

Sliwa, K., & Downes, D. 2017, Astronomy & Astrophysics, Volume 604, id.A2, <NUMPAGES>16</NUMPAGES> pp., 604, A2, doi: `10.1051/0004-6361/201630139`

Sliwa, K., Wilson, C. D., Aalto, S., & Privon, G. C. 2017a, The Astrophysical Journal, 840, L11, doi: `10.3847/2041-8213/aa6ea4`

Sliwa, K., Wilson, C. D., Iono, D., Peck, A., & Matsushita, S. 2014, The Astrophysical Journal, 796, L15, doi: `10.1088/2041-8205/796/1/L15`

Sliwa, K., Wilson, C. D., Matsushita, S., et al. 2017b, The Astrophysical Journal, 840, 8, doi: `10.3847/1538-4357/aa689b`

Sliwa, K., Wilson, C. D., Petitpas, G. R., et al. 2012, Astrophysical Journal, 753, doi: `10.1088/0004-637X/753/1/46`

Sliwa, K., Wilson, C. D., Krips, M., et al. 2013, Astrophysical Journal, 777, doi: `10.1088/0004-637X/777/2/126`

Sofia, U. J., Lauroesch, J. T., Meyer, D. M., & Cartledge, S. I. B. 2004, The Astrophysical Journal, 605, 272, doi: `10.1086/382592`

Solomon, P. M., Downes, D., Radford, S. J. E., & Barrett, J. W. 1997, The Astrophysical Journal, 478, 144, doi: `10.1086/303765`

Solomon, P. M., Rivolo, A. R., Barrett, J., & Yahil, A. 1987, The Astrophysical Journal, 319, 730, doi: `10.1086/165493`

Solomon, P. M., & Vanden Bout, P. A. 2005, Annual Review of Astronomy and Astrophysics, 43, 677, doi: 10.1146/annurev.astro.43.051804.102221

Strong, A. W., & Mattox, J. R. 1996, Astronomy and Astrophysics, 308, L21

Sun, J., Leroy, A. K., Schruba, A., et al. 2018, The Astrophysical Journal, 860, 172, doi: 10.3847/1538-4357/aac326

Sun, J., Leroy, A. K., Schinnerer, E., et al. 2020a, ApJL, 901, L8, doi: 10.3847/2041-8213/abb3be

Sun, J., Leroy, A. K., Ostriker, E. C., et al. 2020b, ApJ, 892, 148, doi: 10.3847/1538-4357/ab781c

Sun, J., Leroy, A. K., Rosolowsky, E., et al. 2022, The Astronomical Journal, 164, 43, doi: 10.3847/1538-3881/ac74bd

Sun, J., Leroy, A. K., Ostriker, E. C., et al. 2023, Star Formation Laws and Efficiencies across 80 Nearby Galaxies, doi: 10.48550/arXiv.2302.12267

Teng, Y.-H., Sandstrom, K. M., Sun, J., et al. 2022, The Astrophysical Journal, 925, 72, doi: 10.3847/1538-4357/ac382f

—. 2023, The Physical Drivers and Observational Tracers of CO-to-H2 Conversion Factor Variations in Nearby Barred Galaxy Centers, doi: 10.48550/arXiv.2304.04732

Ueda, J., Iono, D., Petitpas, G., et al. 2012, The Astrophysical Journal, 745, 65, doi: 10.1088/0004-637X/745/1/65

Van Der Tak, F. F., Black, J. H., Schöier, F. L., Jansen, D. J., & Van Dishoeck, E. F. 2007, Astronomy and Astrophysics, 468, 627, doi: 10.1051/0004-6361:20066820

Vigroux, L., Audouze, J., & Lequeux, J. 1976, Astronomy and Astrophysics, 52, 1

Vlahakis, C., van der Werf, P., Israel, F. P., & Tilanus, R. P. J. 2013, Monthly Notices of the Royal Astronomical Society, 433, 1837, doi: 10.1093/mnras/stt841

Whitmore, B. C., Brogan, C., Chandar, R., et al. 2014, ApJ, 795, 156, doi: 10.1088/0004-637X/795/2/156

Wilson, C. D., Rangwala, N., Glenn, J., et al. 2014, The Astrophysical Journal, 789, L36, doi: `10.1088/2041-8205/789/2/L36`

Wilson, C. D., Scoville, N., Madden, S. C., & Charmandaris, V. 2003, The Astrophysical Journal, 599, 1049, doi: `10.1086/379344`

Wilson, C. D., Petitpas, G. R., Iono, D., et al. 2008, The Astrophysical Journal Supplement Series, 178, 189, doi: `10.1086/590910`

Wilson, C. D., Warren, B. E., Israel, F. P., et al. 2012, Monthly Notices of the Royal Astronomical Society, 424, 3050, doi: `10.1111/j.1365-2966.2012.21453.x`

Wolfire, M. G., Hollenbach, D., & McKee, C. F. 2010, The Astrophysical Journal, 716, 1191, doi: `10.1088/0004-637X/716/2/1191`

Young, J. S., & Scoville, N. Z. 1991, Annual Review of Astronomy and Astrophysics, 29, 581, doi: `10.1146/annurev.aa.29.090191.003053`

Zhang, Q., Fall, S. M., & Whitmore, B. C. 2001, Observatory, 10

Zhu, M., Seaquist, E. R., & Kuno, N. 2003, The Astrophysical Journal, 588, 243, doi: `10.1086/368353`

Chapter 5

Summary and Future Work

5.1 Summary

Starburst galaxies represent a common population of galaxies in the early universe and hence are great laboratories to study the star formation (SF) in these most extreme environments. In particular, these starburst galaxies show an enhanced rate of star formation per unit molecular gas (Daddi et al. 2010), which implies real physical differences in the star formation process. In addition to a shorter time to convert gas to stars, observations also show that starburst environments produce a large fraction (up to 80%) of new stars in bound star clusters (e.g. Adamo et al. 2020). The clustering feature of star formation in these extreme environments produces much stronger feedback (Keller et al. 2014), which also brings strong galactic outflow and changes the overall interstellar medium budget (Smith et al. 2021). These studies show that the overall evolution and star formation of individual galaxies are strongly linked to the microphysics of star formation unit (e.g. GMCs and YMCs) at scales of $\sim 1 - 100$ pc. My Ph.D. thesis is hence focused on probing molecular and young star clusters at this extremely small scale using ALMA high-resolution submillimeter data and synthesizing the observational data with simulation predictions to understand the physics that drives the evolution of GMC dynamical states and regulates its efficiency to form stars.

In this thesis, I aimed to answer 3 critical questions concerning star formation at GMC scales. Based on a logical order, the first question is "how do we accurately measure GMC properties in starburst galaxy mergers", which is answered in chapter 4. The biggest challenge in observations so far is to constrain the CO-to-H_2 conversion factor, α_{CO}, that converts our measured CO intensity to actual GMC surface density. I apply RADEX modeling to multiple CO and ^{13}CO transitions of a well-studied starburst merger, the Antennae, from ALMA observations and derive α_{CO} for $\sim$ 1000 GMCs based on RADEX modeled physical quantities. I find that ^{12}CO J=1-0 intensity, ^{13}CO/CO ratio and GMC velocity dispersion/virial parameter are promising observables for α_{CO} calibration of individual GMCs. Then I come to the second question, "how do GMC properties evolve during different merging stages and how do they affect the overall star formation states of the merging galaxy", which is answered in chapter 3. In this project, I compare the FIRE-2 simulated mergers with our observed galaxy mergers, the Antennae and NGC 3256. I find that GMCs during the starburst event will become dispersed and less gravitationally bound. Compared to normal spiral galaxies, the virial parameter of GMCs in the simulated merger during the second passage is constantly higher by a factor of 10 – 100 while star formation activities are enhanced (depletion time decreased by a factor of 10), which suggests that other environmental factors besides GMC self-gravity help with enhancing SFR. I also find a strong anti-correlation between depletion time and molecular gas surface density, which is consistent with the superlinear Kennicutt-Schmidt relation observed in starburst U/LIRGs. This result supports the scenario that the shorter depletion time in starburst mergers could be due to a higher fraction of dense gas for gas with high surface densities. The third question is, "how are the star formation structures organized within GMCs", which is answered in chapter 2. In this chapter, I specifically focus on the unique star formation products of starburst mergers, the young massive clusters (YMCs) in the Antennae using high-resolution ALMA continuum data. I find that for massive GMCs (mass greater than 10^8 $M_\odot$), most new stars are created in these YMCs. I also find a tentative correlation that more massive GMCs tend to produce more massive YMCs. This means that for starburst systems with higher GMC mass, we are likely to find more YMCs that provides much stronger stellar feedback (Keller et al. 2014) than isolated stars. Furthermore, comparing with multi-wavelength observations of YMCs, I find it generally takes $\sim$ 1 Myr for these systems to start emerging from GMCs, which suggests a really short feedback timescale for these YMCs to start clearing up gas. Therefore, we would expect these YMCs might greatly speed up the GMC evolutionary pace, and hence lead to a shorter GMC lifetime.

5.2 Future Work

To understand the nature of star formation in starburst environments, we need high-resolution observations to probe structures such as giant molecular clouds (~ 100 pc) and young star clusters ($\sim$ pc). On the molecular gas side, ALMA has significantly changed the game and enabled us to probe the resolved molecular gas structures of massive starbursts such as those produced by major mergers that are traditionally too distant away to detect. Currently in the ALMA archive there are ~ 40 galaxies with GMC-resolution CO 2-1 data, which is a great treasure yet to be explored. On the star formation side, the recent launch of JWST provides us with a new frequency window to probe young massive star clusters (YMCs) that are still embedded in thick molecular clouds. Several Cycle 1 GO projects are targeting these YMCs in starburst systems (e.g. ERS 1328, GO 1701, 2581). In addition to observations, simulation tools have also been greatly improved and now have the ability to probe GMCs and YMCs (e.g. He et al. 2023; Li et al. 2022). Taking all these development together, now it is a great era to combine all the resources we have and focus on the star formation in these starburst galaxies.

My thesis provides a starting point to understand the molecular gas and star formation in the most extreme starburst environments. For a more comprehensive understanding of physics behind star formation in these systems and the ultimate goal to answer all the three critical questions I mentioned in the previous section, the two key aspects are: 1. to enlarge sample size of starburst galaxies we study; 2. to synthesize multi-wavelength high-resolution data from different observations.

The first key is crucial for us to obtain statistically robust conclusions on general star formation physics in starburst mergers. In this thesis, I mostly focused on the Antennae and NGC 3256, both of which are in an intermediate stage about to pass or just passed their second passage. Therefore, we still lack the observational data to resolve GMCs in the early and final stage of the merging process. Furthermore, their IR luminosity and SFR are actually at the lower end of U/LIRGs and also significantly lower than the extreme high-z starbursts (Daddi et al. 2010). To understand how galaxies evolve to their current status in the local universe, it is important to find closer analogues from U/LIRGs to high-z starburst galaxies. For extending my

$\alpha_{\rm CO}$ analyses to more U/LIRGs, I plan to use C I data from my recently accepted ALMA proposal (2023.1.00228.S) to constrain $\alpha_{\rm CO}$ in two LIRGs, NGC 5104 and IRAS F18293-3413). With the two C I lines, I can reliably determine the gas excitation temperature and column density, and hence provides another constraint on $\alpha_{\rm CO}$. This will also test the recent argument that $\alpha_{\rm CO}$ in U/LIRGs might be similar to that of Milky Way based on C I analyses (Dunne et al. 2022). For extending the GMC analyses FIRE-2 simulation project, I plan to apply the analyses a broader sample of U/LIRGs (~ 40) using GMC-resolution ALMA archival CO data. This will enable us to probe GMCs across different merging stages and perform a better matched comparison with simulation predictions.

The second key is crucial for us to build a complete picture of star formation process at different stages and ISM components featuring different wavelengths. Specifically, with the launch of JWST telescope, we can recover a large sample of embedded YMCs that are still hidden in GMCs. Both the Antennae and NGC 3256 have been observed with JWST with the focus to study star cluster formation. It is likely that the JWST IR detected YMCs are not as deeply embedded as ALMA radio detected YMCs, and hence are probably at a more evolved stage. By cross-matching these two types of clusters, we can better quantify the timescale for these YMCs at different stages. Furthermore, it is still not clear yet which stellar feedback mechanisms are dominant in dispersing the gas and terminating the star formation. Specifically, it has been argued whether the dust reprocessed infrared radiation is effective in dispersing gas (Krumholz et al. 2019, Menon et al. 2022). Combining ALMA radio continuum data with JWST infrared data, we can perform a dust SED fitting, which will enable us to accurately determine the infrared radiation pressure and compare it with other feedback pressures (e.g. photon-ionzing pressure, direct-radiation pressure and stellar wind) calculated from HST optical data.

Bibliography

Adamo, A., Zeidler, P., Kruijssen, J. M. D., et al. 2020, Space Science Reviews, 216, 69, doi: `10.1007/s11214-020-00690-x`

Daddi, E., Elbaz, D., Walter, F., et al. 2010, The Astrophysical Journal, 714, L118, doi: `10.1088/2041-8205/714/1/L118`

Dunne, L., Maddox, S. J., Papadopoulos, P. P., Ivison, R. J., & Gomez, H. L. 2022, Monthly Notices of the Royal Astronomical Society, 517, 962, doi: `10.1093/mnras/stac2098`

He, H., Bottrell, C., Wilson, C., et al. 2023, Molecular Gas and Star Formation in Nearby Starburst Galaxy Mergers, doi: `10.48550/arXiv.2301.13250`

Keller, B. W., Wadsley, J., Benincasa, S. M., & Couchman, H. M. P. 2014, Monthly Notices of the Royal Astronomical Society, 442, 3013, doi: `10.1093/mnras/stu1058`

Krumholz, M. R., McKee, C. F., & Bland-Hawthorn, J. 2019, Annual Review of Astronomy and Astrophysics, vol. 57, p.227-303, 57, 227, doi: `10.1146/annurev-astro-091918-104430`

Li, H., Vogelsberger, M., Bryan, G. L., et al. 2022, Monthly Notices of the Royal Astronomical Society, 514, 265, doi: `10.1093/mnras/stac1136`

Smith, M. C., Bryan, G. L., Somerville, R. S., et al. 2021, Monthly Notices of the Royal Astronomical Society, 506, 3882, doi: `10.1093/mnras/stab1896`

Appendix A

Tracking ALMA System Temperature with Water Vapor Data at High Frequency

The content of this chapter is a second revision of the manuscript text for publication under the following citation:

He, H.; Dent, W.R.F; Wilson, C. D. 2022, “Tracking ALMA System Temperature with Water Vapor Data at High Frequency", PASP, 134, 125001

Tracking ALMA System Temperature with Water Vapor Data at High Frequency

Abstract

As the world-leading submillimeter telescope, the ALMA observatory is now putting more focus on high-frequency observations at Band 7 – 10 (frequencies from 375 – 950 GHz). However, high-frequency observations often suffer from rapid variations in atmospheric opacity that directly affect the system temperature $T_{\rm sys}$. Current observations perform discrete atmospheric calibrations (Atm-cals) every few minutes, with typically 10 – 20 occurring per hour for high frequency observation and each taking 30 – 40 seconds. In order to obtain more accurate flux measurements and reduce the number of atmospheric calibrations (Atm-cals), a new method to monitor $T_{\rm sys}$ continuously is proposed using existing data in the measurement set. In this work, we demonstrate the viability of using water vapor radiometer (WVR) data to track the $T_{\rm sys}$ continuously. We find a tight linear correlation between $T_{\rm sys}$ measured using the traditional method and $T_{\rm sys}$ extrapolated based on WVR data with scatter of 0.5% – 3%. Although the exact form of the linear relation varies among different data sets and spectral windows, we can use a small number of discrete $T_{\rm sys}$ measurements to fit the linear relation and use this heuristic relationship to derive $T_{\rm sys}$ every 10 seconds. Furthermore, we successfully reproduce the observed correlation using atmospheric transmission at microwave (ATM) modeling and demonstrate the viability of a more general method to directly derive the $T_{\rm sys}$ from the modeling. We apply the semi-continuous $T_{\rm sys}$ from heuristic fitting on a few data sets from Band 7 to Band 10 and compare the flux measured using these methods. We find the discrete and continuous $T_{\rm sys}$ methods give us consistent flux measurements with differences up to 5%. Furthermore, this method has significantly reduced the flux uncertainty due to $T_{\rm sys}$ variability for one dataset, which has large precipitable water vapor (PWV) fluctuation, from 10% to 0.7%.

Keywords: *instrumentation: interferometers, atmospheric effects, techniques: interferometirc, telescope: ALMA*

A.1 Introduction

A.1.1 Flux Calibration in ALMA

Calibration is the process by which the astronomer converts electronic signals from the telescope into meaningful astronomical data. Accurate calibration is crucial for the Atacama Large Millimeter/submillimeter Array (ALMA), as millimeter and submillimeter wavelength radiation will be adversely affected by the atmosphere and the electronic signal path in a variety of ways, and the antennas will also be affected by the observing environment (Remjian et al. 2019, ALMA technical handbook, Chapter 10). One of the important calibration processes is the amplitude and flux calibration. The aim of this calibration is to convert the raw visibilities (and auto-correlations) from the correlator into brightness temperature or flux density by carefully tracking the instrumental and atmospheric variations and determining accurate conversion factors. Because of the large and rapidly varying opacity of water vapor, standard calibration procedures are less accurate at submillimeter wavelengths. For the flux calibration, a well defined scientific goal can be elucidated and set as the requirement. In numerous meetings and discussions, the scientific community originally made clear its desire to reach 1% flux density accuracy (e.g. Bachiller et al. 2003, report of the spring 2003 ASAC meeting), which means that we must be able to determine the overall flux density scale (and apply it to the visibilities and total power measurements) to 1% accuracy. In addition, the capability of achieving a dynamic range of 10000 or higher in ALMA images means that we must track the amplitude fluctuations to better than 1% (Yun et al. 1998). A later study by Moreno & Guilloteau (2002) showed that it is impractical to achieve 1% at submillimeter wavelengths, and so a requirement of 3% has been adopted for frequencies >300 GHz. The current achieved calibration accuracy for ALMA is 5% at the lower bands (100 GHz), 10% in mid-bands (200–400 GHz) and 20% in the higher bands (>400 GHz) (Remjian et al. 2019). This paper is part of the work being done to improve the overall flux calibration accuracy.

Currently there are two flux calibration strategies, the astronomical flux calibration and the direct instrumental amplitude calibration. The astronomical flux calibration method uses an astronomical source with known flux and scales up the recorded amplitude based on that flux standard. This method requires the astronomical source to be bright and have stable flux. Currently planets are used as the primary flux standard while quasars are also used as an alternative flux standard due to their compact size and availability over the sky. However, the estimated accuracy of the planets' fluxes is only about 10% (Remjian et al. 2019, 10.4.7). Therefore, people are still searching for ideal flux calibrators with high accuracy, especially at high frequencies. In addition to the flux calibrator standard, the relative sky transmission on the calibrator and the science target, as well as the time variability of the transmissions will also affect the overall flux calibration. This is the standard method currently used by ALMA. On the other hand, for a stable system, one can directly translate the measured counts in total power into flux units using a direct instrumental amplitude calibration method. Both methods rely on accurate measurement of the sky opacity and tracking its variations during the observation. At millimeter wavelengths, the changes in atmospheric transparency will usually be very modest, under 1% over 10 minutes about 80% of the time. Since the same amount of water vapor results in much larger opacities in the submillimeter, the transparency fluctuations in the submillimeter over characteristic calibration time scales will be much larger, typically several percent during median stability conditions and sometimes $>$ 10%.

For ALMA, both calibration methods require the precise measurement of the system temperature $T_{\rm sys}$ and complex gain G. $T_{\rm sys}$ represents the total thermal noise of the measurement. $T_{\rm sys}$ includes contributions from the sky, receiver, and system losses, with a large contribution coming from the sky temperature. Since ALMA is equipped with receivers of sufficiently low noise, the sky noise often dominates the total thermal noise. Therefore, it is necessary to track the changes in system temperatures caused by the fluctuations in the atmosphere. Current ALMA $T_{\rm sys}$ measurements use discrete atmosphere (ATM) calibrations done every few minutes with a cadence depending on the observing band. At low frequencies ($<$ 300 GHz), ALMA generally perform 2 or 3 $T_{\rm sys}$ measurements over a typical hour-long observation due to the assumed small variation in the atmosphere transmission. At high frequencies ($>$ 300 GHz), due to the rapid opacity change in atmosphere, ALMA generally perform 10 $\sim$ 20 ATM calibrations per hour. So the time overheads just due to ATM calibration can become quite significant – up to 15-20% at the highest bands (9 and 10, at 602–950 GHz). Moreover the variations of $T_{\rm sys}$ on timescales faster than the ATM calibration interval are not tracked with this discrete ATM calibration method. Therefore, one of the major goals in high-frequency flux calibration is to track $T_{\rm sys}$ more closely while also reducing the time spent on discrete ATM calibrations.

A.1.2 $T_{\rm sys}$ Measurements in Flux Calibration

The system temperature ($T_{\rm sys}$) is the fundamental parameter to determine the system sensitivity and the real flux of the source. Tsys includes various contributions, and can be written in a basic form as (adapted from Mangum 2017)

$$T_{\rm sys} = \frac{1}{\eta_{\rm f} e^{-\tau_{\rm sky}}} \left(T_{\rm rx} + \eta_{\rm f} T_{\rm sky} + (1 - \eta_{\rm f}) \times T_{\rm amb}\right) \tag{A.1}$$

where

- $T_{\rm rx}$ is receiver temperature
- $T_{\rm sky}$ is sky temperature
- $T_{\rm amb}$ is ambient temperature where spillover is assumed to be terminated
- $\eta_{\rm f}$ is the forward efficiency. This is equal to the fraction of the antenna power pattern that is contained within the forward hemisphere and is currently assumed to be 0.95
- $e^{-\tau_{\rm sky}}$ is the fractional transmission of the atmosphere, where $\tau_{\rm sky}$ is equal to the atmospheric opacity along the target's line of sight.

Note this equation is for single sideband (SSB) and sideband separating (2SB) receivers, which are used for ALMA Band 3 – 8 observation. For this configuration, the image sideband gain is assumed negligibly small. The Band 9 and 10 receivers are using the double sideband configuration and hence $T_{\rm sys}$ are calculated differently (Mangum 2017, Eq. 6). $T_{\rm sky}$ and $T_{\rm amb}$ can be further expressed as

$$\begin{aligned} T_{\rm sky} &= T_{\rm atm}(1 - e^{-\tau_{\rm sky}}) \\ T_{\rm amb} &\approx T_{\rm atm} \end{aligned} \tag{A.2}$$

where $T_{\rm atm}$ is the representative atmosphere temperature. Note that $T_{\rm amb} \approx T_{\rm atm}$ is a reasonable approximation when the opacity originates close to the ground (e.g. due to water vapor). Therefore, by combining equation A.1 and A.2, $T_{\rm sys}$ can be calculated as

$$\begin{aligned} T_{\rm sys} &= \frac{1}{\eta_{\rm f} e^{-\tau_{\rm sky}}} \left[T_{\rm rx} + T_{\rm amb}(1 - \eta_{\rm f} e^{-\tau_{\rm sky}}) \right] \\ &\approx \frac{1}{e^{-\tau_{\rm sky}}} \left(T_{\rm rx} + T_{\rm sky} \right) \text{ (where } \eta_{\rm f} \sim 1) \end{aligned} \tag{A.3}$$

This equation suggests that the key parameters to measure $T_{\rm sys}$ are $T_{\rm rx}$ and $T_{\rm sky}$ (as $\tau_{\rm sky}$ can be derived from $T_{\rm sky}$ using Eq. A.2).

In ALMA flux calibration, the intensity of the observed source is directly proportional to $T_{\rm sys}$ by the following equation (e.g. Brogan 2018)

$$S_{\rm final} \sim S_0 \times \sqrt{T_{\rm sys}(i) T_{\rm sys}(j)} \times \Gamma \tag{A.4}$$

where S_0 and $S_{\rm final}$ are the fluxes measured before and after the flux calibration. Γ is the antenna efficiency factor to convert K to Jy and i and j represent the two antennas forming the baseline. Note that ALMA uses an antenna-based calibration method to simplify the calibration process. Nearly all of the changes to the visibility function (e.g. atmosphere, system noise, amplitude changes, delay changes) can be decomposed into the two complex antenna-based gain factors associated with any baseline. This approach reduces the number of gain correction terms for an N-element array from $N(N-1)/2$ baselines to N antennas. In this case, $T_{\rm sys}$ is associated with each antenna and $S_{\rm final}$ is associated with each baseline.

$T_{\rm sys}$ also determines the achieved rms noise of the observation (e.g. Condon & Ransom 2016, a modified form of radiometer equation)

$$\text{rms} \approx \frac{c T_{\rm sys}}{\sqrt{\Delta\nu t_{\rm int}}} \tag{A.5}$$

where $\Delta\nu$ is the frequency bandwidth, $t_{\rm int}$ is the integration time of the observation and c includes the quantization and correlator efficiencies, and is typically 0.8-0.9 for ALMA. Therefore, higher $T_{\rm sys}$ means the data has a larger noise within one observation. In addition, for ALMA the weighting function used to combine visibility data is inversely proportional to $T_{\rm sys}$ as

$$\text{Weight} \propto \frac{1}{T_{\rm sys}(i) T_{\rm sys}(j)} \tag{A.6}$$

A.1.3 Traditional Method to Measure T_{sys}

As noted above, T_{sys} is highly dependent on the sky opacity (eq. A.2). ALMA antennas use a two-load system for T_{sys} measurement in Band 3 and higher, which is different from the one-load system used for other radio telescopes. The two-load system in theory can achieve a T_{sys} measurement accuracy of 1%, which is significantly better than that of a one-load system ("chopper wheel") of 5% (Yun et al. 1998). For ALMA, T_{sys} is obtained from an atmospheric calibration (ATM-cal) scan where a hot load, ambient load and sky are consecutively placed in front of the feed using an Amplitude Calibration Device (ACD; Casalta et al. 2008). Typically this process takes 30-40 seconds, including antenna slew time and overheads. At frequencies below about 400 GHz, where the system temperatures are more stable (except in the 183 and 325 GHz water lines), an ATM-cal scan is made every 10 to 20 minutes. However, at higher frequencies, and wherever the opacity is large and more variable, every scan on the astronomical target will have an associated ATM-cal measurement (Remjian et al. 2019), implying a cadence of ATM calibration as fast as once every 2-3 minutes. From the two-load system, we can also measure T_{rx}. In this case, the measured power can be expressed as (Mangum 2002)

$$\begin{aligned} P_{\text{hot}} &= K\ (T_{\text{rx}} + T_{\text{hot}}) \\ P_{\text{amb}} &= K\ (T_{\text{rx}} + T_{\text{amb}}) \\ P_{\text{sky}} &= K\ (T_{\text{rx}} + T_{\text{sky}}) \end{aligned} \tag{A.7}$$

where K is the gain to convert the temperature to the measured power. T_{hot} and T_{amb} are generally about 350 K and 290 K. Based on the equation above, we can express T_{rx} and T_{sky} as

$$\begin{aligned} T_{\text{rx}} &= \frac{T_{\text{hot}} P_{\text{amb}} - T_{\text{amb}} P_{\text{hot}}}{P_{\text{hot}} - P_{\text{amb}}} \\ &= \frac{T_{\text{hot}} - Y_1 T_{\text{amb}}}{Y_1 - 1} \\ T_{\text{sky}} &= \frac{P_{\text{sky}} T_{\text{amb}} - (P_{\text{amb}} - P_{\text{sky}}) T_{\text{rx}}}{P_{\text{amb}}} \\ &= Y_2 T_{\text{amb}} - (1 - Y_2) T_{\text{rx}} \end{aligned} \tag{A.8}$$

where $Y_1 \equiv P_{\rm hot}/P_{\rm amb}$ and $Y_2 \equiv P_{\rm sky}/P_{\rm amb}$. Unlike the atmosphere, $T_{\rm rx}$ is relatively constant throughout the observation. Measurements performed by ALMA show fluctuations of $T_{\rm rx}$ are generally smaller than 1% during normal sidereal tracking. With the measurement of $T_{\rm sky}$, we can further derive the optical depth based on Eq. A.2 and calculate the $T_{\rm sys}$ based on Eq. A.3. In summary, the expressions for the key quantities to measure $T_{\rm sys}$ are

$$\begin{aligned} T_{\rm rx} &= \frac{T_{\rm hot} - Y_1 T_{\rm amb}}{Y_1 - 1} \approx {\rm const} \\ T_{\rm sky} &= Y_2 T_{\rm amb} - (1 - Y_2) T_{\rm rx} \\ T_{\rm sys} &\approx \frac{1}{e^{-\tau_{\rm sky}}} \left(T_{\rm rx} + T_{\rm sky} \right) \end{aligned} \tag{A.9}$$

Therefore, during each ATM cal, we point the array to hot load, ambient load and sky to measure $T_{\rm rx}$ and $T_{\rm sky}$ and then calculate the $T_{\rm sys}$ at that time.

A.1.4 Candidate Data to Track the Continuous $T_{\rm sys}$

As mentioned above, the current method takes extra time to obtain a spot measurement of $T_{\rm sys}$ every few minutes. If we want to continuously track $T_{\rm sys}$, in theory there are 3 types of measurement data available from ALMA to achieve this goal: Water Vapor Radiometer (WVR) data, auto-correlation (AC) data or square law detector (SQLD) data. We will describe where these data arise, and the theory behind each method below. The advantages and disadvantages of each method are summarized in Table. A.1.

Table A.1: Summary of different methods to track T_{sys}

	WVR[1]	AC & SQLD[2]
Advantage	1. Continuously calibrated to measure T_{WVR}[a]	1. Directly proportional to T_{sys} when τ_{sky} is small
	2. Not affected by internal electronic gain drift[b]	2. At same frequency as the science target
Disadvantage	1. At different frequency as the science target	1. The data is not calibrated.
	2. Directly tracks T_{sky} not T_{sys}	2. Affected by electronic gain drift[b] or gain variations
		3. For AC, no linearity correction in FDM mode.

Columns: 1. Water vapor radiometer data. 2. Auto-correlation and square law detector data.
References: a. Hills et al. (2001). b. Payne et al. (2001).

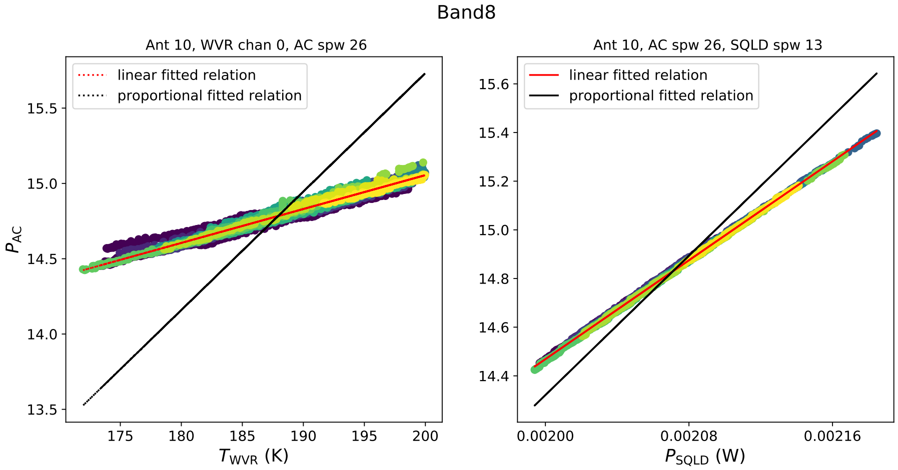

Figure A.1: The correlation between water vapor radiometer (WVR) data, autocorrelation (AC) data and square law detector (SQLD) data for antenna 10 for dataset Band8 data. The scatter plots are color coded by the scan number. (Left) AC data versus WVR data. The red line is the best linear fit and black line is the proportional fit through 0. We have excluded WVR data greater than 200 as those are from samples taken on the hot load and ambient load. (Right) AC data versus SQLD data.

The WVR data are used by ALMA to track the optical depth of the water vapor along the line of sight to each antenna, and hence are used to correct for the resulting effective pathlength and delay errors. The WVRs do Dicke switching and have internal calibrated loads, so the output from each WVR is the calibrated sky temperature (T_{WVR}) at 4 frequencies (184.19, 185.25, 186.485 and 188.51 GHz respectively; Hills 2004) around the 183 GHz water line taken every 1.152 seconds (Remjian et al. 2019, Section A.6). By comparing T_{WVR} with T_{amb}, we can calculate the precipitable water vapour (PWV), which is proportional to the atmospheric opacity caused by the water absorption. Since T_{sky} at our observing frequency (Eq. A.9) and T_{WVR} are tracking sky temperatures at different frequencies, we would expect

$$\begin{aligned} \tau_{\mathrm{sky}} &= C \times \tau_{\mathrm{WVR}} + \tau_{\mathrm{dry}} \\ T_{\mathrm{sky}} &= C \times T_{\mathrm{WVR}} + T_{\mathrm{sky,dry}} \quad (\tau_{\mathrm{sky}}, \tau_{\mathrm{WVR}} << 1) \end{aligned} \tag{A.10}$$

where τ_{sky} is the sky opacity at the observed frequencies , τ_{WVR} is the optical depth at the WVR channel frequency, τ_{dry} and $T_{\mathrm{sky,dry}}$ are the optical depth and sky temperature contribution for the dry component at the observing frequency, and C is a constant. A small dry contribution to τ_{WVR} and T_{WVR} is not explicitly shown but does not change the form of the relationship. The overall sky opacity includes contributions from the wet component (H_2O lines from the troposphere which are relatively wide due to pressure broadening), and from the dry component (mostly due to lines of O_2 and O_3, but also including a continuum component as well as other molecules). If optical depth is small enough, we would expect the observed temperature is proportional to the optical depth and hence the proportion relation between the two optical depths holds also for the two measured temperatures. Since the major change in $T_{\rm sys}$ is caused by the variation in $T_{\rm sky}$, we would expect that T_{WVR} is tracking $T_{\rm sys}$. The major advantage of using the WVR data to trace $T_{\rm sys}$ is that the radiometer is constantly monitoring the sky and internally calibrating itself. Therefore, we can extrapolate $T_{\rm sys}$ throughout the entire observation based on the WVR data. Furthermore, since T_{WVR} is internally calibrating and tracking the sky variation, it does not suffer from the internal electronic drift or small changes in system gain, which can affect the measured values of an uncalibrated signal (see Table A.1).

Alternatively, we would expect $T_{\rm sys}$ is tightly correlated with the total power signal received by each antenna. To be more precise, the total power signal should be directly proportional to $(T_{\rm rx}+T_{\rm sky})$, which can be used to calculate $T_{\rm sys}$ given the optical depth $\tau_{\rm sky}$ using Eq. A.9 (see detailed discussion in Section A.4). The total power signal received by each antenna is measured by a square-law detector (SQLD) built into the ALMA signal path, whose data is also recorded in the datasets. Additionally, the autocorrelation data recorded in the measurement set should also give us the total signal received by each antenna. We would expect

$$T_{\rm rx} + T_{\rm sky} \propto P_{\mathrm{AC}} \propto P_{\mathrm{SQLD}} \tag{A.11}$$

where P_{AC} and P_{SQLD} are the power of auto-correlation data and SQLD data read from the measurement set, respectively. If $\tau_{\rm sky}$ is small, we would expect direct proportionality between $T_{\rm sys}$ and the total power received which could help us derive continuous $T_{\rm sys}$. In addition, both AC and SQLD data cover the same frequency rangels as the actual observed science data so we do not need to assume atmosphere variation has the same effect on data at different wavelengths (the constant C in Eq. A.10 and the explicit dry contributions).

In Fig. A.1, we plot the correlation between AC and WVR and SQLD data. We can see the AC and SQLD data follow a tighter linear correlation. These two types of data are expected to be equivalent and thus should follow a proportional correlation. We see an offset from direct proportionality between AC and SQLD data in this observation as no linearity correction for the effect of the 3 bit samplers is applied in this correlator mode, and there can be residual DC offsets in the SQLD data. On the other hand, we can see that the WVR and AC data do not follow the same proportional relation. This can be caused by various reasons summarized in Table A.1. In particular, the distribution in the AC data at similar WVR levels on the left panel is indicative of slightly different system gains in different scans during the observation, or the differing wet and dry opacity contributions at different aimasses. In this case, we need to compare the two types of data to explore which one is better in tracking $T_{\rm sys}$.

A.1.5 Outline of This Paper

In the following sections, we will explore how well different data track $T_{\rm sys}$ measurements. In Section 2, we explore the viability of using $T_{\rm WVR}$ to track $T_{\rm sys}$. In Section 3, we use the Atmospheric Transmission at Microwave (ATM) modeling to test the theory behind the tight $T_{\rm sys}$ vs $T_{\rm WVR}$ correlation. In Section 4, we explore the viability to use AC or SQLD data to track $T_{\rm sys}$. What we find is that those two types of data do not work well in tracking $T_{\rm sys}$. In Section 5, we describe our new calibration method to use alternative $T_{\rm sys}$ derived from $T_{\rm WVR}$ and how it compares to the original discrete calibration method.

For our analysis, we use measurement sets from several projects in Bands 7, 8, 9 and 10 (Mahieu et al. 2012; Sekimoto et al. 2008; Baryshev et al. 2015; Gonzalez et al. 2014). We also include two projects with multiple measurement sets from Band 7 and 9. The summary of the data we use is given in Table A.2.

Table A.2: Summary of Data

Dataset Label (1)	Project (2)	Band (3)	Target (4)	Data uid (5)	PWV (mm) (6)	Elev. (deg) (7)
Band10	2015.1.00271.S	10	Arp 220	uid://A002/Xbe0d4d/X12f5	0.28	43
Band9a	2016.1.00744.S	9	IRAS16293-B	uid://A002/Xbf792a/X14cc	0.37	63 – 76
Band8	2018.1.01778.S	8	SPT0311-58	uid://A002/Xdb7ab7/X1880b	0.85	53 – 55
Band7a	E2E8.1.00003.S	7	HT-Lup	uid://A002/Xec4ed2/X912	0.59	52 – 66
Band7b1	2018.1.01210.S	7	AS205A	uid://A002/Xda1250/X2387	0.69	50 – 64
Band7b2				uid://A002/Xda1250/X32df	0.53	80 – 85
Band7b3				uid://A002/Xda845c/X35d1	0.5	55 – 70
Band7b4				uid://A002/Xda1250/X3e39	0.51	60 – 75
Band7b5				uid://A002/Xda1250/X4db3	0.49	35 – 50
Band7b6				uid://A002/Xd99ff3/X15d7b	0.42	65 – 80
Band7b7				uid://A002/Xd99ff3/X1702c	0.51	63 – 77
Band7b8				uid://A002/Xd99ff3/X17da2	0.53	40 – 55
Band9b1	2019.1.00013.S	9	Circinus	uid://A002/Xed9025/X769c	0.43	34 – 42
Band9b2				uid://A002/Xed8123/X7b1	0.37	37 – 43
Band9b3				uid://A002/Xed4607/X1208a	0.34	31 – 39

Columns: (1) Label for each dataset used in this paper (2) ALMA project code (3) Observed Band. (4) The name of the science target to be observed (5) The ALMA Unique Identifier (UID) of each execution (6) The precipitable water vapor (PWV) column. (7) Elevation range of the science target

A.2 WVR Data to Track $T_{\rm sys}$

In this section, we examine how well $T_{\rm WVR}$ tracks $T_{\rm sys}$ and explore how the correlation is affected by various parameter choices. We mainly use the dataset Band8 (uid://A002/Xdb7ab7/X1880b) for illustration purposes. Examples from additional datasets are given in Appendix **??**.

A.2.1 $T_{\rm sys}$ versus $T_{\rm WVR}$

To check whether $T_{\rm sys}$ is tracked by the WVR data, we first need to match the WVR data taken at the same time as the $T_{\rm sys}$ measurements. We then average the WVR values that are within 10 s around the time when $T_{\rm sys}$ is measured and compare the averaged $T_{\rm WVR}$ with its corresponding $T_{\rm sys}$. 10 s is a typical time for one Atm-cal scan and hence is the shortest timescale we expect $T_{\rm sys}$ to change. We also note that $T_{\rm sys}$ recorded in the measurement set is a spectrum with two polarizations. In our analyses to compare $T_{\rm sys}$ with $T_{\rm WVR}$, we average $T_{\rm sys}$ from both polarizations and also along the spectral axis within one spectral window (spw).

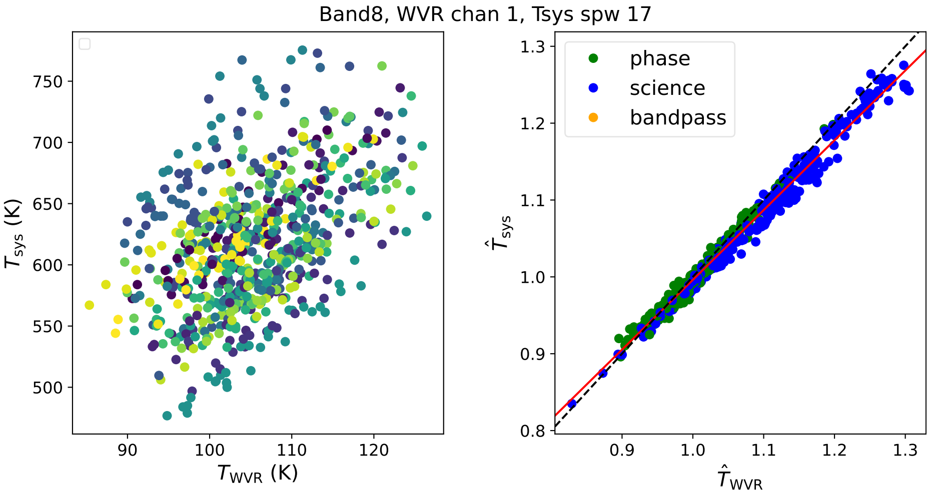

Figure A.2: (Left) $T_{\rm sys}$ vs $T_{\rm WVR}$ for dataset Band8 color coded by different antennas. (Right) $T_{\rm sys}$ and $T_{\rm WVR}$ normalized to the value of first scan of each target (bandpass, phase, science) for each antenna. We can see the normalized $\hat{T}_{\rm sys}$ and $\hat{T}_{\rm WVR}$ follows a tight linear correlation.

We first plot $T_{\rm sys}$ versus $T_{\rm WVR}$ from all antennas for each data set. One example of $T_{\rm sys}$ versus $T_{\rm WVR}$ is shown in the left panel of Fig. A.2. For this case, we select $T_{\rm WVR}$ from WVR channel 1. We will discuss in Section A.2.2 how the selection of different WVR channels affects the relation between $T_{\rm WVR}$ and $T_{\rm sys}$. As we can see, there is a significant correlation between $T_{\rm sys}$ and $T_{\rm WVR}$ for each spw. However, the scatter is large along the direction perpendicular to the trend, as expected due to the differences in the receiver ($T_{\rm rx}$ and sideband gains) and WVR between antennas. Furthermore, since bandpass, phase-cal and science observations are observing targets at different elevations, it is possible that the scatter is also caused by data from different types of observations. Therefore, to see if the WVR tracks the time variation of $T_{\rm sys}$, we normalize $T_{\rm sys}$ and $T_{\rm WVR}$ by the first measurement for each observing target (bandpass, phase-cal and science) of each antenna as

$$\begin{aligned} \hat{T}_{\rm sys,source}(t) &= \frac{T_{\rm sys,obs}(t)}{T_{\rm sys,obs}(1^{\rm st})} \\ \hat{T}_{\rm WVR,obs}(t) &= \frac{T_{\rm WVR,obs}(t)}{T_{\rm WVR,obs}(1^{\rm st})} \end{aligned} \tag{A.12}$$

where $\hat{T}_{\rm sys}$ and $\hat{T}_{\rm WVR}$ are the normalized values of $T_{\rm sys}$ and $T_{\rm WVR}$, the subscript 'obs' is the generalized term for each type of observing target (bandpass, phase and science) and $1^{\rm st}$ in the bracket means the value when the first $T_{\rm sys}$ for each observing target is measured.

The correlation between the $\hat{T}_{\rm sys}$ and $\hat{T}_{\rm WVR}$ is shown in the right panel of Fig. A.2. We can see that these two variables have a tight linear correlation, with scatter less than 1%. This tight linear correlation is also seen in other data sets, as illustrated in Appendix **??**. This indicates that $T_{\rm WVR}$ can be used to track the $T_{\rm sys}$ if the slope and intercept can be determined for each spw or frequency. As described by eq. A.10, the relation is expected to be frequency dependent, and it further differs from 1-to-1 due to the other contributions to $T_{\rm sys}$ apart from $T_{\rm sky}$ (e.g. Eq. A.1 and A.3). In Section A.3, we explore the relationship using an atmospheric opacity model, but here we take a heuristic approach to determine the linear relationship from the data itself.

We can then use the fitted linear relation to extrapolate the continuous $T_{\rm sys}$ based on the first $T_{\rm sys}$ value for each observing target and the stream of $T_{\rm WVR}$ values. The exact equation can be expressed as

$$\begin{aligned} T_{\rm sys}(t) &= T_{\rm sys}(1^{\rm st}) \cdot \hat{T}_{\rm sys,obs}(t) \\ &= T_{\rm sys}(1^{\rm st}) \cdot \left[m\ \hat{T}_{\rm WVR,obs}(t) + b\right] \end{aligned} \tag{A.13}$$

where $T_{\rm sys}(1^{\rm st})$ are $T_{\rm sys}$ values used to normalize each antenna and each type of observing targets. m and b are the slope and intercept of the fitted linear function. For making the extrapolation, we also sample and average the WVR data every 10 seconds to be consistent with our fitting parameter choice. An example of extrapolated $T_{\rm sys}$ for one antenna is shown in Fig. A.3. As we can see, the extrapolated continuous $T_{\rm sys}$ is consistent with the original discrete $T_{\rm sys}$ values for all 4 spectral windows. The trend is also quite continuous with no obvious glitches due to the measurement noise. The trends for all 4 spectral windows are similar.

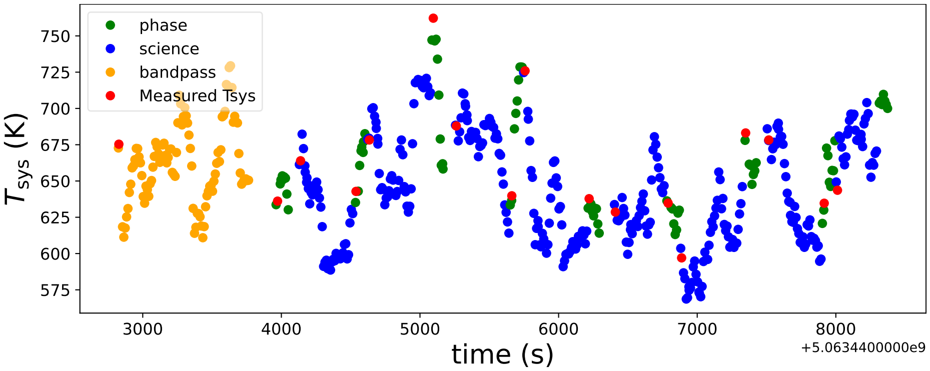

Figure A.3: The extrapolated $T_{\rm sys}$ versus the original $T_{\rm sys}$ for antenna 10 of the dataset Band8 at spw 17. The orange, green and blue points are extrapolated continuous $T_{\rm sys}$ for each observing target based on Eq. A.13 while the red points are original $T_{\rm sys}$ measurements.

Examples of fitting and $T_{\rm sys}$ extrapolation for other datasets are shown in Appendix ??. We can see for all datasets that $\hat{T}_{\rm sys}$ and $\hat{T}_{\rm WVR}$ have a tight linear correlation but with different slopes and intercepts. The extrapolation also works well for most of the data sets.

A.2.2 Extrapolate $T_{\rm sys}$ with Other WVR Channels and PWV

The ALMA WVRs have 4 filter channels at frequencies (184.19, 185.25, 186.485 and 188.51 GHz respectively) close to the 183GHz H_2O line (Hills et al. 2001). These channels have different sensitivities to the line-of-sight water content (PWV) and hence $T_{\rm sys}$, depending on the actual PWV at the observing time. In this section, we explore how the different parameter choices will affect the correlation between $T_{\rm sys}$ and $T_{\rm WVR}$. In Section A.2.1, we selected $T_{\rm WVR}$ in channel 1 to track $T_{\rm sys}$. Here we compare how well $T_{\rm WVR}$ from different WVR channels track the $T_{\rm sys}$ from different spectral

Table A.3: RMS of the T_{sys} residual from the fitting

T_{sys} spws / WVR chans	17	19	21	23
0	1%	1.1%	0.9%	0.9%
1	0.9%	1.1%	0.8 %	0.8%
2	1%	1.1%	0.9%	0.9%
3	1.4%	1.7%	1.3%	1.3%
$\mathrm{PWV}_{\mathrm{los}}$	0.8%	0.9%	0.7%	0.7%

The root mean square (RMS) of the residual from the linear fitting using T_{WVR} from different WVR channels and calculated PWV values along the line of sight (without elevation correction) for dataset Band8. The $\mathrm{PWV}_{\mathrm{los}}$ value for dataset Band8 is $\sim$ 1.05 mm.

windows by calculating the scatter of the data residual from the fitting (Table A.3). We can see that for these observing conditions ($\mathrm{PWV}_{\mathrm{los}}$ of 1.05 mm), the normalized $\hat{T}_{\mathrm{WVR}}$ from different WVR channels have a similarly tight correlation with normalized $\hat{T}_{\mathrm{sys}}$ with scatter of $\sim$ 1%. For dataset Band8, $\hat{T}_{\mathrm{WVR}}$ from WVR channel 1 gives us the tightest linear correlation. We will discuss the reason later in this section.

For single dish telescopes such as APEX and JCMT, WVR data has been used to continuously track optical depth at the observed frequencies (e.g. Dempsey et al. 2013). The method converts T_{WVR} values from multiple WVR channels into a single PWV value and use it to track the optical depth at any given time, which reduces the effect of measurement noise from a single channel. Given what we are doing is similar, as T_{sys} is mostly affected by the change in atmospheric optical depth, we can try to use PWV along the line of sight ($\mathrm{PWV}_{\mathrm{los}}$) instead of T_{WVR} from a specific channel to track T_{sys}. We calculate the $\mathrm{PWV}_{\mathrm{los}}$ by fitting the Lorentz profile for the water line given the T_{WVR} from multiple WVR channels. We then normalize the $\mathrm{PWV}_{\mathrm{los}}$ values the same way as we do for T_{WVR} (Eq. A.12). The scatter of fit residual using $\mathrm{PWV}_{\mathrm{los}}$ is also listed in Table A.3. As we can see, $\mathrm{PWV}_{\mathrm{los}}$ actually gives a tighter correlation, which is consistent with our expectation since it is less affected by the measurement noise from the single channel.

In our later analysis to apply the continuous T_{sys} in data calibration, we select WVR channels to maximize the following weighting function

$$w = \overline{T}_{\mathrm{WVR}}(\overline{T}_{\mathrm{WVR}} - 275) \tag{A.14}$$

where $\overline{T}_{\rm WVR}$ is the averaged $T_{\rm WVR}$ in one channel and 275 K is the approximate atmosphere temperature. The principle for this selection criterion is to make $T_{\rm WVR}$ neither too small to be robust against noise (in the case of low opacity) nor too large to be saturated (in the case of high opacity). Based on this criterion, we generally select WVR channel 0 or 1 for datasets in our analysis.

A.2.3 Fewer Atm-cal scans to Fit the Relation

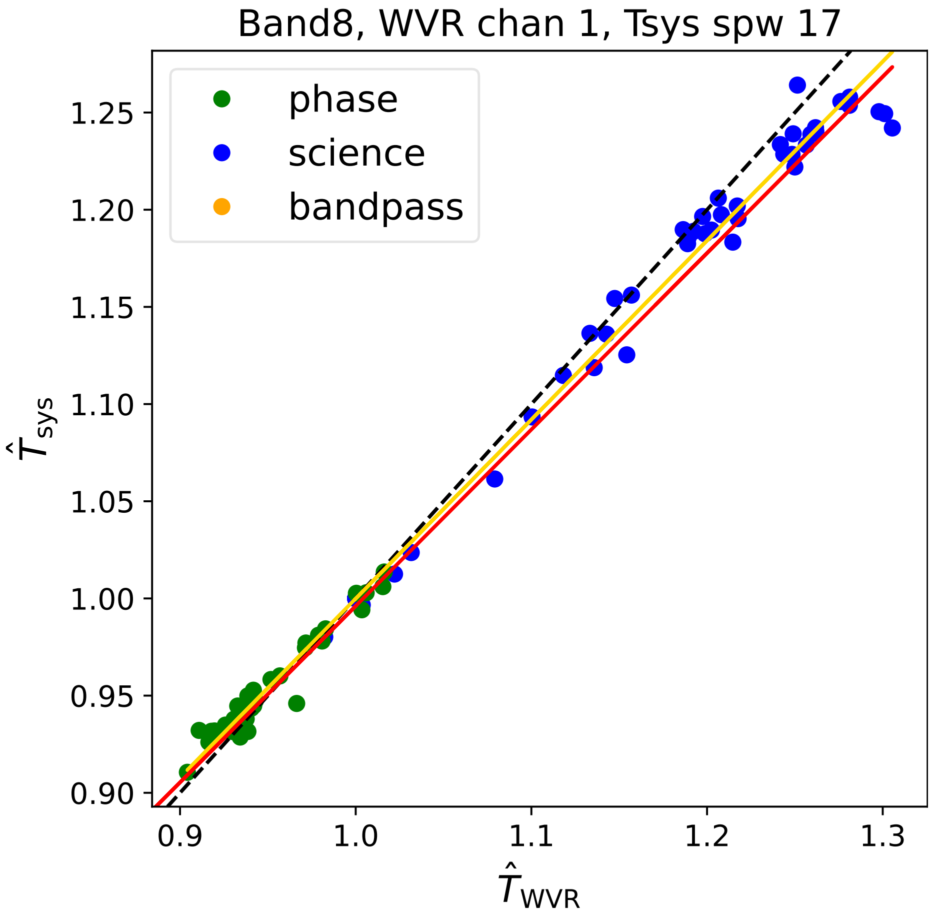

Figure A.4: The correlation between $\hat{T}_{\rm sys}$ and $\hat{T}_{\rm WVR}$ for the 4 Atm-cal scans we selected to fit the linear relation. The red and gold lines are the fitting relation with all Atm-cal scans or just 4 Atm-cal scans. The black dashed line indicates the 1-to-1 relation. We can see the fitting using all Atm-cal scans are almost the same as just using 4 scans.

As discussed in Section A.2.1, the $T_{\rm sys}$ in different spectral windows have different linear relations with $T_{\rm WVR}$. As mentioned, a goal is to reduce the number of $T_{\rm sys}$

measurement scans within each observation to increase observing efficiency. However, this leads to less data to fit the relations of $T_{\rm sys}$ to $T_{\rm WVR}$ or PWV. In Section A.2.5 we investigate determining the relations from atmosphere opacity models, but here we test the reliability of fitting the relations to a small number of $T_{\rm sys}$ measurement scans. Since we need to calculate the normalized $T_{\rm sys}$, we need at least two Atm-cal scans to fit the linear correlation. To make the fitting more robust, we use 4 Atm-cal scans for the fitting with 2 from phase target and 2 from the science target. The 4 Atm-cal scans give us 2 independent $\hat{T}_{\rm sys}$ values if we normalize the $T_{\rm sys}$ from phase and science target independently. For the Atm-cal scan selection, we select 2 Atm-cal scans at the start and 2 Atm-cal scans in the middle. One example of the fits using 4 Atm-cal scans is shown in Fig. A.4. As we can see, the fits based on data from all Atm-cal scans have almost no difference from the fits based on only 4 Atm-cal scans. The scatter of all the data points around the new relation has almost the same scatter of 1%.

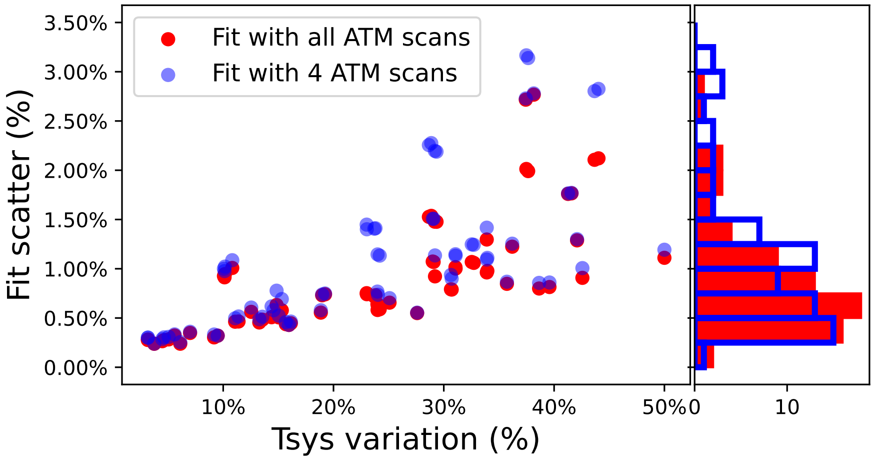

Figure A.5: The scatter of data points around the $T_{\rm sys}$ vs $T_{\rm WVR}$ fits with all the antennas versus the maximal difference in $\hat{T}_{\rm sys}$ values for each $T_{\rm sys}$ spw of each dataset. The red and blue points are from fitting with all Atm-cal scans or just 4 Atm-cal scans respectively. The histogram at the right side shows the distribution of the fit scatters using the two different methods. We can see the scatter of the fitting only increases slightly using just 4 Atm-cal scans.

Fits using 4 Atm-cal scans for other data sets are also shown in Appendix **??**. We can see that the fits do not change much for almost all the datasets except Band9b1, which we will in Section A.2.5. In Fig. A.5, we plot the relative scatter around the fit versus the maximal difference divided by mean value of the T_{sys} for every T_{sys} spw of all the data sets. As we can see, the scatter using both fitting methods is generally below 3%. Fitting with just 4 scans only slightly increases the scatter compared with fitting with all scans. From this quantitative comparison, we can see it is viable to reduce the number of discrete T_{sys} measurements when using T_{WVR} to track T_{sys}.

A.2.4 Normalize Only to the Science target

For some ALMA data, T_{sys} for the phase-cal target is not measured. Instead, the calibration uses the nearest science T_{sys} values as the phase-cal T_{sys}. If we can normalize all T_{sys} values to the first T_{sys} of the science target instead of the first T_{sys} of each type of observing target itself, we can further reduce the number of T_{sys} measurements and thus no longer need to measure T_{sys} for phase-cal with our new method.

In this case, the normalized T_{sys} is calculated as

$$\begin{aligned}\hat{T}_{\text{sys,obs}}(t) &= \frac{T_{\text{sys,obs}}(t)}{T_{\text{sys,sci}}(1^{\text{st}})}\\ \hat{T}_{\text{WVR,obs}}(t) &= \frac{T_{\text{WVR,obs}}(t)}{T_{\text{WVR,sci}}(1^{\text{st}})}\end{aligned} \tag{A.15}$$

where $\hat{T}_{\text{sys,obs}}(t)$ is the normalized T_{sys} averaged along the spectral axis and $\hat{T}_{\text{WVR,obs}}(t)$ is the normalized T_{WVR}. An example of $\hat{T}_{\text{sys}}$ versus $\hat{T}_{\text{WVR}}$ using the new normalization method are shown in Fig. A.6. We can see that phase-cal and science target generally follows the same linear trend, which is consistent with our expectation since phase-cal and science targets are close in elevation. In contrast, we see offsets between the trends of the bandpass target and phase-cal/science targets. We also expect this to happen since bandpass target usually has significant different elevations from the phase-cal/science targets. We will further discuss the cause of the offsets with the help of atmospheric modeling in Section A.3.2. In general, these tests show that we can further reduce the phase-cal and bandpass T_{sys} measurements as we can derive it from T_{sys} measurements for only the science target.

Note that for early ALMA cycles, the T_{sys} measurements are purely done for the phase-cal target. The T_{sys} for the science target is then assumed to be the same as the T_{sys} for the closest phase-cal scan. As we can see from this section, even though the phase-cal and science targets have different elevations, they generally follow the same $\hat{T}_{\text{sys}}$ vs $\hat{T}_{\text{WVR}}$ linear relation. Therefore, we can better extrapolate the science

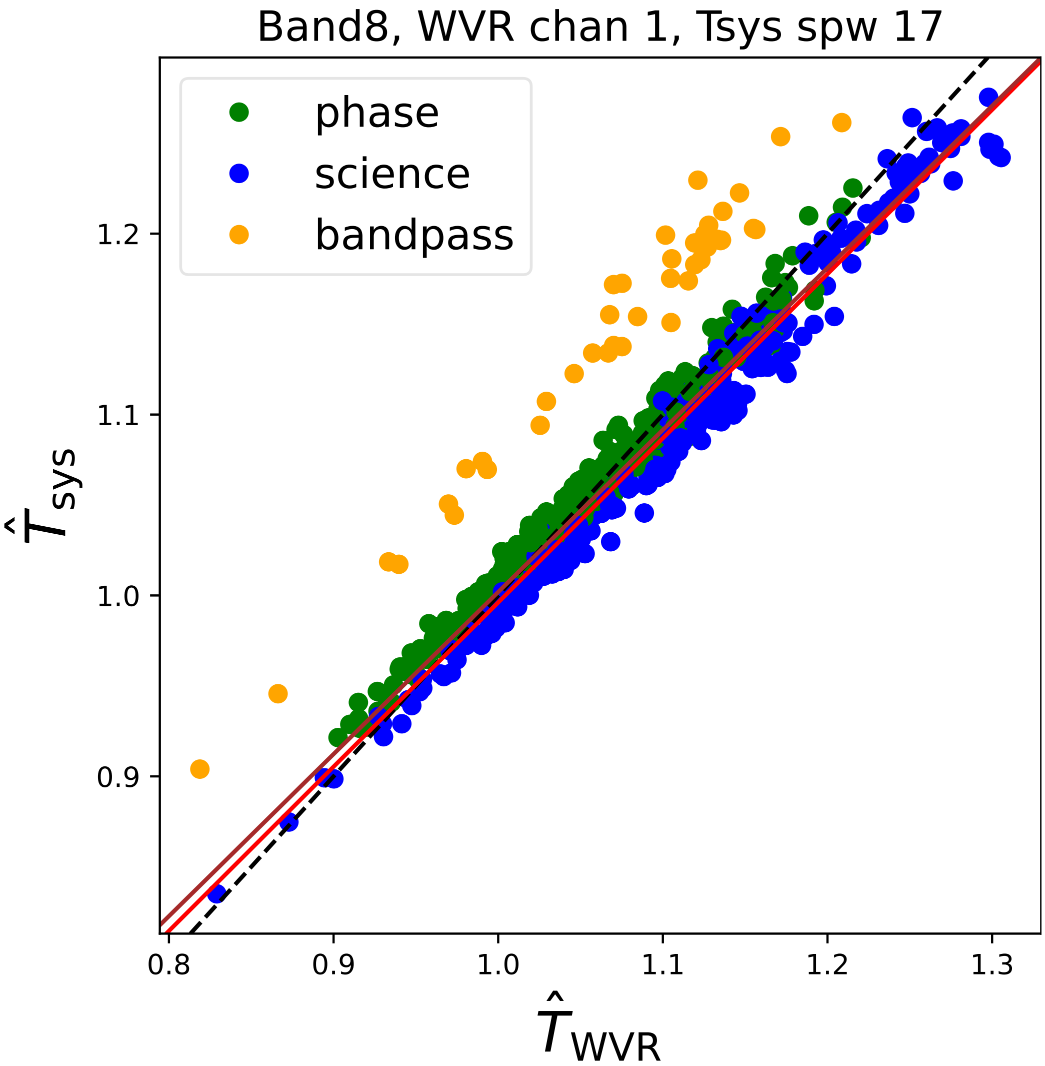

Figure A.6: $T_{\rm sys}$ versus $T_{\rm WVR}$ normalized to the first science Atm-cal scan for the dataset Band8. The black dashed line is the 1-to-1 relation. The brown solid line is the linear fitting to the data excluding the bandpass data. The red solid line is the original fitting relation to the data normalized to each type of observing target. We can see the two fitting relation are almost the same. The bandpass data for spw 0 has a significant offset from the fitted relation, which is due to the elevation difference between bandpass target and phase-cal/science targets (see discussion in Section A.3.2).

$T_{\rm sys}$ from the phase-cal $T_{\rm sys}$ using the fitted linear relation.

A.2.5 Test with significant opacity and large $T_{\rm sys}$ variation

We would expect the linear relation between $T_{\rm sys}$ and $T_{\rm WVR}$ holds when $\tau_{\rm sky}$ is small. In this case, we would have

$$T_{\rm sys} \approx T_{\rm rx} + T_{\rm sky} = T_{\rm rx} + C \times T_{\rm WVR} + T_{\rm sky,dry} \tag{A.16}$$

where C is a constant. However, at higher frequencies such as Band 9 and 10, $\tau_{\rm sky}$ are quite high and we can no longer ignore the opacity term in $T_{\rm sys}$ (e.g. Eq. A.3). In this case, the increase in $T_{\rm sys}$ is dominated by the increase in $\tau_{\rm sky}$ in the exponential form.

We test if the $\hat{T}_{\rm sys}$ vs $\hat{T}_{\rm WVR}$ linear relation still holds on dataset Band9b, which has large $\tau_{\rm sky}$ and $T_{\rm sys}$ range ($\sim 50\%$). In Fig. A.7, we show $T_{\rm sys}$ fitting and extrapolation using all Atm-cal scans or just 4 Atm-cal scans for one measurement set in this project. We can clearly see there is a difference in the fitting functions derived from all Atm-cal scans or just 4 Atm-cal scans. It seems the slope becomes steeper due to data points with higher $T_{\rm sys}$ values, which are not included if we use just 4 scans. This is also reflected in the extrapolation plot at the right side of Fig. A.7, as the predicted $T_{\rm sys}$ is lower than the measured $T_{\rm sys}$ for higher $T_{\rm sys}$ values.

This is consistent with our expectation that the slope of $T_{\rm sys}$ vs $T_{\rm WVR}$ relation is increasing. We would expect the curving-up feature also happens to other datasets but we do not have large enough $T_{\rm sys}$ ranges in the other datasets we analyzed.

A.3 Atmospheric Transmission at Microwave (ATM) Modeling

In the previous sections, we fit $T_{\rm sys}$ vs $T_{\rm WVR}$ heuristically and use the fitted relation to extrapolate the $T_{\rm sys}$ continuously. We find in most cases the correlation between $T_{\rm sys}$ and $T_{\rm WVR}$ is linear. However, the exact slopes and intercepts of the correlations vary across different frequencies. Although we can use less than 4 Atm-cal scans to fit the relation for each spw in each dataset, there might be cases when our selected Atm-cal scans have similar $T_{\rm sys}$ values, and hence might give us inaccurate fitting

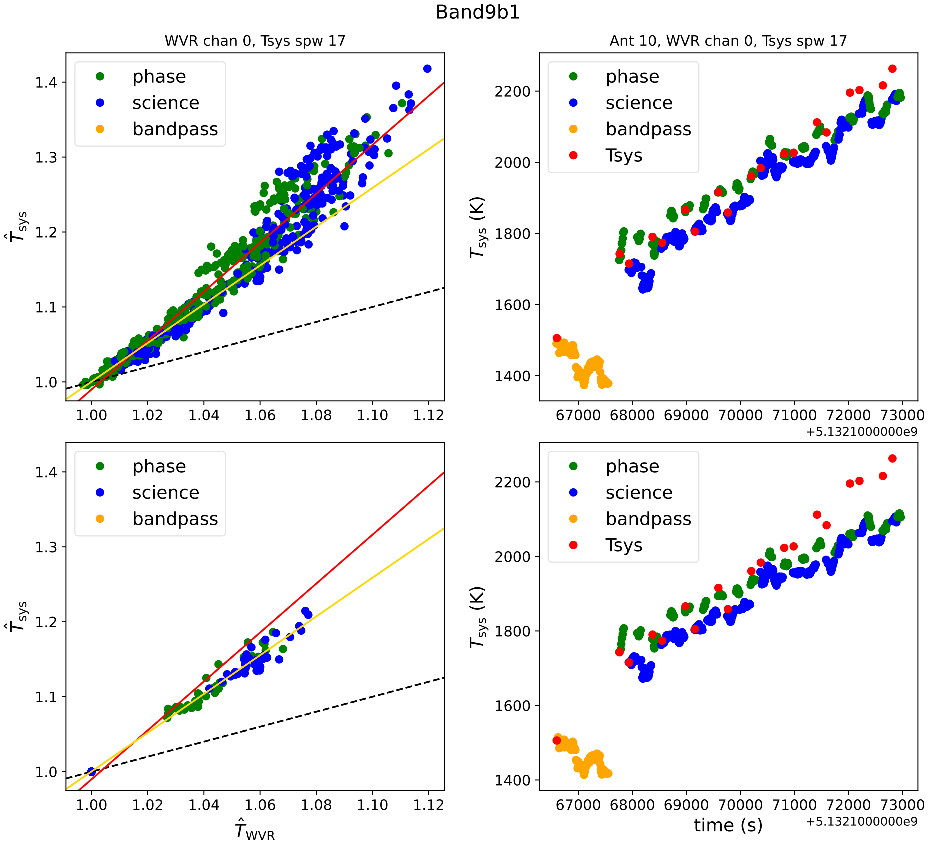

Figure A.7: (Left) $\hat{T}_{\rm sys}$ (spw 17) versus $\hat{T}_{\rm WVR}$ (channel 0) for dataset Band9b1. The upper left panel shows $\hat{T}_{\rm sys}$ versus $\hat{T}_{\rm WVR}$ in spw 17 using all Atm-cal scans while the lower left panel shows the correlation with selected 4 Atm-cal scans. The red and yellow lines are the fits derived using all Atm-cal scans and just 4 Atm-cal scans. (Right) The measured and extrapolated $T_{\rm sys}$ for different observing targets as a function of time. Red points are measured $T_{\rm sys}$ values. $T_{\rm sys}$ in upper panel is extrapolated based on fits with all Atm-cal scans while $T_{\rm sys}$ in lower panel is extrapolated based on fits using only selected 4 Atm-cal scans. We can see in this case we will underestimate the $T_{\rm sys}$ value if we just use part of Atm-cal scans to fit the correlation.

relation among small $T_{\rm sys}$ ranges. Furthermore, as described in Section A.2.5, the linear approximation becomes insufficient when the opacity becomes significant or $T_{\rm sys}$ variations become large. A more robust method is to use an atmospheric opacity modeling code and an estimate of the $T_{\rm rx}$ and other static contributions to predict the $T_{\rm sys}$ vs $T_{\rm WVR}$ relation at the relevant frequencies, elevation and PWV ranges of the observation. In this section we use the Atmospheric Transmission at Microwave frequencies (ATM) model (Pardo et al. 2001) to predict the $T_{\rm sys}$ vs $T_{\rm WVR}$ relation for various datasets and compare the results with our heuristic method.

A.3.1 Modeling $T_{\rm sys}$ spectrum

We note that in previous sections when we explore the correlation between $T_{\rm sys}$ and $T_{\rm WVR}$, we average $T_{\rm sys}$ for each spectral window along its spectral axis. Therefore, when we extrapolate the continuous $T_{\rm sys}$, we are assuming that the $T_{\rm sys}$ spectrum does not vary significantly. In this subsection, we test this assumption with ATM modeling on the two representative datasets we have, Band8 and Band7a. We use the version of ATM included in CASA (McMullin et al. 2007; Emonts et al. 2020; Bean et al. 2022), accessed via a helper function `plotAtmosphere`[1] to generate $T_{\rm sys}$ and $T_{\rm WVR}$ spectra for the frequency ranges of a given spw in the data. We set most of the parameters to the default for the ALMA site (height 5000 m, pressure 557 mb and temperature 274 K). For each dataset, we set the PWV and elevation values to be the same as the value of the first Atm-cal scan for the science target as our start point. Note that `aU.plotAtmosphere` only gives $T_{\rm sky}$ and $\tau_{\rm sky}$. Therefore, we calculate the $T_{\rm sys}$ spectrum from the modeled $T_{\rm sky}$ and $\tau_{\rm sky}$ using Eq. A.1 by assuming $T_{\rm rx}$ to be 100 K.

We show our modeled results in Fig. A.8. As we can see, spw 17 for dataset Band8 has a significant dry opacity contribution as it sits at one of the O_2 lines. On the contrary, dataset Band7a is dominated by the wet component. We then increase the PWV and airmass ($1/\sin m_{\rm el}$, $m_{\rm el}$ is the elevation) by a factor of 1.2 to see if they have different effects on increasing the $T_{\rm sys}$ spectrum. For both dataset Band8 and Band7a, we can see increasing airmass is more effective in increasing the overall values of the $T_{\rm sys}$ spectrum. This is what we expect since increasing airmass will increase both wet and dry opacity while increasing PWV only increases the wet opacity. If we

---

[1] `https://safe.nrao.edu/wiki/bin/view/ALMA/PlotAtmosphere`

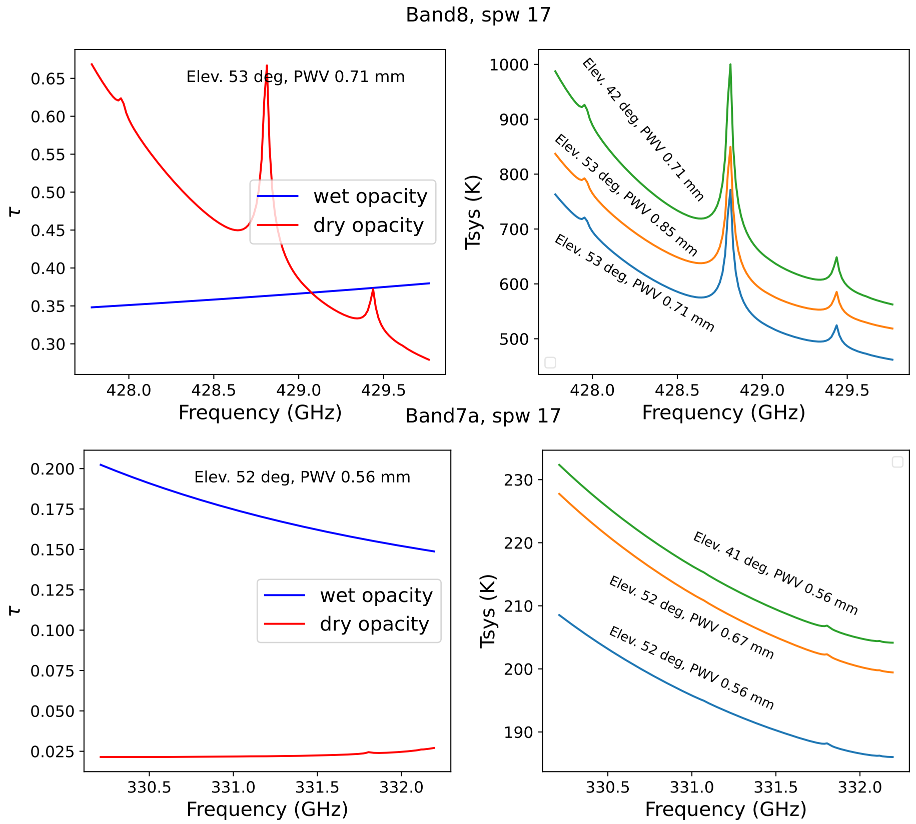

Figure A.8: The ATM modeling opacity τ_{sky} and T_{sys} spectrum for dataset Band8 (upper) and Band7a (lower). For each row, the left panel shows the τ_{sky} spectrum for the wet and dry component. We can see that the dry component is significant for dataset Band8 but the water component is dominant for Band7a. The right panel shows the modeled T_{sys} spectrum for 3 sets of different PWV and elevation values. The blue line is the baseline while we increase PWV or airmass value by 1.2 respectively for orange and green lines. We can see increasing airmass will increase T_{sys} faster since it increase T_{sky} from both wet and dry components.

compare dataset Band8 with Band7a, we can see the difference between increasing PWV and airmass is more significant for Band8 as the spectral window has significant dry opacity contribution.

The change of $T_{\rm sys}$ spectrum shape is generally small by increasing the PWV or airmass by 20%. However, a small change is noticeable when increasing airmass for spw 17 in dataset Band8, due primarily to the significant $\tau_{\rm sky}$ from the dry component and its large variation across the spw. Not tracking such small $T_{\rm sys}$ spectrum shape changes will have negligible impact on continuum observations, and for spectral lines the error in the extrapolation based on $T_{\rm WVR}$ or PWV will be within $\sim \pm 3\%$ (see Section A.5.4 for more discussion). A future improvement might be to correct the data spectrally rather than using a single channel-averaged value per timestamp.

A.3.2 Reproduce the Observed $\hat{T}_{\rm sys}$ vs $\hat{T}_{\rm WVR}$ correlation

In this section we will try to reproduce the observed $\hat{T}_{\rm sys}$ vs $\hat{T}_{\rm WVR}$ correlation in various cases. According to Eq. A.3, $T_{\rm sys}$ are determined by $T_{\rm rx}$ and $T_{\rm sky}$. $T_{\rm sky}$ can be further determined by the measurement of PWV and elevation through ATM modeling. Therefore, we can generate modeled $T_{\rm sys}$ spectrum with given $T_{\rm rx}$, PWV and elevation at a certain frequency range. To reproduce the $T_{\rm sys}$ measured in observation, we set the frequency range to be the same as the $T_{\rm sys}$ spectral window we want to model, with total bandwidth of $\sim$ 2 GHz. The modeled $T_{\rm sys}$ spectrum is then averaged to a single $T_{\rm sys}$ value as we did with the observations. We also use a similar method to generate $T_{\rm WVR}$ at different WVR channels with given PWV and elevations ($T_{\rm WVR}$ is just $T_{\rm sky}$ at the WVR channel frequencies).

For most of the ALMA data, $T_{\rm rx}$ stays relatively constant throughout the observations. However, different antennas generally have different $T_{\rm rx}$ values, which might give us slightly different shapes of correlation. Therefore, we first test how varying $T_{\rm rx}$ could affect the shape of the $\hat{T}_{\rm sys}$ vs $\hat{T}_{\rm WVR}$ correlation for dataset Band8 spw 17 (Fig. A.9). The $T_{\rm sys}$ and $T_{\rm WVR}$ are generated with varying $T_{\rm rx}$ and PWV values but with fixed elevation of 53 deg. We note that dataset Band8 has relatively constant elevations (see Table A.2) for the science target throughout the entire observation, hence the $T_{\rm sys}$ variations across time are mostly due the the change in PWV values. After generating the modeled $T_{\rm sys}$ and $T_{\rm WVR}$, we then normalize both quantities to the values when the PWV value is equal to that of the first science Atm-cal scan for each $T_{\rm rx}$ value. As we can see in Fig. A.9, the ATM modeling shows a slight

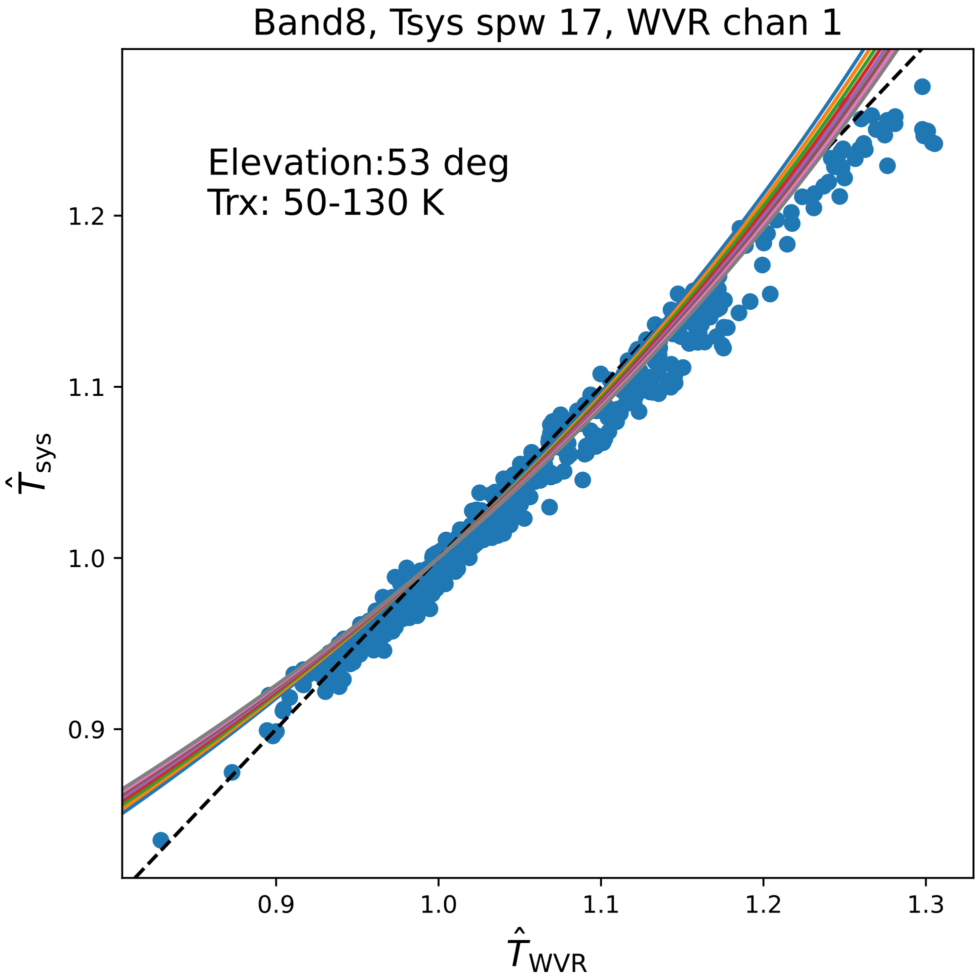

Figure A.9: The correlation between $\hat{T}_{\rm sys}$ and $\hat{T}_{\rm WVR}$ (Fig. A.2) overlaid by the predicted correlation curves from ATM modeling. Curves of different colors represent modeling using different $T_{\rm rx}$ values. The modeled $T_{\rm sys}$ and $T_{\rm WVR}$ are normalized to the value when PWV is 0.71 mm, which is the PWV value for the first Atm-cal scan for the science target. The $T_{\rm rx}$ range we use for ATM modeling is similar to the $T_{\rm rx}$ range of dataset Band8. We can see that varying $T_{\rm rx}$ generally does not affect the correlation we get.

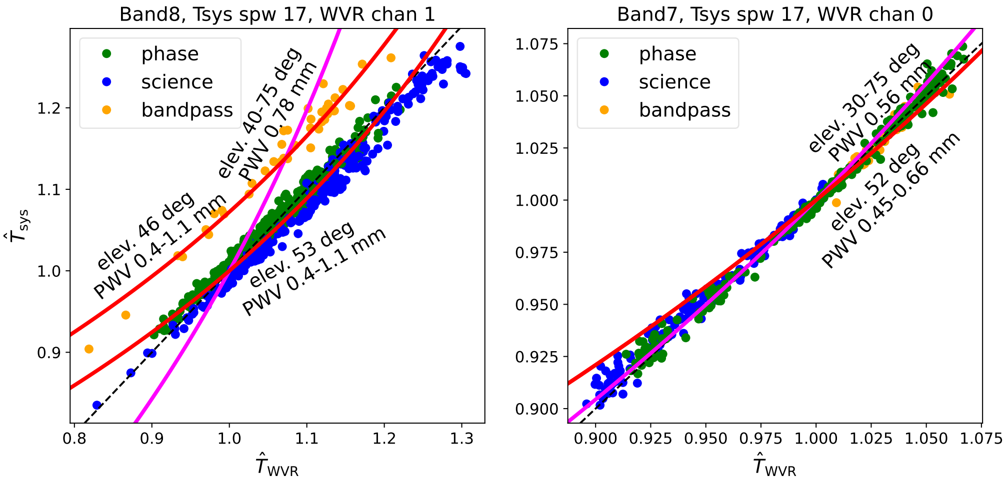

Figure A.10: The correlation between $\hat{T}_{\rm sys}$ and $\hat{T}_{\rm WVR}$ overlaid by the predicted correlation curves from ATM modeling for dataset Band8 (left) and Band7a (right). Note that in this case both $T_{\rm sys}$ and $T_{\rm WVR}$ are normalized to the first Atm-cal scan for the science targets (Eq. A.15). The magenta line represent varying elevations while keeping the PWV value to be the same and the red line keeps elevation constant but varies PWV. The $T_{\rm rx}$ are set to be equal to that of the first antenna of the data. The ATM modeled $T_{\rm sys}$ and $T_{\rm WVR}$ are normalized to the value when PWV and elevation are equal to those of the first science Atm-cal scans in the data. We can see that for dataset Band8 where the dry component is significant, varying PWV or elevation gives us correlations of different slopes. Since the bandpass and science/phase targets have different elevations, we therefore see the offsets between $T_{\rm sys}$ for these two targets. In contrast, for dataset Band7a where the wet component is dominant, varying PWV or elevation gives us similar $\hat{T}_{\rm sys}$ vs $\hat{T}_{\rm WVR}$ correlations. In this case, all 3 targets follow the same linear trend.

non-linear curvature for a high range of $T_{\rm sys}$, which depends slightly on the assumed $T_{\rm rx}$ and the elevation. However, the modeling curve is generally within the range of the data scatter. Varying $T_{\rm rx}$ also gives a similar correlation within data scatter of $\sim$ 1%. Therefore, $T_{\rm rx}$ values do not seem to affect the $\hat{T}_{\rm sys}$ vs $\hat{T}_{\rm WVR}$ correlation we get.

We then explore how varying PWV or elevation can affect the $\hat{T}_{\rm sys}$ vs $\hat{T}_{\rm WVR}$ correlation. As we have mentioned in Section A.3.1, varying PWV or elevation might have different effects on changing $T_{\rm sys}$ values depending on how significant the dry opacities are at given frequency. Dataset Band8 and Band7a represent two cases where one has significant dry opacity contribution while the other is dominated by the wet opacity. Therefore, it is natural for us to explore what drives the $\hat{T}_{\rm sys}$ vs $\hat{T}_{\rm WVR}$ correlation in these two cases. Fig. A.10 shows the comparison between modeling and observation for these two datasets where red and magenta lines represent changing PWV and elevation respectively. In this comparison, the measured $T_{\rm sys}$ and $T_{\rm WVR}$ are normalized to the values in the first science Atm-cal scan instead of the first Atm-cal scan for each target (see Section A.2.4 for more description). The modeled $T_{\rm sys}$ and $T_{\rm WVR}$ are then normalized to the values when PWV and elevation are equal to those of the first science Atm-cal scan. We can see in both cases the ATM modeling successfully reproduces the observed $\hat{T}_{\rm sys}$ vs $\hat{T}_{\rm WVR}$ correlation. For dataset Band8, the correlation is mainly driven by varying PWV values as the elevation for the science target stays relatively constant. By varying the elevation, we see a steeper slope of the correlation between $\hat{T}_{\rm sys}$ and $\hat{T}_{\rm WVR}$. This is due to the fact that changing elevations (and therefore airmass) will be more effective to change $T_{\rm sys}$ values when the dry opacity contribution is significant (see discussion in Section A.3.1). $T_{\rm sys}$ for the bandpass target shows significant offsets from the main trend of phase/science target mainly due to the elevation difference, and hence sits at the red track of a different constant elevation value. Since the single bandpass $T_{\rm sys}$ measurement for each antennae has the same elevation but might point towards slightly different part of skys with different PWV values, we see the bandpass data points still follow the track of constant elevation. On the other hand, we get a similar $\hat{T}_{\rm sys}$ vs $\hat{T}_{\rm WVR}$ correlation by varying PWV or elevation for dataset Band7. This is probably due to the fact that the wet component is dominant at this spectral window, hence changing PWV or elevation achieves a similar effect. We can also see in this case the $T_{\rm sys}$ for the bandpass target lie along the same trend as the phase-cal/science targets, which is what we expect since there is no specific parameter variation that could bring these data points out of the linear track.

As we have discussed in Section A.2.5, dataset Band9b1 shows a non-linear $\hat{T}_{\rm sys}$ vs $\hat{T}_{\rm WVR}$ correlation as the $T_{\rm sys}$ variation becomes significantly large ($\sim 40\%$). Therefore, it is also worth testing if we can reproduce the curving feature for this dataset. We show the comparison in Fig. A.11 using the same method described in the previous paragraph. As we can see, this dataset also has significant contribution from the dry opacity and hence shows different slopes when varying PWV or the elevation values. The observed $T_{\rm sys}$ generally agrees well with the ATM modeling relation with fixed PWV values. This suggests the $T_{\rm sys}$ variation shown for this dataset is mainly due to the elevation change. This is consistent with what we see in Fig. A.7 as $T_{\rm sys}$ is

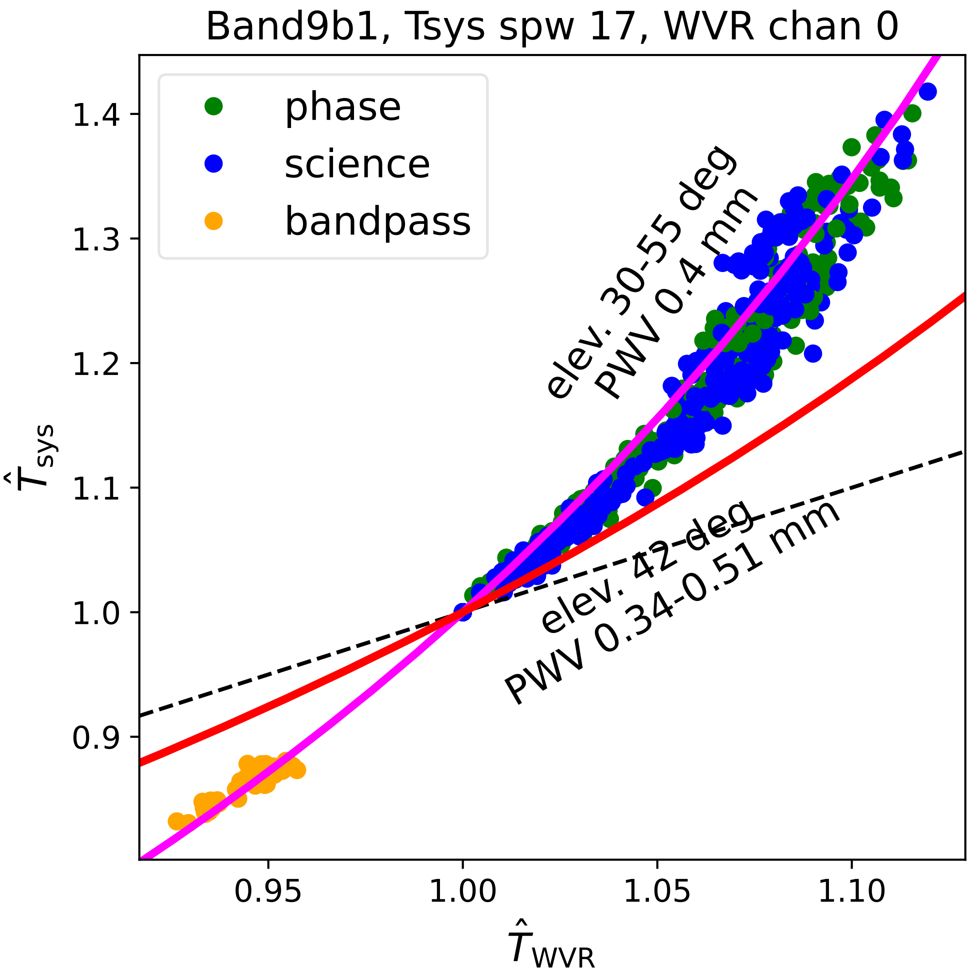

Figure A.11: Similar plot as Fig. A.10 but for dataset Band9b1. The dry component is also significant for this dataset. We can see that Band9b1 has a relatively constant PWV while the T_{sys} and T_{WVR} variation is mainly due to changing elevations.

smoothly increasing as the function of time without any short-time fluctuation. The bandpass data points also lie along the fixed PWV trend but with smaller values, which is probably due to the larger elevation of the bandpass target. We also see some second-order scatter around the fixed PWV line for higher $T_{\rm sys}$ values, which might be due to the intrinsic scatter of PWV values during the observation. However, to first order we can just measure $T_{\rm sys}$ once and predict the following $T_{\rm sys}$ based on the elevation change during the observation.

A.3.3 General Applicability of the current method and future direction for improvement

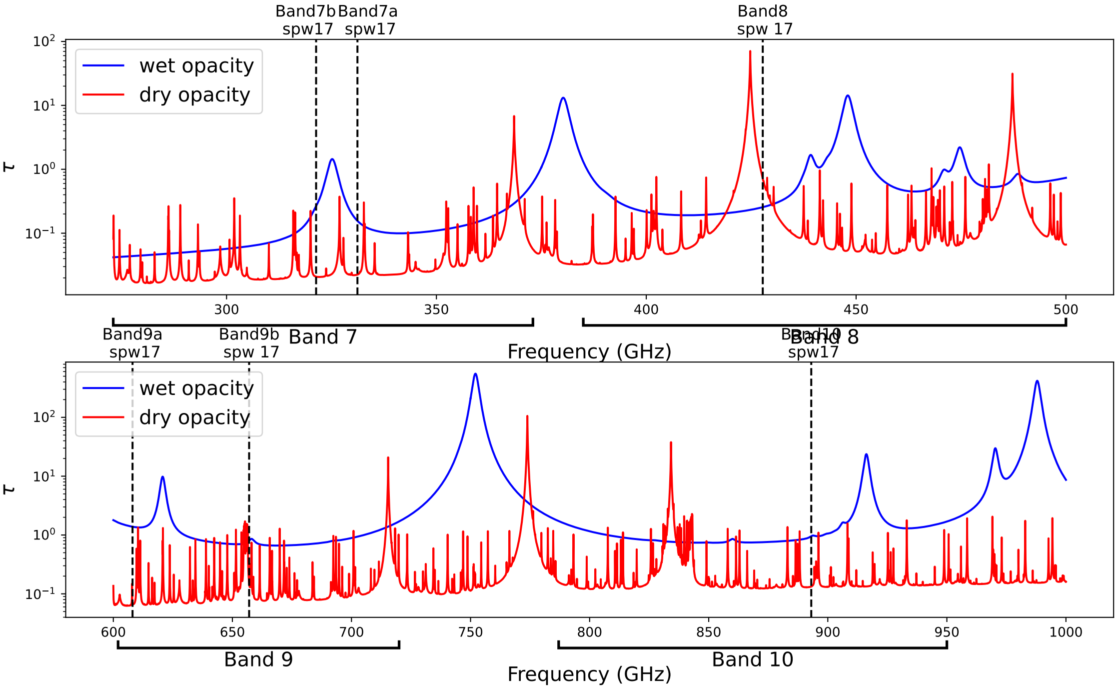

Figure A.12: The wet and dry opacity from ATM modeling for the entire ALMA high frequency bands (from Band 7 to 10). We set the PWV value to be 0.5 mm and elevation to be 50 deg. The dashed line indicates the position of spectral window of ALMA data we have. We can see all of our dataset except for Band8 and Band9b are dominated by the wet component, which means changing PWV or elevations should give the similar $\hat{T}_{\rm sys}$ vs $\hat{T}_{\rm WVR}$ correlation for these datasets.

In the previous section, we have successfully reproduced the $\hat{T}_{\rm sys}$ vs $\hat{T}_{\rm WVR}$ correlation for 3 datasets with ATM modeling. However, we also find the correlation is not driven by a single parameter. For both dataset Band8 and Band9b1 where dry opacity is significant, the correlation is driven either by varying PWV or elevation. If both PWV and elevation have significant variation, we would not be able to get the tight correlation since the data points are driven up and down along different tracks. In contrast, for dataset Band7a where wet opacity is dominant, we can expect a tight $\hat{T}_{\rm sys}$ vs $\hat{T}_{\rm WVR}$ correlation even though both PWV and elevation have significant variation, as they are moving data up and down along the similar track. Therefore, it is safer to apply our current heuristic method to datasets observed at frequencies where wet opacity is dominant. In Fig. A.12, we model the wet and dry opacity spectrum covering the entire ALMA high frequency bands from Band 7 to Band 10. We assume PWV of 0.5 mm, which is a typical value for high-frequency ALMA observations, and elevation of 50 deg. For the wet opacity, we see several smooth line features, which indicate the presence of the H_2O line. For the dry opacity, we generally see a lot of Ozone lines as narrow spikes. These Ozone lines are generally much narrower than the typical bandwidth of a spw of 2GHz and hence have a relatively small effect on the averaged $T_{\rm sys}$ values. On the other hand, we also see some broader spikes caused by O_2 lines. One of our datasets, Band8, sits right at the wings of one O_2 line and thus has significant dry opacity contribution. For all of our datasets used in this paper, only datasets Band8 and Band9b show significant dry opacity contribution, which is consistent with our expectation as all of the other datasets in this paper exhibit a tight linear correlation (Fig. **??**, **??** and **??**).

However, we can expect that in lots of cases, the $\hat{T}_{\rm sys}$ vs $\hat{T}_{\rm WVR}$ might not follow a tight linear correlation due to various reasons mentioned above. In these cases, the best way is to directly derive $T_{\rm sys}$ from the ATM modeling. As shown in Section A.3.2, with known $T_{\rm rx}$, PWV and elevations for each Atm-cal scan, we can successfully reproduce the $T_{\rm sys}$ measured in observations. *In the future, the best strategy for tracking $T_{\rm sys}$ is to derive PWV values from continuous $T_{\rm WVR}$ measurements at different WVR channels. By combining PWV, elevation and $T_{\rm rx}$ values, we can then reproduce the continuous $T_{\rm sys}$ throughout the observation.*

A.4 AC & SQLD Data in Tracking $T_{\rm sys}$

As mentioned in Section A.1.4, we can also explore whether to use AC or SQLD data to track $T_{\rm sys}$ variation. Since AC and SQLD data are equivalent to one another (see

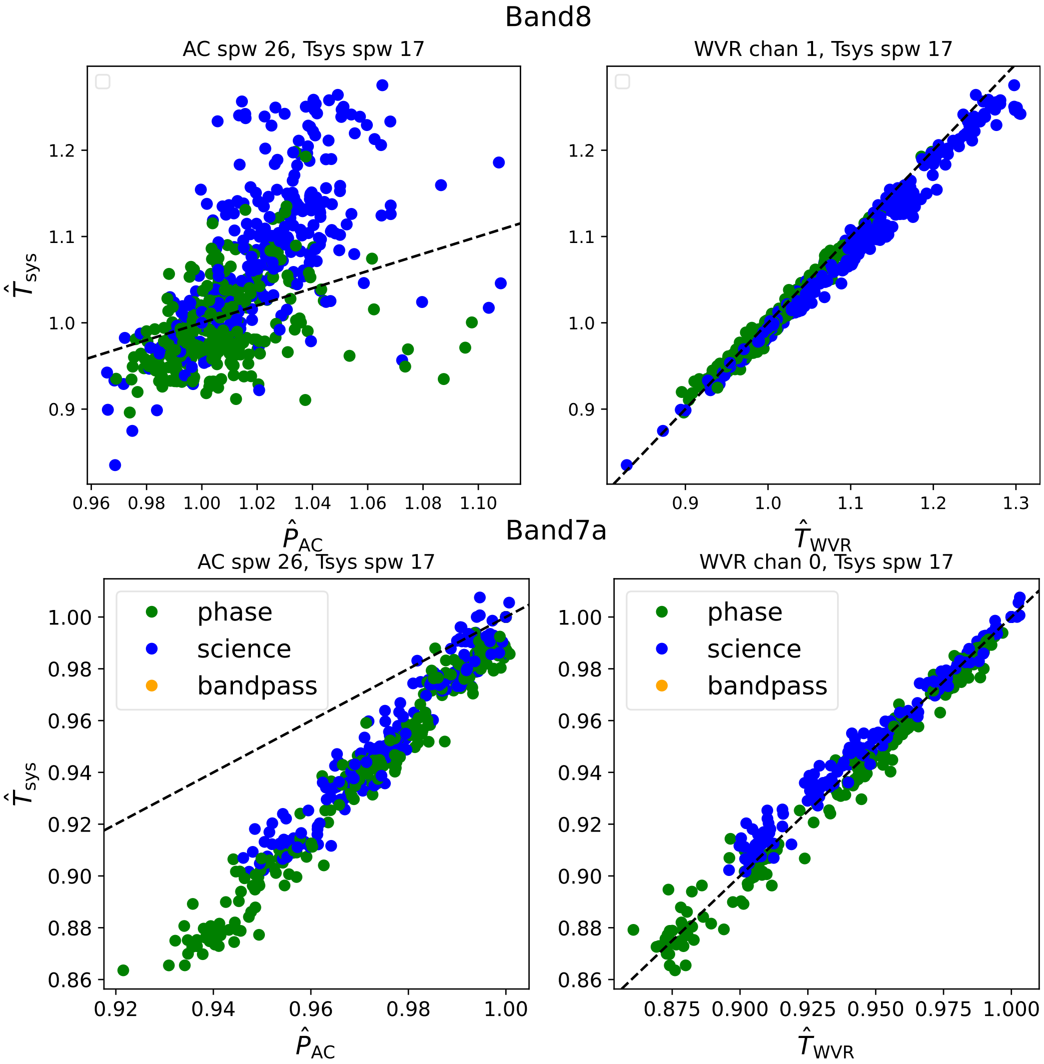

Figure A.13: The correlation between the $\hat{T}_{\mathrm{sys}}$ and matched $\hat{T}_{\mathrm{WVR}}$ and normalized P_{AC} for all the antennas. Both WVR and auto-correlation data is averaged over 10 seconds.

Fig. A.1 right panel), we only need to compare T_{sys} with one of the two quantities. We use AC data for comparison since the data size is much smaller. We use a similar method to normalize the AC data and compare it with the normalized T_{sys}. Fig. A.13 shows the comparison between T_{sys} versus AC and T_{sys} versus WVR correlation for dataset Band8 and Band7a. We can see that the AC data also has a tight correlation with T_{sys} for dataset Band7. However, the correlation does not work well for dataset Band8 with a large scatter. Therefore, we cannot just fit the relation to several Atm-cal scans to calculate the continuous T_{sys} with good precision.

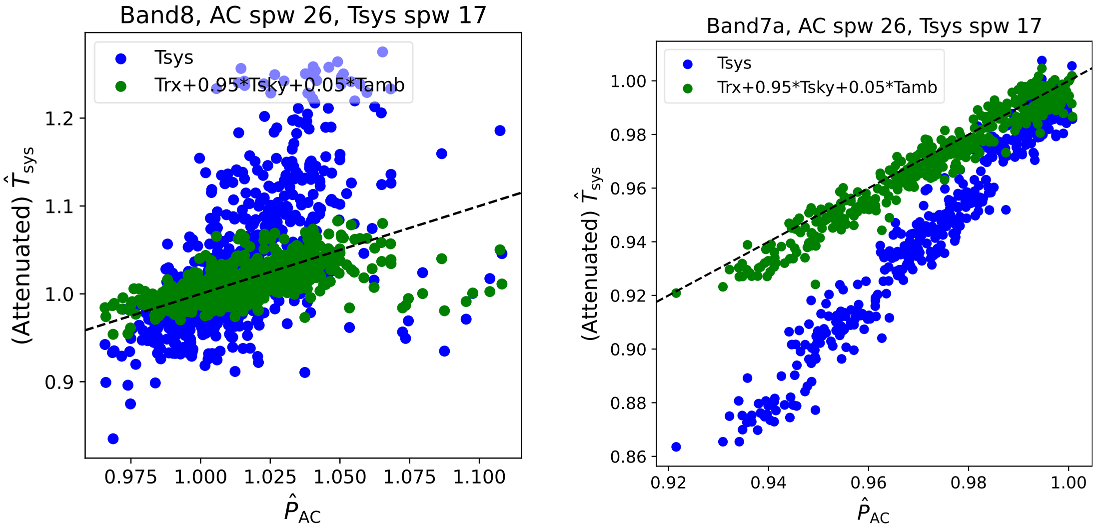

Figure A.14: The correlation between the normalized T_{sys} (blue) and attenuated T_{sys} (green) and normalized AC data for the dataset Band8 and Band7a we have for all antennas of one spectral window. As we can see, the attenuated T_{sys} follows the 1-to-1 correlation with AC data, which proves equation A.17 to be right.

The other thing we find is that AC and T_{sys} do not follow the proportional correlation as might be expected. The major reason is that AC data track the total signal received after the atmosphere attenuation while T_{sys} tracks the total signal before it comes through the atmosphere, as shown in the diagram in Fig. A.15. The AC data is directly proportional to the total signal received by the antenna, which is mainly comprised of emission from the sky ($\eta_{\mathrm{f}} T_{\mathrm{sky}}$), the receiver itself ($T_{\mathrm{rx}}$), and other fixed losses terminating at ground ($(1 - \eta_{\mathrm{f}}) \times T_{\mathrm{amb}}$). However, based on Eq. A.1, T_{sys} is not directly proportional to these 3 components added together. Instead, T_{sys} can be thought of as brightness temperature of a fake source in space that generates a signal equal to the 3 components added together after atmosphere attenuation. In other words, for a single band setting,

$$\begin{aligned} P_{\mathrm{AC}} &\propto \eta_{\mathrm{f}} e^{-\tau_0 \sec z} T_{\mathrm{sys}} \\ &\approx T_{\mathrm{rx}} + \eta_{\mathrm{f}} T_{\mathrm{sky}} + (1 - \eta_{\mathrm{f}}) \times T_{\mathrm{amb}} \end{aligned} \tag{A.17}$$

We call the right side of the equation attenuated T_{sys}. We also normalize the attenuated T_{sys} the same way as we do for the original T_{sys} and compare it with normalized AC data. The comparison between T_{sys} and attenuated T_{sys} versus AC correlation is shown in Fig. A.14. As we can see, the normalized attenuated T_{sys} follows the 1-to-1

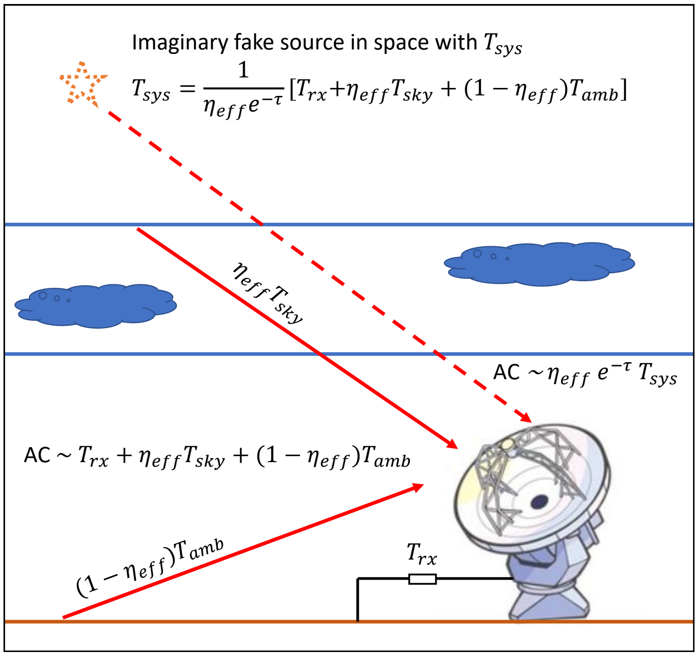

Figure A.15: Illustration of the theoretical relationship between the autocorrelation signal AC and $T_{\rm sys}$. AC is proportional to the total power signal received by an antenna, which includes receiver noise ($T_{\rm rx}$), sky noise ($T_{\rm sky}$), and thermal noise due to losses and spillover terminating around the ambient temperature ($(1-\eta_{\rm f}) \times T_{\rm amb}$). However, $T_{\rm sys}$ is corrected for a source outside the atmosphere, and includes an extra term due to the atmospheric attenuation.

relation with normalized AC as suggested by Eq. A.17. If we rearrange Eq. A.17, it becomes

$$T_{\rm sys} \propto \frac{P_{\rm AC}}{e^{-\tau_{\rm sky}}} \approx \frac{P_{\rm AC}}{1 - T_{\rm sky}/T_{\rm amb}} \tag{A.18}$$

Therefore, even though we have the AC data, we still need a method to continuously determine $T_{\rm sky}$ or $\tau_{\rm sky}$ to obtain $T_{\rm sys}$. A possible work-around is to use AC data to track $T_{\rm sky}$ first by combining Eq. A.3, A.2 and A.18 as we can generally assume $T_{\rm amb}$ and $T_{\rm rx}$ to be constant. This technique has been applied to correct $T_{\rm sys}$ values in Agliozzo et al. (2017). However, in our case to extrapolate continuous $T_{\rm sys}$, we need to note that the AC and SQLD data also suffer from gain drift and gain step changes between scans, as noted above and seen in Fig. A.1.

A.5 Applying Continuous $T_{\rm sys}$ to the Calibration

In Section A.2, we demonstrated the viability to use WVR data to track $T_{\rm sys}$ continuously. In this section, we apply the extrapolated continuous $T_{\rm sys}$ in calibration to test whether our new method for measuring $T_{\rm sys}$ works. We calibrate each dataset with the original $T_{\rm sys}$ table, the new continuous $T_{\rm sys}$ table extrapolated using all Atm-cal scans and that using just 4 Atm-cal scans with CASA package. We then make images from data calibrated using these 3 different methods and see if the measured fluxes for the same target are more consistent with each other using our new methods. The detailed description of the scripts we use for the data processing can be found at `https://github.com/heh15/ALMA_intern_Tsys.git`.

A.5.1 Creation of $T_{\rm sys}$ Table

In this subsection we discuss how we construct the new $T_{\rm sys}$ table used for the calibration. We note that the original $T_{\rm sys}$ table used for calibration is a spectrum with two polarizations. Recording all the extrapolated $T_{\rm sys}$ spectra in one big table would take a lot of disk space. Based on our check of the $T_{\rm sys}$ spectrum plots generated using the original calibration script, the shape of the $T_{\rm sys}$ spectrum of each spectral window does not vary much as a function of time. Therefore, we can just record the initial $T_{\rm sys}$ for each observing target in the $T_{\rm sys}$ table and record the ratio of the extrapolated $T_{\rm sys}$ relative to the initial $T_{\rm sys}$ into an amplitude gain table. In this case, the two tables we provide for $T_{\rm sys}$ calibration are

$$\begin{aligned} T_{\rm sys}(t,\nu) &= T_{\rm sys,obs}(1^{\rm st},\nu) \\ G(t) &= \sqrt{1\Big/\left[\frac{T_{\rm sys}(t)}{T_{\rm sys}(1^{\rm st})}\right]_{\rm fit}} \end{aligned} \tag{A.19}$$

where $T_{\rm sys}(t,\nu)$ is the recorded $T_{\rm sys}$ spectrum as a function of time t and frequency ν, and G is the derived gain as a function of t, $T_{\rm sys,obs}(1^{\rm st},\nu)$ is the first $T_{\rm sys}$ spectrum measured for each type of observation of given antenna and spectral window and $\left[\frac{T_{\rm sys}}{T_{\rm sys}(1^{\rm st})}\right]_{\rm fit}$ is the extrapolated normalized $T_{\rm sys}$ from the fitting. We note that G is not directly equal to the $\hat{T}_{\rm sys}$ values. This is due to the different methods that CASA uses to handle $T_{\rm sys}$ and gain table. For each baseline, the correlated amplitude is

$$S(i,j) \propto \sqrt{T_{\rm sys}(i) T_{\rm sys}(j)} \propto \frac{1}{G(i)G(j)} \tag{A.20}$$

Therefore, the G is written so that it can be properly translated to the variation in $T_{\rm sys}$.

In Section A.2.3, we tested using only 4 $T_{\rm sys}$ measurements to fit the linear relation between $\hat{T}_{\rm sys}$ and $\hat{T}_{\rm WVR}$. We saw that the difference between this method and using all $T_{\rm sys}$ measurements is small. However, we still need to quantify if the small difference in the linear fits makes much difference in the measured flux of the image product. In this case, we also apply Eq. A.19 to create the alternative $T_{\rm sys}$ table with the fitting relation derived from 4 Atm-cal scans.

A.5.2 Calibrating and Imaging the Data

After we create the $T_{\rm sys}$ table, we then apply the continuous $T_{\rm sys}$ in calibration. The calibration script we use is generated from the command `es.generateReducScript()` (Petry et al. 2014). We then modify the script to use the alternative $T_{\rm sys}$ and amplitude gain tables created (see details in `https://github.com/heh15/ALMA_intern_Tsys.git`). We also run the original calibration script to calibrate the data with the original discrete $T_{\rm sys}$ method for comparison.

After calibration, we then proceed with making continuum images. We generally adopt the default settings using the command `tclean`. We set the `robust` parameter to be 2.0 instead of the default 0.5 to maximize the sensitivity and hence flux accuracy. We also set the number of iterations to be 0 to only make the dirty image. This process will reduce any effects from `tclean` itself when making comparisons between fluxes from different calibration datasets. For projects with multiple datasets, we directly compare the measured fluxes from different datasets to see if they are consistent with each other. For projects with just one measurement set, we further make images using just the first half or the second half of the science scans and then compare fluxes among these 3 images. The top panel in Fig. A.16 shows an example of images made with the 3 different methods for dataset Band8. We can see that the structure of these images looks almost the same. This is what we expect since $T_{\rm sys}$ should only affect the intensity scale of the final image. The bottom panel of Fig. A.16 shows the images of the same target made with all scans or just half of the scans using the

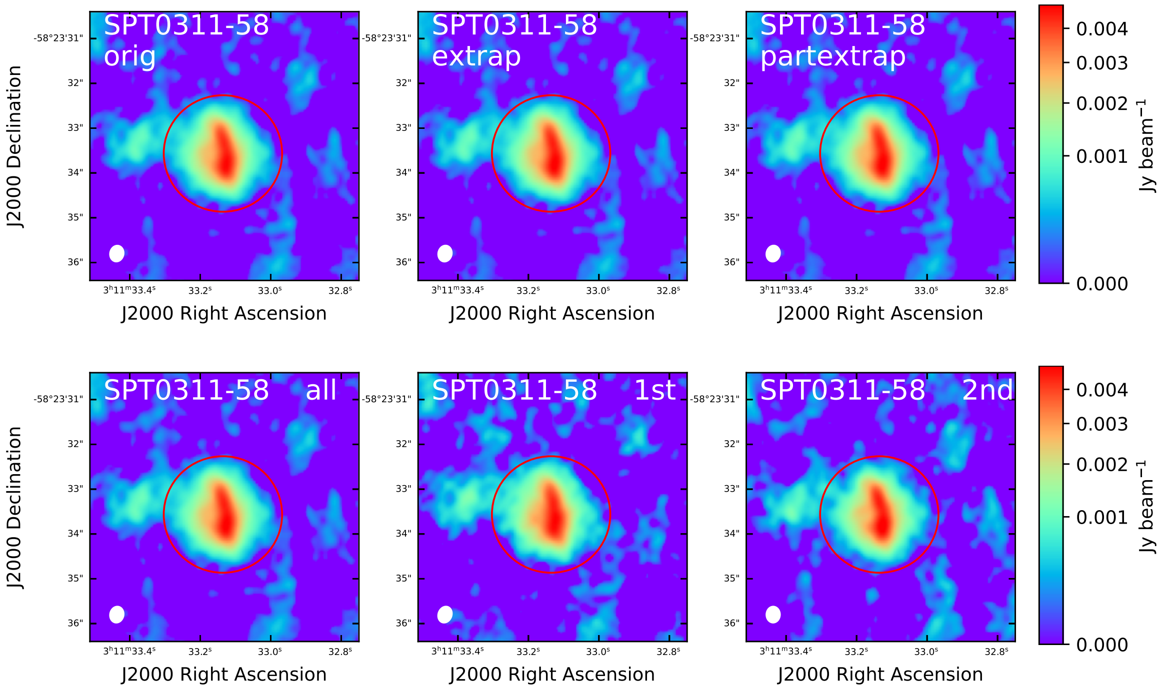

Figure A.16: (Top) dirty images made using originally measured T_{sys} (orig), extrapolated continuous T_{sys} with all Atm-cal scans (extrap) and that with just 4 Atm-cal scans (partextrap) for dataset Band8 of SPT0311-58. The red circle is the aperture used for flux measurements. The fluxes for these 3 images are 0.0425, 0.0429 and 0.0407 Jy. (Bottom) dirty images made using alternative continuous T_{sys} table derived from fitting all Atm-cal scans. The 3 columns are images made using all, 1st half and 2nd half of the science scans. The fluxes for these 3 images are 0.0429, 0.0432 and 0.0428 Jy.

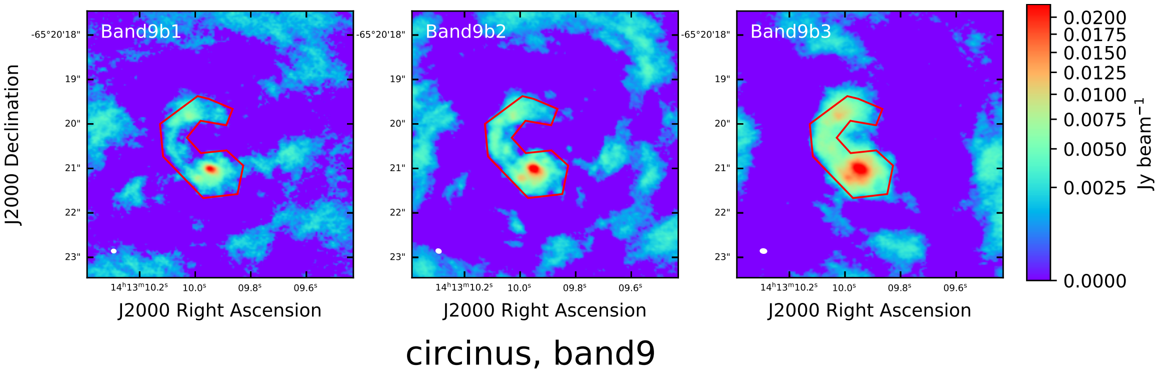

Figure A.17: Dirty images made using alternative continuous T_{sys} table using all Atm-cal scans for the 3 data sets in the Band 9 project 2019.1.00013.S. The red polygons are apertures used to measure the flux. The fluxes for these 3 images are 0.875, 1.0 and 1.35 Jy.

new method to extrapolate T_{sys} from all Atm-cal scans. We can see the structures of these images are also almost the same, which is also what we expect as images from the same dataset should have similar *uv* coverage. On the other hand, if we compare images made from different datasets, we can see there is a larger difference in image structure. This is most obvious in the Band 9 project 2019.1.00013.S shown in Fig. A.17. The beam sizes for the 3 different images are also significantly different from each other. For dataset Band7b, all images have similar beam shapes so differences among the image structures are not that significant.

Once the images are made, we draw an aperture around the central point source to measure the flux. Since the change in T_{sys} does not change the structure of the continuum image, we can compare the fluxes measured from the same aperture for the same target (as long as the aperture is not missing any flux, or there is no decorrelation – as decorrelation will reduce the total flux potentially). The apertures we used to measure the fluxes are shown in Fig. A.16, A.17 and **??**. Note that as well as changes in T_{sys}, changes in phase decorrelation during a single observation and between observations may also affect the measured fluxes, and account for some of the scatter in fluxes in Table A.4, A.5 and A.6. However, we assume this effect is the same in all reductions, independent of the T_{sys} calibration method.

Table A.4: Flux measured for project with only one dataset

Data Label	Target	Scans used	Flux (Jy)			Meas. Err. (Jy)	Beam (")
			Tsys_orig	Tsys_extrap	Tsys_partextrap		
(1)	(2)	(3)	(4)	(5)	(6)	(7)	(8)
Band10	Arp 220	all	7.169	7.146	7.187	0.39	0.5 x 0.47
		1st half	7.1638	7.135	7.171	0.42	0.52 x 0.45
		2nd half	7.1077	7.09	7.133	0.4	0.48 x 0.48
		MAX. DIFF^a	0.06	0.056	0.054		
Band9a	IRAS16293-B	all	10.43	10.36	10.324	0.34	0.34 x 0.27
		1st half	10.4	10.32	10.32	0.36	0.35 x 0.27
		2nd half	10.47	10.4	10.34	0.38	0.34 x 0.26
		MAX. DIFF.	0.07	0.04	0.02		
Band8	SPT0311-58	all	0.0425	0.0429	0.0429	0.0015	0.35 x 0.3
		1st half	0.0453	0.0432	0.0433	0.0019	0.36 x 0.29
		2nd half	0.0407	0.0428	0.0429	0.0017	0.35 x 0.3
		MAX. DIFF	0.0046	0.0003	0.0003		
Band7a	HT-Lup	all	0.173	0.178	0.178	0.0038	0.22 x 0.12
		1st half	0.169	0.175	0.175	0.0044	0.22 x 0.12
		2nd half	0.175	0.18	0.18	0.0045	0.22 x 0.12
		MAX. DIFF.	0.006	0.005	0.005		

Columns: (1) The label of each dataset (see Table A.2) (2) The target name. (3) The science scans used to make images. (4) Fluxes of the source with images made using original calibration script. (5) Fluxes of the source with images made using modified script with alternative $T_{\rm sys}$ table. The $T_{\rm sys}$ is extrapolated based on all Atm-cal scans. (6) The images made with modified script but $T_{\rm sys}$ is extrapolated from 4 Atm-cal scans. (7) The measured flux errors for the images made with original $T_{\rm sys}$ table (8) The beam size of images using original $T_{\rm sys}$ table.

Rows: a. The maximal differences for fluxes at each column.

Table A.5: Flux measured for data for Band7b project (AS205A)

Dataset Label	Flux (Jy)			Meas. Err. (Jy)	Beam (")
	Tsys_orig	Tsys_extrap	Tsys_partextrap		
(1)	(2)	(3)	(4)	(5)	(6)
Band7b1	0.7699	0.759	0.7594	0.031	1.13 x 0.79
Band7b2	0.713	0.7146	0.7129	0.029	0.96 x 0.77
Band7b3*	1.001	1.005	1.003	0.043	0.68 x 0.53
Band7b4	0.747	0.7378	0.7359	0.028	1.03 x 0.78
Band7b5*	0.556	0.58	0.58	0.029	1.31 x 0.72
Band7b6	0.749	0.7534	0.7533	0.03	0.91 x 0.08
Band7b7	0.7355	0.7347	0.7348	0.029	1.01 x 0.81
Band7b8	0.768	0.737	0.7372	0.029	1.24 x 0.79
AVG.[a]	0.7471	0.7394	0.7389		
STD.[b]	0.0194	0.0143	0.0149		

Columns: (1) The label for each dataset (see Table A.2). (2) Flux of the data set using the original T_{sys} table. (3) Flux of the data set using alternative continuous T_{sys} table with the linear relation fitted using all Atm-cal scans. (4) Flux of the data set using continuous T_{sys} table with the linear relation fitted using part of Atm-cal scans. (5) Measured flux errors using original T_{sys} table. (6) Beams of the image using original T_{sys} table.
Rows: a. The average value for each column. b. The standard deviation for each column.
Notes: * denotes data with unusual fluxes. Fluxes from these data are not included in the calculation of the average and standard deviation value.

A.5.3 Flux Comparison

The measured fluxes are recorded in Table A.4, A.5 and A.6. The flux uncertainty can be separated into two parts, the measurement error and the calibration error. The measurement error is calculated as

$$\text{Meas.Err} = \text{rms}\sqrt{N_{\text{beam}}} \tag{A.21}$$

where the rms is the measured noise of the image and N_{beam} is the number of beams across the aperture used to measure the flux. On the other hand, our alternative method to measure T_{sys} should mainly work on reducing the calibration error. To test if our new method improves the flux calibration accuracy, we need to quantify the calibration error for each method we use. For projects with a single dataset, we

Table A.6: Flux measured for data for dataset Band9b (Circinus)

Dataset Label	Flux (Jy)			Meas. Err. (Jy)	Beam (")
	Tsys_orig	Tsys_extrap	Tsys_partextrap		
(1)	(2)	(3)	(4)	(5)	(6)
Band9b1	0.85	0.875	0.849	0.018	0.086 x 0.065
Band9b2	0.96	1	0.983	0.021	0.104 x 0.077
Band9b3	1.27	1.35	1.34	0.016	0.131 x 0.085
AVG.	1.027	1.075	1.057		
STD.	0.178	0.201	0.207		

Columns: (1) The label for each dataset (see Table A.2). (2) Flux of the data set using the original $T_{\rm sys}$ table. (3) Flux of the data set using alternative continuous $T_{\rm sys}$ table with the linear relation fitted using all Atm-cal scans. (4) Flux of the data set using continuous $T_{\rm sys}$ table with the linear relation fitted using part of Atm-cal scans.
Rows: a. The average value for each column. b. The standard deviation for each column.

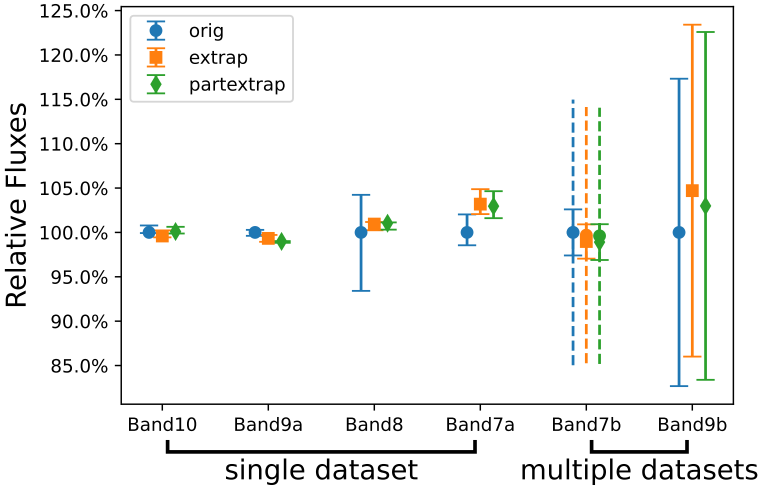

Figure A.18: Comparison of fluxes of images made using the original $T_{\rm sys}$ (orig), continuous $T_{\rm sys}$ extrapolated from all Atm-cal scans (extrap) and that extrapolated from 4 Atm-cal scans (partextrap). The vertical axis are the ratio of fluxes to the fluxes using original method. The first 4 projects contain single dataset while the last two projects contain multiple datasets. The dashed line for Band7b project shows the error including the two datasets that has abnormal flux values (see Table .A.5). We can see the flux consistency is generally better for most of the projects with smaller uncertainties. See description in Section A.5.3.

compare fluxes of images made with 1st half, 2nd half and all scans and calculate the maximal difference between the 3 flux values as the calibration error. For projects with multiple datasets, the calibration error is calculated as the standard deviation of fluxes of the different datasets. Both measurement and calibration errors are recorded in Table A.4, A.5 and A.6.

To further compare how our methods work for datasets from different frequency bands, we normalize the flux values to the flux value using the original discrete $T_{\rm sys}$ calibration method with all Atm-cal scans. The relative uncertainties are calculated as the calibration error divided by the flux value for each method using all Atm-cal scans. The comparison is shown in Fig. A.18. We can see that fluxes using the original $T_{\rm sys}$ table do not differ significantly from the fluxes using alternative $T_{\rm sys}$ and gain tables, with maximal differences smaller than 5%. We also demonstrate that the extrapolated $T_{\rm sys}$ using 4 Atm-cal scans gives us fluxes that are almost the same as when using all Atm-cal scans, which proves it is viable to significantly reduce the number of $T_{\rm sys}$ measurements by using WVR-tracked $T_{\rm sys}$. Furthermore, it seems for most of the datasets, our new methods give better flux consistency, especially for dataset Band8 which brings down the flux calibration uncertainty contribution due to $T_{\rm sys}$ variability from $\sim$ 10% to 0.7%. As we have shown in Section A.3.2, the $T_{\rm sys}$ variation for this dataset is mainly driven by the PWV variation at short time-scale. In this case, the discrete $T_{\rm sys}$ measurements poorly sampled the fluctuations of the real $T_{\rm sys}$ (Fig. A.3). Our new method instead catches the variation in $T_{\rm sys}$ between the discrete ATM calibrations, and thus keeps the flux consistent.

This method also works for dataset Band7b with multiple datasets for which relative flux uncertainties reduce from 2.5% to 1.9%. The only project that gives us larger flux uncertainties using our new methods is the dataset Band9b. For this project, the uncertainties using all 3 methods are quite large ($\sim$ 15%). The large uncertainties are probably due to different uv-coverages, the complex target structure, the relatively high phase noise and maybe the time variability of the flux calibrator in these datasets. This is also a tricky dataset for which the linear fitting does not work as well as for other data sets. In our future work, we will explore if the larger uncertainty is caused by imperfect fitting of the $\hat{T}_{\rm sys}$ versus $\hat{T}_{\rm WVR}$ relation.

A.5.4 Additional considerations for the continuous $T_{\rm sys}$ method

For some targets, the source brightness temperature in single-dish measurements can be significant compared with $T_{\rm sys}$. For example, this may occur for bright galactic targets in 12CO, bright masers, or for some Solar System objects in continuum. As the widths of galactic spectral lines are generally negligible ($< 1\%$) compared with the normal bandwidth (2GHz) used to measure $T_{\rm sys}$, and the continuous $T_{\rm sys}$ method uses a spectrally-averaged broad-band $T_{\rm sys}$, then the effect of bright lines in such cases will be negligible. But for very bright continuum sources such as planets, the spectrally-averaged $T_{\rm sys}$ will potentially be affected by the target brightness. However, the beam of the WVR unit on each antenna is offset from the optical axes of the receiver beams by several arc minutes (depending on the receiver band in use - see ALMA Technical handbook); this means that the WVRs are not pointing to the science target, and in general will not be affected by its strong continuum. Additionally, it has recently become apparent that the method used by ALMA to measure $T_{\rm sys}$, using off-source data along with the normalisation of the visibilities using the autocorrelation, introduces a calibration error for bright sources[2][3]. The planned change is to measure $T_{\rm sys}$ on-source. Again, this should not significantly affect the continuous $T_{\rm sys}$ method, for reasons given above. However, we need to note that this technique cannot be applied to solar observing because $T_{\rm WVR}$ from all WVR channels will be heavily saturated.

For spectral lines, an assumption is made that $T_{\rm sys}$ is mainly affected by PWV, and the correlation of $T_{\rm sys}$ with PWV uses $T_{\rm sys}$ averaged over the spectral window. This is considered reasonable for continuum and most spectral lines, but for calibration of spectral lines coincident with deep Ozone absorption (e.g. see Fig. A.8), the correlation will have a slightly different slope and intercept. In general this is considered a second-order effect; for example, a line exactly coincident with the strong O_3 peak at 428.8GHz in Fig. A.8, the error in the correction of $T_{\rm sys}$ based on the PWV would be $\sim \pm\, 3\%$. A future improvement might be correct the data spectrally rather than using a single channel-averaged value per timestamp. However, this would make the correction table significantly larger (see Section A.5.1).

An additional use of the continuous $T_{\rm sys}$ method could be to correct for the increase in $T_{\rm sys}$ due to shadowing of the antennas. On ALMA, the default is that data taken with any slight blocking of the beam from an antenna, for example by a nearby antenna or building, is flagged and removed during data reduction. In general this cannot be corrected for using the gain calibrator amplitude solution, as this is not ob-

---

[2] https://help.almascience.org/kb/articles/what-are-the-amplitude-calibration-issues-caused-by-alma-s-normalization-strategy

[3] https://help.almascience.org/kb/articles/what-errors-could-originate-from-the-correlator-spectral-normalization-and-tsys-calibration

served at the same sky location as the target. However, if the corresponding increase in T_{sys} due to shadowing is measured continuously, it may be possible to calibrate out some degree of shadowing. Further investigation of this technique should be done.

A.6 Conclusions and Future Work

In this paper, we explore a new method to use continuous datastreams available from WVR monitoring to track the atmospheric opacity and hence T_{sys} in mm and submm data. The aim is to improve flux calibration in conditions where the sky opacity is rapidly varying, and to reduce overheads needed for frequent discrete calibration using internal loads. Here we summarize our main conclusions regarding initial tests of this method.

- There is a tight linear correlation between normalized T_{sys} and T_{WVR}, with typical scatter of $\sim 1\%$. For the worst case of Band 9 data with large T_{sys} variations (50%), the simple linear fit would give us scatter of $\sim 4\%$, which is due to the non-linearity of the relation at high opacities with large T_{sys} variations. Although the exact form of the linear relation varies among different spectral windows and different data sets, we can use as few as 4 Atm-cal scans to determine the slope and intercept of the linear relation, which suggests it is possible to significantly reduce the number of discrete T_{sys} measurements during observations, particularly at high frequencies. Furthermore it is not necessary to perform separate calibrations on the phase calibrator and science target, as the continuous T_{sys} method is able to track differences in T_{sys} between the two.
- We have successfully reproduced the observed tight $\hat{T}_{\text{sys}}$ vs $\hat{T}_{\text{WVR}}$ correlation using ATM modeling for several datasets. The ATM modeling suggests that changing elevation or PWV will give us $\hat{T}_{\text{sys}}$ vs $\hat{T}_{\text{WVR}}$ relation of different slopes when the dry opacity is significant at the observing frequencies. This suggests that we might not get the tight $\hat{T}_{\text{sys}}$ vs $\hat{T}_{\text{WVR}}$ correlation at these frequencies if both PWV and elevation varies significantly. A better strategy to track T_{sys}, especially in the cases mentioned above, would be to calculate the PWV using the continuous T_{WVR} measurements from different WVR channel and combine the measured PWV, elevation and T_{rx} for the dataset to derive the continuous T_{sys} based on the ATM modeling.

- We apply the continuous T_{sys} in calibration and find that it generally gives us more consistent fluxes for the same target. For the dataset Band8 which has the largest PWV variation, the flux calibration uncertainty contribution due to T_{sys} variability is reduced from 10% to 0.7%. The only exception is the dataset Band9b as our new methods give higher flux uncertainties. We suspect part of reasons are due to the imperfect linear fitting of the T_{sys} vs T_{WVR} relation. Since the uv-coverages for the data sets in this project are significantly different, it is hard to confirm this scenario for this data set.

- If this method is used for sub-mm observatories such as ALMA, it can reduce the number of T_{sys} measurements required for high-frequency observations from $10 \sim 20$ down to 5 (4 T_{sys} measurements for the fitting and 1 bandpass T_{sys}) or fewer. Assuming each observation block takes ~ 60 mins and each T_{sys} measurement takes about 30 – 40 seconds, it has the potential to save $\sim 10\%$ of observing time for high frequency observing, which is made more valuable as the amount of time in such good conditions is limited.

Bibliography

Agliozzo, C., Trigilio, C., Pignata, G., et al. 2017, ApJ, 841, 130, doi: `10.3847/1538-4357/aa72a1`

Bachiller, R., Carilli, C., Cox, P., et al. 2003, ALMA Science Advisory Committee (ASAC), 2003, "`https://www.nrao.edu/archives/items/show/34475`"

Baryshev, A. M., Hesper, R., Mena, F. P., et al. 2015, A&A, 577, A129, doi: `10.1051/0004-6361/201425529`

Bean, B., Bhatnagar, S., Castro, S., et al. 2022, PASP, 134, 114501, doi: `10.1088/1538-3873/ac9642`

Brogan, C. 2018, Advanced Calibration Topics - I, "`https://science.nrao.edu/science/meetings/2018/16th-synthesis-imaging-workshop/talks/Brogan_Adv_Cal_1.pdf`"

Casalta, J. M., Molins, A., Bassas, M., et al. 2008, in Society of Photo-Optical Instrumentation Engineers (SPIE) Conference Series, Vol. 7018, Advanced Optical and

Mechanical Technologies in Telescopes and Instrumentation, ed. E. Atad-Ettedgui & D. Lemke, 701838, doi: `10.1117/12.788756`

Condon, J. J., & Ransom, S. M. 2016, Essential Radio Astronomy

Dempsey, J. T., Friberg, P., Jenness, T., et al. 2013, MNRAS, 430, 2534, doi: `10.1093/mnras/stt090`

Emonts, B., Raba, R., Moellenbrock, G., et al. 2020, in Astronomical Society of the Pacific Conference Series, Vol. 527, Astronomical Data Analysis Software and Systems XXIX, ed. R. Pizzo, E. R. Deul, J. D. Mol, J. de Plaa, & H. Verkouter, 267. `https://arxiv.org/abs/1912.09437`

Gonzalez, A., Fujii, Y., Kaneko, K., et al. 2014, in Society of Photo-Optical Instrumentation Engineers (SPIE) Conference Series, Vol. 9153, Millimeter, Submillimeter, and Far-Infrared Detectors and Instrumentation for Astronomy VII, ed. W. S. Holland & J. Zmuidzinas, 91530N, doi: `10.1117/12.2055598`

Hills, R. 2004, ALMA Memo No. 495

Hills, R., Gibson, J., Richer, J., et al. 2001, ALMA memo 352

Mahieu, S., Maier, D., Lazareff, B., et al. 2012, IEEE Transactions on Terahertz Science and Technology, 2, 29, doi: `10.1109/TTHZ.2011.2177734`

Mangum, J. 2002, ALMA Memo No. 434

—. 2017, ALMA Memo No. 602

McMullin, J. P., Waters, B., Schiebel, D., Young, W., & Golap, K. 2007, in Astronomical Society of the Pacific Conference Series, Vol. 376, Astronomical Data Analysis Software and Systems XVI, ed. R. A. Shaw, F. Hill, & D. J. Bell, 127

Moreno, R., & Guilloteau, S. 2002, ALMA memo 372

Pardo, J. R., Cernicharo, J., & Serabyn, E. 2001, IEEE Transactions on Antennas and Propagation, 49, 1683, doi: `10.1109/8.982447`

Payne, J., Vaccari, A., Emerson, D., & Mangum, J. 2001, ALMA Construction Project Book, Chapter 3 Section 2.

Petry, D., Vila-Vilaro, B., Villard, E., Komugi, S., & Schnee, S. 2014, in Society of Photo-Optical Instrumentation Engineers (SPIE) Conference Series, Vol. 9152, Software and Cyberinfrastructure for Astronomy III, ed. G. Chiozzi & N. M. Radziwill, 91520J, doi: `10.1117/12.2054715`

Remjian, A., Biggs, A., Cortes, P. A., et al. 2019, ALMA Technical Handbook,ALMA Doc. 7.3, ver. 1.1, 2019, doi: `10.5281/zenodo.4511522`

Sekimoto, Y., Iizuko, Y., Satou, N., et al. 2008, in Ninteenth International Symposium on Space Terahertz Technology, ed. W. Wild, 253–257

Yun, M., Bastian, T., Holdaway, M., Mangum, J., & Welch, J. 1998, ALMA Memo No. 211